Next generation neural mass models : working memory, all-brain modelling and multi-timescale phenomena

Halgurd Taher

To cite this version:

Halgurd Taher. Next generation neural mass models : working memory, all-brain modelling and multi-timescale phenomena. Modeling and Simulation. Université Côte d'Azur, 2021. English. NNT : 2021COAZ4097 . tel-03561431

HAL Id: tel-03561431
https://theses.hal.science/tel-03561431
Submitted on 8 Feb 2022

UNIVERSITÉ
CÔTE D'AZUR

ÉCOLE DOCTORALE
SCIENCES
FONDAMENTALES
ET APPLIQUÉES

THÈSE DE DOCTORAT

Modèles de masse neuronale de nouvelle génération : mémoire de travail, modélisation du cerveau entier et phénomènes multi-échelles de temps

Halgurd TAHER

Inria Sophia Antipolis - Méditerranée Research Centre

Présentée en vue de l'obtention du grade de docteur en Physique
d'Université Côte d'Azur
Dirigée par : Mathieu Desroches
Co-encadrée par : Simona Olmi
Soutenue le : 09/12/2021

Devant le jury, composé de :
Daniele Avitabile, Associate Prof., VU
Bruno Cessac (président du jury), DR Inria, Inria
Mathieu Desroches, CR Inria, Inria
Olivier Faugeras, DR Inria, Inria
Ernest Montbrió, Associate Prof., UPF
Simona Olmi, CR CNR, CNR
Alessandro Torcini, Prof., CYU
Krasimira Tsaneva-Atanasova, Prof., UoE

Inria

Modèles de masse neuronale de nouvelle génération : mémoire de travail, modélisation du cerveau entier et phénomènes multi-échelles de temps

Jury:

Président du jury
Bruno Cessac, DR Inria, Inria Sophia Antipolis-Méditerranée Research Centre

Rapportrices et rapporteurs
Ernest Montbrió, Associate Prof., Universitat Pompeu Fabra
Krasimira Tsaneva-Atanasova, Prof., University of Exeter

Examinatrices et examinateurs
Daniele Avitabile, Associate Prof., Vrije Universiteit Amsterdam
Mathieu Desroches, CR Inria, Inria Sophia Antipolis-Méditerranée Research Centre
Olivier Faugeras, DR Inria, Inria Sophia Antipolis-Méditerranée Research Centre
Simona Olmi, CR CNR, Consiglio Nazionale delle Ricerche
Alessandro Torcini, Prof., CY Cergy Paris Université

Modèles de masse neuronale de nouvelle génération : mémoire de travail, modélisation du cerveau entier et phénomènes multi-échelles de temps

---

Résumé

Dans cette thèse, nous présentons de nouvelles extensions et applications des modèles de masse neurale de nouvelle génération. Montbrió, Pazó et Roxin (MPR) ont montré que le comportement collectif d'un ensemble de neurones intègre-et-tir quadratiques (QIF) peut être décrit en termes de potentiel de membrane moyen et de taux de décharge de façon exacte, ramenant la dimension du problème d'un réseau microscopique infiniment grand à une description macroscopique de petite dimension. Vu que la masse neurale donne accès aux potentiels de membrane moyens, elle peut être utilisée comme un indicateur pour le potentiel de champ local et les signaux EEG.

Une des contributions de cette thèse est l'implémentation de la plasticité synaptique à court terme (STP) dans le modèle MPR. Sur la base d'une théorie synaptique de la mémoire de travail (WM), nous reproduisons les mécanismes de la WM avec un réseau QIF et de sa limite champ moyen exacte dans une configuration multi-population. Le modèle de masse neurale présente des oscillations dans la bande β-γ durant le chargement et le maintien de la mémoire, comme observé dans les expériences, alors que nous rencontrons des bandes β-γ vides en avec un modèle heuristique. De plus, nous indiquons comment ces bandes de puissance sont formées par des résonances entre les fréquences fondamentales, liées au nombre d'éléments retenus en mémoire. Nous fournissons aussi une estimation analytique de la capacité maximale de la WM d'environ cinq éléments.

La deuxième contribution est l'application d'un modèle multi-population pour tester l'hypothèse clinique de la propagation des crises épileptiques. Nous utilisons des connectomes structurels obtenus à partir de scans de MRI de diffusion de sujets sains et de patients épileptiques. Nous décrivons comment les événements de type crise épileptique peuvent être modélisés comme un recrutement d'un état de faible activité à un état de forte activité. Des entrées externes peuvent déclencher un tel événement et conduire à une cascade de recrutements, imitant ainsi la propagation spatio-temporelle des crises. Les résultats numériques suggèrent que les patients épileptiques sont plus sensibles aux événements de recrutement étendus que les sujets sains. Nous trouvons aussi un bon accord entre les premières aires cérébrales à être recrutées dans notre modèle et l'évaluation pré-chirurgicale des réseaux secondaires recrutés.

Comme troisième contribution, nous étudions le réseau et la masse neurale en présence de STP en utilisant des dynamiques lentes-rapides. En fonction de l'amplitude d'un courant périodique lent appliqué à la population, le comportement collectif peut être soit dans un régime d'oscillations sous-seuil, soit dans un régime de bursting, c'est-à-dire alternant entre une dérive quasi-statique et des oscillations rapides de grande amplitude. Les deux régimes sont séparés par un étroit intervalle de paramètres, ressemblant à une *explosion de canards*. Dans cette région, nous signalons des *jump-on canards*, qui s'approchent d'ensembles invariants normalement répulsifs. Pour des séparations d'échelles de temps intermédiaires, le bursting émerge d'une manière continue via des mécanismes d'addition de spike organisés par des *mixed-type torus canards*, des trajectoires qui évoluent à proximité de familles d'équilibres et de cycles limites répulsifs. Pour une séparation d'échelles de temps plus forte, la transition continue est bloquée par des jump-on canards. Les mécanismes observés dans la masse neurale sont également responsables de l'émergence du bursting dans le réseau.

Pour résumer, cette thèse place les modèles de masse neurale de nouvelle génération dans un contexte plus large de modélisation en neurosciences et fournit de nouvelles perspectives pour des travaux futurs. Cela inclut des approches visant à prendre en compte de meilleurs modèles de STP et des idées pour des masses neurales exactes basées sur des modèles de neurones biologiquement plausibles.

Mots clés : systèmes complexes, dynamique non linéaire, théorie du champ moyen, modèle de masse neurale, mémoire de travail, épilepsie, dynamiques lentes-rapides, canards

Next generation neural mass models: working memory, all-brain modelling and multi-timescale phenomena

Abstract

In this thesis we report new extensions and applications of next generation neural mass models. Montbrió, Pazó, and Roxin (MPR) have shown that the collective behavior of an ensemble of quadratic integrate and fire (QIF) neurons can be described in terms of the mean membrane potential and firing rate in an exact manner, reducing the dimension of the problem from an infinitely large microscopic network to a low dimensional macroscopic description. Since the neural mass gives access to the mean membrane potentials, it can be used as a proxy for local field potential and EEG signals.

One contribution of this thesis is the implementation of short-term synaptic plasticity (STP) into the MPR model. Based on a synaptic theory of working memory (WM), we reproduce WM mechanisms using a QIF network and its exact mean-field limit in a multi-population setup. In particular, we report agreement between the behavior of the network and the extended neural mass model and we make a comparison between our model and experimental results on cortical oscillations associated to WM tasks. The neural mass model exhibits oscillations in the β-γ range during memory loading and maintenance, as also observed in experiments, while we encounter empty β-γ bands using a heuristic model. Furthermore we report how these power bands are formed by resonances among fundamental frequencies, which are linked to the number of items retained in memory. We also provide an analytical estimate for the maximal WM capacity of around five items.

The second contribution is the application of a multi-population model in order to test clinical hypothesis of seizure propagation. We use structural connectomes obtained from dMRI scans of healthy subjects and epileptic patients. We describe how seizure-like events can be modeled as a recruitment from low activity to high activity states. External inputs can trigger such an event and lead to a cascade of recruitments, hence mimicking the spatio-temporal propagation of seizures. The numerical results suggest that epileptic patients are more susceptible to extensive recruitment events than healthy subjects. We also find good agreement between the first brain areas to be recruited in our model and the pre-surgical assessment of recruited secondary networks.

As a third contribution we study the network and neural mass in presence of STP using slow-fast dynamics. Depending on the amplitude of a slow periodic current applied to the population, the collective behavior can be either in a regime of subthreshold oscillations or bursting, i.e., alternating between a quasi-static drift and fast large amplitude oscillations. The two regimes are separated by a narrow parameter interval, resembling a *canard explosion*. In this region we report *jump-on canards*, which approach otherwise repelling invariant sets. We study their impact on the emergence of bursting. For intermediate timescale separations bursting emerges in a continuous manner via a spike-adding mechanisms mediated by *mixed-type-like torus canards*, trajectories which evolve nearby families of repelling equilibria and limit cycles. For stronger timescale separation the continuous transition is blocked by jump-on canards. The mechanisms observed in the neural mass are also responsible for the emergence of bursting in the network.

To summarize, this thesis puts next generation neural mass models into a broader context of modeling in neuroscience and provides new perspectives for future work. This includes approaches to take better models of STP into account and ideas for exact neural masses based on biologically plausible neuron models.

Keywords: complex systems, non-linear dynamics, mean-field theory, neural mass model, working memory, epilepsy, slow-fast dynamics, canards

Contents

Chapter 1

Introduction

One of the fundamental goals of neuroscience is to understand the functioning of cognition and behavior, and how it arises from biophysical processes [1]. A desired way of approaching this problem would be to start with first principles of physics, like the Maxwell equations, and build up an accurate mathematical description of the dynamics, which encapsulates the entirety of the known mechanisms. However, given the sheer complexity of biological and specifically neuronal systems, that approach is virtually impossible to perform [2]. A more applicable one is given by mathematical modeling, that is, the attempt to capture the dynamics of the system partially, whilst still allowing to gain insight and to make predictions. Naturally, models are only valid within a specific scope, of which the extent typically (but not always) depends on the level of implemented details.

The upsurge of computational power in the past decades allows for more and more sophisticated simulations of models in computational neuroscience. Here the complexity of neuronal systems can be increased across orders of magnitudes of spatial scales: from chemical processes on molecular level in single cells to large-scale neuronal network models of the human brain. In recent years neuron simulators have become more and more elaborate [3], while at the same time full brain network models, that try to bridge the scale from single neuron dynamics, through microcircuits, towards experimentally accessible macroscopic measures of brain activity [4], have come into play.

Despite the increasing feasibility of large-scale and detailed biophysical simulations, the need for simple models remains unalteredly high, for two main reasons. First of all, detailed models might perform better in predicting and describing experimental results, than simplified ones. Yet, one inevitable characteristic remains and is related to the large number of problem-defining equations and parameters. They can render the model a *black box*, just like the real brain [5], and aggravate the goal of drawing fundamental conclusions from properties of the system.

Secondly, many experimental measurements are of macroscopic nature, e.g. given by local field potential (LFP), electroencephalography (EEG), magnetoencephalography (MEG) or magnetic resonance imaging (MRI) signals. A common approach to improve the interpretation of these signals and to understand how they arise from the microscale, is to model the dynamics starting from the smallest units, e.g. neurons and synapses, and fit the model parameters to the experimental data. However, one is challenged with high-dimensional and ill-posed inverse-problems [6]. As an example, a specific LFP signal distribution across the scalp might arise from a multitude of cellular activity patterns.

An attempt towards simpler macroscopic models is given by *neural mass* models. They aim to capture the dynamics of neuronal populations on macroscopic scale, for example using a firing rate description. Neural mass models are often related to *mean-field* models, but the terms have to distinguished: neural mass refers to population models in general, while mean-field models are typically macroscopic descriptions of an underlying microscopic system, obtained by averaging state variables over the ensemble. Neural mass models on the other hand are often based on heuristic arguments, like the well-established

Wilson-Cowan (WC) model [7]. The applications of neural mass model, neural field models and statistical approaches to questions of computational neuroscience range from memory [8], in particular working memory [9, 10], over perception [11] and motor planning [12], towards cognition [13] and behavior [14].

1.1 Next generation neural mass models

In recent years a new class of neural mass models has emerged, that is at the interface of population modeling in neuroscience and mean-field theory in statistical physics [15, 16]. The basis of applying methods from mean-field theory to neuronal dynamics is given by the idea that neurons represent oscillators. Their interactions can give rise to complex dynamical behavior, like asynchronous firing patterns, synchronization, chimera states, quasi-periodicity, chaos and bursting [17–19], many of which are evidenced by experimental studies [20–23]. As a matter of fact, LFP and EEG signals arise due to synchronized activity of single neurons [24, 25], that results in an aggregated and measurable electric field potential [26].

These *next generation neural mass models* [27] are not of heuristic nature, but directly derived from the single neuron dynamics and the interactions in the network. Hence, as opposed to heuristic models, the parameters of the microscopic system have direct macroscopic counterparts and one can link the two scales in order to understand the emerging dynamics. One of the remarkable properties of this approach is the *exactness* of the mean-field limit: in the thermodynamic limit and under some assumptions, the collective dynamics of the microscopic network is exactly described by the resulting mean-field equations, without the necessity of heuristics or approximations. In other words, it is derived from first principles given by the underlying network.

The starting point of the exact model by Montbrió, Pazó, and Roxin (MPR) are quadratic integrate and fire (QIF) neurons [16], a phenomenological model for spiking neuron dynamics. Given a fully coupled network of QIF neurons, including heterogeneities, as well as synaptic interactions via action potentials, an exact mean-field limit can be performed. The approach is based on the pioneering work of Ott and Antonsen (OA), who showed that under certain conditions, the dynamics of infinitely sized networks of phase oscillators will converge to a low dimensional manifold, hence reducing the number of variables and equations, required to describe the macroscopic dynamics [15, 28]. The OA ansatz can serve as a recipe to perform this exact reduction and was firstly applied to the prototypical model for synchronization, namely the Kuramoto model [29]. Remarkably, the OA ansatz is applicable to a broader class of phase oscillator networks and thereby has founds its way into the field of computational neuroscience. Under certain assumptions (see Chapter 2) the QIF neuron is rendered equivalent to the Ermentrout-Kopell model [30], also referred to as θ-model, which represents a phase oscillator model for neuronal dynamics and indeed fits into the class of problems, which can be treated within the OA framework. The OA ansatz applied to an ensemble of QIF neurons, in the seminal work of MPR, has lead to an upsurge of next generation neural mass models.

These models try to capture the macroscopic dynamics of networks of spiking neurons using just a few variables, namely the population firing rate and mean membrane potential. They hence contribute crucially to studies of collective phenomena in these otherwise high-dimensional dynamical systems and allow for simple analytical and numerical treatment. Various applications of the MPR model has been studied in recent years. They range from the inclusion of delayed synaptic interactions [31], giving rise to chaos, to studies of cortical oscillations in multi-population models [32] and cross-frequency coupling [33]. While the original MPR model accounts for chemical synapses, the methodology can straightforwardly been applied to include as well electrical synapses, formed by gap junctions between neurons [34, 35]. Extensions of the MPR model towards sparse networks [36] and fluctuation driven dynamics have been proposed [37].

1.2 Outline

The content of this work is divided into four main chapters, which aim to find novel applications of these next generation neural mass model, propose extensions to include more biologically relevant phenomena and study the effect of timescale separation. The thesis will exemplify how next generation neural mass models can give meaningful insight into neuronal firing rhythms, cognitive processes and brain pathologies, despite being idealized mathematical descriptions of complex systems.

Model derivation and mathematical framework

First of all, in Chapter 2 the microscopic and macroscopic models are not only introduced and derived, but also put into the general context of modeling in neuroscience. This is particularly important in order to understand the limitations and capabilities, as well as the advantages and novelties of next generation neural mass models. Specifically, we go through the key aspects of the derivation of the MPR model, starting from a population of interacting point neurons [16]. The groundwork for this exact reduction methodology was done by OA [15]. It will be shown that under certain assumptions, the MPR model can be extended to account for short-term synaptic plasticity (STP), i.e, dynamically changing synaptic weights [38, 39], without the loss of exactness. This way one can bridge the spatial scale, from single neuron dynamics to collective population dynamics, through first principles, whilst keeping biologically relevant effects like spike synchrony and STP.

Working memory

This forms the foundation for one of the main results, that is, the application of the extended model with STP towards working memory (WM). In Chapter 3 we introduce this cognitive system and explain the candidates that are thought to be its neural correlates, like persistent firing [40–42] and so-called *population bursts* (PBs) [9, 43]. For this chapter two approaches are compared: (1) using a large-scale microscopic network of hundreds of thousands of QIF neurons with STP and (2) a system of neural masses with only 10 equations. Naturally we find perfect agreement, owing to the exactness of the mean-field limit. The contribution of this chapter is first of all a proof-of-concept for the application of the next generation neural mass to WM. Like previous neural mass approaches [10], the model is capable of mimicking mechanisms like working memory loading, maintenance and rehearsal. It is also able to yield an estimate of the maximum working memory capacity of around five items, as well as providing insight into the so-called primacy and recency effect [44, 45] . Beyond encompassing the capabilities of previous models, we find a significantly better agreement between theoretical and experimental results regarding the role of cortical oscillations during WM tasks. The widely used WC type models do not account for subthreshold oscillations and spike synchrony, i.e, when many neurons in a population fire nearly simultaneously [32, 46], hence lack essential characteristic of cortical oscillations, that are observed experimentally. For example, EEG measurements in humans and LFP measurements in monkeys show β and γ band activity during working memory tasks [47–49], which are absent in WC type models, but can be reproduced using the next generation neural mass with STP. In addition we provide a deep analysis, using a multi-population WM network built of neural masses, on how the frequency bands of cortical oscillations are shaped by resonance lines and how their structure changes, depending on how many items are maintained in WM. The investigation of the various frequency bands relies on the fact that the next generation models account for spike synchrony and give direct access to the mean membrane potential of the neural population, that can be used as a proxy for LFP and EEG signals.

All-brain modeling

Electroencephalography, in particular intracranial EEG (iEEG) and stereotactic EEG (SEEG), plays also an essential role for clinicians who work with patients suffering from drug-resistant epilepsy. For these patients, one possible line of treatment is the surgical resection of brain tissue, that is preceded by qualitative presurgical evaluation by clinicians, based on various imaging techniques. The aim of the assessment is to identify the epileptogenic zone (EZ), referring to a patient-specific brain region, where seizures arise [50] and start to recruit secondary networks known as propagation zones (PZs) [51–54]. An alternative way of assessing EZs and PZs is given by iEEG and SEEG. Additionally, a non-invasive imaging method called diffusion-weighted MRI (dMRI) has been developed in recent years and is able to gain structural information of the whole brain. Using these patient-specific *connectomes*, coupled with phenomenological models of seizure generation, one can try to predict surgical outcomes [55–57]. In these computational models, each brain region is represented by a network node and the network topology is derived from the structural connectomes obtained by dMRI or other imaging modalities. In Chapter 4 we demonstrate how each of the nodes in an all-brain network can be represented by a next generation neural mass model, in order to simulate seizure-like events. The employed data set comprises dMRI connectivities of 20 healthy subjects and 15 epileptic patients. For the latter, data on the presurgical evaluation is available, identifying the nodes that are supposedly either a EZ or PZ. Using the empirical data, we show how the multi-population neural mass model can reproduce seizure-like events. The system can be placed in a multistable regime, characterized by low activity (LA) and high activity (HA) states of single nodes. Exciting a node corresponding to the EZ via a transient external current, can lead to a switch from LA to HA and trigger a cascade of recruitments of other nodes to the HA state, eventually leading to recruitment of the whole network. This cascade of recruitments is what we refer to as seizure-like event. One of the striking results is an agreement between the simulations and the clinical data: the recruitment order predictions of the exact multi-population model are in line with the presurgical assessment of the PZs. Multistability between LA and HA states in the multi-population network are fundamental for complex firing rhythms to emerge and at the basis of seizure-like events.

Slow-fast dynamics in large networks

Complex dynamical behavior can also arise due to interactions across timescales and in particular when dynamical system exhibit multistability. One of the most prominent examples for this is neuronal *bursting*, describing an alternation between quiescence and fast repetitive firing as observed in many experiments [22, 23, 58–63]. Bursting emerges due to a separation of timescales, into slow and fast dynamics, and it can be understood using singular perturbation techniques. To this end, the basic principles of slow-fast dissection [64, 65] are introduced in Chapter 2 and used to revise the famous *canard* solutions [66], which are trajectories evolving nearby otherwise repelling locally invariant sets. While slow-fast dissection serves as a powerful tool for low dimensional systems, computational limitations complicate the analysis in higher dimensional systems, like networks of spiking neurons. Here OA approach and exact neural mass models come into play. Only a few recent works exploit the OA framework in order to understand emerging slow-fast dynamics in large networks [67, 68]. In Chapter 5 we study the transition from quasi-static low activity firing rhythms to bursting in a population of QIF neuron with STP, subject to a slow external current. The neural mass model linked with slow-fast dissection facilitates the understanding on how bursting emerges in the microscopic QIF network and gives insight into a complicated interplay of slow-fast phenomena. The results comprise surprising mechanisms, namely so-called *jump-on canards* which are related to the additional timescales coming along with the presence of STP. Moreover, we find that bursting can emerge in a continuous manner through a spike-adding mechanisms, that is mediated by mixed-type-like torus canards [69]. Typically canards are observed in highly timescale separated problems. Here however the continuous emergence of bursting via mixed-type-like torus canards is being interfered by the jump-on canards and breaks down for strong timescale separations, ultimately leading to a differentiation of the routes to bursting.

Chapter 2

Neural mass model, synaptic plasticity and slow-fast dynamics

Overall, modeling of brain dynamics is a multiscale problem. Spatially extended neurons can be modeled in a realistic manner, using detailed biophysical multi-compartment approaches that take morphology and the spatiotemporal propagation of electrical currents along the axon and dendritic tree into account [70]. However, due to the heavy computational and numerical load that comes along with the numerical integration of partial differential equations, modeling large network of spiking neurons with such level of detail is challenging.

An alternative way of capturing the rich dynamics of real neurons are point neuron models, one of the most studied ones being the Hodgkin-Huxley model for the squid giant axon [71]. As illustrated in Fig. 2.1, it has been the gold standard for point neuron model in terms of biophysical plausibility over many decades, but comes at high cost in terms of computational load. On the other end of the scale we can find the integrate and fire (IF) models, in particular the leaky integrate and fire (LIF) neuron, known for its simplicity and widely used in theoretical studies [9, 72–75]. In general IF model consist of a differential equation describing the temporal evolution of the membrane potential, together with a reset rule. The latter accounts for the spiking behavior of the neuron, i.e, when a certain voltage threshold is reached, an action potential is generated and the membrane potential instantaneously reset to some lower value. For the LIF neuron the membrane potential is the only state variable and its dynamics is characterized by a linear voltage term.

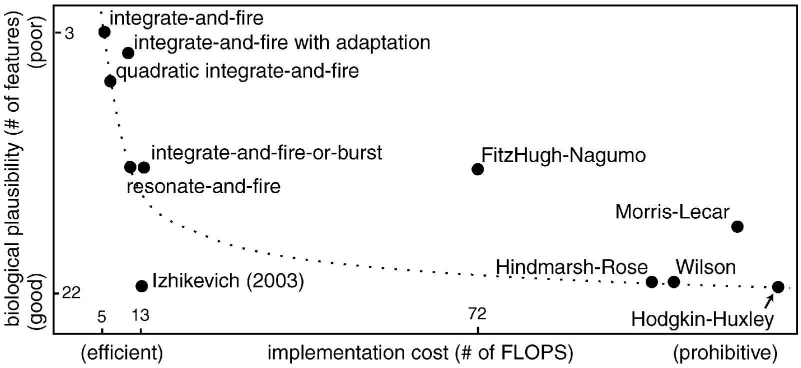

Figure 2.1: Comparison of point neuron models. Biological plausibility in terms of the number of reproduced features vs. the computational load. Extracted from [76].

Over the years various improvements for the LIF model have been suggested in order to loosen its limitations, for example by implementing a quadratic voltage term and neural adaptation as in the Izhikevich model [77]. Other generalizations and extensions of the LIF model, named *GLIF* and *E-GLIF* (extended generalized LIF), were proposed and enrich the variety of possible firing patterns, while keeping biophysically meaningful model parameters [78, 79]. The *adaptive exponential integrate and fire* (AdEx) model [80], which tries to combine simplicity, plausibility and meaningfulness, has proven to predict spike times of detailed biophysical models with high accuracy and is also subject of recent studies [81, 82].

The focus of this work lies on the QIF neuron (see also Fig. 2.1). In terms of plausibility and simplicity it can be placed between the standard LIF model and the Izhikevich model (in absence of adaption). It is outstanding in the family of IF models, since it represents the canonical model for Saddle-Node on Invariant Circle (SNIC) bifurcations (see Section 2.1 below) [30, 83].

In the following the various elements of the model underpinning this work will be introduced, starting from the microscopic scale at single neuron level. These neurons are then considered in a network setup, accounting for a single neuronal population with recurrent synapses. Here one can introduce the synaptic dynamics in form of short-term synaptic plasticity. Under certain conditions, in particular imposed on the heterogeneity among neurons, one can achieve an exact mean-field reduction of the system to a low dimensional model, based on the Ott-Antonsen ansatz [15, 16].

2.1 Excitability types and canonical model

Spiking neuron models can be characterized by their response to the injection of a current, which is often measured in terms of the f-I curve, determining the relation of firing frequency f versus input current I. The dynamics of Hodgkin-Huxley type neurons can either be in the excitable or tonic regime [71]. Excitable neurons in the absence of input approach an equilibrium. However, a sufficient input can excite the membrane potential beyond a threshold leading to the firing of a single action potential, before going back to the rest state. Tonic neurons on the other hand fire periodically with a frequency f. Based on the behavior at the transition from excitable to tonic dynamics, one can distinguish (at least) two classes of membranes. For class I neurons the f-I continuously transitions from quiescence ($f = 0$) to repetitive firing with arbitrarily slow frequencies ($f > 0$). Typically it occurs at a SNIC bifurcation. Class II neurons on the other hand exhibit a discontinuous f-I curve, leading to finite firing rates at the onset of tonic firing, and they are usually associated with a Hopf bifurcation. This Hopf bifurcation is often subcritical, for example in the Hodgkin-Huxley, FitzHugh-Nagumo [84, 85] and Morris-Lecar model [86]. Here we want to study the dynamics of class I neurons, characterized by SNIC bifurcations, for which the QIF model represents a canonical model. We will start with the AdEx neuron and show how the QIF model can be directly obtained by performing a series expansion.

2.1.1 Adaptive exponential integrate and fire

The dynamics of the AdEx neuron is governed by two differential equations [Eqs. (2.1)] and two reset rules [Eqs. (2.2)], which describe the temporal evolution of the membrane potential and adaptation variable.

$$C\frac{\mathrm{d}V}{\mathrm{d}t} = -g_\mathrm{L}(V - E_\mathrm{L}) + g_\mathrm{L}\Delta_T \mathrm{e}^{\frac{V-V_T}{\Delta_T}} - w + I \tag{2.1a}$$

$$\tau_w\frac{\mathrm{d}w}{\mathrm{d}t} = a(V - E_\mathrm{L}) - w \tag{2.1b}$$

$$\text{reset rule 1: if } V > V_\mathrm{thresh}\colon\ V \leftarrow V_\mathrm{reset} \tag{2.2a}$$

$$\text{reset rule 2: if } V > V_\mathrm{thresh}\colon\ w \leftarrow w + b \tag{2.2b}$$

The parameters of the AdEx neuron provide biological interpretability and are described in Table 2.1.

Table 2.1: Parameters of the AdEx model and their units.

Symbol	Description	Unit
C	Membrane capacitance	$1\,\mathrm{F} = \mathrm{A}^2\ \mathrm{s}^4/(\mathrm{kg\ m}^2)$
g_L	Leak conductance	$1\,\mathrm{S} = \mathrm{A}^2\ \mathrm{s}^3/(\mathrm{kg\ m}^2)$
E_L	Leak reversal potential	$1\,\mathrm{V} = \mathrm{kg\ m}^2/(\mathrm{A\ s}^3)$
V_T	Voltage threshold for spike initiation	$1\,\mathrm{V} = \mathrm{kg\ m}^2/(\mathrm{A\ s}^3)$
Δ_T	Slope of spike initiation	$1\,\mathrm{V} = \mathrm{kg\ m}^2/(\mathrm{A\ s}^3)$
I	Input current	$1\,\mathrm{A}$
τ_w	Adaptation timescale	$1\,\mathrm{s}$
a	Adaptation coupling parameter	$1\,\mathrm{S} = \mathrm{A}^2\ \mathrm{s}^3/(\mathrm{kg\ m}^2)$
b	Adaptation increment	$1\,\mathrm{S} = \mathrm{A}^2\ \mathrm{s}^3/(\mathrm{kg\ m}^2)$

For simplicity we will neglect the adaptation term in the following ($w = \text{const.} = 0$) and approximate the right hand side of Eq. (2.1a) for V values nearby the spike initiation threshold V_T. Specifically, we perform a Taylor series expansion in V, up to the second order term and obtain:

$$C\frac{\mathrm{d}V}{\mathrm{d}t} = \frac{g_\mathrm{L}(V - V_T)^2}{2\Delta T} + g_\mathrm{L}\left(E_\mathrm{L} + \Delta T - V_T\right) + I \quad . \tag{2.3}$$

Eq. (2.3) can be rewritten by rescaling the membrane potential as $\hat{V} = V/(2\Delta T)$, yielding:

$$\tau_\mathrm{m}\frac{\mathrm{d}\hat{V}}{\mathrm{d}t} = \hat{V}^2 - A\hat{V} + \hat{I} \quad . \tag{2.4}$$

Here the new quantities are as follows:

$$\tau_\mathrm{m} = \frac{C}{g_\mathrm{L}} \tag{2.5a}$$

$$A = \frac{V_T}{\Delta T} \tag{2.5b}$$

$$\hat{I} = \frac{1}{2} + \frac{1}{2\Delta T}\left(E_\mathrm{L} - V_T + \frac{V_T^2}{2\Delta T} + \frac{I}{g_\mathrm{L}}\right) \tag{2.5c}$$

The Izhikevich model displays the same form of the right hand side as Eq. (2.4), but has additionally the adaptation dynamics described in Eq. (2.1b).

If we instead use the transformation $\hat{V} = (V - V_T)/(2\Delta T)$ we obtain the quadratic integrate & fire (QIF) model as stated below,

$$\tau_\mathrm{m}\frac{\mathrm{d}\hat{V}}{\mathrm{d}t} = \hat{V}^2 + \hat{I} \quad , \tag{2.6}$$

this time with

$$\hat{I} = \frac{1}{2} + \frac{1}{2\Delta T}\left(E_\mathrm{L} - V_T + \frac{I}{g_\mathrm{L}}\right) \quad . \tag{2.7}$$

2.1.2 Quadratic integrate & fire neuron

As shown above, the QIF model can be seen as an approximation of the AdEx model and is equivalent to the Izhikevich one, both in absence of adaptation. We will write the dynamics of the membrane potential $V(t)$ of a QIF neuron as follows[1],

$$\tau_\mathrm{m}\frac{\mathrm{d}V(t)}{\mathrm{d}t} = \tau_\mathrm{m}\dot{V} = V^2 + \eta + I_\mathrm{S}(t); \qquad \text{reset rule: if } V > V_\mathrm{thresh}\text{: } V \leftarrow V_\mathrm{reset}, \tag{2.8}$$

where τ_m is the membrane time constant, which can be eliminated via a time rescaling $t \to t/\tau_\mathrm{m}$. In the rescaled QIF model the dynamics reads:

$$\dot{V} = V^2 + \eta + I_\mathrm{S}(t) \quad , \tag{2.9}$$

and time is measured in units of τ_m. Parameter η represents a constant external current, that determines the neuronal excitability. In absence of the additional time dependent current $I_\mathrm{S}(t)$, the QIF neuron exhibits two possible dynamics, depending on the sign of η. The different cases are depicted in Fig. 2.2 and described below.

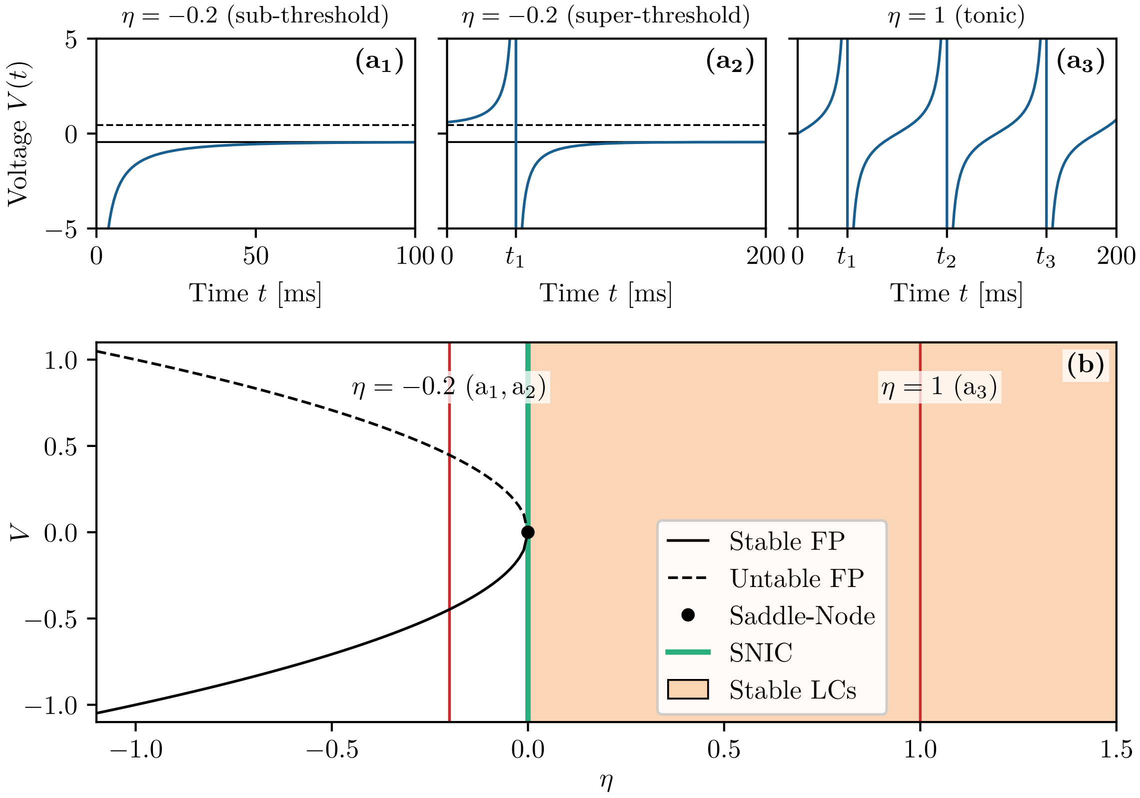

Figure 2.2: Dynamics of a single QIF neuron. **($\mathbf{a_1}$)** shows the excitable case with $V(0) < \sqrt{|\eta|}$, **($\mathbf{a_2}$)** with $V(0) > \sqrt{|\eta|}$ and **($\mathbf{a_3}$)** corresponds to tonic firing. The solid and dashed black lines mark $V = \mp\sqrt{|\eta|}$ and spike times are denoted by t_1, t_2, t_3. **(b)** Bifurcation diagram V versus η. The solid and dashed black lines show the stable and unstable fixed points (FP) of Eq. (2.9). The saddle-node bifurcation at $(V = 0, \eta = 0)$ is marked by a black dot; the SNIC bifurcation at $\eta = 0$ by a green line. The orange region marks $\eta \geq 0$, for which stable limit cycles exist. Parameter values are: $\tau_\mathrm{m} = 20\,\mathrm{ms}$.

---

[1] For the sake of simplicity we will omit the hat symbols introduced in Eq. (2.4) in the following and additionally set $I = \eta + I_\mathrm{S}(t)$ to be in line with notations found in literature.

Excitable dynamics

(a_1) If η is negative, the neuron is excitable. For any initial condition $V(0) < \sqrt{|\eta|}$, it approaches the resting potential $V = -\sqrt{|\eta|}$ [dashed line in Fig. 2.2(a)] asymptotically. The value $V = -\sqrt{|\eta|}$ corresponds to the stable fixed point branch in Fig. 2.2(b). The unstable fixed point is a saddle equilibrium. Both branches disappear via a saddle-node (SN) bifurcation.

(a_2) For initial values $V(0) > \sqrt{|\eta|}$ the membrane potential grows unbounded, until the reset mechanism in Eq. (2.8) applies. This describes the spiking behavior of the QIF neuron: whenever $V(t)$ reaches the threshold value V_{thresh}, the neuron spikes (or fires) and an action potential is generated. Each spike leads to an instantaneous reset of the membrane potential to the reset value V_{reset}. The time of the k-th spike is denoted t_k.

Tonic firing

(a_3) If η is positive, the neuron fires tonically and emits a regular train of spikes with frequency $\nu_0 = \sqrt{\eta}/\pi$. Tonic firing is related to the emergence of stable limit cycles via a SNIC bifurcation located at $\eta = 0$. The SNIC bifurcation can be understood more easily in the θ-model, introduced below.

2.1.3 From point neuron to phase oscillator

The entire dynamics of a single QIF neuron described above can be transformed to that of a phase oscillator, given the limit $V_{\text{thresh}} = -V_{\text{reset}} \to \infty$, using the following variable transformation:

$$V(t) = \tan\frac{\theta(t)}{2} \tag{2.10a}$$

$$\theta(t) = 2\arctan V(t) \quad . \tag{2.10b}$$

One can now calculate the dynamics of θ via $\frac{\mathrm{d}\theta}{\mathrm{d}t}$ and obtain the well-known Ermentrout-Kopell model, also referred to as θ-model [30].

$$\dot{\theta} = (1-\cos\theta) + (1+\cos\theta)(\eta + I_{\text{S}}) \tag{2.11}$$

The spiking behavior of the QIF neuron is reflected in the θ-neuron by the fact that $\lim_{\theta\to\pi^-}\tan\frac{\theta}{2} = \infty$ and $\lim_{\theta\to\pi^+}\tan\frac{\theta}{2} = -\infty$. Hence, in the limit $V_{\text{thresh}} = -V_{\text{reset}} \to \infty$, the reset rule $V > V_{\text{thresh}}$: $V \leftarrow V_{\text{reset}}$ applies exactly when θ crosses $\theta = \pi$ from below.

Using the θ description of the QIF neuron, we can see that the firing of a spike is mediated by the saddle, that repels the trajectory, forcing it through $\theta = \pi$, see the trajectory (a_2) in Fig. 2.2. Saddle and node collide at the critical value $\eta = 0$ and vanish for $\eta > 0$, leaving a stable limit cycle.

2.2 Network model and mean-field limit

In order to investigate the emerging dynamics of interacting neurons, one can consider an ensemble of synaptically coupled point neurons, in this case, QIF neurons. In such a network of $i = 1, \ldots N$ QIF neurons, the dynamics of the system reads

$$\dot{V}_i = V_i^2(t) + \eta_i + \frac{1}{N}\sum_{j=1}^{N}\tilde{J}_{ij}(t)S_j(t) + I_{\text{S}}(t) \quad , \tag{2.12}$$

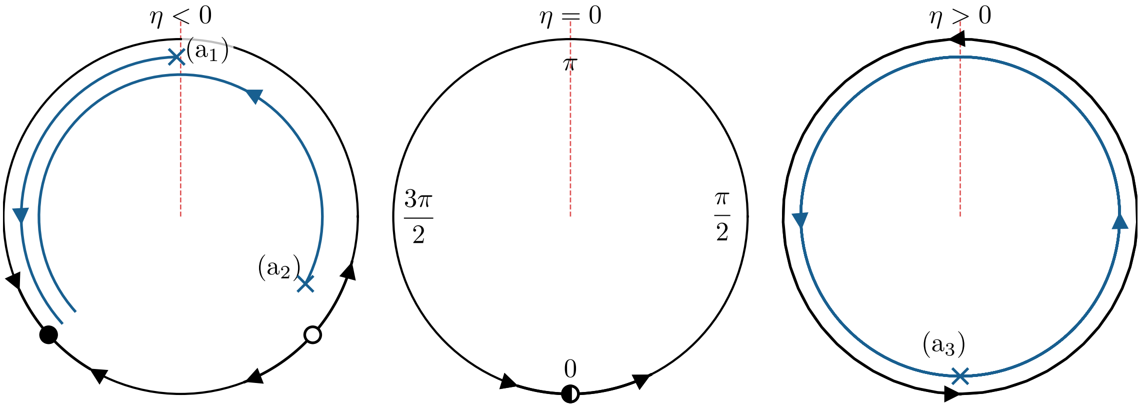

Figure 2.3: Dynamics of the θ-neuron. The blue trajectories (a_1 - a_3) correspond to the ones shown in Fig. 2.3(a) and blue crosses mark their initial conditions. The filled black circle represents a node equilibrium, the empty one a saddle. For $\eta = 0$ they form a saddle-node. The arrows point in the direction of $\dot{\theta}$ given in Eq. (2.11). Whenever a trajectory crosses the red line at $\theta = \pi$ from below, the neuron emits a spike.

with the strength of the direct synapse $\tilde{J}_{ij}(t)$ from neuron j to i that, in absence of plasticity, we assume to be constant in time and all identical, i.e. $\tilde{J}_{ij}(t) = J$. The sign of J determines if the neurons are excitatory ($J > 0$) or inhibitory ($J < 0$). Moreover the excitability parameters η_i can be heterogeneously distributed. Now the total synaptic current due to the recurrent connections with presynaptic neurons reads $s(t) = \frac{1}{N}\sum_{j=1}^{N} S_j(t)$ and we can rewrite the dynamics as:

$$\dot{V}_i = V_i^2(t) + \eta_i + Js(t) + I_\mathrm{S}(t) \quad . \tag{2.13}$$

For instantaneous postsynaptic potentials (corresponding to Dirac δ-spikes) the neural activity $S_j(t)$ of neuron j is given by

$$S_j(t) = \sum_{t_j(k)<t} \delta(t - t_j(k)), \tag{2.14}$$

where $S_j(t)$ is the spike train produced by the j-th neuron and $t_j(k)$ denotes the k-th spike time in such sequence. In such a case the total synaptic current $s(t)$ is identical to the instantaneous mean firing rate of the network, given by the superposition of all spike trains:

$$r(t) = \frac{1}{N}\sum_{j=1}^{N}\sum_{t_j(k)<t} \delta(t - t_j(k)) = \frac{1}{N}\sum_{j=1}^{N} S_j(t) = s(t) \quad . \tag{2.15}$$

In general, the dynamics of S_j might be more complex, for example, given by a first-order differential equation with time scale τ_s, driven by the single neuron spike train, as stated below.

$$\tau_s \dot{S}_j = -S_j + \sum_{t_j(k)<t} \delta(t - t_j(k)) \tag{2.16}$$

We will restrict the derivation to the case of instantaneous synapses for which $s(t) = r(t)$. However, it is worth noting, that the application of the mean-field framework introduced in Section 2.2.1 can also be applied in presence of exponentially decaying synaptic activities obeying Eq. (2.16) [68, 87].

2.2.1 Thermodynamic limit

In order to derive a macroscopic model for the collective dynamics of Eq. (2.13), we will follow the derivation of Montbrió, Pazó, and Roxin [16], which has a QIF network as a starting point. Alternatively, one might start from the θ-neuron Eq. (2.11) within the OA framework. However, it has been shown in Ref. [16] that the two approaches, namely, the *Lorentzian* ansatz (to be introduced below) and the OA ansatz, are equivalent. The derivation comprises two different steps of dimensionality reduction, in order to go from an infinitely large microscopic network of QIF neurons to a finite-dimensional macroscopic description of the collective dynamics.

We start the derivation of the exact neural mass model by considering Eq. (2.13) in the thermodynamic limit $N \to \infty$, thereby passing from a discrete description of the microscopic network in terms of the $V_i(t)$ to a continuous one in terms of a probability density function (PDF) denoted by $\rho(V|\eta,t)$. The PDF $\rho(V|\eta,t)$ determines the fraction $\mathrm{d}V\rho(V|\eta,t)$ of neurons which have a membrane potential $V \in [V, V+\mathrm{d}V]$, given a fixed value η. Analogously, the η_i become distributed according to a PDF $g(\eta)$ and at any time t it must hold that

$$\int_{-\infty}^{\infty} \mathrm{d}V\rho(V|\eta,t) = g(\eta) \quad . \tag{2.17}$$

Moreover, a natural consequence of the conservation of the number N of particles, i.e, neurons, in the system is the *continuity equation* (2.18), which describes the dynamics of the distribution, given the drift $\frac{\mathrm{d}V}{\mathrm{d}t} = \dot{V}(V|\eta,t)$ for a fixed η.

$$\frac{\partial \rho}{\partial t} + \frac{\partial}{\partial V}\left[\rho \dot{V}\right] = 0 \tag{2.18}$$

With the right hand side (RHS) of Eq. (2.13) put into Eq. (2.18) we obtain:

$$\frac{\partial \rho}{\partial t} + \frac{\partial}{\partial V}\left[\rho(V^2 + I(\eta,t))\right] = 0 \quad , \tag{2.19}$$

where $I(\eta,t) = \eta + Jr(t) + I_\mathrm{S}(t)$ denotes the total current.

Stationary solution

The next step is to realize that the continuity Eq. (2.19), given $I_\mathrm{S}(t) = 0$, possesses a trivial stationary solution $\rho_0(V|\eta)$, i.e, for $\frac{\partial \rho}{\partial t} = 0$:

$$\frac{\partial}{\partial V}\left[\rho_0 \dot{V}\right] = 0 \tag{2.20}$$

$$\Leftrightarrow \rho_0 \dot{V} = \text{const.} \tag{2.21}$$

$$\Leftrightarrow \rho_0 \propto (\dot{V})^{-1} = \frac{1}{V^2 + \eta + Jr} \quad . \tag{2.22}$$

The form of Eq. (2.22) is known as Lorentzian distribution and reveals already physical properties of the system as follows. First of all the density is inversely proportional to the velocity $\dot{V}$, hence neurons will lay dense along V regions with low velocity and sparse along V regions with high velocity. Secondly, for non-tonic neurons with $\eta + Jr < 0$, as in Fig. 2.2(a, b), the density $\rho_0(V|\eta)$ possesses a singularity, when the denominator $V^2 + \eta + Jr$ of Eq. (2.22) becomes zero, i.e., at $V = \pm\sqrt{-(\eta + Jr)}$. That corresponds to the equilibria of a single QIF neuron, as can be seen from Eq. (2.9), of which only the negative one is stable. In other words, the stationary PDF $\rho_0(V|\eta)$, given quiescent neurons, takes the form of a Dirac-δ located at the resting potential (see also Section 2.1.2).

2.2.2 First reduction: Lorentzian ansatz

In [16] it was suggested that for every fixed η, the PDF $\rho(V|\eta, t)$ converges to a Lorentzian, even for the non-stationary case and independent of initial conditions. This is the first reduction of the dimensionality of our problem. With this assumption we can make the following *Lorentzian ansatz*:

$$\rho(V|\eta, t) = \frac{1}{\pi} \frac{x(\eta, t)}{[V - y(\eta, t)]^2 + x^2(\eta, t)} \quad . \tag{2.23}$$

This $\rho(V|\eta, t)$ corresponds to a generic Lorentzian distribution with a time and η-dependent half width at half maximum (HWHM) $x(\eta, t)$ and center $y(\eta, t)$. A priori, this ansatz represents a strong assumption, namely that the dynamics takes place in this lower dimensional space of Lorentzian distributions. Nevertheless, as mentioned before, it turns out that the Lorentzian ansatz is equivalent to the OA ansatz for phase oscillator networks in the thermodynamic limit. For that, convergence to the so-called OA manifold (here corresponding to Lorentzian distributions) has been proven under certain conditions [28, 88].

For the moment we will stay within the framework of QIF neurons and the Lorentzian ansatz, in order to facilitate the physical interpretation of the reduction, specifically of $x(\eta, t)$ and $y(\eta, t)$. The ultimate goal of the mean-field theory here is to obtain a finite dimensional description of the macroscopic dynamics in the limit $N \to \infty$. Naturally the observables of interest are the mean membrane potential $v(t)$ and the mean firing rate $r(t)$ of the QIF ensemble. It stands to reason to calculate the means $v(\eta, t)$, $r(\eta, t)$ for a given, fixed η, and later on calculate the mean over η via the PDF $g(\eta)$.

The firing rate enters into the equation of motion Eq. (2.19), hence is required for the self-consistency of the approach and can be seen as the probability flux through infinity, yielding

$$\begin{aligned} r(\eta, t) &= \lim_{V \to \infty} \rho(V|\eta, t)\dot{V}(V, \eta, t) = \lim_{V \to \infty} \frac{x(V^2 + I)}{\pi(x^2 + (V - y)^2)} \\ &= \frac{1}{\pi} x(\eta, t) \quad . \end{aligned} \tag{2.24}$$

This simple result links the firing rate of a population of QIF neurons with excitability η to the width parameter $x(\eta, t)$ of the Lorentzian ansatz Eq. (2.23).

For the mean membrane potential $v(\eta, t)$ we can calculate the Cauchy principal value and obtain

$$\begin{aligned} v(\eta, t) &= \text{p.v.} \int_{-\infty}^{\infty} \rho(V|\eta, t) V \mathrm{d}V = \lim_{R \to \infty} \int_{-R}^{R} \rho(V|\eta, t) V \mathrm{d}V \\ &= y(\eta, t) \quad , \end{aligned} \tag{2.25}$$

which is identical to the center $y(\eta, t)$ of the Lorentzian ansatz Eq. (2.23) for a given η. The final ensemble means $r(t)$ and $v(t)$ result from an integration over η, weighted by the distribution $g(\eta)$:

$$r(t) = \frac{1}{\pi} \int_{-\infty}^{\infty} x(\eta, t) g(\eta) \mathrm{d}\eta \tag{2.26a}$$

$$v(t) = \int_{-\infty}^{\infty} y(\eta, t) g(\eta) \mathrm{d}\eta \quad . \tag{2.26b}$$

Complex formulation

In the following the goal will be to find equations of motion for $x(\eta, t)$ and $y(\eta, t)$. We start by inserting the Lorentzian ansatz Eq. (2.23) into the continuity equation Eq. (2.19) and obtain:

$$0 = \frac{\partial \rho}{\partial t} + \frac{\partial}{\partial V}\left[\rho(V^2 + I)\right] \tag{2.27}$$

$$= \frac{\dot{x}}{\pi\Lambda} - \frac{2x\left[x\dot{x} - (V-y)\dot{y}\right]}{\pi\Lambda^2} + \frac{2Vx}{\pi\Lambda} - \frac{2x(V^2+I)(V-y)}{\pi\Lambda^2} \quad , \tag{2.28}$$

with $\Lambda = (V-y)^2 + x^2$. In order to solve for $\{\dot{x}, \dot{y}\}$, we can simplify this equations further by multiplying by $\frac{\pi\Lambda^2}{2}$:

$$0 = \frac{\dot{x}\Lambda}{2} - x\left[x\dot{x} - (V-y)\dot{y}\right] + Vx\Lambda - x(V^2+I)(V-y) \quad . \tag{2.29}$$

The RHS of Eq. (2.29) is a polynomial in V and we sort by the orders of V, after inserting Λ:

$$\begin{aligned} 0 = {} & V^2\left(\dot{x} - 2xy\right) \\ & + V^1\left(-2Ix + 2x^3 + 2xy^2 - 2y\dot{x} + 2x\dot{y}\right) \\ & + V^0\left(2Ixy - x^2\dot{x} + y^2\dot{x} - 2xy\dot{y}\right) \end{aligned} \tag{2.30}$$

Eq. (2.30) must be valid for any $V \in \mathbb{R}$, hence the coefficients of the V^k, $k \in \{0, 1, 2\}$ must be zero, yielding an algebraic system of equations, that can be solved for $\{\dot{x}, \dot{y}\}$:

$$\dot{x} = 2xy \tag{2.31a}$$

$$\dot{y} = y^2 - x^2 + I \quad . \tag{2.31b}$$

As a final step one can express the dynamics in terms of a complex quantity $w(\eta, t) := x(\eta, t) + iy(\eta, t)$:

$$\begin{aligned} \dot{w} &= \dot{x} + i\dot{y} \\ &= 2xy + i(y^2 - x^2 + I) \\ &= i\left[I - w^2\right] \\ &= i\left[\eta + Jr + I_{\mathrm{S}}(t) - w^2\right] \end{aligned} \tag{2.32}$$

The entire dynamics of the QIF ensemble is now expressed in terms of this new complex quantity $w(\eta, t)$, in an exact manner and with the remarkable property of being V-independent. However, it is still infinite dimensional, given the dependence on η. Additional it is worth noting that the total firing $r(t)$ enters into Eq. (2.32), rendering it an integro-differential equation through Eq. (2.26a).

2.2.3 Second reduction: Lorentzian distributed heterogeneities

To obtain the total means $r(t)$ and $v(t)$ one can impose a specific distribution $g(\eta)$ which is as well of Lorentzian type, given by:

$$g(\eta) = \frac{1}{\pi}\frac{\Delta}{(\eta - \bar{\eta})^2 + \Delta^2} \quad . \tag{2.33}$$

centered at $\bar{\eta}$ and with HWHM Δ. This choice allows to obtain analytic expressions for Eqs. (2.26), by performing a contour integral in the complex η-plane and applying the residue theorem. This way we only have to evaluate $x(\eta, t)$ and $y(\eta, t)$ at the lower pole of $g(\eta)$ located at $\bar{\eta} - i\Delta$:

$$\pi r(t) = \int_{-\infty}^{\infty} x(\eta, t) g(\eta) \mathrm{d}\eta = x(\bar{\eta} - i\Delta, t) \tag{2.34a}$$

$$v(t) = \int_{-\infty}^{\infty} y(\eta, t) g(\eta) \mathrm{d}\eta = y(\bar{\eta} - i\Delta, t) \tag{2.34b}$$

Straightforwardly, the dynamics of $r(t)$ and $v(t)$ is given via the real and imaginary parts of Eq. (2.32), evaluated at $\bar{\eta} - i\Delta$:

$$\begin{aligned} \pi\dot{r} + i\dot{v} = \dot{w}(\bar{\eta} - i\Delta, t) &= i\left[\bar{\eta} - i\Delta + Jr + I_{\mathrm{S}}(t) - w^2(\bar{\eta} - i\Delta, t)\right] \\ &= \Delta + 2\pi r(t)v(t) + i\left[\eta + Jr(t) + I_{\mathrm{S}}(t) + v^2(t) - \pi^2 r^2(t)\right] \quad . \end{aligned} \tag{2.35}$$

Finally, separating real and imaginary part, the dynamics of $r(t)$ and $v(t)$ is given by:

$$\dot{r} = \frac{\Delta}{\pi} + 2rv \tag{2.36a}$$

$$\dot{v} = v^2 - (\pi r)^2 + \eta + Jr + I_{\mathrm{S}}(t) \quad . \tag{2.36b}$$

Eqs. (2.36) is referred to as *firing rate equations* (FRE), MPR model or exact neural mass model and is the starting point of this thesis.

The upcoming Section 2.3 is dedicated to an extension of the underlying QIF network Eq. (2.12), to account for synaptic dynamics, i.e., when $\tilde{J}_{ij}(t)$ changes in time. We will show that a treatment of short-term synaptic plasticity on mesoscopic scale allows for a straightforward application of the mean-field limit, without the loss of exactness. The final neural mass model consists of Eqs. (2.36), with adjustments to the recurrent synaptic current Jr, and two additional equations that describe the STP dynamics.

2.3 Short-term synaptic plasticity

In order to reproduce WM mechanisms in the prefrontal cortex (PFC) in Chapter 3, we follow [9] and assume that excitatory-to-excitatory synapses display depressing and facilitating transmission, described by the phenomenological model of STP developed by Markram, Tsodyks and collaborators [38, 39, 89]. Example traces of such dynamics, using a single QIF neuron, are shown in Fig. 2.4.

Depression

Short-term synaptic depression is related to neurotransmitter depletion. Each neuron i has a limited amount $X_i(t) \in [0, 1]$ of resources (i.e. vesicles ready to be released). Spiking is followed by the emittance of presynaptic action potentials. Upon their arrival at the synaptic terminal a fraction $U_i(t) \in [U_0, 1]$ of the neurotransmitters is released into the synaptic cleft, resulting in the generation of postsynaptic potentials (PSPs). Therefore, each presynaptic spike is linked to the utilization and reduction of resources available for the generation of upcoming PSPs [see Fig. 2.4(b)], consequently leading to a decrease of future postsynaptic excitations. The resource X_i exponentially recovers to its base value of $X_i = 1$ on a timescale $\tau_{\mathrm{d}} = 200\,\mathrm{ms}$ (depression timescale) [90].

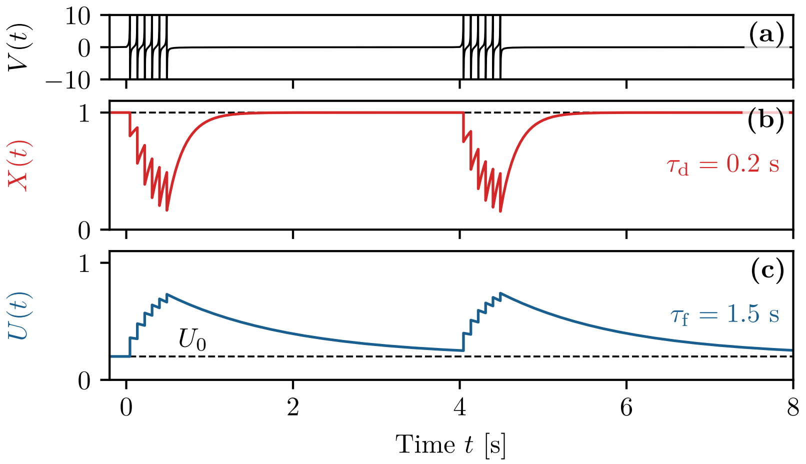

Figure 2.4: Short-term synaptic plasticity. **(a)** Membrane potential $V(t)$, **(b)** available resources $X(t)$ and **(c)** utilization $U(t)$ of a single QIF neuron as a function of time t. In the time windows $0\,\mathrm{s} < t < 0.5\,\mathrm{s}$ and $4\,\mathrm{s} < t < 4.5\,\mathrm{s}$ and external step current $I_{\rm S}(t)$ of amplitude $\Delta I = 0.5$ is applied to the neuron. The dynamics obey Eqs. (2.37) and Eq. (2.38). Parameter values are: $\tau_{\rm m} = 20\,\mathrm{ms}$, $\tau_{\rm d} = 200\,\mathrm{ms}$, $\tau_{\rm f} = 1500\,\mathrm{ms}$, $\eta = 0$.

Facilitation

Facilitation, as opposed to depression, leads to enhanced PSPs and is related to the neurotransmitter release probability at the synaptic terminals, which is modeled by the utilization factor U_i. The release probability (and therefore U_i) depends on the intracellular calcium concentration. The neurotransmitter release is associated with the accumulation of calcium ions in the presynaptic terminal, hence each spike leads to an increase of U_i [see Fig. 2.4(c)]. Calcium concentration and the utilization factor decay to the base level $U_i = U_0$ on the facilitation timescale $\tau_{\rm f} = 1500\,\mathrm{ms}$ [90].

QIF network with STP

As done in a previous analysis [91], we also assume for the sake of simplicity, that all the efferent synapses of a given neuron follow the same dynamical evolution, therefore they can be characterized by the index of the presynaptic neuron. In a QIF network with STP, the dynamics of the membrane potential and the synaptic variables $X_i(t)$ and $U_i(t)$ is ruled by the following ordinary differential equations:

$$\dot{V}_i = V_i^2(t) + \eta_i + \frac{1}{N}\sum_{j=1}^{N} \tilde{J}_{ij}(t) S_j(t) + I_{\rm S}(t) \tag{2.37a}$$

$$\dot{X}_i = \frac{1 - X_i(t)}{\tau_{\rm d}} - X_i(t) U_i(t) S_i(t) \tag{2.37b}$$

$$\dot{U}_i = \frac{U_0 - U_i(t)}{\tau_{\rm f}} + U_0(1 - U_i(t)) S_i(t) \ . \tag{2.37c}$$

In the Markram and Tsodyks STP model $U_i X_i$ represents the amount of resources employed to produce a postsynaptic potential, therefore in presence of STP the synaptic coupling $\tilde{J}_{ij}(t)$ entering into Eq. (2.12) will be modified as follows:

$$\tilde{J}_{ij}(t) = J U_j(t) X_j(t) \quad \forall i = 1, \ldots, N \quad . \tag{2.38}$$

Overall, taking instantaneous synapses and STP into account, the state variables of the system change in the following way at the k-th spike of neuron j:

$$V_i(t^+) = \frac{J}{N} U_j(t^-) X_j(t^-) \quad \forall i = 1, \dots, N \tag{2.39a}$$

$$X_j(t^+) = X_j(t^-) - U_j(t^-) X_j(t^-) \tag{2.39b}$$

$$U_j(t^+) = U_j(t^-) + U_0 \left(1 - U_j(t^-)\right) \quad . \tag{2.39c}$$

For simplicity the spike time is denoted by t, the time before the increment is denoted by t^-, the time after by t^+. Note that for the synaptic variables only the j-th neuron is affected, while the membrane potentials V_i of all neurons are changed, due to the all-to-all coupling.

2.3.1 Mesoscopic description

The spiking network model with μ-STP (μ-STP), given in Eqs. (2.37), consists of $3N$ differential equations: one for the membrane potential and two for the synaptic variables of each neuron. In order to reduce the system size effects and to obtain accurate simulations reproducing the neural mass dynamics, large network sizes are required, namely $N > 100,000$.

For these network simulations massive numerical resources are required, however the complexity of the synaptic dynamics can be noticeably reduced, by treating the STP at a mesoscopic level under the assumption that the spike trains emitted by each neuron are Poissonian [39, 92]. In this framework, the mesoscopic description of the synapse can be written as

$$\dot{x} = \frac{1 - x(t)}{\tau_\mathrm{d}} - u(t) x(t) A(t) \tag{2.40a}$$

$$\dot{u} = \frac{U_0 - u(t)}{\tau_\mathrm{f}} + U_0 (1 - u(t)) A(t) \quad , \tag{2.40b}$$

where $x = \langle X_i \rangle$ and $u = \langle U_i \rangle$ represent the average of the microscopic variables $\{X_i\}$ and $\{U_i\}$ over the whole population[2] and $A(t) = \langle S_j(t) \rangle$ is the mean firing rate.

The synaptic coupling entering in Eq. (2.12) now becomes:

$$\tilde{J}_{ij}(t) = J u(t) x(t) \quad \forall\ 1 \leq i, j \leq N \quad . \tag{2.41}$$

The dynamics of the QIF network with the mesoscopic STP (m-STP) obeys the $N + 2$ ODEs given in Eqs. (2.42),

$$\dot{V}_i = V_i^2 + \eta_i + J u x A(t) + I_\mathrm{S}(t) \tag{2.42a}$$

$$\dot{x} = \frac{1 - x}{\tau_\mathrm{d}} - u x A(t) \tag{2.42b}$$

$$\dot{u} = \frac{U_0 - u}{\tau_\mathrm{f}} + U_0 (1 - u) A(t) \quad , \tag{2.42c}$$

with $A(t) = \frac{1}{N} \sum_{j=1}^{N} S_j(t)$.

It should be noted that the synaptic variables $X_i(t)$ and $U_i(t)$ for the same synapse are correlated, since they are both driven by the same spike train $S_i(t)$ of neuron i. These correlations are neglected in the derivation of the m-STP model, therefore one can write $\langle U_i(t) X_i(t) \rangle = \langle U_i(t) \rangle \langle X_i(t) \rangle = u(t) x(t)$. This approximation is justified in [39] by the

---

[2] The population average $\langle \cdot \rangle = \frac{1}{N} \sum_{i=1}^{N} \cdot$ is performed over all the neurons N in the population

fact that the coefficients of variation of the two variables U_i and X_i are particularly small for facilitating synapses. Indeed it is possible to write a stochastic mesoscopic model for the STP that includes the second order moments for U_i and X_i, i.e. their correlations and fluctuations [92].

2.4 Exact neural mass model with STP

So far we have seen the derivation of an exact mean-field limit, following Ref. [16], for the heterogeneous QIF network with instantaneous synapses and in absence of synaptic dynamics, given in Eqs. (2.13) and (2.14). However, by including a dynamical evolution for the synapses and therefore additional collective variables, this neural mass model can be extended to more realistic postsynaptic potentials, see e.g. [46] for exponential synapses or [27] for conductance based synapses with α-function profile.

In our case the synaptic dynamics at a mesoscopic level is given by Eqs. (2.42b) and (2.42c), therefore it will be sufficient to include the dynamical evolution of the m-STP in the Eqs. (2.36) to obtain an exact neural mass model for the QIF spiking network with STP. Specifically, we consider Eqs. (2.42) for membrane potential and m-STP dynamics and we substitute the population activity $A(t)$ with the instantaneous firing rate $r(t)$, which corresponds to its coarse grained estimation in the limit $N \to \infty$. Furthermore, the synaptic coupling entering in Eqs. (2.36) will become $Ju(t)x(t)$, such that the complete neural mass model reads

$$\tau_{\mathrm{m}}\dot{r} = \frac{\Delta}{\tau_{\mathrm{m}}\pi} + 2rv \tag{2.43a}$$

$$\tau_{\mathrm{m}}\dot{v} = v^2 - (\pi\tau_{\mathrm{m}}r)^2 + J\tau_{\mathrm{m}}uxr + \bar{\eta} + I_{\mathrm{S}}(t) \tag{2.43b}$$

$$\dot{x} = \frac{1-x}{\tau_{\mathrm{d}}} - uxr \tag{2.43c}$$

$$\dot{u} = \frac{U_0 - u}{\tau_{\mathrm{f}}} + U_0(1-u)r \quad . \tag{2.43d}$$

Note that here the time rescaling described in Section 2.1.2 has been reverted, hence the appearance of τ_{m} in the equations. The macroscopic dynamics generated by the neural mass model Eqs. (2.43) and by the QIF network with μ-STP and m-STP are compared in Section 3.2.1.

Numerical simulation of QIF networks and neural mass with STP

For the numerical simulation of the models employed in this thesis see Section 2 in Appendix C.

2.5 Multi-populations models

The discussed models can be easily extended to account for multiple interconnected neuronal populations. In the following we restrict this extension to the QIF network with m-STP Eqs. (2.42) and the corresponding neural mass model, since the simulations we performed for the QIF network with μ-STP Eqs. (2.37) are limited to a single population.

We consider a network composed of one inhibitory and N_{pop} excitatory interacting neural populations. Therefore the dynamics of the membrane potential $V_{i,k}(t)$ of the i-th QIF neuron of the k-th population ($k = 0, \dots, N_{\mathrm{pop}}$) and of the mesoscopic synaptic variables $(u_k(t), x_k(t))$ for the excitatory populations $(k > 0)$ can be written as follows

$$\dot{V}_{i,k} = V_{i,k}^2 + \eta_{i,k} + I_{\mathrm{S}}^{(k)}(t) + \sum_{l=0}^{N_{\mathrm{pop}}} \frac{\tilde{J}_{kl}(t)}{N_l} \sum_{j(l)=1}^{N_l} S_{j,l}(t) \tag{2.44a}$$

$$\text{For } i = 1, \dots, N_k :$$

$$\dot{x}_k = \frac{1 - x_k}{\tau_{\mathrm{d}}} - u_k x_k A_k \tag{2.44b}$$

$$\dot{u}_k = \frac{U_0 - u_k}{\tau_{\mathrm{f}}} + U_0(1 - u_k) A_k \ ; \tag{2.44c}$$

where $I_{\mathrm{S}}^{(k)}(t)$ is the stimulation current applied to the population k and $A_k(t)$ is the population activity of the k-th population. Each population l consists of N_l neurons, which are indexed by j. We assume that the synaptic couplings $\tilde{J}_{kl}$ depend on the population indices k and l but not on the neuron indices; moreover we assume that the neurons are globally coupled both at the intra- and inter-population level. The synaptic couplings for excitatory-excitatory connections are plastic, therefore they can be written as

$$\tilde{J}_{kl}(t) = J_{kl} u_l(t) x_l(t) \ , \tag{2.45}$$

while if one of the populations k or l is inhibitory, the expression for the synaptic coupling will be simply set to $\tilde{J}_{kl}(t) = \text{const.} = J_{kl}$. The sign is determined by the pre-synaptic population l, with $J_{kl} > 0$ for excitatory and $J_{kl} < 0$ for inhibitory populations. In Chapter 3 a multi-population network is considered that comprises one inhibitory population and multiple excitatory ones. In such case, the inhibitory population is indexed as $k = 0$. The corresponding multi-population neural mass model, without time rescaling, can be straightforwardly written as

$$\tau_{\mathrm{m}}^k \dot{r}_k = \frac{\Delta_k}{\tau_{\mathrm{m}}^k \pi} + 2 r_k v_k \quad k = 0, 1, \dots, N_{\mathrm{pop}} \tag{2.46a}$$

$$\tau_{\mathrm{m}}^k \dot{v}_k = v_k^2 + \bar{\eta}_k + I_{\mathrm{S}}^{(k)}(t) - (\pi \tau_{\mathrm{m}}^k r_k)^2 + \tau_{\mathrm{m}}^k \sum_{l=0}^{N_{\mathrm{pop}}} \tilde{J}_{kl} r_l \tag{2.46b}$$

$$\dot{x}_l = \frac{1 - x_l}{\tau_{\mathrm{d}}} - u_l x_l r_l \tag{2.46c}$$

$$\dot{u}_l = \frac{U_0 - u_l}{\tau_{\mathrm{f}}} + U_0(1 - u_l) r_l \qquad l = 1, \dots, N_{\mathrm{pop}} \quad ; \tag{2.46d}$$

where for excitatory-excitatory population interactions

$$\tilde{J}_{kl}(t) = J_{kl} u_l(t) x_l(t) \quad ; \tag{2.47}$$

and whenever population k or l is inhibitory $\tilde{J}_{kl}(t) = J_{kl}$.

2.6 Neuronal dynamics across spatio-temporal scales

In Sections 2.1 to 2.5 of this chapter various models have been introduced, which describe neuronal dynamics on different spatial scales: from the single neuron Eq. (2.8) and synaptic dynamics Eqs. (2.37), via the QIF network and mesoscopic description of short-term synaptic plasticity Eqs. (2.42), to the multi-population model Eq. (2.46). Multi-population models are employed in Chapter 3 to working memory and in Chapter 4 for modeling seizure-like events. In both cases the interesting aspects of the models are given by the emerging dynamics across spatial scales, triggered by an external time dependent current. Understanding these responses requires a view on the dynamical properties of the system, like the bifurcation structure. As an example, seizure-like events are modeled by a switch from a low to a high activity state and mediated by bistability. In this specific case, bistability arises due to saddle-node bifurcations of Eqs. (2.36).

Dynamical properties also include the timescales appearing in the system. Naturally, as discussed in Section 2.3, short-term synaptic plasticity, which is present in the working memory model, comes along with two additional timescales for depression and facilitation. On one hand, multiple timescales might enrich the possible firing patterns, but they also complicate the analysis of the dynamics. On the other hand, a clear separation of timescales can be exploited, in order to investigate slow and fast dynamics separately. The methodology of this *slow-fast* dissection is introduced in Section 2.7, exemplified using the prototypical van der Pol (VdP) oscillator and finally applied to the single population neural mass model with STP Eqs. (2.43) in Chapter 5, in order to understand the response to a slow external current.

2.7 Slow-fast theory and canards

The dynamics of systems with multiple timescales, also referred to as slow-fast dynamics, can be regarded in terms of fast variables $\mathbf{X}_\mathrm{f}(t) \in \mathbb{R}^k$ and slow variables $\mathbf{X}_\mathrm{s}(t) \in \mathbb{R}^l$. Their dynamics is governed by the differential equations given in Eqs. (2.48) and here referred to as *full system*,

$$\dot{\mathbf{X}}_\mathrm{f} = \mathbf{F}(\mathbf{X}_\mathrm{f}, \mathbf{X}_\mathrm{s}) \tag{2.48a}$$

$$\dot{\mathbf{X}}_\mathrm{s} = \varepsilon \mathbf{G}(\mathbf{X}_\mathrm{f}, \mathbf{X}_\mathrm{s}) \tag{2.48b}$$

with fast-time parametrization t (the overdot denoting differentiation with respect to t), $\mathbf{F}(\mathbf{X}_\mathrm{f}, \mathbf{X}_\mathrm{s}) : \mathbb{R}^k \times \mathbb{R}^l \rightarrow \mathbb{R}^k$ and $\mathbf{G}(\mathbf{X}_\mathrm{f}, \mathbf{X}_\mathrm{s}) : \mathbb{R}^k \times \mathbb{R}^l \rightarrow \mathbb{R}^l$. Here the separation of timescales is reflected by a small parameter $0 < \varepsilon \ll 1$. We will refer to this type of system as k-fast l-slow system.

A different formulation of the full system is obtained in Eqs. (2.49) by parametrizing it in slow time $\tau := \varepsilon t$.

$$\varepsilon \mathbf{X}_\mathrm{f}' = \mathbf{F}(\mathbf{X}_\mathrm{f}, \mathbf{X}_\mathrm{s}) \tag{2.49a}$$

$$\mathbf{X}_\mathrm{s}' = \mathbf{G}(\mathbf{X}_\mathrm{f}, \mathbf{X}_\mathrm{s}) \quad . \tag{2.49b}$$

The derivative with respect to slow time τ is denoted by $(\_)' := \mathrm{d}/\mathrm{d}\tau(\_) = \frac{1}{\varepsilon}(\dot{\_})$. The two representations Eqs. (2.48) and Eqs. (2.49) are equivalent, but they allow to exploit the premise of slow-fast systems, namely the timescale separation given by a small value of ε, in different ways. It is natural to consider the *singular limit* $\varepsilon = 0$ and take the fast and slow-time parametrizations into account. One obtains two different subsystems, which represent a dissection of slow and fast dynamics of the full system.

In the first case we obtain the *fast subsystem* Eqs. (2.50). This limit can be used to understand dynamics of the full system for which $\mathbf{X}_\mathrm{f}$ evolves fast and results in the following $k + l$ ODEs, l of which being trivial:

$$\dot{\mathbf{X}}_\mathrm{f} = \mathbf{F}(\mathbf{X}_\mathrm{f}, \mathbf{X}_\mathrm{s}) \tag{2.50a}$$

$$\dot{\mathbf{X}}_\mathrm{s} = \mathbf{0} \tag{2.50b}$$

Indeed, the dynamics of the slow variables $\mathbf{X}_\mathrm{s}$ is trivial and their value does not change in time. As a matter of fact they can be treated as parameters entering into the dynamics of $\mathbf{X}_\mathrm{f}$.

The second limit $\varepsilon \to 0$, now done in the slow-time parametrization Eqs. (2.49), yields the *slow subsystem*, namely:

$$\mathbf{0} = \mathbf{F}(\mathbf{X}_\mathrm{f}, \mathbf{X}_\mathrm{s}) \tag{2.51a}$$

$$\mathbf{X}'_\mathrm{s} = \mathbf{G}(\mathbf{X}_\mathrm{f}, \mathbf{X}_\mathrm{s}) \quad . \tag{2.51b}$$

Eqs. (2.51) is also referred to as the *reduced system* and it is represented by a differential-algebraic system, in which the dynamics of the slow variables remains unchanged with respect to the full system and is governed by $\mathbf{X}'_\mathrm{s} = \mathbf{G}(\mathbf{X}_\mathrm{f}, \mathbf{X}_\mathrm{s})$. The dynamics of the fast variables on the other hand are hidden within the k algebraic constraints Eq. (2.51a). They define the *critical manifold*:

$$S_0 = \{(\mathbf{X}_\mathrm{f}, \mathbf{X}_\mathrm{s}) \mid \mathbf{F}(\mathbf{X}_\mathrm{f}, \mathbf{X}_\mathrm{s}) = 0\} \quad , \tag{2.52}$$

usually a l-dimensional manifold embedded in $\mathbb{R}^{(k+l)}$.

In the slow subsystem the dynamics of the fast variables is slaved to the slow variables, their relation is given by the critical manifold's equations, which defines the state space of this limiting problem: motion of the slow subsystem takes place on S_0. At the same time points of S_0 correspond to equilibria of the fast subsystem, as is clear from equation Eq. (2.50a). By joining solutions of the different subsystems at specific points, *singular orbits* can be constructed. They are trajectories resulting from the concatenation of slow and fast segments, for which the dynamics is determined by the respective subsystem.

Solutions of systems of the type of Eqs. (2.48) with both slow and fast segments are ε-perturbations of singular orbits and the prototypical slow-fast cycles are *relaxation oscillations* [93]. The way these cycles emerge in the parameter space is rather peculiar and related to the famous canard solutions. After introducing the *slow flow* below, we review these solutions in Section 2.7.2 in the context of the classical VdP system system.

2.7.1 Slow flow

We make further use of the dissection by studying the *slow flow* on the critical manifold S_0. In the slow subsystem Eqs. (2.51) the state space is reduced to S_0, described by four algebraic conditions in Eq. (5.6), the solutions of which depend on the slow variable I_1 entering into the membrane potential equation. The state variables in this limit are subject to the slow flow $(\mathbf{X}'_\mathrm{f}, \mathbf{X}'_\mathrm{s})$ describing their dynamics on S_0. For $\mathbf{X}_\mathrm{s} = (I_1, I_2)$ this is explicitly given via the Hopf normal form Eq. (5.4b). For the fast variables $\mathbf{X}_\mathrm{f} = (r, v, x, u)$ however, the algebraic constraints define $\mathbf{X}_\mathrm{f}$ as well as $\mathbf{X}'_\mathrm{f}$ on S_0 implicitly. In this case the flow can be obtained by taking the total (slow) time derivative of Eq. (2.51a) as done in Eq. (2.53),

$$\mathbf{0} = \frac{\mathrm{d}}{\mathrm{d}\tau}\mathbf{F}(\mathbf{X}_\mathrm{f}(\tau), \mathbf{X}_\mathrm{s}(\tau)) = \frac{\partial \mathbf{F}}{\partial \mathbf{X}_\mathrm{f}}\frac{\mathrm{d}\mathbf{X}_\mathrm{f}}{\mathrm{d}\tau} + \frac{\partial \mathbf{F}}{\partial \mathbf{X}_\mathrm{s}}\frac{\mathrm{d}\mathbf{X}_\mathrm{s}}{\mathrm{d}\tau} \quad , \tag{2.53}$$

where $\frac{\partial(\cdot)}{\partial \boldsymbol{a}}$ is the Jacobian of $(\cdot)$ with respect to $\mathbf{a}$. If the Jacobian $\frac{\partial \mathbf{F}}{\partial \mathbf{X}_\mathrm{f}}$ is invertible, i.e., $\det\left(\frac{\partial \mathbf{F}}{\partial \mathbf{X}_\mathrm{f}}\right) \neq 0$, then the slow flow of $\mathbf{X}_\mathrm{f}$ can be calculated and results in Eq. (2.54).

$$\frac{\mathrm{d}\mathbf{X}_\mathrm{f}}{\mathrm{d}\tau} \equiv \mathbf{X}_\mathrm{f}' = -\left(\frac{\partial \mathbf{F}}{\partial \mathbf{X}_\mathrm{f}}\right)^{-1}\left(\frac{\partial \mathbf{F}}{\partial \mathbf{X}_\mathrm{s}}\mathbf{X}_\mathrm{s}'\right) \tag{2.54}$$

This slow flow is only defined on S_0 and represents a system of ODEs capturing the dynamics of $\mathbf{X}_\mathrm{f}$ and $\mathbf{X}_\mathrm{s}$ on the manifold.

2.7.2 Classical canards in the van der Pol oscillator

Here we briefly present the essentials of classical canards in the prototypical VdP system given in Eqs. (2.55), consisting of one fast variable x and one slow variable y. Once written in first-order form, the system's equations read:

$$\dot{x} = y - \frac{x^3}{3} + x \tag{2.55a}$$

$$\dot{y} = \varepsilon(a - x) \quad . \tag{2.55b}$$

Critical manifold

The critical manifold S_0 is one dimensional and S-shaped, parametrized by x as $y(x) = \frac{x^3}{3} - x$ [see green curve in Fig. 2.5(b)]. In VdP the critical manifold $\{(x, y);\ y = y(x)\}$ has a local maximum and a local minimum, at $x = \pm 1$, respectively. Therefore S_0 folds twice and has three branches, of which the middle one is repelling and the other two attracting. They correspond to unstable and stable equilibria of the fast subsystem, respectively. The slow nullcline, determined by $\dot{y} = 0$, is the straight line $\{x = a\}$ and, at $a = \pm 1$, it intersects S_0 at the fold points perpendicularly.

Canard explosion in the full system

Overall, the VdP system, with $0 < \varepsilon \ll 1$ and a as a bifurcation parameter [see Fig. 2.5(a)], displays various regimes, from a stable equilibrium branch, via Hopf cycles and canards, to relaxation oscillations. The subthreshold regime, i.e, the branch of stable equilibria, terminates at a supercritical Hopf bifurcation, at which stable small Hopf cycles emanate. These cycles are not yet of relaxation type and only exist in an $O(\varepsilon)$ distance from the Hopf point [Fig. 2.5(b_1)]. They revolve around the unstable equilibrium at the intersection of S_0 and slow nullcline $x = a$

This regime is followed by an exponentially narrow parameter interval, for which the orbits grow in an explosive manner when the parameter is varied [Fig. 2.5(b_2 - b_5)]. This phenomenon is known as a *canard explosion* [94] and the associated *canards* separate the small Hopf cycles from relaxation oscillations [66]. They evolve for some time near the repelling sheet of S_0, before jumping to one of the attracting sheets. Two types of canards can be distinguished, the ones with a head [Fig. 2.5(b_2 - b_4)], including the *maximal canard*, which reaches until the fold at $a = 1$, and those without a head [Fig. 2.5(b_5)], which follow after the maximal canard. After the canard explosion a wide regime of relaxation oscillation follows, an exemplary trajectory is shown in Fig. 2.5(b_6). In approximation, relaxation oscillations can be found in $-1 \lessapprox a \lessapprox 1$ and they terminate at a second Hopf bifurcation near $a \approx 1$, by following the inverse procedure of their emergence: from relaxation oscillations, via canards and Hopf cycles, to stable equilibria.

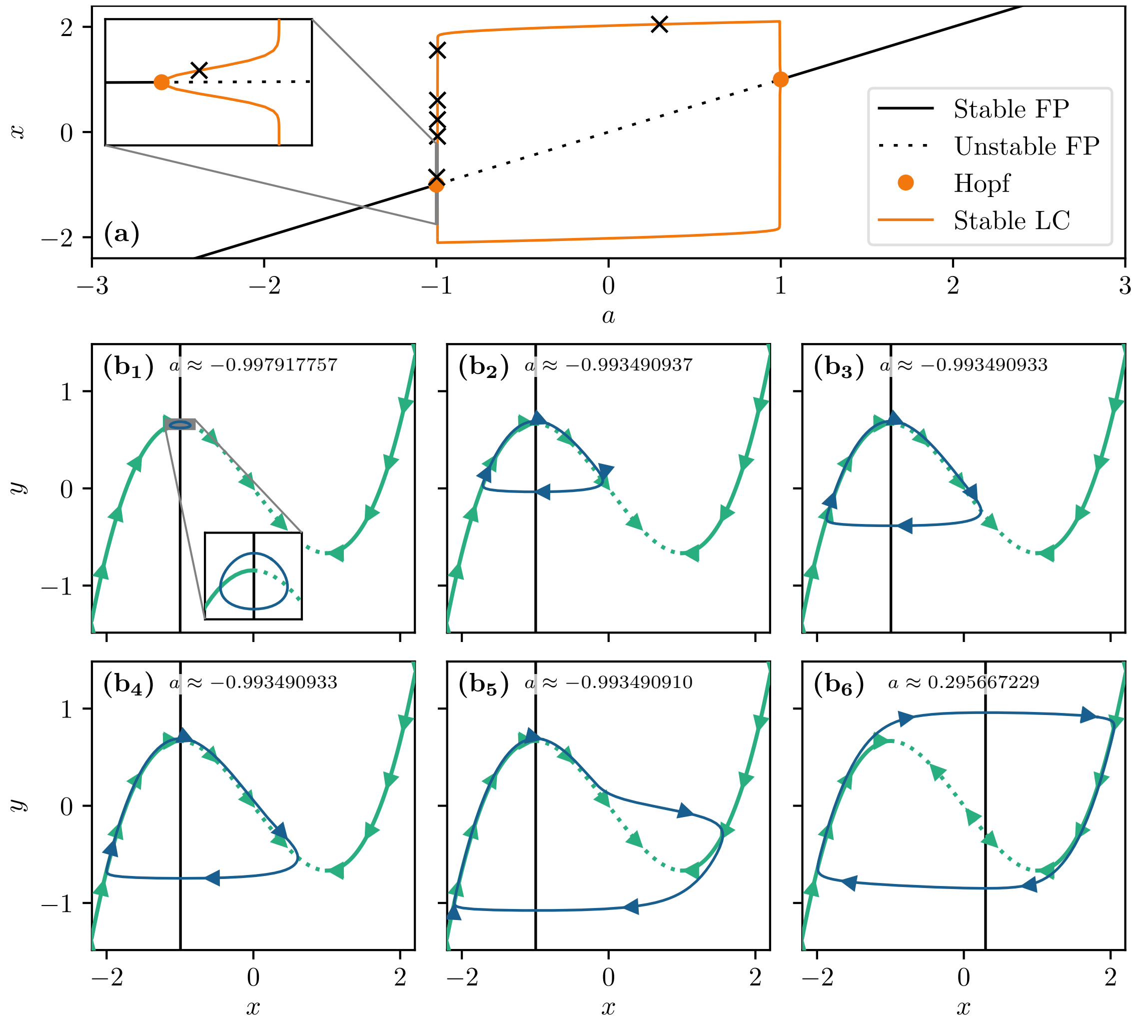

Figure 2.5: Canard dynamics in the van der Pol system. (a) Bifurcation diagram x versus a of the full system Eqs. (2.55) with $\varepsilon = 0.05$. **(b)** Solutions of the full system (blue) superimposed on critical manifold $S_0 = \{(x, y);\ y(x) = \frac{x^3}{3} - x\}$ (green) and slow nullcline $x = a$ (black). The a values in (b_1 - b_6) are marked in (a) by crosses and in increasing order. For (b_1 - b_5) the a values are exponentially close. In (b) the solid green line reflects the fact that S_0 is attracting, the dashed one that it is repelling, while the green arrows depict the slow flow defined in Eq. (2.53) and given by $(x', y') = (\frac{a-x}{x^2-1}, a - x)$ for VdP.

Slow flow and emergence of a canard point

Canards represent a mechanism which allows to connect the attracting sheet of the critical manifold to the repelling one and they can be understood by taking into account the slow flow of the fast variable x, given in Eq. (2.54) and describing the slow dynamics on S_0. For VdP, also taking into account y'', we obtain the slow flow $(x', y') = (\frac{a-x}{x^2-1}, a - x)$, which is in general undefined at the folds ($x = \pm 1$). However, its x-component reduces to $x' = -\frac{1}{x \pm 1}$ for $a = \pm 1$. In this case the flow remains defined at the corresponding fold $x = \pm a$, but undefined at the other fold $x = \mp a$. Despite the intersection of the slow nullcline $x = a$ with the cubic nullcline, no equilibrium exists. Instead a *turning point* forms, which allows for a continuous passage through the corresponding fold without any obstruction. This passage from the attracting to the repelling sheet of S_0 occurs in finite time and is the basis of singular ($\varepsilon = 0$) canard orbits. Therefore the turning point is also referred to as *canard point*. As we will see in Chapter 5 and in many other problems involving bursting solutions, canard dynamics play an essential role. They separate the subthreshold regime from the one where bursting can occur.

Folded-saddle canards

The understanding of canards based on the VdP system can be extended towards 1-fast 2-slow systems. In the most simple case the parameter a of the VdP system is subject to a slow drift given by $\dot{a} = \varepsilon\mu$, with a constant speed μ. Naturally, the slow nullcline is absent in this case and the intersection with the fast subsystem's fold, which is forming the *turning point*, can not occur. Nevertheless canards can be found and are a result of a slow passage effect: the parameter a dynamically transitions through the canard explosion of the original problem.

In VdP the existence of turning points is conditioned by the fact that the slow variable receives feedback from the fast variable , leading to a “turn" of the slow flow direction, depending on the value of x. In the neural mass model with STP in presence of external periodic forcing, however, this feedback is absent. The turn of the slow flow appears naturally via the form of the external forcing. In both cases the passage through the fold underlies the same mechanisms and it is well understood by making use of an auxiliary system, called the *desingularized reduced system* (DRS), which is introduced in Chapter 5.

Making use of the DRS, the formation of canards as described above, is reflected by so-called *folded-saddle singularities*, which allow for a passage from the attracting to the repelling sheet of S_0. Ultimately, this leads to the existence of canard orbits in the extended VdP system, as well as in the neural mass with STP in presence of periodic forcing.

Torus and mixed-type canards

The term canard is not restricted to dynamics taking place in the vicinity of (or on) attracting and repelling manifolds, which represent equilibria. In general, it refers to any type of solution evolving near attracting and repelling locally invariant sets associated with the fast subsystem. These invariant sets can correspond to equilibria but also to limit cycles. Following this definition, a particular type of canard can be found in elliptic bursters [95], which require at least a 2-fast 1-slow system. Here elliptic bursting can arise due to a subcritical Hopf-Bifurcation (in the fast subsystem) giving rise to unstable limit cycles, which stabilize via a fold bifurcation of cycles. The Hopf bifurcation initiates the burst, while the fold of cycles marks their termination. Usually in elliptic bursters the full dynamics follows the family of stable limit cycles of the fast subsystem. However so-called *torus canards* can be found for small enough ε [96, 97]. They describe orbits following a stable family of fast subsystem cycles and switching to the unstable one past the fold.

A hybrid of classical canards and torus canards, so-called mixed-type canards, were reported in [69]. They describe trajectories that spend time near repelling branches of equilibria as well as limit cycles, and can therefore be seen as a mix of classical canards and torus canards. Segments of these solutions evolve nearby unstable equilibria and connect to unstable limit cycles of the fast subsystem. These last types of canards are found in bursting systems, which are ubiquitous in the modeling of neural activity at both single-cell and population level.

Chapter 3

Working memory and cortical oscillations

A synaptic theory of working memory (WM) has been developed in the last decade as a possible alternative to the persistent spiking paradigm. In this context, we employ the neural mass model derived in Chapter 2, which reproduces exactly the dynamics of heterogeneous spiking neural networks encompassing realistic cellular mechanisms for short-term synaptic plasticity. This population model reproduces the macroscopic dynamics of the network in terms of the firing rate and the mean membrane potential. The latter quantity allows us to gain insight of the local field potential and electroencephalographic signals measured during WM tasks to characterize the brain activity. More specifically synaptic facilitation and depression integrate each other to efficiently mimic WM operations via either synaptic reactivation or persistent activity. Memory access and loading are related to stimulus-locked transient oscillations followed by a steady-state activity in the β-γ band, thus resembling what is observed in the cortex during vibrotactile stimuli in humans and object recognition in monkeys. Memory juggling and competition emerge already by loading only two items. However more items can be stored in WM by considering neural architectures composed of multiple excitatory populations and a common inhibitory pool. Memory capacity depends strongly on the presentation rate of the items and it maximizes for an optimal frequency range. In particular we provide an analytic expression for the maximal memory capacity. Furthermore, the mean membrane potential turns out to be a suitable proxy to measure the memory load, analogous to event driven potentials in experiments on humans. Finally we show that the γ power increases with the number of loaded items, as reported in many experiments, while θ and β power reveal non monotonic behaviors. In particular, β and γ rhythms are crucially sustained by the inhibitory activity, while the θ rhythm is controlled by excitatory synapses.

Publication:
The results presented in this chapter are published [98]: H. Taher, A. Torcini, and S. Olmi. "Exact Neural Mass Model for Synaptic-Based Working Memory". *PLOS Computational Biology* 16.12 (Dec. 2020), e1008533

3.1 Introduction

Working memory allows us to keep recently accessed information, available for manipulation: it is fundamental in order to pass from reflexive input-output reactions to the organization of goal-directed behavior [99–104]. Starting from the seminal work of Fuster and Alexander [105], several experiments have shown that neurons in higher-order cortex, including the PFC, are characterized by elevated levels of spiking activity during memory delays related to WM tasks. Experimental results seem to suggest that WM maintenance is enhanced by delayed spiking activity, engaging executive functions associated with large part of the cortex, from frontal to posterior cortical areas [106, 107]. In particular, it has been shown that neurons in the PFC exhibit persistent activity selective to the sample cue during oculomotor delayed-response task [40] as well as during vibrotactile response task [42] and that this activity is robust to distractors [41]. Therefore, classic models proposed persistent spiking for online maintenance of information, since neural ensembles in an active state appear more prone to fast processing [108, 109]. These models have been able to describe multi-item loading and maintenance in WM [62], spatial WM in the cortex [110], and two interval discrimination tasks [111].

A further relevant aspect, associated with WM operations, is the presence of neural oscillations, whose increase in the oscillatory power during WM maintenance and rehearsal has been reported for humans in the θ-band (4-8 Hz) [112, 113], as well as in the β (12-25 Hz) and γ-range (25-100 Hz) [114, 115], while for monkeys it has been reported in the θ and γ-range [116, 117] joined to a decrease in the β-band [117]. The results for the activity in the α-band (8-11 Hz) are somehow more complex: on one side it has been shown that during WM retention in humans no variations are observable [114] while, on the other side, that it can be associated with the inhibitory action suppressing irrelevant stimuli [118]. Despite many studies, the role played by oscillations in WM is still unclear; however numerical studies have suggested that different cycles of a high frequency oscillation in the γ-band can encode a sequence of memory items if nested within a slower θ or β rhythm [119–121]. Moreover, it has been shown in computational models that oscillatory forcing in different frequency bands may provide effective mechanisms for controlling the persistent activity of neural populations and hence the execution of WM tasks [32, 91].

Recently, the persistent state paradigm has been criticized on the basis of the inconsistencies emerging in data processing: persistent activity is the result of specific data processings, being neural spiking averaged over time and across trials. Averaging across trials can create the appearance of persistent spiking even when, on individual trials, spiking is actually sparse [49, 122]. Nevertheless, there are examples of single neurons that show real persistent spiking on individual trial rasters, but they represent a small percentage, while the bulk of neurons spike sparsely during WM delays [123, 124].

A pioneering study [90] revealed that the interactions among pyramidal neurons in the PFC display synaptic facilitation lasting hundreds of milliseconds. This study paved the way for a development of an alternative model for WM based on synaptic features. More specifically, memory items can be stored by spiking-induced changes in the synaptic weights and these items can be maintained in WM by brief bursts of spiking restoring the synaptic strengths [9, 125–127]. As a result this kind of model is more justifiable from a metabolic point of view, since the memory requires less resources to be held with respect to the persistent activity. Moreover, multiple memory items can be maintained in WM at the same time by having different neuronal populations emitting short bursts at different times. This would solve problems usually observables in models based on persistent spiking: namely, the interference among different stored items and the disruption of memories associated with new sensory inputs [48, 127].

In this context, a fundamental model for WM based on STP has been introduced by Mongillo *et al.* in [9]. In this model, synapses among pyramidal neurons display depressed and facilitated transmissions based on realistic cellular mechanisms [38, 39, 89]. Synaptic facilitation allows the model to maintain an item stored for a certain period in WM, without the need of an enhanced spiking activity. Furthermore, synaptic depression is responsible for the emergence of population bursts (PBs), which correspond to a subpopulation of neurons firing almost synchronously within a short time window [128, 129]. This WM mechanism is implemented in [9] within a recurrent network of spiking neurons, while a simplified firing rate model is employed to gain some insight into the population dynamics. The rate model, like most of the models investigated in literature [7, 10], is heuristic, i.e. the macroscopic description had not a precise correspondence with the microscopic neuronal evolutions.

Recent results for the primate PFC have revealed that the mnemonic stimuli are encoded at a population level allowing for a stable and robust WM maintenance, despite the complex and heterogeneous temporal dynamics displayed by the single neurons [130]. This analysis suggests that the development of population models which are capable of reproducing the macroscopic dynamics of heterogeneous spiking networks can be extremely useful to shed further light on the mechanisms at the basis of WM. An ideal candidate to solve this task is represented by a neural mass model of new generation able to exactly reproduce the macroscopic dynamics of spiking neural networks [16, 131, 132]. This exact derivation is possible for networks of QIF neurons, representing the normal form of Hodgkin's class I excitable membranes [30], thanks to the analytic techniques developed for coupled phase oscillators [15]. This new generation of neural mass models has been recently used to describe the emergence of collective oscillations (CO) in fully coupled networks [27, 46, 133, 134] as well as in balanced sparse networks [36]. Furthermore, it has been successfully employed to reveal the mechanisms at the basis of theta-nested gamma oscillations [33, 87] and of the coexistence of slow and fast gamma oscillations [135]. However, to our knowledge, such models have not been yet generalized to spiking networks with plastic synapses.

Our aim is to use a next generation neural mass model encompassing short-term synaptic facilitation and depression [39]. This model will enable us to revise the synaptic theory of working memory [9] with a specific focus on the emergence of neural oscillations and their relevance for WM operations. The neural mass model captures the macroscopic evolution of the network not only in terms of the firing rate, as the standard heuristic models do [7], but also of the mean membrane potential [16]. This will allow for a more direct comparison with the results of electrophysiological experiments often employed to characterize WM processes. Indeed, as shown in [136], electroencephalograms (EEGs), event-related potentials (ERPs) and local field potentials (LFPs) have the same information content as the mean membrane potentials.

The chapter is organized as follows. First, we will report clear evidence that the neural mass model reproduces, with extreme accuracy, the macroscopic dynamics of heterogeneous networks of QIF neurons with STP. Secondly, we will show that the model is able to mimic the fundamental operations required for WM functioning, whenever memory items are maintained either via spontaneous and selective reactivation or via persistent activity. We will devote particular attention to the spectral features of COs emerging during such operations and to their analogy with experimental findings reported for EEG responses to vibrotactile stimuli in primary somatosensory cortex in humans [47] and for LFP measurements performed in PFC of primates during objects coding in WM [48, 49]. In this context, we will show that a heuristic firing rate model, despite being specifically designed to reproduce the mean-field dynamics of QIF networks, is unable to sustain fast oscillations, which usually characterize the neural activity during WM tasks. Then we will perform a detailed analysis of the competition between two consecutively loaded memory items, whenever the memory maintenance is realized in terms of either synaptic facilitation or persistent spiking. Additionally, we will analyze how the memory capacity depends on the presentation rate of a sequence of items and which frequency bands are excited during loading and maintenance of multiple items in WM. We will also derive an analytic estimation of the maximal working memory capacity for our model, by extending recent results obtained in [10]. Furthermore, we will show that the mean membrane potential can represent a proxy to investigate memory load and capacity, in analogy with a series of experiments on neurophysiological measures of the WM capacity in humans [103, 137]. Finally, we will conclude with a discussion on the obtained results and their possible relevance for the field of neuroscience.

3.2 Results

We develop a model for WM able to memorize discrete items by following [138] and considering N_{pop} coupled excitatory populations, each coding for one item, and a single inhibitory population connected to all the excitatory neurons. This architecture is justified by recent experimental results indicating that GABAergic interneurons in mouse frontal cortex are not arranged in sub-populations and that they densely innervate all pyramidal cells [139]. The role of inhibition is to avoid abnormal synchronization and to allow for a competition of different items once stored in the excitatory population activity. Furthermore, in order to mimic synaptic-based WM we assume that only the excitatory-excitatory synapses are plastic displaying short-term depression and facilitation [9].

The macroscopic activity of N_{pop} excitatory and one inhibitory populations of heterogeneous QIF neurons can be described in terms of the population firing rate $r_k(t)$ and mean membrane voltage $v_k(t)$ of each population k by the following set of ODEs, which were derived in Chapter 2:

$$\tau_{\mathrm{m}}^{n}\dot{r}_k = \frac{\Delta_k}{\tau_{\mathrm{m}}^{n}\pi} + 2r_k v_k \qquad k = 0, 1, \dots, N_{\mathrm{pop}} \tag{3.1a}$$

$$\tau_{\mathrm{m}}^{n}\dot{v}_k = v_k^2 - (\pi\tau_{\mathrm{m}}^{n} r_k)^2 + H_k + I_{\mathrm{B}} + I_{\mathrm{S}}^{(k)}(t) + \tau_{\mathrm{m}}^{n}\sum_{l=0}^{N_{\mathrm{pop}}}\tilde{J}_{kl}(t) r_l \quad ; \tag{3.1b}$$

where τ_{m}^{n} denotes the membrane time constant of excitatory (inhibitory) populations $n = \mathrm{e}$ ($n = \mathrm{i}$) and I_{B} denotes a background current common to all populations, whereas H_k and the (time dependent) stimulus current $I_{\mathrm{S}}^{(k)}(t)$ may be population specific[1]. Excitatory populations are characterized by $k > 0$, the inhibitory one by $k = 0$. In absence of STP and for instantaneous synapses the synaptic weights are constant in time $\tilde{J}_{kl}(t) = J_{kl}$ and their sign determines whether the connections are excitatory ($J_{kl} > 0$) or inhibitory ($J_{kl} < 0$). The heterogeneous nature of the neurons is taken into account by considering randomly distributed neural excitabilities, reflecting their biological variability. Specifically, we assume that the distribution of the neural excitabilities is a Lorentzian characterized by a median H_k and a half width half-maximum (HWHM) Δ_k This choice allows us to derive the neural mass model from the spiking QIF network analytically. However, the overall dynamics does not change substantially by considering other distributions for the neural excitabilities, like Gaussian and Binomial ones [16, 135].

The inclusion of the depression and facilitation STP mechanisms in the spiking networks is reflected in the modification of the synaptic weights entering in the neural mass model Eqs. (3.1). In particular, these are rewritten as $\tilde{J}_{kl}(t) = J_{kl}u_l(t)x_l(t)$ if k and l

---

[1] Here the center $\bar{\eta}_k$ of the Lorentzian distribution found in Eq. (2.46) has been decomposed into $H_k + I_{\mathrm{B}}$.

are both excitatory populations, and simply as $\tilde{J}_{kl}(t) = J_{kl}$ if either k or l is inhibitory. The terms $x_k(t)$ and $u_k(t)$ represent the mean available resources and the mean utilization factor of the population k, respectively. If we neglect the very fast inactivation of the depression terms, the dynamical evolution of x_k and u_k is regulated by the following ODEs

$$\frac{\mathrm{d}x_k(t)}{\mathrm{d}t} = \frac{1 - x_k(t)}{\tau_\mathrm{d}} - u_k(t)x_k(t)r_k(t) \tag{3.2a}$$

$$\frac{\mathrm{d}u_k(t)}{\mathrm{d}t} = \frac{U_0 - u_k(t)}{\tau_\mathrm{f}} + U_0(1 - u_k(t))r_k(t) \qquad k = 1, \dots, N_\mathrm{pop} \quad ; \tag{3.2b}$$

where $U_0 = 0.2$ is the baseline value of the utilization factor. Furthermore, it is fundamental that the facilitation timescale τ_f ($\sim 1\,\mathrm{s}$) is longer than that associated with the recovery from depression τ_d ($\sim$ hundreds of milliseconds) [9]. In this way the information provided by the stimulus will be carried over a time τ_f by the facilitated synapse. Here we set $\tau_\mathrm{d} = 200\,\mathrm{ms}$ and $\tau_\mathrm{f} = 1500\,\mathrm{ms}$ according to [9, 90]. These parameter values remain fixed for all the simulations reported in this chapter.

The model given by Eqs. (3.1) and (3.2) describes the dynamics of one inhibitory and N_pop excitatory coupled neuronal populations with STP in terms of their population firing rates r_k, mean membrane voltages v_k, mean available resources x_k and mean utilization factors u_k. Details on the derivation of the neural mass model Eqs. (3.1) and (3.2) and on the underlying spiking networks can be found in Sections 2.2, 2.4 and 2.5 of Chapter 2.

3.2.1 Network dynamics versus neural mass evolution

The neural mass model Eqs. (3.1) reproduces exactly the population dynamics of a network of QIF spiking neurons, in absence of STP, in the infinite size limit, as analytically demonstrated and numerically verified in [16]. In order to verify if this statement is valid also in presence of STP, we will compare the macroscopic evolution of a single excitatory neural population, given by Eqs. (3.1) and (3.2), with those obtained by considering QIF networks with synaptic plasticity implemented at a microscopic (μ-STP) and at a mesoscopic (m-STP) level. The results of these comparisons are reported in Fig. 3.1(a) for μ-STP and in Fig. 3.1(b) for m-STP.

A spiking network of N neurons with μ-STP is described by the evolution of $3N$ variables, since each neuron is described in terms of its membrane voltage and the two synaptic variables $U_i(t)$ and $X_i(t)$ accounting for the dynamics of its N efferent synapses. The explicit dynamical model is reported in Eqs. (2.37) and Eq. (2.38) in Section 2.3 of Chapter 2. In the m-STP model, the dynamics of all synapses is treated as a mesoscopic variable in terms of only two macroscopic variables, namely $u(t)$ and $x(t)$. In this case the network model reduces to a set of $N+2$ ODEs, namely Eqs. (2.42) reported in Section 2.3.

In order to compare the different models we examine their response to the same applied stimulus $I_\mathrm{S}(t)$, which consists of two identical rectangular pulses of height $\Delta I = 2$ and duration $\Delta T = 0.15\,\mathrm{s}$, separated by a time interval of $0.15\,\mathrm{s}$ [see Fig. 3.1(b)]. The stimulus is presented when the system is in a quiescent state, i.e. it is characterized by a low firing rate. For both comparisons the neural mass model has been integrated starting from initial values of r,v,x and u as obtained from the microscopic state of the considered networks.

The response is the same in both network models: each pulse triggers a series of four PBs of decreasing amplitude followed by low activity phases in absence of stimuli [see Fig. 3.1(a)]. As shown in Fig. 3.1(c), the population firing rate $r(t)$ obtained from the neural mass model (solid line) is almost coincident with the results of the network simulations both with μ-STP and m-STP (shaded curves). For all models, the average synaptic variables x and u displayed in Fig. 3.1(d, e) reveal the typical temporal evolution of STP

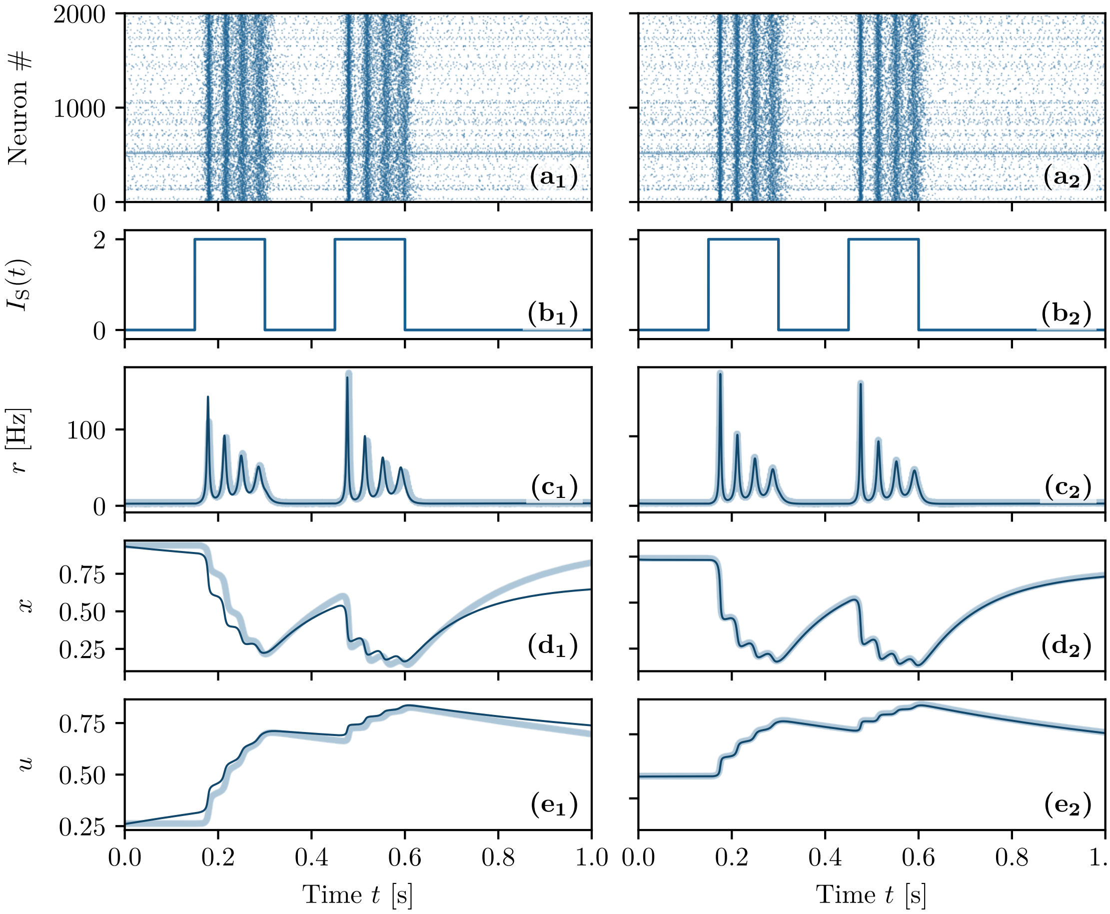

Figure 3.1: Comparison among neural mass and network models. The results of the neural mass model (solid line) are compared with the network simulations (shaded lines) for a single excitatory population with µ-STP [column **(1)**] and with m-STP [column **(2)**]. **(a)** Corresponding raster plots for a subset of 2000 neurons. **(b)** Profiles of the stimulation current $I_S(t)$. **(c)** Instantaneous population firing rate $r(t)$. **(d)** Available synaptic resources $x(t)$. **(e)** Utilization factor $u(t)$. The variables of the neural mass model are initialized to values coinciding with those of the corresponding network simulations. Since the numerical experiments for the single excitatory population with µ-STP and with m-STP are independent, the initial values of the synaptic variables do not coincide, even though a similar dynamical evolution is observable in both cases. Simulation parameters are $\tau_m^e = 15$ ms, $H = 0$, $\Delta = 0.25$, $J = 15$, $I_B = -1$ and network size $N = 200,000$.

upon excitatory stimulation: the available resources x (utilization factor u) decrease (increases) due to the series of emitted PBs in a step-wise fashion. Furthermore, in the absence of stimulation x and u tend to recover to their stationary values $x = 1$ and $u = U_0$ for µ-STP ($x = 0.73$ and $u = 0.59$ for m-STP) over time-scales dictated by τ_d and τ_f, respectively. Due to the fact that $\tau_d \ll \tau_f$, the synapses remain facilitated for a time interval $\simeq 1$ s after the pre-synaptic resources have recovered from depression. The time courses of x and u for the neural mass compared to the network ones, shown in Fig. 3.1(d, e), reveal an almost perfect agreement with the simulations of the network with m-STP, while some small discrepancies are observable when compared with the network with µ-STP. We have verified that these discrepancies are not due to finite size effects. Further increasing the network size, did not improve the agreement. Instead, these residual discrepancies are probably due the presence of so-called *silent neurons* and due to the correlations and fluctuations of the microscopic variables $\{X_i\}$ and $\{U_i\}$, which are not taken into account in the mesoscopic model for STP [39], as pointed out in [92] (see also the discussion on this aspects reported in Section 2.3 of Chapter 2 and in Appendix A). We can conclude this sub-section by affirming that the developed neural mass model reproduces in detail the macroscopic dynamics of spiking networks of QIF neurons with both μ-STP and m-STP, therefore in the following we can safely rely on the mean-field simulations to explore the synaptic mechanisms at the basis of WM.

3.2.2 Multi-Item Architecture

In order to illustrate the architecture employed to store more than one item simultaneously in WM, we will analyze the simplest non-trivial situation where we want to store two items. For this purpose, we consider two excitatory populations with STP employed to store one item each, and an inhibitory one, necessary to allow for item competition and a homeostatic regulation of the firing activity. We restrict to non-overlapping memories: neurons belonging to a certain excitatory population encode only one working memory item. Furthermore, incoming information on a WM item, in form of an external stimulus, target only the excitatory population which codes for that item, hence making the response selective.

As previously mentioned, only excitatory-excitatory synapses are plastic, therefore we will have no time dependence for the synaptic weights towards or from the inhibitory population. Moreover, the WM items should be free to compete among them on the same basis, therefore we assume that the synaptic couplings within a population of a certain type (inhibitory or excitatory) and among populations of the same type are identical. In summary, we have

$$\begin{aligned}&\tilde{J}_{00}(t) = J_{\mathrm{ii}}, \;\; \tilde{J}_{0k}(t) = J_{\mathrm{ie}}, \;\; \tilde{J}_{k0}(t) = J_{\mathrm{ei}}, \;\; \text{for } \; k > 0 \quad ; \\ &\tilde{J}_{kk}(t) = J^{(\mathrm{s})}_{\mathrm{ee}} x_k(t) u_k(t), \;\; J_{kj}(t) = J^{(\mathrm{c})}_{\mathrm{ee}} x_j(t) u_j(t), \quad \forall k, j > 0\end{aligned} \tag{3.3}$$

where we have denoted inhibitory (excitatory) populations by i (e) index. Furthermore, synaptic connections within each excitatory population, coding for a certain memory, will be stronger than connections between different excitatory populations, thus we assume $J^{(\mathrm{s})}_{\mathrm{ee}} > J^{(\mathrm{c})}_{\mathrm{ee}}$. A common background input current I_{B} impinges on all three populations, thus playing a crucial role in controlling the operational point of the network. The selective storage and retrieval of memory items induced by incoming stimuli is mimicked via time dependent external currents $I^{(k)}_{\mathrm{S}}(t)$ applied to the excitatory populations. The discussed multi-item architecture is displayed in Fig. 3.2.

Due to the fact that each excitatory population is indistinguishable from the others and we have only one inhibitory pool, we set for clarity $H_0 = H^{(\mathrm{i})}$, $H_k = H^{(\mathrm{e})}$ $\forall k > 0$ and $\Delta_0 = \Delta^{(\mathrm{i})}$, $\Delta_k = \Delta^{(\mathrm{e})}$ $\forall k > 0$. Furthermore, in order to highlight the variations of the synaptic parameters better, we report the normalized available resources $\tilde{x}_k$ and normalized facilitation factors $\tilde{u}_k$ in the following [2].

3.2.3 Memory maintenance with synaptic facilitation

To show the capability of our model to reproduce WM activity we report three different numerical experiments in this sub-section. We will show that the model is able to reproduce specific computational operations required by WM: namely, memory load, memory maintenance during a delay period, selective or spontaneous reactivation of the memory and memory clearance. The results of this analysis are reported in Fig. 3.3, where we compare the neural mass simulations with the network dynamics with m-STP for the

---

[2] These variables are normalized with respect to the difference of their maximal and minimal value taken within the displayed time interval.

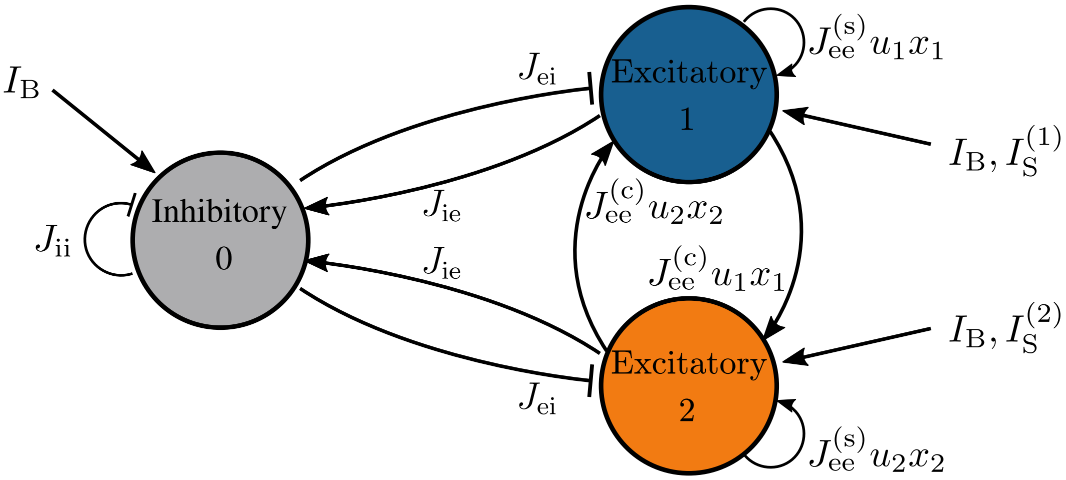

Figure 3.2: Two-item architecture. The reported network is composed of two identical and mutually coupled excitatory populations and an inhibitory one: this architecture can at most store two WM items, one for each excitatory population.

topological architecture displayed in Fig. 3.2. More specifically, we considered three coupled populations for the network simulations, consisting of 600,000 neurons in total. An analogous comparison is also reported in Fig. 3.5, where the competition between two memory items is studied.

Selective Reactivation

Let us start from an example of selective reactivation of the target item via a non specific read-out signal, targeting both excitatory populations, as shown in column (1) of Fig. 3.3. Since the observed dynamics does not depend on the population into which an item is loaded, we always load the item in population one (coded by the blue color in Fig. 3.3), without the loss of generality. The system is initialized in an asynchronous state of low firing activity common to both populations, as shown in Fig. 3.3($\rm e_1$), therefore the synaptic variables have equal values (namely, $\tilde{x}_1 = \tilde{x}_2 = 0.79$ and $\tilde{u}_1 = \tilde{u}_2 = 0.26$) dictated by the average firing rate [see Fig. 3.3($\rm f_1, g_1$)].

The memory load is performed at time $t = 0$ s, by applying a stimulation current in the form of a step with amplitude $\Delta I_1 = 0.2$ and width $\Delta T_1 = 350$ ms only to population one [Fig. 3.3($\rm b_1$)]. In response to this stimulus, the population displays PBs, as shown by the raster plot in Fig. 3.3($\rm a_1$). The frequency of these COs is in the β band (namely, $\simeq 21.6$ Hz), as evident from the spectrogram in Fig. 3.3($\rm h_1$). In addition to this, the PBs in population one trigger PBs in the inhibitory population with a delay of $\simeq 1 - 2$ ms, while the same COs' frequency is maintained, as evident from the inhibitory population spectrogram in Fig. 3.3($\rm j_1$). Therefore, the PBs are generated via a mechanism analogous to the pyramidal interneuronal network gamma (PING) one [140], despite the fact that the frequency of the COs is now in the β band.

The intense firing of neurons in population one changes the internal state of its efferent synapses, thus leading to an initial drop (increase) of x_1 (u_1) [Fig. 3.3($\rm f_1, g_1$)]. Depression prevails on short time scales $\simeq \tau_{\rm d}$, while at longer times $t > 0.5$ s, $\tilde{x}_1$ recovers to almost its initial value and the synapses remain facilitated, with $\tilde{u}_1 > 0.73$, for one or two seconds [Fig. 3.3($\rm g_1$)]. Population two (denoted by the orange color in Fig. 3.3) is not particularly affected by the memory loading. Indeed, population two shows only a slight reduction in its asynchronous activity, which is reflected in a small increase (decrease) of $\tilde{x}_2$ ($\tilde{u}_2$) [Fig. 3.3($\rm c_1, f_1, g_1$)]. This is due to the action of the inhibitory bursts, which are unable

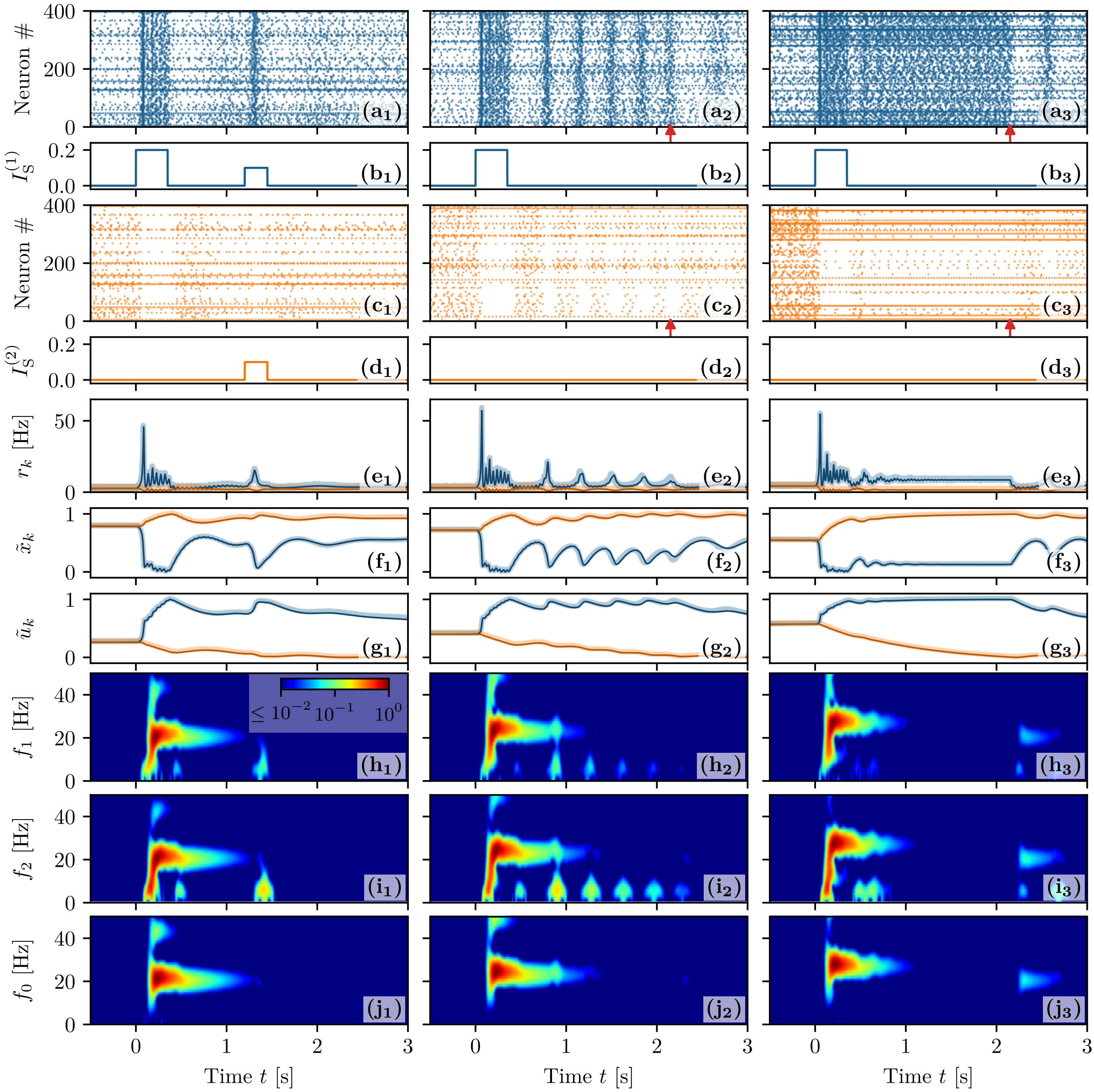

Figure 3.3: Memory loading, maintenance and rehearsal. The results of three experiments are reported here for different background currents: column **(1)** $I_B = 1.2$, selective reactivation of the target population; column **(2)** $I_B = 1.532$, WM maintenance via spontaneous reactivation of the target population and column **(3)** $I_B = 2$, WM maintenance via a persistent asynchronous activity. **(a)** Raster plots of the network activity for the first (blue) and **(c)** second (orange) excitatory population; the activity of only 400 out of 200,000 neurons is shown for each population. **(b)** Profiles of the stimulation current $I_S^{(k)}(t)$ for the first and **(d)** second excitatory population. **(e)** Population firing rates $r_k(t)$, **(f)** normalized available resources $\tilde{x}_k(t)$ and **(g)** normalized utilization factors $\tilde{u}_k(t)$ of the excitatory populations calculated from the simulations of the neural mass model (solid line) and of the network (shading). Spectrograms of the mean membrane potentials **(h)** $v_1(t)$, **(i)** $v_2(t)$, and **(j)** $v_0(t)$ obtained from the neural mass model; for clarity the frequencies in these three cases have been denoted as f_1,f_2 and f_0, respectively. Red arrows in columns (2) and (3) indicate the time $t = 2.15$ s at which the background current is set to the value $I_B = 1.2$ employed in column (1). The network simulations have been obtained by considering three populations of $N = 200,000$ neurons each and arranged with the architecture displayed in Fig. 3.2. For the estimation of the spectrograms see Section 1 of Appendix C. Other parameters values are: $\tau_m = 15\,\text{ms}$ $H^{(i)} = H^{(e)} = 0$, $\Delta^{(i)} = \Delta^{(e)} = 0.1$, $J_{ee}^{(c)} = 5\sqrt{a}$, $J_{ee}^{(s)} = 35\sqrt{a}$, $J_{ie} = 13\sqrt{a}$, $J_{ei} = -16\sqrt{a}$, $J_{ii} = -14\sqrt{a}$ with $a = 0.4$.

to support PBs in population two, but sufficient to modulate its asynchronous activity as revealed by the spectrogram in Fig. 3.3(i_1).

Since the information on the initial stimulus is stored in the facilitation of the synapses, we expect that, by presenting a weak non-specific read-out signal to both populations, the memory will be reactivated, even if the population activity is back to the spontaneous level. Indeed, if after a delay period of 1.2 s from the initial memory load, we inject a weak stimulation current of amplitude $\Delta I = 0.1$ for a time interval $\Delta T = 250$ ms to all the excitatory neurons, we observe that only neurons of the blue population respond by emitting a PB of brief duration. The other neurons not associated with the loaded item remain at the baseline activity level, despite the stimulus [Fig. 3.3(c_1)]. The emission of the PB in population one has also the effect to refresh the memory, i.e. the utilization factor u_1 which has decreased towards the initial value during the delay period, returns to the value reached when the item was loaded. Therefore the memory can be maintained for a longer time period.

Spontaneous Reactivation

In a second example, shown in the central column (2) of Fig. 3.3, we consider a case where the target population reactivates spontaneously by emitting a regular series of PBs even in absence of read-out signals. To obtain such situation we increase the background signal from $I_{\mathrm{B}} = 1.2$ up to $I_{\mathrm{B}} = 1.532$, thus the system is in a regime where the spontaneous low activity state coexists with states in which one of the excitatory populations periodically emits PBs (for more details on the emerging states see the bifurcation analysis in Section 3.4.1). As in the previous experiment, the system is initialized in a low firing activity state, where only spontaneous activity is present. The memory item is loaded in population one [Fig. 3.3(a_2 - e_2)]. In this case population one encodes the item by emitting a series of PBs with a slightly higher frequency ($\simeq 24.1$ Hz) with respect to the previous case, due to the increase in I_{B}, but still in the β range, as shown in Fig. 3.3(h_2 - j_2). After a short time delay, PBs emerge regularly in a self-sustained manner: each reactivation leads to an increase of $\tilde{u}_1$ and a decrease of $\tilde{x}_1$. The time interval between two PBs is dictated by the time required to recover sufficient synaptic resources in order to emit a new PB, i.e. by the time scale τ_{d} controlling the depression [128, 129] [Fig. 3.3(f_2)]. Thus, we have memory maintenance through synaptic facilitation, which is refreshed by PBs. As one can appreciate from the spectrogram of population one reported in Fig. 3.3(h_2), whenever a PB is delivered, a transient oscillation in the δ band, at a frequency $\simeq 3$ Hz, is observed. Similar transient oscillations have been observed when items are loaded in the PFC of monkeys during WM tasks [48]. Signatures of these oscillations are present also in the spectrogram of the other excitatory population [Fig. 3.3(i_2)] but, in this case, they are due to a modulation of the subthreshold membrane potentials and not to PBs. It is interesting to note that δ-oscillations are only sustained by the activity of the excitatory populations, since in the inhibitory spectrogram [Fig. 3.3(j_2)] there is no trace of them.

The sequence of PBs can be terminated by reducing the excitation I_{B}: this operation is performed at time $t = 2.15$ s after the initial stimulation and signaled by the red arrow in Fig. 3.3(a_2, c_2). Also in this experiment the memory load and retrieval is selective, since the second population activity is almost unaffected by these operations as it turns out from the raster plot reported in Fig. 3.3(c_2).

Persistent Activity

As a third experiment, we consider a situation where the memory item is maintained via the persistent activity of the target population, as shown in column (3) of Fig. 3.3. This is possible when the non-specific background input I_B is increased further such that we can observe multistability among three asynchronous states: one corresponding to the spontaneous activity at low firing rate of both excitatory populations and the other two corresponding to population one (two) in a persistent state with increased firing activity and population two (one) at a spontaneous level of activity. More details can be found in Bifurcation analysis. When at time $t = 0$ the memory item is loaded in population one, the population responds by emitting a series of PBs at a frequency $\simeq 27.2$ Hz in the β-γ band [Fig. 3.3($\mathrm{h_3}$ - $\mathrm{j_3}$)]. As shown in Fig. 3.3($\mathrm{a_3, e_3}$), once the loading is terminated the blue population enters into a regime of persistent firing characterized by an almost constant firing rate $r_1 \simeq 8.6$ Hz joined to constant values of the synaptic variables. In particular, the available resources of population one remain at a constant and low value due to the continuous firing of the neurons ($\tilde{x}_1 = 0.13$) [Fig. 3.3($\mathrm{f_3}$)]. However, the lack of resources is compensated by the quite high utilization factor $\tilde{u}_1 = 0.98$, reported in Fig. 3.3($\mathrm{g_3}$). Indeed in this case the memory is continuously refreshed by the persistent spiking activity. At time $t = 2.15$ s, indicated by red arrows in Fig. 3.3($\mathrm{a_3, c_3}$), the value of I_B is reduced to $I_B = 1.2$ and the persistent activity is interrupted. This would correspond to a memory clearance if WM would be based on the spiking activity only. Instead in this case, it represents only the interruption of the persistent activity, the memory clearance occurring when the facilitation returns to its original value after few more seconds (the decay of u_1 is evident in Fig. 3.3($\mathrm{g_3}$)). The second population, not involved in the memory loading, remains always in a low firing rate regime [Fig. 3.3($\mathrm{c_3, e_3}$)].

As expected, the neural mass dynamics reproduces almost perfectly the network dynamics with m-STP for all the three considered experiments. In particular, this can be appreciated through the agreement among shaded lines, corresponding to network simulations, and solid ones, referring to the neural mass evolution, reported in Fig. 3.3(e - g).

Furthermore, it should be remarked that memory loading is characterized by similar spectral features for all three experiments. As shown in Fig. 3.3(h, i), a transient broad-band response of the excitatory populations is observable in the range 3-18 Hz, locked with the stimulation onset and followed by a steady-state activity in the β-γ range (namely 21-27 Hz), which lasts for the whole duration of the stimulation. The broad-band oscillations emerge due to the excitation of the harmonics of a fundamental frequency $\simeq 2 - 3$ Hz, associated with one item loading in the memory. Similarly, the β-γ activity is initiated by memory loading that induces, in this case, damped oscillations towards a focus equilibrium state in the stimulated excitatory population: the damped oscillations are sustained by the inhibitory pool via a PING-like mechanism. Quite astonishingly, similar evoked power spectra have been reported for stimulus-locked EEG responses to vibrotactile stimuli in primary somatosensory cortex in humans [47]. In more details, as shown in Fig 1B of Ref. [47], the stimulus onset induces a broad-band activity in the 4-15 Hz range followed by a stationary activity at $\simeq 26$ Hz during the vibrotactile stimulations.

Comparison with a heuristic firing rate model

To close this sub-section, let us compare the population dynamics obtained by employing the exact neural mass model with STP [Eqs. (3.1) and (3.2)] and a heuristic firing rate model developed to mimic the dynamics of a QIF network with m-STP (for more details see Section 3.4.2 of this chapter). Recent studies have shown that this firing rate model, in absence of plasticity, is unable to capture some macroscopic behavior displayed by the corresponding QIF networks [32, 46]. In particular, it does not reproduce fast COs present in inhibitory networks [46] and it does not feature memory clearance via nonlinear resonance with an external β-forcing, contrary to the spiking network under forcing [32].

Here, we want to understand which network's dynamics are eventually lost by employing such a heuristic model with STP.

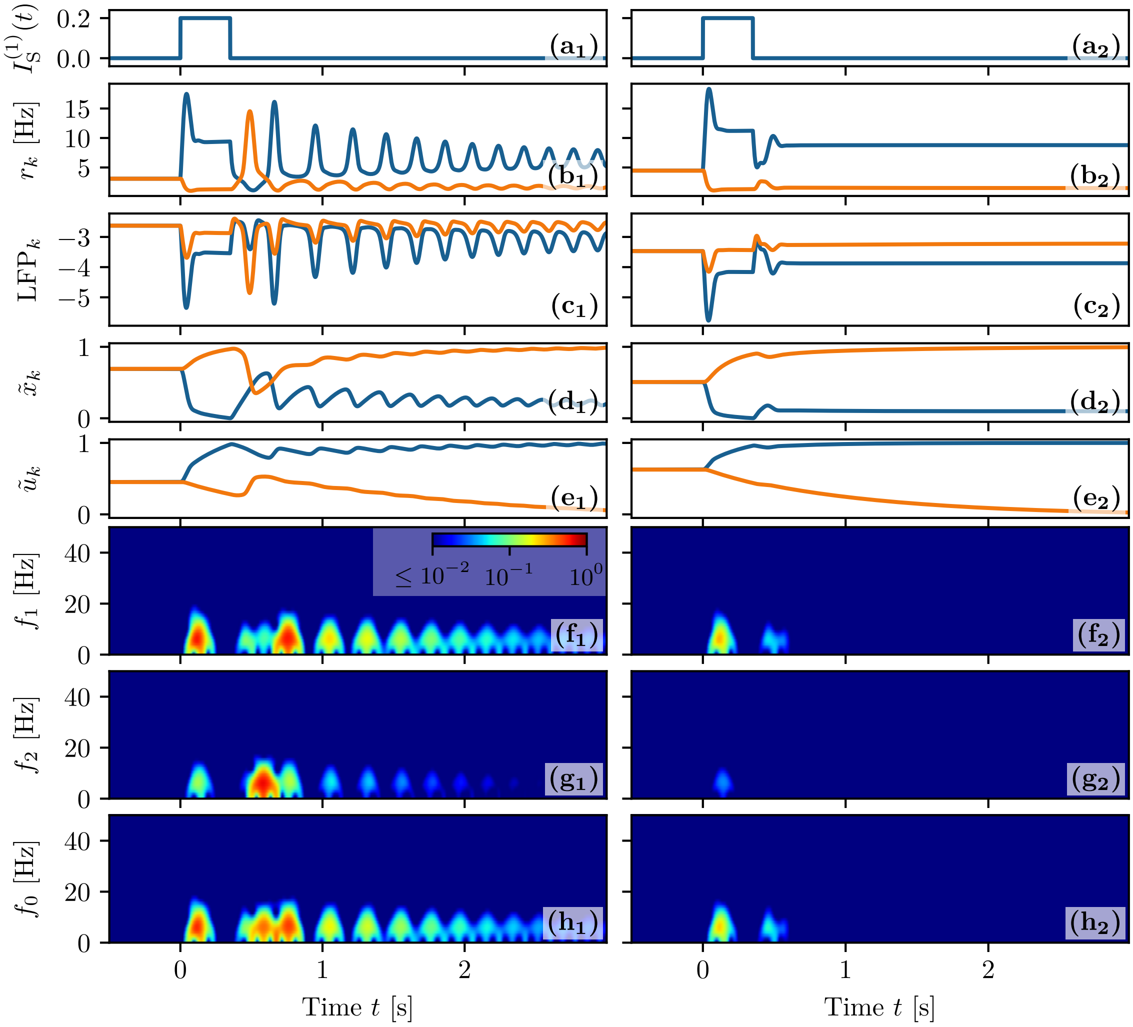

Figure 3.4: WM operations for a heuristic firing rate model. The results of two experiments are reported here for different background currents: column **(1)** $I_\mathrm{B} = 1.520$, WM maintenance via spontaneous reactivation of the target population and column **(2)** $I_\mathrm{B} = 2.05$, WM maintenance via persistent asynchronous activity. **(a)** Profiles of the stimulation current $I_\mathrm{S}^{(k)}(t)$, **(b)** population firing rates $r_k(\mathrm{t})$, **(c)** local field potentials LFP$_k$, **(d)** normalized available resources $\tilde{x}_k(t)$ and **(e)** normalized utilization factors $\tilde{u}_k(t)$ of the excitatory populations, calculated from simulations of the firing rate model Eqs. (3.5) and (3.7). Spectrograms of the local field potentials: **(f)** LFP$_1(t)$, **(g)** LFP$_2(t)$, and **(h)** LFP$_0(t)$. For the estimation of LFP$_k$ and the spectrograms see Section 1 of Appendix C. Other parameter values are as in Fig. 3.3.

Therefore we have repeated the experiments leading to memory maintenance via spontaneous reactivation and persistent activity, previously reported in columns (1) and (2) of Fig. 3.3, with the same topological configuration. The results of this analysis are shown in Fig. 3.4: column (1) is devoted to spontaneous reactivation and column (2) to persistent activity. In more detail, the multi-population network is initialized in the quiescent state with asynchronous activity and low firing rates [Fig. 3.4(b)]; at time $t = 0$ s, a current step of amplitude $\Delta I_1 = 0.2$ and duration $\Delta T_1 = 350$ ms is injected into population one (blue line), as shown in Fig. 3.4(a). When a background current $I_\mathrm{B} = 1.520$ is chosen, as soon as the stimulation is removed, population one enters into a cycle of periodic PBs, each one refreshing the synaptic facilitation and allowing for the memory maintenance (column (1)).

By increasing the current to $I_\mathrm{B} = 2.05$, the stimulus leads population one into a state of persistent firing activity, which maintains the synaptic variables at almost constant values (column (2)). Therefore, the heuristic firing rate model is able to reproduce the WM operations performed by the exact neural mass model. However, when comparing the firing rate time traces of the QIF network and of the exact neural mass model [Fig. 3.3($\mathrm{e}_2, \mathrm{e}_3$)] with the ones corresponding to the heuristic firing rate model [Fig. 3.4(b)], we note that, after the onset of stimulation, the population firing rates of the QIF network and of the exact neural mass model exhibit fast damped COs in the β-γ range, which are completely absent in the heuristic rate model. These findings are confirmed by the spectrograms[3], which reveal a vanishingly small power in the β-γ bands for the heuristic model in both experiments [compare Fig. 3.3(h_2 - j_2) and Fig. 3.3(h_3 - j_3) with Fig. 3.4(f - h)].

The reason for this absence is related to the fact that the stimulation leads population one in an excited state, which turns out to be a stable node equilibrium and not a focus, as for the exact neural mass model; therefore in this case it is not possible to observe transient PBs associated with memory loading. As a consequence, the heuristic model does not show any activity in the β and γ bands, despite this kind of activity has been reported experimentally in the PFC of monkeys performing WM tasks [49] and in the primary somatosensory cortex of humans due to vibrotactile stimuli [47], and associated with memory loading and recall in WM models [141]. Furthermore, as we will discuss in detail in Section 3.2.5, the loading of many items in WM is usually associated with γ-power enhancement, as shown by various experiments [115, 142, 143]. While this effect is present in our exact neural mass model, where the high frequency oscillations are enhanced due to a resonant mechanism with the transient oscillations towards the focus equilibrium, this aspect cannot be clearly reproduced by this heuristic firing rate model.

3.2.4 Competition between two memory items

In this sub-section we verify the robustness of the investigated set-up when two memory items are loaded, one for each excitatory population. In particular, we will examine the possible outcomes of the competition between two loaded items with emphasis on the mechanisms leading to memory juggling [144]. More specifically, we will consider three different operational modes, where the items are maintained in the WM due to different mechanisms: namely, in the first case thanks to periodic stimulations; in the second one due to self-sustained periodic PBs and in the last one to persistent spiking activity.

Periodic Stimulations

First we analyze the two-item memory juggling in presence of a periodic unspecific stimulation to the excitatory populations. As shown in column (1) of Fig. 3.5, at time $t = 0$ we load the first item in population one by stimulating the population for $\Delta T_1 = 350$ ms, with an excitatory step of amplitude $\Delta I_1 = 0.2$ [Fig. 3.5(b_1)]. Population one encodes the item via the facilitation of its efferent synapses. This is a consequence of a series of PBs emitted via a PING-like mechanism at a frequency $\simeq 21.6$ Hz in the β-range, as evident from the spectrograms in Fig. 3.5(h_1 - j_1). Subsequently a periodic sequence of unspecific stimulations of small amplitude and brief duration is delivered to both populations (namely, step currents of amplitude 0.1 and duration 150 ms applied at intervals of 400 ms). These are sufficient to refresh the memory associated with population one, that

---

[3] The spectrograms for the heuristic model have been evaluated for the local field potentials LFP_k defined in Eqs. (6.14) of Appendix C and reported in Fig. 3.4(c); this is due to the fact that the rate model cannot provide any information on the membrane potentials.

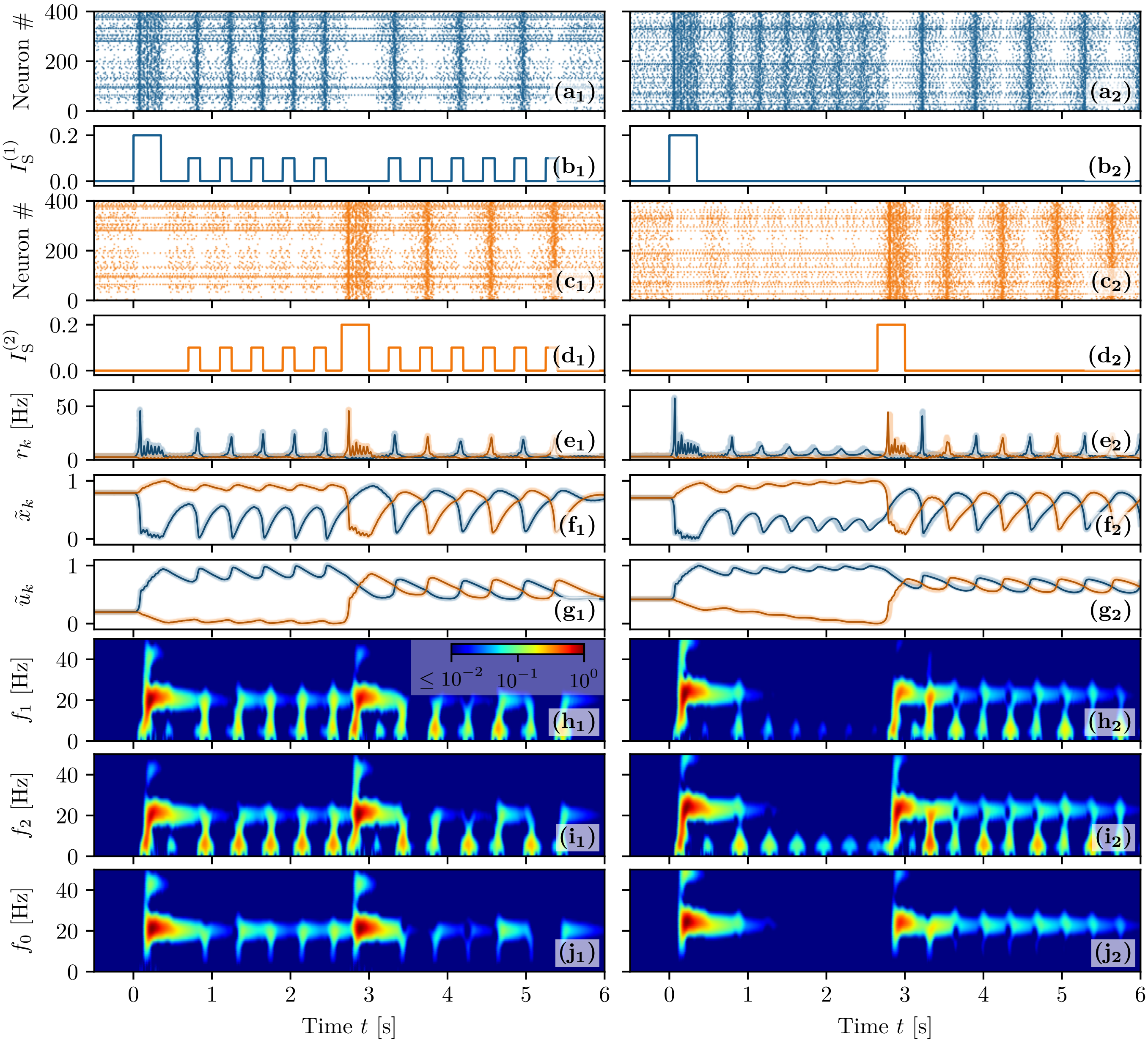

Figure 3.5: Juggling between two memory items. The memory juggling is obtained in two experiments with different background currents: column **(1)** $I_B = 1.2$, in presence of a periodic unspecific stimulation and column **(1)** $I_B = 1.532$, in the case of spontaneous WM reactivation. **(a)** Raster plots of the network activity for the first (blue), and **(c)** second (orange) excitatory population. **(b)** Profiles of the stimulation current $I_S^{(k)}(t)$ for the first and **(d)** second excitatory population. **(e)** Population firing rates $r_k(\mathrm{t})$, **(f)** normalized available resources $\tilde{x}_k(t)$ and **(g)** normalized utilization factors $\tilde{u}_k(t)$ of the excitatory populations calculated from the simulations of the neural mass model (solid line) and of the network (shading). Spectrograms of the mean membrane potentials **(h)** $v_1(t)$, **(i)** $v_2(t)$ and **(j)** $v_0(t)$ obtained from the neural mass model. For the estimation of the spectrograms see Section 1 of Appendix C. Other parameter values are as in Fig. 3.3.

reacts each time, by emitting a brief PB able to restore $\tilde{u}_1$ to a high value [Fig. 3.5(g$_1$)]. On the contrary population two remains in the low activity regime [Fig. 3.5(c$_1$, e$_1$)].

The second item is loaded at time $t = 2.65$ s, by presenting to population two a signal equal to the one presented at time $t = 0$ [Fig. 3.5(d$_1$)]. Also the loading of this item is associated with PBs emitted in the β range and involving the inhibitory population. During the presentation of the second item, the previous item is temporarily suppressed.

However, when the unspecific stimulations are presented again to both population, PBs are triggered in both populations, resulting to be in anti-phase, i.e. PBs alternate between the two populations at each read-out pulse. The period related to each item is therefore twice the interval between read-out signals [Fig. 3.5(a_1, c_1)]. This is due to the fact that a PB in one excitatory population stimulates the action of the inhibitory neurons in population zero which, as a consequence, suppresses the activity of the other excitatory population, leading to the observed juggling between the two items in working memory. As clear from the spectrograms in Fig. 3.5(h_1 - j_1), the unspecific stimulations of the excitatory populations induce localized peaks in their spectrograms around 2-3 Hz, not involving the inhibitory population. The latter instead oscillates at a frequency $\simeq$ 21.6 Hz, thus inducing a modulation of the neural activity of the two excitatory populations. This explain the presence of the series of peaks in the three spectrograms around 20-25 Hz.

Self-Sustained Population Bursts

Let us now consider a higher background current (namely, $I_{\mathrm{B}} = 1.532$), where self-sustained periodic PBs can be emitted by each excitatory population. In this case it is not necessary to deliver unspecific periodic stimuli to refresh the synaptic memory. The loading of the two items is done by applying the same currents as before ($\Delta I_1 = \Delta I_2 = 0.2$, $\Delta T_1 = \Delta T_2 = 350$ ms) to the two populations, as shown in Fig. 3.5(b_2, d_2). The memory loading occurs, once more, via series of bursts emitted with frequency in the β range, through a PING-like mechanism. Once the item is loaded, a series of subsequent PBs is emitted regularly, at a frequency $\simeq$ 2.90 Hz [Fig. 3.5(a_2, e_2)].

The second population remains quiescent until the second item is loaded [Fig. 3.5(c_2, d_2)]. During the loading period, the activity of the first population is temporarily suppressed while, at later times, both items are maintained in the memory by subsequent periodic reactivations of the two populations. In particular it turns out that periodic reactivations are in anti-phase, with frequency $\simeq$ 1.5 Hz, i.e., one observes juggling between the two working memory items [Fig. 3.5(e_2)]. Also in this case, the inhibitory population is responsible for sustaining the β rhythm, while the excitatory ones for the slow oscillations, as revealed by the spectrograms in [Fig. 3.5(h_2 - j_2)]. As testified by the comparisons reported in Fig. 3.5(e - g), the agreement among the network simulations (solid lines) and the neural mass results (shaded lines) is impressive even for the two experiments discussed so far in this Section.

For the setup analyzed in column (2) of Fig. 3.5, the competition between the two memory items can have different final outcomes, depending on the characteristics of the stimuli, namely their amplitude and duration. For simplicity we fix these parameters for the first stimulation and vary those of the second stimulation. As shown in Fig. 3.6(a - d), three outcomes are possible for stimuli with the same amplitude $\Delta I_2 = 0.2$ but different pulse duration: item one wins, item two wins or they both coexist in the memory (juggling). If ΔT_2 is too short, the facilitation u_2 has no time to become sufficiently large to compete with that of population one [Fig. 3.6 column (1)]. Therefore, once the second stimulus is removed, population one recovers its oscillatory activity and population two returns to the low firing asynchronous activity [Fig. 3.6(b_1)]. For intermediate durations ΔT_2 [Fig. 3.6 column (2)], at the end of the stimulation period, the facilitation u_2 reaches the value u_1 [Fig. 3.6(d_2)], thus leading the two items to compete. Indeed, as shown in Fig. 3.6(b_2), the two populations display COs of the same period but in phase opposition, analogous to the case reported in column (2) of Fig. 3.5 . The stimulation of the second population suppresses the activity of the first, leading to a relaxation of the facilitation to the baseline. Hence, whenever ΔT_2 is sufficiently long [Fig. 3.6 column (3)], the facilitation of population two prevails on that of population one and as a final outcome, population two displays COs, while population one has a low activity.

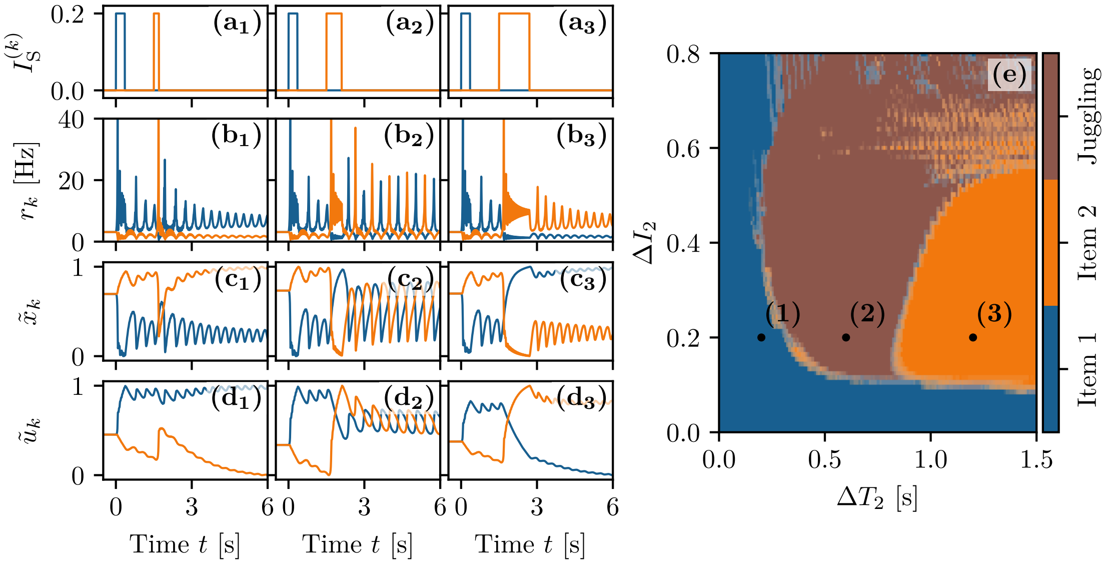

Figure 3.6: Competition between two memory items. The loading of two memory items is performed in three different ways via two step currents of equal amplitudes $\Delta I_1 = \Delta I_2 = 0.2$, the first one delivered at $t = 0$ and the second one at $t = 1.5$ s. The first step has always a duration of $\Delta T_1 = 0.35$ s; the second one $\Delta T_2 = 0.2$ s [column **(1)**], $\Delta T_2 = 0.6$ s [column **(2)**] and $\Delta T_2 = 1.2$ s [column **(3)**]. **(a)** Stimulation currents $I_S^{(k)}(t)$, **(b)** instantaneous population firing rates $r_k(t)$, **(c)** normalized available resources $\tilde{x}_k(t)$ and **(d)** normalized utilization factors $\tilde{u}_k(t)$ for the first (blue) and second (orange) excitatory population. **(e)** Final memory states as a function of the amplitude ΔI_2 and width ΔT_2 of the stimulus to population two. Here the labels (1), (2), (3) refer to the states examined in the corresponding columns. The data reported in panel (e) has been obtained by delivering the second stimulation at different phases ϕ with respect to the period of the CO of the first population: 20 equidistant phases in the interval $\phi \in [0, 2\pi)$ have been considered. For each of the three possible outcomes an image has been created with a level of transparency corresponding to the fraction of times it has been measured. The three images have been merged resulting in panel (e). Other parameter values are as in Fig. 3.3 with $I_B = 1.532$.

The results of a detailed analysis for different amplitudes ΔI_2 and durations ΔT_2 are summarized in Fig. 3.6(e). Population one always receives the same stimulus at time $t = 0$ ($\Delta I_1 = 0.2$ and $\Delta T_1 = 0.35$ s), while ΔI_2 and ΔT_2 of the second stimulus, delivered at time $t = 100$ s, are varied[4]. In particular, the amplitude has been varied in steps of 0.01 within the interval $\Delta I_2 \in [0, 0.8]$, while the duration in steps of 0.01 s for $\Delta T_2 \in [0, 1.5]$ s. The classification of the final states has been performed three seconds after the second stimulation, by estimating the time averaged firing rates $\langle r_1 \rangle$ and $\langle r_2 \rangle$ over an interval of one second. From this we get the indicator $P := \frac{\langle r_1 \rangle}{\langle r_1 \rangle + \langle r_2 \rangle}$. If $P > 0.7$ ($P < 0.3$) item one (item two) has been memorized, otherwise we have juggling between the two items. From Fig. 3.6(e), we see that, for sufficiently small amplitudes $\Delta I_2 < 0.11$ or durations $\Delta T_2 < 0.2$ s, the second stimulation is unable to change the memory state, that remains on item one. This can be understood by looking at the bifurcation diagram shown in Fig. 3.14(b) of Section 3.4.1, from which it is clear that population two, being in the low firing regime, has a low value of the membrane potential v_2 and that such state is separated by the high activity regime from a barrier Δv_2, which is of the order of the distance from the saddle (dotted line in the figure). A frequent outcome of the experiments

---

[4] The long interval of 100 seconds between the two stimuli is chosen in order to ensure that the outcome is independent of the characteristic of the first stimulus: namely, ΔI_1 and ΔT_1.

is the coexistence between the two memory items, that we observe in a large parameter region for intermediate pulse durations, namely 0.2 s $< \Delta T_2 <$ 0.8 s. For sufficiently long perturbations $\Delta T_2 >$ 0.8 s and intermediate amplitudes $0.11 < \Delta I_2 < 0.53$, item two is memorized. It is unexpected that, for larger amplitudes, we observe a multistability among all the three possible outcomes. Indeed, small variations of amplitude, duration or delivering time can induce a completely different outcome, thus suggesting that for these parameter values, some transient chaotic behavior is observable [145, 146].

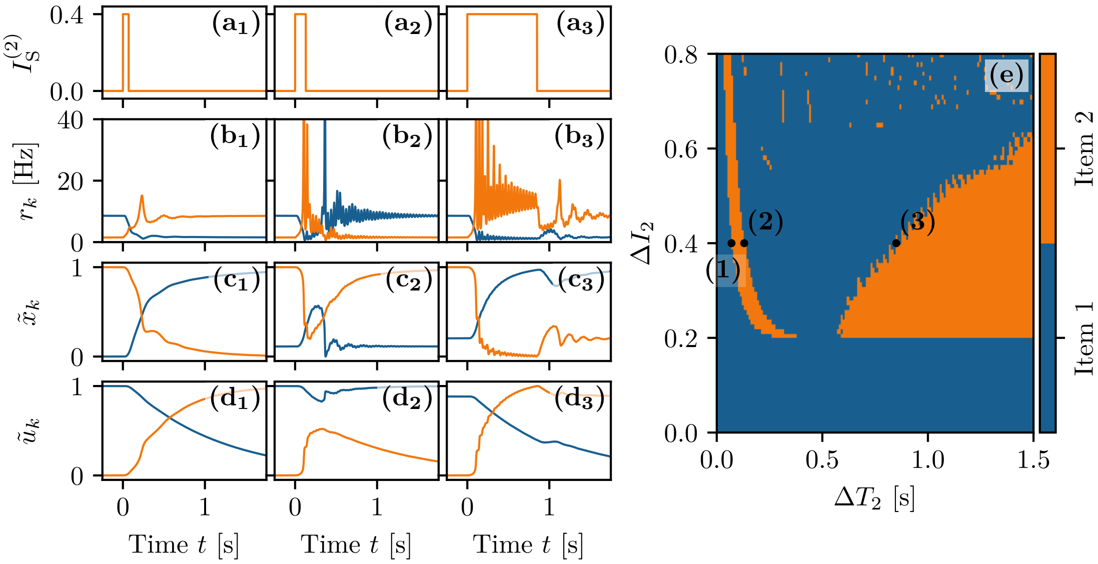

Figure 3.7: Memory item switching with persistent activity. The three columns (1-3) refer to three values of ΔT_2, given a background current $I_B = 2$ that supports persistent state activity. **(1)** Duration of $\Delta T_2 = 70$ ms, **(2)** $\Delta T_2 = 130$ ms and **(3)** $\Delta T_2 = 850$ ms. **(a)** Stimulation currents $I_S^{(k)}(t)$, **(b)** instantaneous population firing rates $r_k(t)$, **(c)** normalized available resources $\tilde{x}_k(t)$ and **(d)** normalized utilization factors $\tilde{u}_k(t)$ for the first (blue) and second (orange) excitatory population. **(e)** Final memory states as a function of the amplitude ΔI_2 and width ΔT_2 of the stimulus to population two. Here the labels (1), (2), (3) refer to the states examined in the corresponding columns. Other parameters values are as in Fig. 3.3 with $I_B = 2$.

Persistent State Activity

We have performed the same analysis for the higher current value $I_B = 2$, which supports a persistent state activity of one of the two populations. We set initially population one in the persistent state and we deliver a stimulus in form of a step current to population two. In this case we can obtain only two possible final outcomes: item one (two) loaded corresponding to population one (two) in the persistent state, while the other in the low activity regime. No memory juggling has been observed with persistent states in our model. The results of this investigation are summarized in Fig. 3.7(e); for what concerns the final prevalence of item two, the results are similar to the ones obtained in the previous analysis, where the item was encoded in self-sustained periodic COs. The main differences with the previous case are: (i) the minimal perturbation amplitude needed to observe an item switching, that is now larger, namely $\Delta I_2 \simeq 0.2$; (ii) the existence of a narrow stripe in the $(\Delta T_2, \Delta I_2)$-plane where item two can be finally selected for brief stimulation duration. The increased value of the minimal ΔI_2 required to switch to item two is justified by the fact that, for $I_B = 2$, the barrier Δv_2 that has to be overcome to access the high firing regime, is higher than before, as evident from the phase diagram reported in Fig. 3.14(b) of Section 3.4.1. The origin of the stripe can be understood by examining the results reported in Fig. 3.7(a - d), for three stimulations with the same amplitude $\Delta I_2 = 0.4$ and different durations. The effect of the stimulation is to increase the activity of population two and indirectly, also the inhibitory action on population one. However, for short $\Delta T_2 < 70$ ms, the activity of population two is not sufficient to render its efferent synapses stronger than those of population one. As a matter of fact, when the stimulation is over, population one returns into the persistent state. For longer $\Delta T_2 \geq 70$ ms, population one is not able to recover its resources before population two elicits a PB. Population two takes over and the dynamics relax back, maintaining item two in WM via the persistent activity [Fig. 3.7 column (1)]. For $\Delta T_2 \geq 130$ ms we observe the emission of two or more successive PBs in population two during the stimulation period. These PBs noticeably depress x_2, which is unable to recover before population one, characterized by a larger amount of available resources x_1, emits a PB and item one takes over [Fig. 3.7 column (2)]. However, for much longer $\Delta T_2 \geq 850$ ms, the absence of activity in population one leads to a noticeable decrease of the utilization factor u_1. As a matter of fact at the end of the stimulation period, the item two is finally selected [Fig. 3.7 column (3)].

To summarize, item two can be selected when the duration of the stimulation is restricted to a narrow time interval, sufficiently long to render the efferent synapses of population two stronger than those of population one, but not so long to highly deplete the resources of the same synapses. Furthermore, item two can be selected when ΔT_2 is sufficiently long to allow for the decay of the synaptic facilitation of population one towards its baseline value.

3.2.5 Multi-Item Memory Loading

In order to be able to load a higher number of memory items in WM, we consider the neural mass model with m-STP (Eqs. (3.1) and (3.2)) arranged in a more complex architecture composed by $N_{\text{pop}} = 7$ excitatory and one inhibitory populations, each excitatory population coding for one memory item. The system is initialized with all the populations in the silent state. Then, each item is loaded by delivering an excitatory pulse of amplitude $\Delta I_k = 1$ and duration of $\Delta T_k = 0.2\,\text{s}$ to the chosen population, while successive items are loaded at intervals of 1.25 s.

Let us first consider the successive loading of $N_L = 3$ items shown in Fig. 3.8. As one can appreciate from the spectrogram reported in Fig. 3.8(d), during the loading phase, each stimulated excitatory population emits a sequence of PBs in the $\beta - \gamma$ range ($\simeq 27$ Hz) via a PING-like mechanism mediated by the inhibitory population. This is joined to stimulus locked transient oscillations in the δ-band around 2 Hz. Furthermore, during each loading period, the activity of the other populations is interrupted and it recovers when the stimulation ends. These results resemble the LFP measurement performed in PFC of primates during coding of objects in short term-memory [48, 49]. In particular, the experimentally measured power spectrum of the LFP displays transient oscillations at $\simeq 2 - 4$ Hz in the δ range, phase-locked to stimulus presentation, together with tonic oscillations at $\simeq 32$ Hz.

As shown in Fig. 3.8(a), the loading of each item is followed by the emission of PBs from the stimulated population at regular time intervals T_c. Therefore, in this case, the number N_I of items retained in the WM coincides with the number N_L of the loaded ones. The PBs of all the excited populations arrange in a sort of *splay state* with inter-burst periods $T_b = T_c/N_I$ [147]. The period T_c depends on the number of retained items: for $N_I = 3$ we have $T_c \simeq 0.2035$ s.

The non stimulated populations display a low firing activity modulated by the slow PB emission occurring in the excitatory populations and by the fast $\beta - \gamma$ transient oscillations towards the focus equilibrium, sustained by the inhibitory activity [Fig. 3.8(b)].

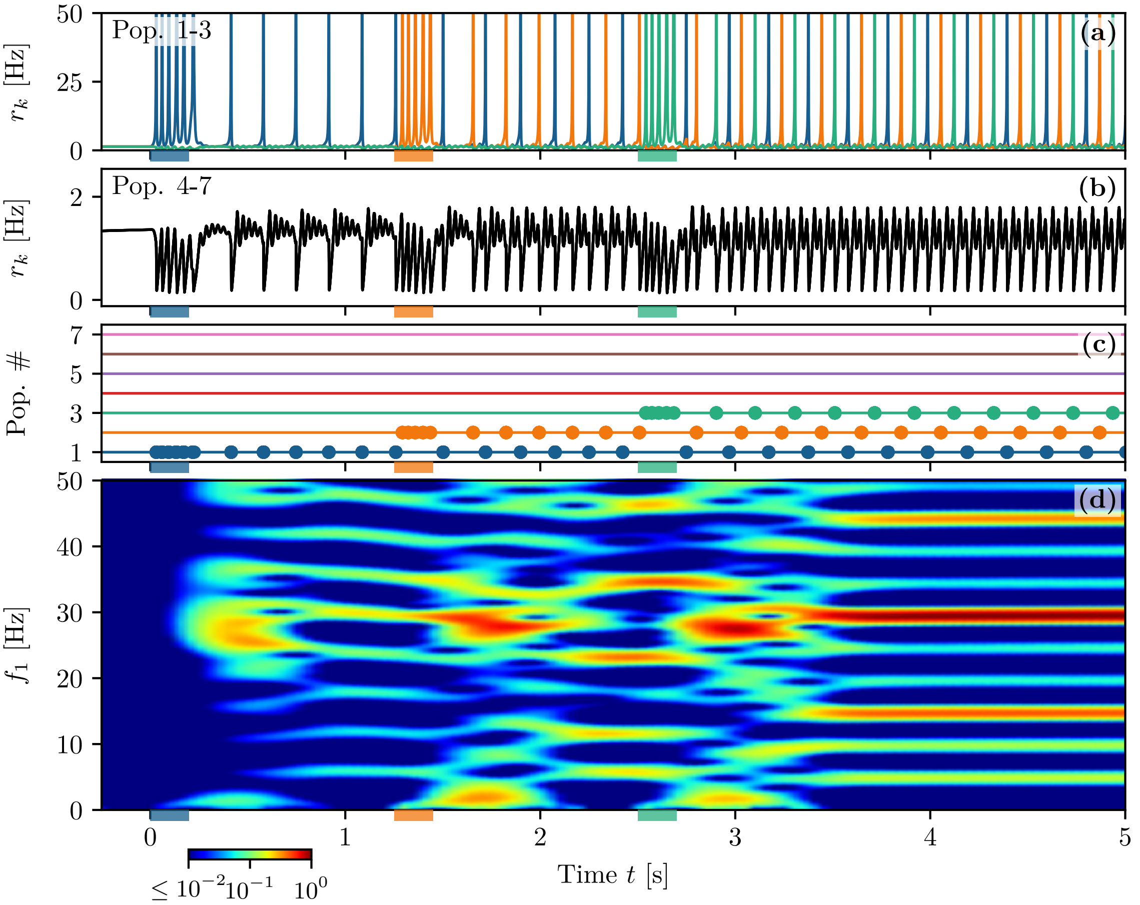

Figure 3.8: Multi-item memory loading (3 items). **(a)** Firing rates $r_k(t)$ of excitatory populations: blue, orange and green curves corresponds to $k = 1, 2, 3$; **(b)** the black curves refers to $k = 4, \ldots, 7$. **(c)** PBs of excitatory populations: horizontal lines in absence of dots indicate low activity regimes; colored dots mark the PBs' occurrences. The colored bars on the time axis denote the presence of a stimulation pulse targeting the corresponding population. Only populations $k = 1, \ldots, 3$ are stimulated in the present example. **(d)** Spectrogram of the average membrane potential $v_1(t)$ of population one. For the estimation of the spectrogram see Section 1 of Appendix C. Parameters values are: $N_{\text{pop}} = 7$, $\tau_{\text{m}}^{\text{e}} = 15$ ms, $\tau_{\text{m}}^{\text{i}} = 10$ ms, $J_{\text{ee}}^{(\text{s})} = 154$, $J_{\text{ee}}^{(\text{c})} = \frac{4}{7} \cdot 18.5$, $J_{\text{ei}} = -26$, $J_{\text{ie}} = \frac{4}{7} \cdot 97$, $J_{\text{ii}} = -60$, $I_{\text{B}} = 0$, $H^{(\text{e})} = 0.05$, $H^{(\text{i})} = -2$, $\Delta^{(\text{e})} = \Delta^{(\text{i})} = 0.1$

In particular, one observes fast COs ($\simeq 27$ Hz) nested in slow oscillations, characterized by a frequency increasing with the number of loaded items (from the θ-band for 1 item to the β-band for 3 items), similar to what has been reported in [119–121].

A more detailed analysis of the spectrogram in Fig. 3.8(d) reveals that, after each loading phase, several harmonics of the fundamental frequency $f_c \equiv 1/T_c \simeq 5$ Hz are excited. In particular after the complete loading of the three items the most enhanced harmonics are those corresponding to $3f_c \simeq 15$ Hz and $6f_c \simeq 30$ Hz. This is due to the coincidence of the frequency $3f_c = f_{\text{b}} \equiv 1/T_{\text{b}}$ with the inter-burst frequency f_{b}, while the main peak in the spectrogram, located at 30 Hz, is particularly enhanced due to the resonance with the proximal $\beta - \gamma$ rhythm associated with the PING-like oscillations emerging during memory loading.

In Figs. 3.9 and 3.10 we perform similar numerical experiments as in Fig. 3.8, but this time stimulating $N_L = 5$ and $N_L \in \{6, 7\}$ excitatory populations, respectively. It is interesting to notice that the transient δ oscillations related to the stimulation phase are only supported by the excitatory population dynamics, as evident by comparing the

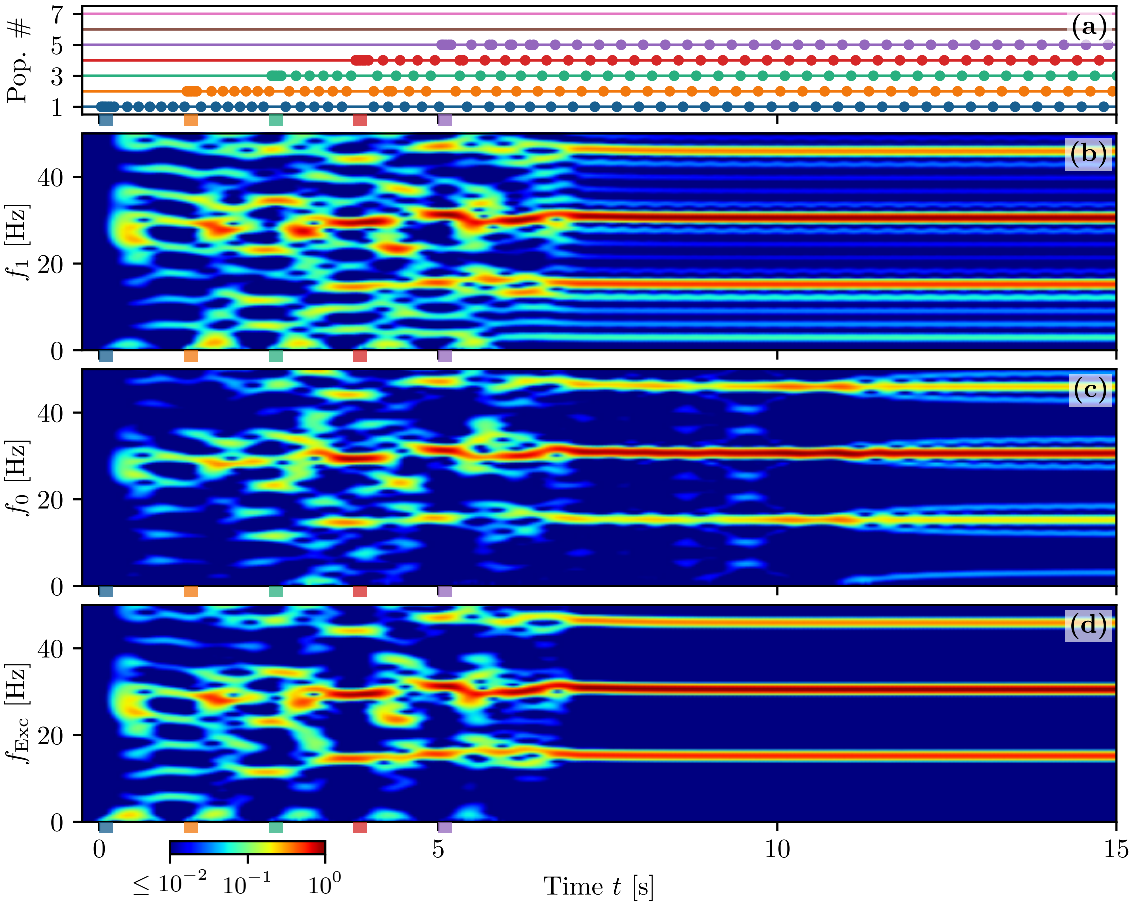

Figure 3.9: Multi-item memory loading (5 items). Response of the system when $N_L = 5$ excitatory populations are subsequently stimulated at a presentation rate of 0.8 Hz. **(a)** PBs of excitatory populations: horizontal lines in absence of dots indicate low activity regimes; colored dots mark the PBs' occurrences. The colored bars on the time axis denote the presence of a stimulation pulse targeting the corresponding population. Only populations $k = 1, \dots, 5$ are stimulated in the present example. **(b)** $v_1(t)$, **(c)** $v_0(t)$ and **(d)** of the mean membrane potentials averaged over all the excitatory populations; for clarity the corresponding frequencies have been denoted as f_1, f_0 and f_{Exc}. For the estimation of the spectrogram see Section 1 of Appendix C. Parameter values are as in Fig. 3.8.

spectrograms for $v_1(t)$ [Fig. 3.9(b) and Fig. 3.10(b)] and for the membrane potential averaged over all excitatory populations [Fig. 3.9(d) and Fig. 3.10(d)] with those for the inhibitory population [Fig. 3.9(c) and Fig. 3.10(c)]. Another important aspect is that only the harmonics of $f_{\mathrm{b}} \equiv N_{\mathrm{I}} f_c$ are present in the spectrogram of the inhibitory population, and in that associated with the average excitatory membrane potential, but not all the other harmonics of f_c. This is related to the fact that, in the average of the mean excitatory membrane potentials, the bursts of all populations will be present with a period T_{b}, therefore in this time signal there is no more trace of the periodic activity of the single population. This is due to the fact that $T_{\mathrm{c}} \equiv N_{\mathrm{I}} T_{\mathrm{b}}$. Furthermore, in the dynamics of the inhibitory population, the activity of all excitatory populations are reflected with the same weight, therefore also in this case there is no sign of the fundamental frequency f_c.

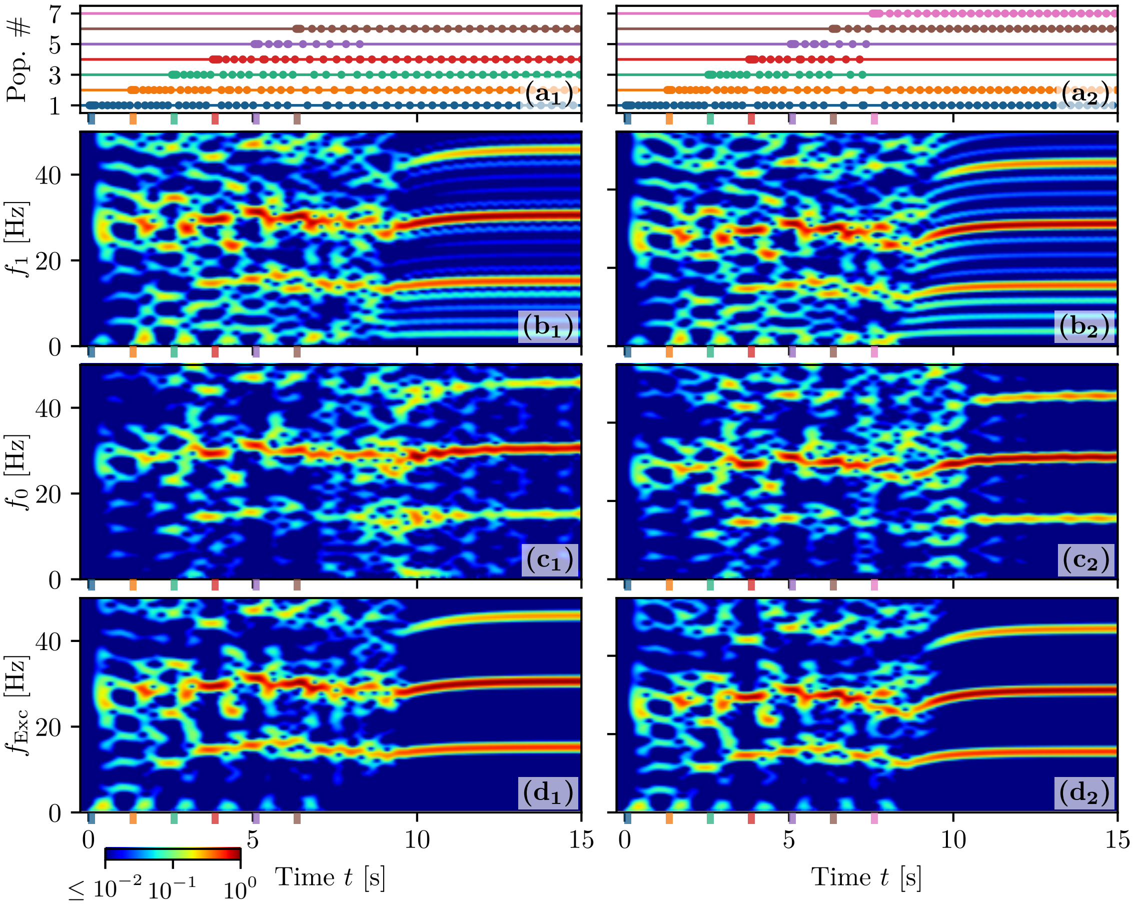

Figure 3.10: Multi-item memory loading (6 and 7 items). Response of the system when $N_L = 6$ [column **(1)**] or $N_L = 7$ [column **(2)**] excitatory populations are successively stimulated at a presentation rate of 0.8 Hz. **(a)** Population bursts of excitatory populations: horizontal lines in absence of dots indicate quiescence phases at low firing rates r_k for populations $k = 1, \ldots 7$. Dots mark PBs of the corresponding population. The colored bars on the time axis mark the starting and ending time of stimulating pulses, targeting each population. Spectrograms of the mean membrane potential **(b)** $v_1(t)$, **(c)** $v_0(t)$ and **(d)** of the mean membrane potentials averaged over all the excitatory populations; for clarity the corresponding frequencies have been denoted as f_1, f_0 and f_{Exc}. Parameter values are as in Fig. 3.8.

Memory Capacity

In Fig. 3.9 the $N_L = 5$ loaded items are retained in WM. However, if we load a sixth item as done in Fig. 3.10 column (1), WM is only able to maintain the loaded $N_\text{L} = 6$ items for a short time interval $\simeq 1$ s, after which population five stops emitting PBs. The corresponding item is not in WM anymore and the memory load returns to $N_\text{I} = 5$. By loading $N_L = 7$ items [Fig. 3.10 column (2)] we can induce more complex instabilities in the WM, indeed the reported experiment reveals that, in the end, only $N_\text{I} = 4$ items can be maintained, suggesting that a too fast acquisition of new memory items can compromise also already stored WM items. As a matter of fact, only the oldest and newest items are retained by WM: this in an example of the so-called *primacy and recency effect*, which has been reported in many contexts when a list of items should be memorized [44, 45].

To investigate more in detail the memory capacity of our model, we have considered different presentation rates f_{pres} for the items. In particular, we have applied stimulation pulses to all the excitatory populations sequentially, from the first to the seventh, with a presentation rate f_{pres}. Each pulse is characterized by an amplitude $\Delta I = 16$ and

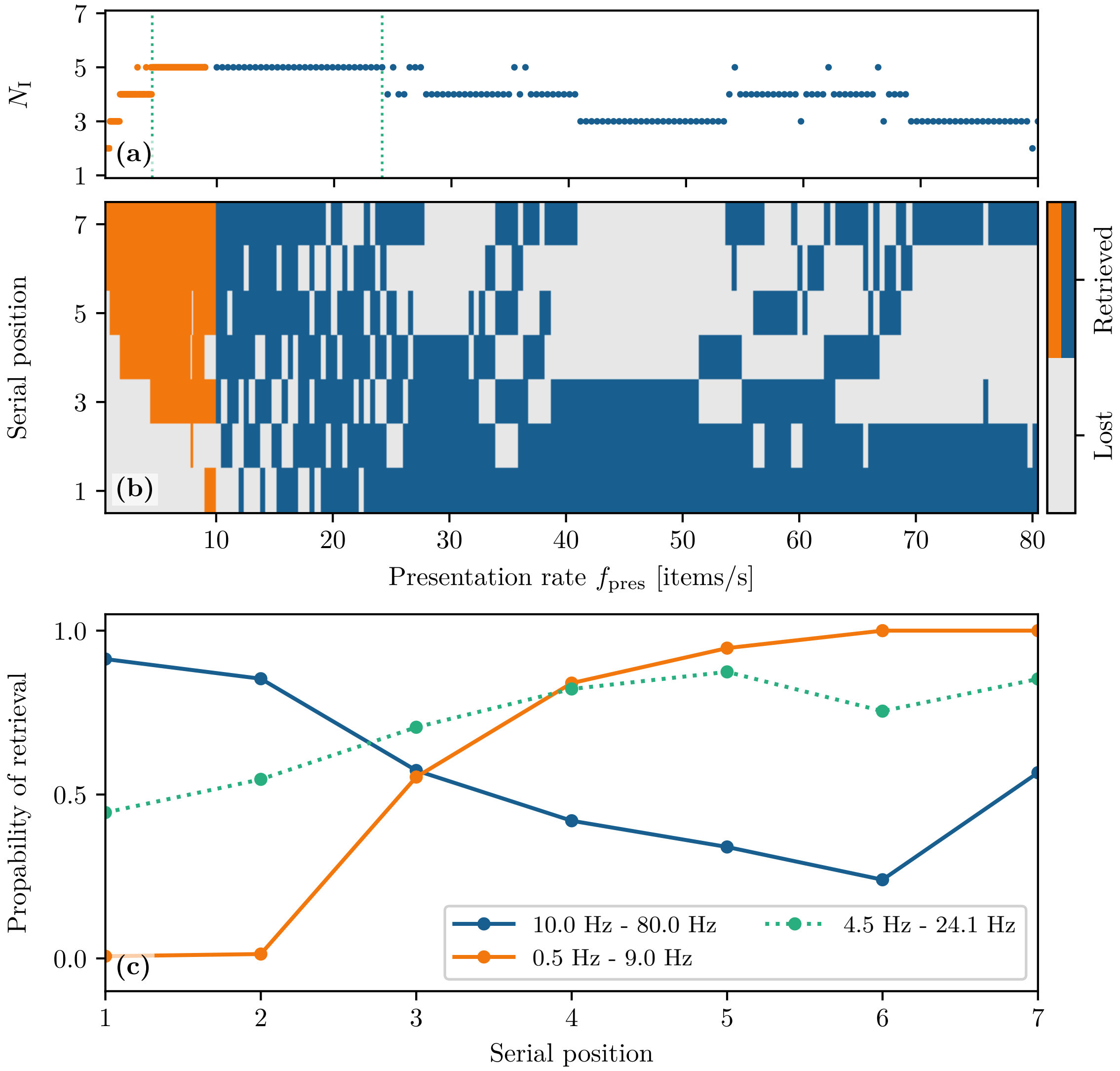

Figure 3.11: Dependence of the memory capacity on the presentation rate. (a) Total number of retrieved items $N_{\rm I}$ vs. presentation frequency $f_{\rm pres}$ for slow ([0.5 : 9.0] Hz, orange) and fast presentation rates ([10 : 80] Hz, blue). The two green dotted vertical lines denote an optimal rate interval where $N_{\rm I}$ is maximal. **(b)** Map showing the retrieved items at a given serial position for presentation rates $f_{\rm pres}$ in the interval [0.5 : 80] Hz. **(c)** Probability of retrieval vs. serial position for slow (orange) and fast (blue) presentation rates. In order to estimate these probabilities 150 equidistant rates are considered in the interval [0.5 : 9] Hz and 150 in [10, 80] Hz. The green dotted line refers to the probability estimated within the rate interval enclosed between two green dotted vertical lines in (a). An item is considered as retrieved if the corresponding population is still delivering PBs 20 s after the last stimulation. All other parameter values are as in Fig. 3.8.

a duration $\Delta T = 1/f_{\rm pres}$. Results are presented in Fig. 3.11 for presentation rates in the interval [0.5 : 80] Hz. From Fig. 3.11(a) it turns out that the maximal capacity is five, a value that can be mostly achieved for presentation rates within an optimal range $f_{\rm pres} \in [4.5 : 24.1]$ Hz, delimited by green dashed lines in Fig. 3.11(a). For these *optimal* rates we have estimated the probability of retrieving a certain item versus its presentation position, as shown in Fig. 3.11(c) (green dashed line). The probability displays very limited variations ($\simeq 45 - 85$ %) for the 7 considered items, suggesting that in this range the retrieval of an item does not strongly depend on its position in the presentation sequence. Conversely, for slow rates ($f_{\rm pres} \leq 9$ Hz) the last loaded items result to be the retained ones (*recency effect*), as evident from the orange regions in Fig. 3.11(b). This is confirmed by the calculation of the probability of retrieval versus the corresponding serial position shown in Fig. 3.11(c) (orange curve), obtained by considering 150 equidistant rate values in the interval $[0.5 : 9]$ Hz. Finally, the *primacy and recency effect* is observable only for presentation rates faster than 9 Hz [blue regions in Fig. 3.11(b)], as confirmed by the probability shown in Fig. 3.11(c) (blue curve), which has been obtained by considering 150 equidistant frequencies within the interval $[10 : 80]$ Hz.

A theoretical estimation of the maximal capacity $N_{\mathrm{c}}^{\max}$ for WM, based on short-term synaptic plasticity, has been recently derived in [10]. By following the approach outlined in [10], we have been able to obtain an analytical expression for $N_{\mathrm{c}}^{\max}$ also for our neural mass model, namely

$$N_{\mathrm{c}}^{\max} \simeq \frac{\tau_{\mathrm{d}}}{\tau_{\mathrm{m}}^{\mathrm{e}}} \ln\left[\frac{\tau_{\mathrm{f}}/\tau_{\mathrm{d}}}{1-U_0}\right] \frac{\sqrt{C}}{\pi} \quad ; \tag{3.4}$$

where $C = \left[H^{(\mathrm{e})} + I_{\mathrm{B}} + \tau_{\mathrm{m}}^{\mathrm{e}}\left(-|J_{\mathrm{ei}}| + \bar{J}\right)\frac{\sqrt{H^{(\mathrm{e})}+I_{\mathrm{B}}}}{\pi}\right]$, with $\bar{J} = [J_{\mathrm{ee}}^{(\mathrm{s})} + (N_{\mathrm{pop}} - 2)J_{\mathrm{ee}}^{(\mathrm{c})}]\bar{x}\bar{u}$. The explicit derivation of Eq. (3.4) is reported in Section 3.4.3. As shown in [10], the value of $N_{\mathrm{c}}^{\max}$ is essentially dictated by the recovery time of the synaptic resources τ_{d} and has a weaker (logarithmic) dependence on the ratio between the facilitation and depression time scales. Furthermore, for our model, the maximal capacity increases by increasing $H^{(\mathrm{e})}$, I_{B} and the recurrent and cross excitatory synaptic couplings, while it decreases whenever the coupling from inhibitory to excitatory population is strengthened.

By employing the theoretical estimation Eq. (3.4) we get $N_{\mathrm{c}}^{\max} \in [3.6, 4.8]$, in pretty good agreement with the measured maximal capacity. We can affirm this in view of the results reported in [10] for a different mean field model, where the analytical predictions overestimate the maximal capacity by a factor two.

Memory Load Characterization

A feature usually investigated in experiments during the loading or juggling of more items is the power associated with different frequency bands. In particular, a recent experiment has examined the frequency spectra of LFPs measured from cortical areas of monkeys while they maintained multiple visual stimuli in WM [148]. These results have revealed that higher-frequency power (50–100 Hz) increased with the number of loaded stimuli, while lower-frequency power (8–50 Hz) decreased. Furthermore, the analysis of a detailed network model, biophysically inspired by the PFC structure, has shown that θ and γ power increased with memory load, while the power in the α-β band decreased [125], in accordance with experimental findings in monkeys [117]. However, for humans, an enhance in the oscillatory power during WM retention has been reported for θ [112, 113], β and γ-bands [114, 115], while no relevant variation has been registered in the α-band [114].

We considered the loading of $N_{\mathrm{L}} \leq 5$ items and estimated the corresponding power spectra, after the loading of all the considered items, for the following variables: (i) the mean membrane potential $v_1(t)$ of the excitatory population one; (ii) the mean membrane potential v_0 of the inhibitory population; (iii) the mean membrane potential averaged over all the excitatory populations. The power has been estimated in the θ, β and γ-bands by integrating the spectra in such frequency intervals. The results for $1 \leq N_{\mathrm{I}} \equiv N_L \leq 5$ shown in Fig. 3.12 reveal that the power in the γ-band is increasing with N_{I} for all the considered signals, as reported experimentally for several brain areas involved in WM [115, 142, 143]. Furthermore, the γ-power obtained for v_0 and the mean excitatory potential are essentially coincident [Fig. 3.12(c)], thus confirming the fundamental role of the inhibition in sustaining γ oscillations via a PING mechanism. Moreover, the power in the β-band, reported in Fig. 3.12(b), increases almost monotonically for v_1, while it displays a non

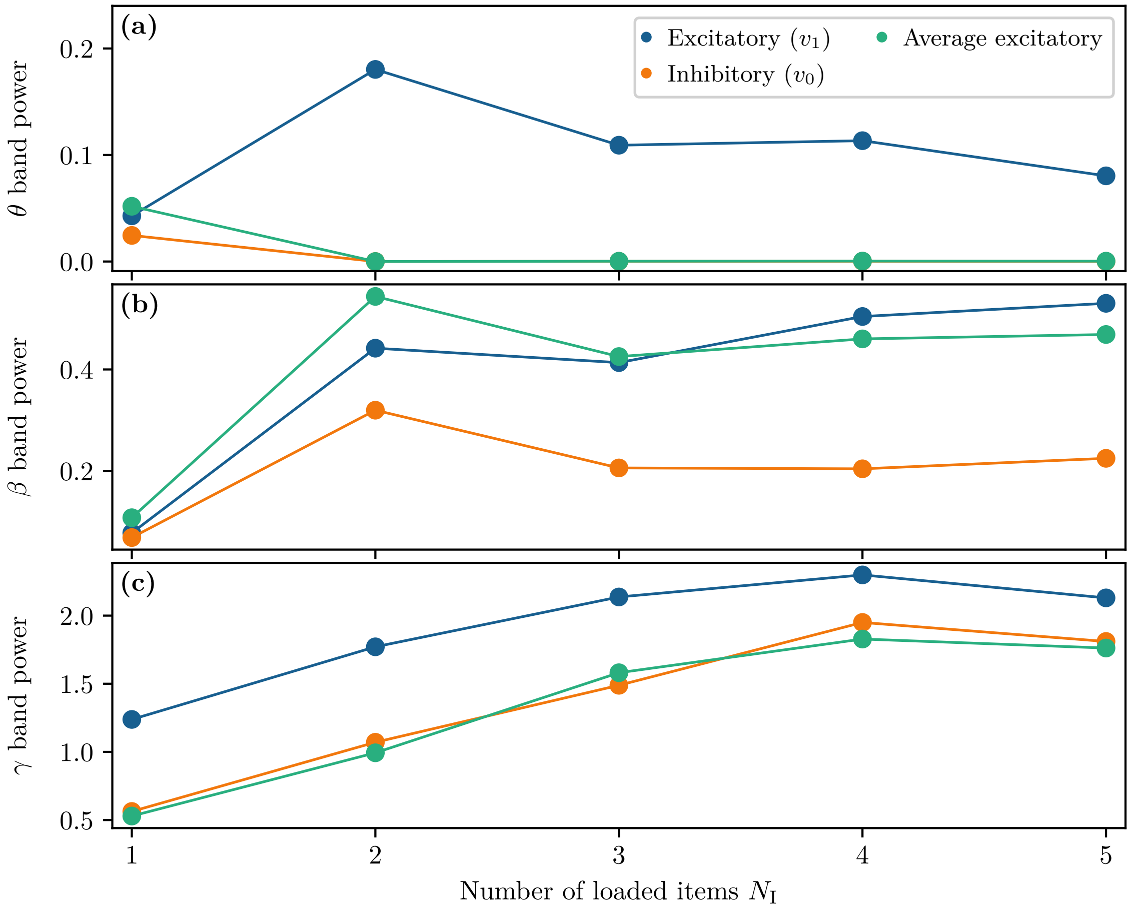

Figure 3.12: Dependence of the power on the number of loaded items. **(a)** Power in the θ-band (3-11 Hz), **(b)** in the β-band (11-25 Hz) and **(c)** in the γ-band (25-100 Hz) as a function of the number $N_\mathrm{L} = N_I \leq 5$ of loaded items. The integral of the power spectra in the specified frequency bands are displayed for the mean membrane potential $v_1(t)$ of the excitatory population one (blue symbols), the mean membrane potential $v_0(t)$ of the inhibitory population (orange symbols) and the mean membrane potentials averaged over all the excitatory populations (green symbols). The power spectra have been evaluated over a 10 s time window, after the loading of N_I items, when these items were juggling in WM. Parameter values as in Fig. 3.8.

monotonic behavior for the inhibitory population and for the average excitatory membrane potential, while saturating to a constant value for $N_I \geq 3$. More striking differences emerge when considering the θ power [Fig. 3.12(a)]: in this case the power spectra for v_0 and the average excitatory membrane potential display almost no variations with N_I, while that for v_1 increases by passing from one to two loaded items before saturating for larger N_I. The observed discrepancies can be explained by the fact that the fundamental frequency f_c and its harmonics are present in the spectrum of v_1, while they are absent both in the spectrum of v_0 and of the average excitatory membrane potential. We have not observed any variation in the α-power, comparable to what is reported in the experimental study [114].

Finally, inspired by a series of experimental works reporting neurophysiological measures of WM capacity in humans [103, 137], we have investigated if a similar indicator can be defined also in our context. In particular, the authors in [103] measured, as a neural correlate of visual memory capacity, the event-related potentials (ERPs) from normal young adults performing a visual memory task. Each patient was presented a bilateral array of 2 × N_L colored squares and he/she was asked to remember the N_L items in only one of the two hemifields. Due to the organization of the visual system, the relevant ERPs associated with this visual stimulation should appear in the controlateral hemisphere. Therefore the difference between controlateral and ipsilateral activity has been measured in order to remove any nonspecific bilateral ERP activity. The authors observed that, by increasing the number of squares N_L, also the ERP difference increases, while it saturates by approaching the maximal capacity (measured during the same test) and even decreases for $N_L > N_c^{\max}$. Thus the ERP difference can be employed as a reliable neurophysiological predictor of memory capacity.

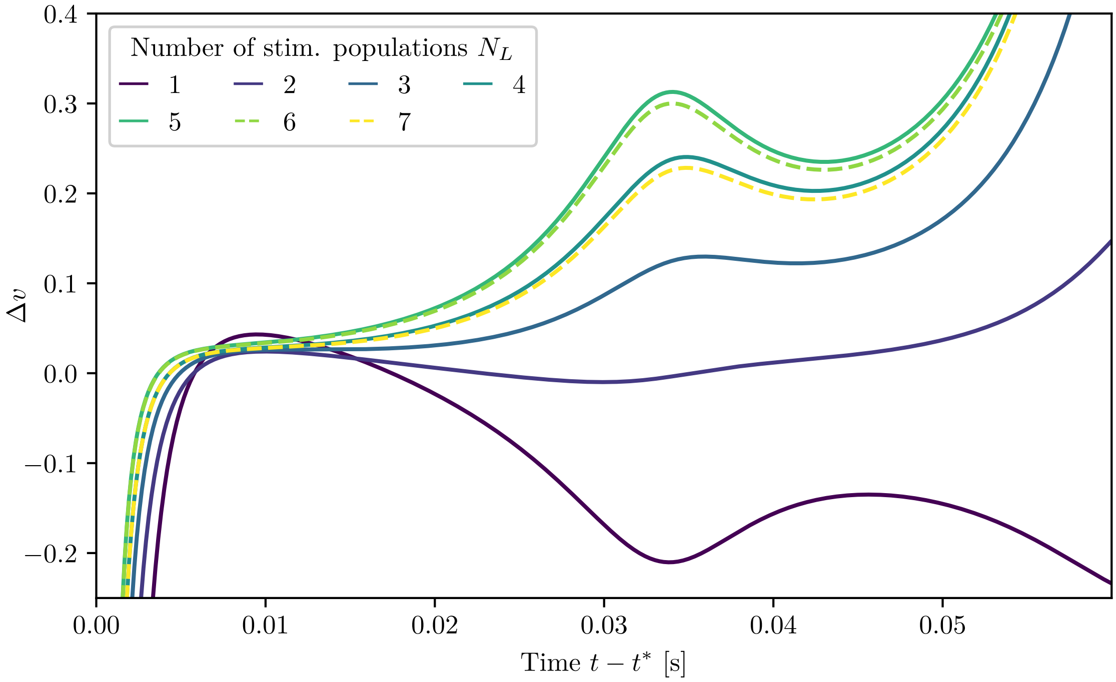

Figure 3.13: Dependence of the membrane potential difference on the number of loaded items. Difference Δv of membrane potentials versus time when stimulating different numbers N_L of populations. The presented time-series are aligned to t^*, which marks the deliverance of a PB from population one. The populations are stimulated sequentially with parameter values as in Fig 3.8.

In order to define a similar indicator in our case, we have calculated the membrane potential difference Δv between the mean membrane potential, averaged over the populations coding, for the retained items [whose activity is reported for example in Fig. 3.8(a)] and the one averaged over the non-coding populations [e.g. see Fig. 3.8(b)]. By measuring Δv just after the emittance of a PB by the first population, we observe a clear growth of this quantity with the number N_L of presented items, as shown in Fig. 3.13(f)or $N_L \in \{1, 2, 3, 4, 5, 6, 7\}$. However, as soon as $N_L > N_c^{\max}$ the membrane difference Δv almost saturates to the profile attained for $N_L = N_c^{\max} = 5$ and even decreases for larger N_L, as evident from the dashed lines corresponding to $N_L \in \{6, 7\}$. Analogous results have been obtained by considering the mean membrane potential of the next to fire populations instead of the difference Δv. Therefore, the results are not biased by the chosen indicator and Δv allows for a better presentation clarity.

To conclude this sub-section, we can affirm that the mean membrane potential can be employed, analogously to the ERP in the experiments [103, 137], as a proxy to measure the memory load and capacity. It is worth noticing that neither the mean membrane potential nor the ERP are accessible for firing rate models.

3.3 Discussion

In this chapter we have introduced a next generation neural mass model for WM based on short-term depression and facilitation. The model has been developed to reproduce exactly the macroscopic dynamics of heterogeneous QIF spiking neural networks with mesoscopic short-term plasticity (m-STP), in the limit of an infinite number of neurons with Lorentzian distributed excitabilities. Even though the choice of the excitability distribution allows for an analytical derivation of the model, it does not limit the generality of the results [16, 135]. As shown in Section 3.2.1, the neural mass model reproduces well not only the QIF network dynamics with m-STP plasticity but, to a large extent, it reproduces also the dynamics of networks with plasticity implemented at a microscopic level (μ-STP). Therefore, the macroscopic dynamics of spiking neural networks made of hundreds of thousands of neurons with synapses evolving accordingly to realistic cellular mechanisms, can be well captured in terms of a four dimensional mean-field model.

The novelty of this neural mass model, besides not being heuristic, but derived in an exact manner from the microscopic underlying dynamics, is that it reproduces the evolution of the population firing rate as well as of the mean membrane potential. This allows us to get insight not only on the synchronized spiking activity, but also on the sub-threshold dynamics and to extract information correlated to LFPs, EEGs and ERPs, that are usually measured during WM tasks to characterize the activity of the brain at a mesoscopic/macroscopic scale. The knowledge of the mean membrane potential evolution is fundamental in order to capture the dynamics displayed by the underlying microscopic QIF network, already in the absence of plasticity. Indeed, at variance with this next generation of neural mass models, a rate model cannot reproduce the fast oscillations observed in purely inhibitory networks [46], nor memory clearance obtained via a resonance mechanism between an external β forcing and the intrinsic network oscillations[32]. As we have shown in Section 3.2.3, a heuristic firing rate model, specifically designed to reproduce the QIF network dynamics with STP, does not display any oscillatory activity in the β-γ range, contrary to what observable in the spiking network itself and in our neural mass model. It should be remarked that this represents a main drawback when employing firing rate models to mimic WM operations, because the emergence of β-γ rhythms is intimately related to short-term memory activity, as shown in several experiments on humans and monkeys [48, 49, 114–117].

The macroscopic model we developed is extremely flexible since, depending on the operational point, it can mimic WM maintenance in terms of persistent spiking activity or in terms of selective and spontaneous reactivation, based on plastic footprints into the synapses. In particular, short-term depression and facilitation complement each other to obtain an efficient WM model based on synaptic reactivation. Facilitation allows us to maintain a trace of the loaded items stored in WM, while depression is responsible for the bursting activity that refreshes the WM content.

Memory loading is characterized, in any operational condition, by collective oscillations (PBs) with frequencies $\simeq 22 - 28$ Hz in the β-γ band. These oscillations emerge spontaneously in the considered model thanks to a PING-like mechanism triggered by the transient oscillations of the selectively stimulated excitatory population towards a focus equilibrium and sustained by the common inhibitory pool. The memory loading also induces stimulus-locked transient oscillations involving the harmonics of a fundamental frequency (i.e. $\simeq 2-3$ Hz). These results strongly resemble the spectral features observed in experiments on humans and monkeys performing WM tasks. Of particular interest are the responses of the primary somatosensory cortex in humans to vibrotactile stimuli [47] and the population activity of the PFC measured during a behavioral task of object recognition, performed by monkeys [48, 49]. In the first experiment stimulus-locked EEG signals have been measured revealing a transient broad-band activity in the 4-15 Hz range, followed by a stationary activity at $\simeq 26$ Hz lasting for the duration of the stimulus [47]. These findings are quite similar to the spectral features displayed by our model during one memory item loading, see Fig. 3.3. In the experiments on primates, the analysis of the LFP spectrograms revealed an evoked response around 2-4 Hz and tonic oscillations around 32 Hz [48, 49], thus resembling the power spectra that we have obtained for multi-item memory loading reported in Figs. 3.8 and 3.10.

Memory maintenance in the synaptic-based model is ensured by facilitation over a time scale of a few seconds, even in absence of spiking activity. The memory can be refreshed, and therefore maintained for a longer period, thanks to the reactivation of the synaptic resources of the excitatory population storing the item. This can be obtained, on one side, via brief non specific stimulations given to all the excitatory populations, analogous to the reactivation of latent working memories performed with single-pulse transcranial magnetic stimulation realized in humans [126]. In particular, to maintain the memory for long time intervals, the stimulations should be delivered with a period smaller than the decay time of the facilitation. On the other side the memory maintenance over long periods can be achieved thanks to the spontaneous emergence of periodic PBs delivered by the excitatory population coding for the loaded item.

An interesting aspect that we have investigated, concerns the competition between two items loaded in non-overlapping populations. When the WM load consists already of one item coded by an excitatory population, the stimulation of the other population can be regarded as a distractor. If the items are stored as repetitive PBs, we can observe three outcomes: for brief stimulations the distractor has no influence on WM, and the first item remains loaded; for sufficiently long stimulations the second item is loaded in WM; for intermediate situations both items are maintained in WM. In this latter case both populations deliver periodic trains of PBs arranged in anti-phase. Such behavior can be seen as a neural correlate to two items juggling in WM [144]. For sufficiently long and strong stimulations one observe a chaotic scenario [146], where the final outcome can be any of the three described above and it depends on small differences in the perturbation deliverance. Our findings can help in elucidating the results reported in [144], where it has been shown that, when an attended and an unattended item are juggling for a long period, the unattended item can prevail leading to a loss of the stored memory.

If the items are stored in WM as persistent states, the memory juggling is no more observable. As in the previous case, for sufficiently long stimulations, the second item substitutes the first one in WM. However, due to synaptic depression and facilitation, even a short stimulation can lead to the loading of the second item in WM, whenever its duration falls in a narrow time interval ($\simeq \mathcal{O}(\tau_\mathrm{d}/2)$) and the amplitude of the stimulation is sufficiently large. This suggests that there are optimal stimulation strategies to ensure a fast learning of a new item in WM.

By considering a neural architecture composed of multiple excitatory populations and a common inhibitory pool, more items can be maintained at the same time in WM as periodic trains of PBs. This is observable despite the possible interference among excitatory populations that are allowed to directly interact, thanks to the couplings present among them, and not only via the inhibitory pool, as in similar architectures considered in the literature [10]. All populations coding for stored items follow the same periodic dynamics, but they deliver PBs at evenly shifted phases, similarly to the splay states observed for globally coupled excitatory neuronal networks [147]. The inter-burst interval of two successive PBs approaches a value $T_\mathrm{b} \simeq 65$ ms when more than 2 items are loaded. This clearly induces the emergence of a peak in the power spectra of the mean membrane potentials in the β band for $f_\mathrm{b} \simeq 15$ Hz. However, the most prominent peak in the spectra is around 30 Hz, due to the resonance of the second harmonic of f_b with the oscillations of the inhibitory population in the $\beta - \gamma$ range. These oscillations are associated with damped oscillations of the excitatory population towards a focus equilibrium, induced by the loading of one memory item and sustained by the inhibitory pool thanks to a PING-like mechanism. The considered architecture allows for the maintenance of multi-items in WM thanks to their spontaneous reactivation, without destructive or interference effects often reported for models based on persistent spiking [127]. Furthermore, the memory of different items is associated with preferential phases with respect to the collective limit cycle behavior of the whole system, characterized by a period $T_\mathrm{c} = N_\mathrm{I} T_\mathrm{b}$, where N_I is the number of retained items. Experimental evidences of phase-dependent neural coding of objects in the PFC of monkeys have been reported in [48].

The memory load N_I of our model depends on the presentation rate f_pres of a sequence of memory items, however it is always limited between $3 \leq N_I \leq 5$ analogous to what is reported in many analysis concerning the WM capacity [149, 150]. In particular, for slow presentation rates ($f_\mathrm{pres} \leq 8$ Hz) we observe that N_I grows proportionally to f_pres and that only the last presented items are retained in the memory. The maximal capacity $N_\mathrm{c}^\mathrm{max} = 5$ can be attained mainly within an optimal range of presentation rates, namely $[4.5 : 21.4]$ Hz. These rates correspond to the characteristic frequencies associated to the PB dynamics of the model, since the inter-burst frequency is $f_\mathrm{b} \simeq 12 - 16$ Hz for $N_I > 2$, while the oscillation frequency of a single population is $f_\mathrm{c} \simeq 3 - 5$ Hz. In this optimal range there is no clear preference for the item retained in the memory and its serial position in the loaded sequence. For faster frequencies $f_\mathrm{pres} > 25$ Hz, a destructive interference among the items leads to a decrease in N_I: this mechanism has been suggested in [150] to be at the origin of the reduced capacity. For sufficiently fast rates $f_\mathrm{pres} \geq 10$ Hz, a *primacy and recency effect* [44, 45] is observable with a prevalence for the first loaded items to be retained.

To obtain a better understanding of the capacity limits of our model, we have derived an analytical expression for the maximal capacity $N_\mathrm{c}^\mathrm{max}$ by following the approach outlined in [10]. The maximal capacity is essentially controlled by the ratio between the recovery time of the available synaptic resources τ_d and the membrane time constant of the excitatory populations; conversely it reveals a weaker dependence on the ratio between facilitation and depression time scales. $N_\mathrm{c}^\mathrm{max}$ is also controlled by the excitatory and inhibitory drives. As a matter of fact, for our parameters we obtained $N_\mathrm{c}^\mathrm{max} \simeq 4 - 5$, in pretty good agreement with the measured maximal capacity.

Furthermore, we observed that the power in the γ-band (25-100 Hz) increases with the number of loaded items N_I, in agreement with several experimental studies related to WM [115, 142, 143]. Interestingly, for the γ-rhythms, the inhibitory pool and the excitatory populations contribute equally to its generation, confirming that its origin is related to a PING-like mechanism. Instead the power in the β-band reveals a non monotonic behavior with N_I, characterized by a rapid increase passing from 1 to 2 items, a small drop from 2 to 3 items while remaining essentially constant for $N_\mathrm{I} \geq 3$. The activity in the θ-band is associated with the single excitatory population dynamics only, due to the fact that the inhibitory population is not involved in the memory maintenance of single items. No variation with N_I have been observed in the α-band, analogous to what is reported for experiments on humans during memory retention in [114].

Finally, we have defined a measure of the memory capacity in terms of the mean membrane potential measured just after a PB deliverance. This quantity increases with the number of loaded items for $N_I < 5$ and saturates for $N_I \geq 5$. These results resemble the ones obtained for the ERPs detected in young adults performing visual memory tasks [103, 151]. This analysis suggests that in our neural mass model the value of the mean membrane potential can be employed to measure memory load and capacity, in analogy with the neurophysiological indicator defined in [103, 137].

However our neural mass model presents several simplifications from a biological point of view, such as the pulsatile interactions or the absence of transmission delays, therefore more realistic aspects should be included in future developments. As shown for this next generation of neural mass models, in absence of plasticity, the inclusion of the time scales associated with the rise and decay of the post-synaptic potentials could induce the emergence of new oscillatory rhythms [27, 46], while the delayed synaptic transmission could lead to more complex macroscopic behaviors [152]. For what concerns the plasticity terms, we expect to further improve the agreement between the neural mass model and the network dynamics with μ-STP by including the correlations and the fluctuation of the microscopic synaptic variables in the mean-field formulation, analogous to what has been done in [92].

A fundamental aspect of WM, not included in our model, is the volitional control, which is a cognitive function that allows for the control of behavior from the environment and to turn it towards our internal goals [100]. A flexible frequency control of cortical oscillations has been recently proposed as an unified mechanism for the rapid and controlled transitions of the WM between different computational operations [32, 108, 141]. In particular, the authors consider as a neural correlate of WM a bistable network with coexisting persistent and resting states that an external periodic modulation can drive from an operating mode to another one depending on the frequency of the forcing. However, in [32] it has been suggested that the forcing term, in order to be considered more realistic, should self-emerge by the network dynamics in form of trains of periodic PBs and not be imposed from the exterior. In our model for synaptic-based WM we have shown that some WM operations are associated with PBs delivered at different frequencies: namely, item loading and recall with transient oscillations in the δ band, as in [32], joined to burst oscillations in $\beta - \gamma$ band as in [141]; multi-item maintenance to harmonics in the $\beta - \gamma$ band. Therefore, we believe that our neural mass model with STP can represent a first building block for the development of an unified control mechanism for WM, relying on the frequencies of deliverance of the self-emerging trains of PBs. However, a development towards realistic neural architectures would require to design a multi-layer network topology to reproduce the interactions among superficial and deep cortical layers [127].

3.4 Methods

3.4.1 Bifurcation analysis

In order to exemplify the dynamical mechanisms underlying the maintenance of different items in presence of STP, we analyze the bifurcation diagram for the model with three populations, given in Eqs. (3.1) to (3.3). In particular, we study the emergence of the different dynamical states occurring in a network made of two excitatory and one inhibitory population corresponding to the network architecture introduced in Section 3.2.2.

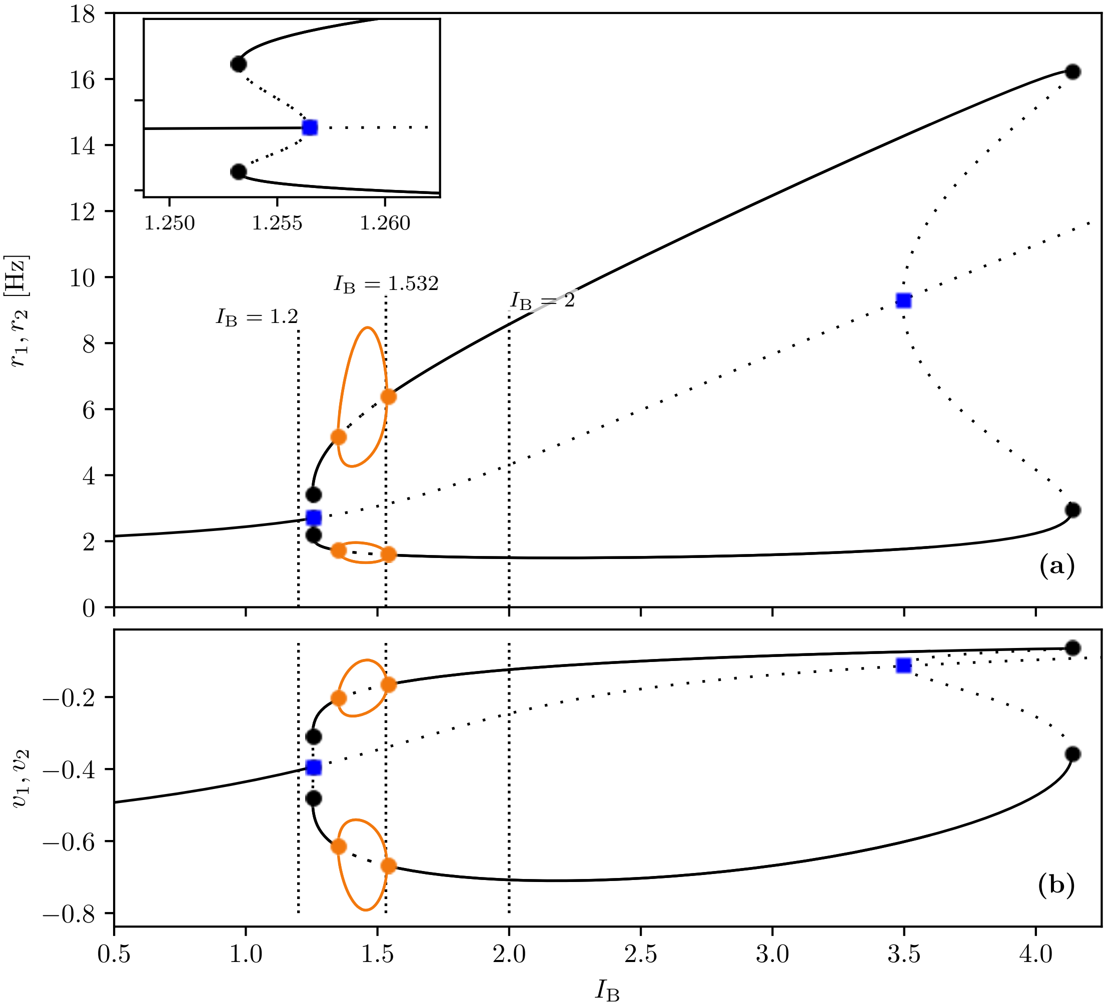

Figure 3.14: Bifurcation diagram for two excitatory populations. Bifurcation diagram displaying the **(a)** instantaneous firing rates r_k and **(b)** mean membrane potentials v_k for the excitatory populations as a function of the background current I_B. Solid (dashed) black lines refer to stable (unstable) asynchronous states, while orange solid lines denote the maxima and the minima of stable collective oscillations. Symbol refer to bifurcation points: branch points (blue squares), Hopf bifurcations (orange circles) and saddle-node bifurcations (black circles). The inset in (a) displays an enlargement of the bifurcation diagram. The lower (upper) branch of equilibria in (a) corresponds to the lower (upper) branch in (b). All the remaining parameters are as in Fig. 3.3. Numerical bifurcation analysis was performed with AUTO-07P [153].

Due to the symmetries in the synaptic couplings and in the structure of Eqs. (3.1) to (3.3). the macroscopic dynamics observable for the two excitatory networks will be equivalent. Therefore, we will display the bifurcation diagram in terms of the instantaneous firing rate $r_k(t)$ and the mean membrane potential $v_k(t)$ of one of the two excitatory populations ($k > 0$) as a function of the common background current I_{B} by fixing all the other parameters of Eqs. (3.1) and (3.2) as in Fig. 3.3. The phase diagram, shown in Fig. 3.14, reveals that at low values of the background current ($I_{\mathrm{B}} \leq I_{\mathrm{sn}}^{(1)} \simeq 1.2532$) there is a single stable fixed point with an asynchronous low firing dynamics. This looses stability at $I_{\mathrm{bp}}^{(1)} \simeq 1.25647$ giving rise to two coexisting stable fixed points with asynchronous dynamics: one at low firing rate due to spontaneous activity in the network and one at high firing rate corresponding to a persistent state. As shown in the inset in Fig. 3.14(a), there is a small region $I_{\mathrm{B}} \in [I_{\mathrm{sn}}^{(1)}, I_{\mathrm{bp}}^{(1)}]$ where we can have the coexistence of these three stable asynchronous states.

At $I_{\mathrm{B}} \equiv I_{\mathrm{hb}}^{(1)} \simeq 1.34998$ we observe the emergence of coexisting collective oscillations (periodic PBs) at low and high firing rates via supercritical Hopf bifurcations. These oscillations exist in a quite limited range of parameters, namely $I_{\mathrm{B}} \in [I_{\mathrm{hb}}^{(1)}, I_{\mathrm{hb}}^{(2)}]$, and they disappear at $I_{\mathrm{hb}}^{(2)} \simeq 1.5363$. Beyond this parameter value we again have a persistent state coexisting with a low firing activity regime, these states finally annihilate with two unstable fixed point branches at $I_{\mathrm{sn}}^{(2)} \equiv 4.13715$.

The knowledge of the bifurcation diagram shown in Fig. 3.14 allows us to interpret the numerical experiments discussed in Section 3.2.3 and displayed in Fig. 3.3. Let us consider the first experiment, reported in column (1) of Fig. 3.3 and showing the selective reactivation of the WM item via a nonspecific read-out signal. The item is firstly loaded into population one via a specific step current of amplitude $\Delta I_1(t) = 0.2$ for a time interval $\Delta T_1 = 350$ ms. The selective reactivation of the target is obtained by applying a non-specific readout signal of amplitude $\Delta I_1(t) = \Delta I_2(t) = 0.1$ to all excitatory neurons in both populations for a shorter time interval, namely $\Delta T_1 = \Delta T_2 = 250$ ms. For this numerical experiment we fixed $I_{\mathrm{B}} = 1.2 < I_{\mathrm{sn}}^{(1)}$, thus the only possible stable regime is a low firing asynchronous activity. The item is loaded into population one by increasing, for a limited time window, the background current only for this population to the level $I_{\mathrm{B}} + \Delta I_1 > I_{\mathrm{hb}}^{(1)}$, thus leading to the emission of a series of PBs, whose final effect is to strongly facilitate the efferent synapses of population one. The subsequent application of a non-specific read-out signal amounts to an effective increase of their common background current to a value beyond $I_{\mathrm{bp}}^{(1)}$, where the persistent state coexists with the low firing activity. Indeed during the read-out stimulation, population one displays a burst of high activity, due to the facilitated state of its synapses, while population two is essentially unaffected by the read-out signal. As soon as the stimulus is removed, the system moves back to the spontaneous activity regime.

The second experiment, shown in the column (2) of Fig. 3.3, concerns spontaneous reactivation of the WM item via collective oscillations (periodic PBs). In this case the background current is set to $I_{\mathrm{B}} = 1.532$, in order to have the coexistence of two stable limit cycles corresponding to periodic PBs with low and high firing rate. The whole system is initialized in the asynchronous regime with spontaneous activity (which is unstable for this value of I_{B}); upon the presentation of the stimulus to population one, this jumps to the upper limit cycle after loading the item into the memory. Once the stimulation is removed, due to the periodic synaptic refreshment, population one reactivates spontaneously by emitting a periodic sequence of PBs that is terminated by reducing I_{B} to a value smaller than $I_{\mathrm{sn}}^{(1)}$.

The last experiment shown in column (3) of Fig. 3.3 refers to the spontaneous reactivation of the memory associated with a persistent state activity. In this case we set $I_{\mathrm{B}} = 2$, thus the system is in an asynchronous regime beyond $I_{\mathrm{hb}}^{(2)}$, where there is coexistence of persistent and low firing activity beyond $I_{\mathrm{hb}}^{(2)}$. As in the previous experiment, the system is initialized in the asynchronous unstable regime. Upon a brief stimulation, population one is led in the high activity persistent regime. Reducing the background current to $I_\mathrm{B} = 1.2$ stops the persistent activity.

3.4.2 Heuristic Firing Rate Model

Firing rate models have been developed to describe heuristically the dynamics of a neuronal population in terms of the associated firing rate r; one of the most known example is represented by the Wilson-Cowan model [7]. These models are usually written as [154]

$$\tau_\mathrm{m}\dot{r} = -r + \Phi(I) \ , \tag{3.5}$$

where I represents the total input current received by each neuron in the population and $\Phi(I)$ is the steady-state firing rate solution, or activation function. This function is usually assumed to be a sigmoidal function and it is determined on the basis of the dynamical features of the neurons in the considered population. As stated in [46], these firing rate models, despite being extremely useful to model brain dynamics, do not take into account synchronization phenomena induced by the sub-threshold voltage dynamics. Therefore, these firing rate models fail in reproducing fast oscillations observed in inhibitory networks, without the addition in their dynamics of an ad-hoc time delay. These collective oscillations are instead captured by the neural mass model introduced in [16] and considered in this chapter.

By following the analysis in [46], we can obtain a heuristic firing rate model corresponding to the exact neural mass ODEs given in Eqs. (3.1) and (3.2). More specifically this firing rate description can be derived for a QIF network of spiking neurons, by considering the corresponding steady-state solution (v^*, r^*) given by

$$0 = \frac{\Delta}{\tau_\mathrm{m}\pi} + 2r^*v^* \tag{3.6a}$$
$$0 = (v^*)^2 - (\pi\tau_\mathrm{m}r^*)^2 + I \tag{3.6b}$$

where $I = H + I_\mathrm{B} + I_\mathrm{S} + \tau_\mathrm{m}\tilde{J}r^*$. This leads to a self-consistent equation for the steady-state firing rate, given by $r^* = \Phi(I)$, where

$$\Phi(I) = \frac{1}{\sqrt{2}\pi\tau_\mathrm{m}}\sqrt{I + \sqrt{I^2 + \Delta^2}} \quad . \tag{3.7}$$

The Eqs. (3.5) and (3.7) represent a firing rate model corresponding to the QIF spiking network with m-STP. This firing rate model has been considered in Section 3.2.3 in order to perform numerical experiments on WM maintenance (see Fig. 3.4).

3.4.3 Maximal Working Memory Capacity

By following [10] we can give an estimate of the maximal memory capacity for our neural mass model with m-STP Eqs. (3.1) and (3.2). The maximal capacity can be estimated as the ratio of two time intervals

$$N_\mathrm{c}^\mathrm{max} \simeq \frac{T_\mathrm{c}^\mathrm{max}}{T_\mathrm{b}} \tag{3.8}$$

where $T_\mathrm{c}^\mathrm{max}$ is the maximal period of the network limit cycle and T_b the inter-burst interval between two successive PBs. In [10], $T_\mathrm{c}^\mathrm{max}$ has been estimated as the time needed to the synaptic efficacy $u_k(t)x_k(t)$ of a generic population k to recover to the maximum value after a PB emission. Since all the excitatory populations are identically connected among them and with the inhibitory population, this time does not depend on the considered population. The approximate expression reported in [10] is the following

$$T_{\rm c}^{\rm max} \simeq \tau_{\rm d} \ln \frac{\tau_{\rm f}/\tau_{\rm d}}{1-U_0} \tag{3.9}$$

As expected the recovery time is essentially ruled by the depression time scale $\tau_{\rm d}$.

It can be shown that $T_{\rm b}$ has three components, i.e. the duration of the previous excitatory PB, the delay of the inhibitory burst triggered by the excitatory PB, plus its duration and the time needed for the next active excitatory population to recover from inhibition and to elicit a PB. In our model framework, we can neglect the first two time intervals and limit ourselves to estimate the latter time.

Let us denote the next firing population as the m-th one; we can assume that during $T_{\rm b}$ the connection strength does not vary much and that the firing rates are essentially constants. Therefore we can rewrite the time evolution of the mean membrane potential appearing in Eqs. (3.1) as follows :

$$\tau_{\rm m}^{\rm e} \dot{v}_k = v_k^2 + \left[H^{(\rm e)} - (\pi \tau_{\rm m}^{\rm e} \bar{r}^{(\rm e)})^2 + I_{\rm B} + \tau_{\rm m}^{\rm e}\left(-|J_{\rm ei}|\bar{r}^{(\rm i)} + \bar{J}\bar{r}^{(\rm e)}\right)\right] = v_k^2 + C \tag{3.10}$$

where $\bar{J} = [J_{\rm ee}^{(\rm s)} + (N_{\rm pop}-2)J_{\rm ee}^{(\rm c)}]\bar{x}\bar{u}$ takes in account the synaptic efficacy of all excitatory synapses in an effective manner, $\bar{r}^{(\rm i)}$ and $\bar{r}^{(\rm e)}$ are the inhibitory and excitatory population rates and C is the constant quantity within square brackets on the right-hand side. The expression of C can be further simplified by noticing that the quadratic term is negligible and by assuming that the excitatory and inhibitory firing rates are similar. Moreover, by assuming that the excitatory neurons are almost uncoupled during $T_{\rm b}$, one gets:

$$C = \left[H^{(\rm e)} + I_{\rm B} + \tau_{\rm m}^{\rm e}\left(-|J_{\rm ei}| + \bar{J}\right)\frac{\sqrt{H^{(\rm e)}+I_{\rm B}}}{\pi}\right] \tag{3.11}$$

where $\bar{r}^{(\rm i)} = \bar{r}^{(\rm e)}$ and $\bar{r}^{(\rm e)} = \frac{\sqrt{H^{(\rm e)}+I_{\rm B}}}{\pi}$ as for an isolated QIF neuron driven by the mean excitability and by the background current.

Therefore the time needed to the mean membrane potential to go from an initial negative value $v_m(0) = V_0$, determined by the discharge of the inhibitory neurons, to a *threshold* value $V_{\rm th}$, where the PB starts to be delivered, is given by

$$T_{\rm b} = \frac{\tau_{\rm m}^{\rm e}}{\sqrt{C}}\left[\arctan\frac{V_{\rm th}}{\sqrt{C}} - \arctan\frac{V_0}{\sqrt{C}}\right] \simeq \frac{\tau_{\rm m}^{\rm e}\pi}{\sqrt{C}} \tag{3.12}$$

where on the right hand side of the equation we have finally assumed that $V_{\rm th} \gg 1$ and $V_0 \ll -1$.

Thus the following expression for the maximal capacity is obtained

$$N_{\rm c}^{\rm max} \simeq \frac{\tau_{\rm d}}{\tau_{\rm m}^{\rm e}} \ln\left[\frac{\tau_{\rm f}/\tau_{\rm d}}{1-U_0}\right]\frac{\sqrt{C}}{\pi} \quad . \tag{3.13}$$

For the parameters employed in Section 3.2.5 we obtained the following theoretical values $T_{\rm c}^{\rm max} \simeq 447$ ms, $T_{\rm b} \simeq 93 - 126$ ms depending on the value of $0.5 \le \bar{x}\bar{u} \le 1.0$, thus $3.6 \le N_{\rm c}^{\rm max} \le 4.8$ not far from the measured value that was $N_{\rm c}^{\rm max} = 5$.

Chapter 4

Testing clinical hypothesis of seizure propagation using human connectomes

Dynamics underlying epileptic seizures span multiple scales in space and time, therefore, understanding seizure mechanisms requires identifying the relations between seizure components within and across these scales, together with the analysis of their dynamical repertoire. In this view, mathematical models have been developed, ranging from single neuron to neural population.

In this study we consider the neural mass model derived in Chapter 2 combined with structural information from non-invasive brain imaging, thus building large-scale brain network models to explore emergent dynamics and test clinical hypothesis. We provide a comprehensive study on the effect of external drives on neuronal networks exhibiting multistability, in order to investigate the role played by the neuroanatomical connectivity matrices in shaping the dynamics. In particular we systematically investigate the conditions under which the network displays a transition from a low activity regime to a high activity state, which we identify with a seizure-like event. This approach allows us to study the biophysical parameters and variables leading to multiple recruitment events at the network level. We further exploit topological network measures in order to explain the differences and the analogies among the subjects and their brain regions, in showing recruitment events at different parameter values.

We demonstrate, along the example of diffusion-weighted magnetic resonance imaging (MRI) connectomes of 20 healthy subjects and 15 epileptic patients, that individual variations in structural connectivity, when linked with mathematical dynamic models, have the capacity to explain changes in spatiotemporal organization of brain dynamics, as observed in network-based brain disorders. In particular, for epileptic patients, by means of the integration of the clinical hypotheses on the epileptogenic zone, i.e. the local network where highly synchronous seizures originate, we have identified the sequence of recruitment events and discussed their links with the topological properties of the specific connectomes. The predictions made on the basis of the implemented set of exact mean-field equations turn out to be in line with the clinical presurgical evaluation on recruited secondary networks.

Publication:

The results presented in this chapter are published [155]: M. Gerster et al. "Patient-Specific Network Connectivity Combined With a Next Generation Neural Mass Model to Test Clinical Hypothesis of Seizure Propagation". *Frontiers in Systems Neuroscience* 15 (2021), p. 79

Authors contributions:

MGe and HT performed the simulations and data analysis, writing original software, and investigating the results. Data curation is contributed by VJ, MGu, FB, AŠ, and JH. All the authors validated the research and participated in the drafting process. SO was responsible for conceptualization, supervision, state-of-the-art review (together with VJ), and the paper write-up.

4.1 Introduction

Epilepsy is a chronic neurological disorder characterized by the occurrence and recurrence of seizures and represents the third most common neurological disorder affecting more than 50 million people worldwide [156]. Anti-epileptic drugs are the first line of treatment for epilepsy and they provide sufficient seizure control in around two-thirds of cases [157]. However, about 30 to 40% of epilepsy patients do not respond to drugs, a percentage that has remained relatively stable despite significant efforts to develop new anti-epileptic medication over the past decades. For drug-resistant patients, a possible treatment is the surgical resection of the brain tissue responsible for the generation of seizures.

As a standard procedure, epilepsy surgery is preceded by a qualitative assessment of different brain imaging modalities in order to identify the brain tissue responsible for seizure generation, i.e. the epileptogenic zone (EZ) [50], which in general represents a localized region or network where seizures arise, before recruiting secondary networks, called the propagation zone (PZ) [51–54]. Outcomes are positive whenever the patient has become seizure-free after surgical operation.

Intracranial electroencephalography (iEEG) is commonly used during the presurgical assessment to find the seizure onset zone [50, 158, 159], the assumption being that the region where seizures emerge, is at least part of the brain tissue responsible for seizure generation. As a part of the standard presurgical evaluation with iEEG, stereotactic EEG (SEEG) is used to help correctly delineating the EZ [160]. SEEG employs penetrating depth electrodes that are implanted through small burr holes in the skull and are positioned using stereotactic guidance [51], thus allowing for the measurement of neural activity in deeper structures of the brain. Alternative imaging techniques such as structural MRI, magnetoencephalography (MEG, electroencephalography (EEG) and positron emission tomography (PET) help the clinician to estimate the position of the EZ. Recently, dMRI (dMRI) started being evaluated as well, thus giving the possibility to infer the connectivity between different brain regions by computing in-vivo fiber tract trajectories in coherently organized brain white matter pathways [161]. dMRI has revealed a quantitative decrease of regional connectivity around the EZ that is associated with a network reorganization and cognitive impairment [162]. In particular it has revealed reduced fractional anisotropy [163, 164] and structural alterations in the connectome of epileptic patients [165–167]. However, epilepsy surgery is often unsuccessful and the long-term positive outcome may be lower than 25% in extra-temporal cases [168, 169], thus meaning that the EZ has not been correctly identified or that the EZ and the seizure onset zone may not coincide [57].

In order to quantitatively examine clinical data and to determine targets for surgery, many computational models have been recently proposed [56, 170–175], that use MRI or iEEG data acquired during presurgical workup to infer structural or functional brain networks. Taking advantages of recent advances in our understanding of epilepsy, that indicate that seizures may arise from distributed ictogenic networks [54, 176, 177], phenomenological models of seizure transitions are used to compute the escape time, i.e., the time that each network node takes to transit from a normal state to a seizure-like state. Nodes with the lowest escape time are then considered as representative of the seizure onset zone and therefore candidates for surgical resection, by assuming seizure onset zone as a proxy for the EZ [171, 174]. Alternatively, different possible surgeries are simulated in silico to predict surgical outcomes [55–57] by making use of synthetic networks and phenomenological network models of seizure generation. Further attention has been paid to studying how network structure and tissue heterogeneities underpin the emergence of focal and widespread seizure dynamics in synthetic networks of phase oscillators [57, 178].

More in general there is a vast and valuable literature on computational modeling in epilepsy, where two classes of models are used: (1) macroscopic mean-field models and (2) detailed microscopic network models. Mean field models are often preferred over the more detailed models since they have fewer parameters and thus simplify the study of transitions from interictal to ictal states and the subsequent EEG analysis of data from epilepsy patients. This is justified as the macroelectrodes used for EEG recordings represent the average local field potential arising from neuronal populations. Indeed, much effort has been made so far to explain the biophysical and dynamical nature of seizure onsets and offsets by employing neural mass models [175, 179–186]. Mechanistic interpretability of the mean field parameters is lost, as many physiological details are absorbed in few degrees of freedom. Since the mean field models remain relatively simple, they can also be employed to describe epileptic processes occurring in “large-scale” systems, e.g. the precise identification of brain structures that belong to the seizure-triggering zone (epileptic activity often spreads over quite extended regions and involves several cortical and sub-cortical structures). However, only recently, propagation of epileptic seizures started to be studied using brain network models, and was limited to small populations number [187], or absence seizures [188], while partial seizures have been reported to propagate at the mesoscopic scale through cortical columns [189, 190], at the macroscopic scale through large-scale networks in humans [191] and animal models [192]. All in all, even though neural mass models are in general easier to analyze numerically because relatively few variables and parameters are involved, they drastically fail to suggest molecular and cellular mechanisms of epileptogenesis.

On the other hand, detailed network models are best suited for understanding the molecular and cellular bases of epilepsy and thus they may be used to suggest therapeutics targeting molecular pathways [193–197]. Due to the substantial complexity of neuronal structures, relatively few variables and parameters can be accessed at any time experimentally. Although biophysically explicit modeling is the primary technique to look into the role played by experimentally inaccessible variables in epilepsy, the usefulness of detailed biophysical models is limited by constraints in computational power, uncertainties in detailed knowledge of neuronal systems, and the required simplification for the numerical analysis. Therefore an intermediate “across-scale” approach, establishing relationships between sub-cellular/cellular variables of detailed models and mean-field parameters governing macroscopic models, might be a promising strategy to cover the gaps between these two modeling approaches [198–200].

In view of developing a cross-scale approach, it is important to point out that large-scale brain network models emphasize the network character of the brain and merge structural information of individual brains with mathematical modeling, thus constituting in-silico approaches for the exploration of causal mechanisms of brain function and clinical hypothesis testing [201–203]. In particular, in brain network models, a network region is a neural mass model of neural activity, connected to other regions via a connectivity matrix representing fiber tracts of the human brain. This form of virtual brain modeling [204–206] exploits the explanatory power of network connectivity imposed as a constraint upon network dynamics and has provided important insights into the mechanisms underlying the emergence of asynchronous and synchronized dynamics of wakefulness and slow-wave sleep [207] while revealing the whole-brain mutual coupling between the neuronal and the neurotransmission systems to understand the flexibility of human brain function despite having to rely on fixed anatomical connectivity [208]. Recent studies have pointed out the influence of individual structural variations of the connectome upon the large-scale brain network dynamics of the models, by systematically testing the virtual brain approach along the example of epilepsy [201–203]. The employment of patient-specific virtual brain models derived from dMRI may have a substantial impact for personalized medicine, allowing for an increase in predictivity concerning the pathophysiology of brain disorders, and their associated abnormal brain imaging patterns. More specifically a personalized brain network model derived from non-invasive structural imaging data would allow for testing of clinical hypotheses and exploration of novel therapeutic approaches.

In order to exploit the predictive power of personalized brain network models, we have implemented, on subject-specific connectomes, the next generation neural mass model that, differently from the previous applied heuristic mean-field models [201–203], is exactly derived from an infinite size network of quadratic integrate-and-fire neurons [16], as shown in Chapter 2. This neural mass model is able to describe the variation of synchrony within a neuronal population, which is believed to underlie the decrease or increase of power seen in given EEG frequency bands while allowing for a more direct comparison with the results of electrophysiological experiments like local field potential, EEG and event-related potentials (ERPs), thanks to its ability to capture the macroscopic evolution of the mean membrane potential.

The next generation neural mass model developed by [16], has been recently extended to take into account time-delayed synaptic coupling [31, 152] and, when integrated in a large-scale brain network, time delays in the interaction between the different brain areas, due to the finite conduction speed along fiber tracts of different lengths [209]. The time delay, together with the effective stochasticity of the investigated dynamics give rise, both on structural connectivity matrices of mice and healthy subjects, to preferred spatiotemporal pattern formation [210, 211] and short-lived neuronal cascades that form spontaneously and propagate through the network under conditions of near-criticality [209]. The largest neuronal cascades produce short-lived but robust co-fluctuations at pairs of regions across the brain, thus contributing to the organization of the slowly evolving spontaneous fluctuations in brain dynamics at rest.

In this chapter we have built brain network models for a cohort of 20 healthy subjects and 15 epileptic patients, implementing for each brain region the neural mass model developed by [16]. As paradigms for testing the spatiotemporal organization, we have systematically simulated the individual seizure-like propagation patterns, looking for the role played by the individual structural topologies in determining the recruitment mechanisms. Specific attention has been devoted to the analogies and differences among the self-emergent dynamics in healthy and epilepsy-affected subjects. Furthermore, for epileptic patients, we have validated the model against the presurgical SEEG data and the standard-of-care clinical evaluation. More specifically Sec. 2 is devoted to the description of the implemented model and the applied methods. In Sec. 3.1 are reported the results specific for healthy subjects, while in Sec. 3.2 is reported a detailed analysis performed on epileptic patients. Finally a discussion on the presented results is reported in Sec. 4.

4.2 Methods

In the following we consider personalized brain models derived from structural data of MRI and Diffusion tensor weighted imaging (DTI), thus implementing different structural connectivity matrices for healthy subjects and epileptic patients. For healthy subjects cortical and volumetric parcellations were performed using the Automatic Anatomical Atlas 1 (AAL1) [212] with $N_{\text{pop}} = 90$ brain regions: each region will be described in terms of a neural mass model. For epileptic subjects cortical and volumetric parcellations were performed using the Desikan-Killiany atlas with 70 cortical regions and 17 subcortical regions [213] (one more empty region is added in the construction of the structural connectivity for symmetry). In this case the structural connectivity matrix is composed, for each epileptic patient, by 88 nodes equipped with the presented region specific neural mass model capable of demonstrating epileptiform discharges.

4.2.1 Multi-population neural mass model

We will make use of the exact multi-population neural mass model described in Section 2.5 of Chapter 2, however, this time in absence of STP. To recall, it describes the dynamics of $k = 1, 2 \dots, N_{\text{pop}}$ coupled populations of QIF neurons with heterogeneously distributed excitabilities $\eta_{i,k}$, of which the dynamics is governed by Eq. (4.1),

$$\tau_{\text{m}} \dot{V}_{i,k} = V_{i,k}^2 + \eta_i^{(k)} + I_{\text{S}}^{(k)}(t) + \frac{\tau_{\text{m}}}{N} \sum_{l=1}^{N_{\text{pop}}} J_{kl} \sum_{j=1}^{N} S_{j,l}(t) \quad , \tag{4.1}$$

with the δ-spike train $S_{j,l}(t)$ of the j-th neuron in population l. The corresponding neural mass model is given by Eqs. (4.2) below.

$$\tau_{\text{m}} \dot{r}_k = \frac{\Delta}{\tau_{\text{m}} \pi} + 2 r_k v_k \tag{4.2a}$$

$$\tau_{\text{m}} \dot{v}_k = v_k^2 + \bar{\eta}^{(k)} + I_{\text{S}}^{(k)}(t) - (\pi \tau_{\text{m}} r_k)^2 + \tau_{\text{m}} \sum_{l=1}^{N_{\text{pop}}} J_{kl} r_l \tag{4.2b}$$

Parameter $\tau_{\text{m}} = 20$ ms is the membrane time constant and the heterogeneity of excitabilities is set to $\Delta = 1$ throughout this chapter. The connectivity matrix $\{J_{kl}\}$ represents the synaptic weights among the populations. Diagonal entries J_{kk} denote intra-population and non-diagonal entries $J_{kl}, k \neq l$ inter-population connections. Entries of J_{kl} are determined via a second matrix $\{\tilde{J}_{kl}\}$, which represents the topology extracted from empirical DTI. The values of $\{\tilde{J}_{kl}\}$ are normalized in the range $[0, 1]$ via rescaling with the maximal entry value, and have $\tilde{J}_{kk} = 0$ on the diagonal. In order to account for strong intra-coupling (recurrent synapses) and intermediate inter-coupling, we choose the entries of each structural connectivity as

$$J_{kl} = \sigma \begin{cases} 5 \;\; \tilde{J}_{kl} & \text{if } k \neq l \\ 20 & \text{if } k = l, \end{cases} \tag{4.3}$$

where σ is a rescaling factor common to all synapses, which we assume to be constant and equal to 1, apart few cases where we investigate the dependence on the synaptic weights. Hence, the synaptic weights for $k \neq l$ are in the range $J_{kl} \in [0, 5]$, while the intra-coupling is set to $J_{kk} = 20$, if not stated differently. This choice of the rescaling factor ensures that the single brain region finds itself in a bistable regime, thus being able to switch from a low-activity to a high-activity regime. The time dependent stimulus current $I_{\text{S}}^{(k)}(t)$ is population specific and a single population at a time is generally stimulated during a numerical experiment. The applied stimulus $I_{\text{S}}^{(k)}(t)$ consists of a rectangular pulse of amplitude ΔI and duration ΔT; the dependence on these parameters is studied in this chapter to support the generality of the results.

4.2.2 Topologies

As a first set of data, we have selected 20 diffusion-weighted magnetic resonance imaging connectomes of healthy subjects (mean age 33 years, standard deviation 5.7 years, 10 females, 2 left-handed) that participated in a study on schizophrenia as a control group [214]. We will refer to the healthy subjects as H1-H20. All subjects were recruited via local advertisements and had none of the following conditions: Personal lifetime history of any psychiatric disorder or substance abuse established by the Mini-International Neuropsychiatric Interview (M.I.N.I.) [215], any psychotic disorder in first or second-degree relatives. Further exclusion criteria included current neurological disorders, lifetime history of seizures or head injury with altered consciousness, intracranial hemorrhage, neurological sequelae, history of mental retardation, history of substance dependence, any contraindication for MRI scanning.

The scans were performed on a 3T Siemens scanner in the Institute of Clinical and Experimental Medicine in Prague, employing a Spin-Echo EPI sequence with 30 diffusion gradient directions, $TR = 8300$ ms, $TE = 84$ ms, $2 \times 2 \times 2mm^3$ voxel size, b-value $900s/mm^2$. The diffusion weighted images (DWI) were analyzed using the Tract-Based Spatial Statistics (TBSS) [216], part of FMRIB's Software Library (FSL) [217]. Image conversion from DICOM to NIfTI format was accomplished using dcm2nii. With FMRIB's Diffusion Toolbox (FDT), the fractional anisotropy (FA) images were created by fitting a tensor model to the raw diffusion data and then, using the Brain Extraction Tool (BET) [218], brain-extracted. FA identifies the degree of anisotropy of a diffusion process and it is a measure often used in diffusion imaging where it is thought to reflect fiber density, axonal diameter, and myelination in white matter. A value of zero means that diffusion is isotropic, i.e. it is unrestricted (or equally restricted) in all directions, while a value of one means that diffusion occurs only along one axis and is fully restricted along all other directions. Subsequently the FA images were transformed into a common space by nonlinear registration IRTK[219]. A mean FA skeleton, representing the centers of all tracts common to the group, was obtained from the thinned mean FA image. All FA data were projected onto this skeleton. The resulting data was fed into voxel-wise cross-subject statistics. Prior to analysis in SPM, the FA maps were converted from NIfTI format to Analyze.

The brains were segregated into 90 brain areas according to the Automated Anatomical Labeling Atlas 1 (AAL1) [212]. The anatomical names of the brain areas for each index k are shown in Table A1 of Appendix B. In each brain network, one AAL brain area corresponds to a node of the network. The weights between the nodes were estimated through the measurement of the preferred diffusion directions, given by a set of $n_s = 5000$ streamlines for each voxel. The streamlines are hypothesized to correlate with the white-matter tracts. The ratio of streamlines connecting area l and area k is given by the probability coefficient p_{lk}. Then, the adjacency matrix J_{kl} is constructed from this probability coefficient. The DTI processing pipeline has been adopted from Ref. [220].

Besides the healthy connectomes, we selected 15 connectomes (9 females, 6 males, mean age 33.4, range 22-56) of patients with different types of partial epilepsy that underwent a presurgical evaluation. The scans were performed at the Centre de Résonance Magnétique et Biologique et Médicale (Faculté de Médecine de la Timone) in Marseille. Throughout the manuscript we refer to the epileptic patients as E1-E15. dMRI images were acquired on a Siemens Magnetom Verio 3T MR-scanner using a DTI-MR sequence with an angular gradient set of 64 directions, $TR = 10700$ ms, $TE = 95$ ms, $2 \times 2 \times 2mm^3$ voxel size, 70 slices, b-value $1000s/mm^2$.

The data processing pipeline [221, 222] made use of various tools such as FreeSurfer [223], FSL [224], MRtrix3 [225] and Remesher [226], to reconstruct the individual cortical surface and large-scale connectivity. The surface was reconstructed using 20,000 vertices. Cortical and volumetric parcellations were performed using the Desikan-Killiany atlas with 70 cortical regions and 17 subcortical regions [213]. The final atlas consists of 88 regions since one more empty region is added in the construction of the structural connectivity for symmetry. After correction of the diffusion data for eddy-currents and head motions using eddy-correct FSL functions, the Fiber orientation was estimated using Constrained Spherical Deconvolution [227] and improved with Anatomically Constrained Tractography [228]. For tractography, 2.5×10^6 fibers were used and, for correction, Spherical-Deconvolution Informed Filtering of Tractograms [229] was applied. Summing track counts over each region of the parcellation yielded the adjacency matrix. Here, the AAL2 was employed for brain segregation leading to 88 brain areas for each patient, see Table A2 of Appendix B.

4.2.3 EEG and SEEG data

All 15 drug-resistant patients, mentioned in the previous Section, affected by different types of partial epilepsy accounting for different epileptogenic zone localizations, underwent a presurgical evaluation (see Tables A3 and A4 of Appendix B). For each patient a first non-invasive evaluation procedure is foreseen, that comprises of the patient clinical record, neurological examinations, PET and EEG along with video monitoring. Following this evaluation, potential EZs are identified by the clinicians. Further elaboration on the EZ is done in a second, invasive phase, which consists of positioning SEEG electrodes in or close to the suspected regions. These electrodes are equipped with 10 to 15 contacts that are 1.5 mm apart. Each contact has a length of 2 mm and measures 0.8 mm in diameter. Recordings were obtained using a 128 channel DeltamedTM system with a 256 Hz sampling rate and band-pass filtered between 0.16 Hz and 97 Hz by a hardware filter. Precise electrode positioning was performed by either a computerized tomography or MRI scan after implanting the electrodes. All patients showed seizures in the SEEG, starting in one or several localized areas (EZ), before recruiting distant regions, identified as the propagation zone. It is worth noticing that, among the operated patients, four of them showed a worthwhile improvement but without resulting completely seizure-free since surgery (Engel's score III), while two resulted almost seizure-free, showing rare disabling seizures since surgery (Engel's score II), thus suggesting that the EZ was correctly identified in a subset of patients only.

Two methods were used for the identification of the propagation zone (see Table A4 of Appendix B). First, the clinicians evaluated the PZs subjectively on the basis of the EEG and SEEG recordings gathered throughout the two-step procedure (non-invasive and invasive). Second, the PZs were identified automatically based on the SEEG recordings: For each patient, all seizures were isolated in the SEEG time series. The bipolar SEEG was considered (between pairs of electrode contacts) and filtered between 1-50 Hz using a Butterworth band-pass filter. An area was defined as a PZ if its electrodes detected at least 30% of the maximum signal energy over all contacts, and if it was not in the EZ. In the following, we call the PZs identified by the subjective evaluation of clinicians $\mathrm{PZ}_{\mathrm{Clin}}$ and the PZs identified through SEEG data $\mathrm{PZ}_{\mathrm{SEEG}}$.

4.2.4 Network Measures

Topological properties of a network can be examined by using different graph measures that are provided by the general framework of the graph theory. These graph metrics can be classified in terms of measures that cover three main aspects of the topology: segregation, integration and centrality. The segregation accounts for the specialized processes that occur inside a restricted group of brain regions, usually densely connected, and it eventually reveals the presence of a dense neighborhood around a node, which results to be fundamental for the generation of clusters and cliques capable to share specialized information. Among the possible measures of segregation, we have considered the *clustering coefficient*, which gives the fraction of triangles around a node and it is equivalent to the fraction of node's neighbors that are neighbors of each other as well. In particular the *average clustering coefficient* C of a network gives the fraction of closed triplets over the number of all open and closed triplets, where a triplet consists of three nodes with either two edges (open triplet) or three edges (closed triplet). The *weighted clustering coefficient* c_i^w [230] considers the weights of its neighbors:

$$c_i^w = \frac{1}{s_i(k_i - 1)} \sum_{j,h} \frac{w_{ij} + w_{ih}}{2} a_{ij} a_{ih} a_{jh}, \tag{4.4}$$

where s_i is the node strength (to be defined below), k_i the node degree, w_{ij} the weight of the link, and a_{ij} is 1 if the link $i \rightarrow j$ exists and 0 if node i and j are not connected. The *average weighted clustering coefficient* C_W is the mean of all weighted clustering coefficients: $C_W = \frac{1}{N} \sum_i c_i$.

The measures of integration refer to the capacity of the network to rapidly combine specialized information from not nearby, distributed regions. Integration measures are based on the concept of communication paths and path lengths, which estimate the unique sequence of nodes and links that are able to carry the transmission flow of information between pairs of brain regions. The *shortest path* d_{ij} between two nodes is the path with the least number of links. The *average shortest path length* of node i of a graph G is the mean of all shortest paths from node i to all other nodes of the network: $L(G, i) = \frac{1}{N-1} \sum_{j \in \mathbb{N}, j \neq i} d_{ij}$. The *average shortest path length* of all nodes is the mean of all shortest paths [231]: $L(G) = \frac{1}{N-1} \sum_{i,j \in \mathbb{N}, i \neq j} d_{ij}$. In a weighted network, distance and weight have a reciprocal relation. If a weight between two adjacent nodes is doubled, their shortest path is cut by half: $L(G) = \frac{1}{N-1} \sum_{i,j \in \mathbb{N}, i \neq j} \frac{d_{ij}}{w_{ij}}$.

Centrality refers to the importance of network nodes and edges for the network functioning. The most intuitive index of centrality is the node degree, which gives the number of links connected to the node; for this measure, connection weights are ignored in calculations. In this manuscript, we employ the network measure *node strength* s_i, which corresponds to the weighted node degree of node i and equals the sum of all its weights: $s_i = \sum_{j \in \mathbb{N}} w_{ij}$. Accordingly, the *average node strength* S corresponds to the mean of all node strengths $S = \frac{1}{N} \sum_i s_i$. All finite networks have a finite number of shortest paths $d(i, j)$ between any pair of nodes i, j. The *betweenness centrality* $c_B(s)$ of node s is equal to all pairs of shortest paths that pass through s divided by the number of all shortest paths in the network: $c_B(s) = \sum_{i,j \in \mathbb{N}} \frac{d(i,j|s)}{d(i,j)}$. For the *weighted betweenness centrality*, the *weighted shorted paths* are used.

4.3 Results

The epileptic attractor is commonly described in terms of a self-sustained limit cycle that comes from the destabilization of the physiological activity while multiple types of transitions allow for the accessibility of seizure activity, status epilepticus and depolarization block, that coexist, as verified experimentally in [232]. The single-population firing rate equations Eqs. (2.36) show, in the absence of forcing, only fixed points as attractors. As it will become clear in the following Section, a stable node and a stable focus are observable, separated by a bistability region between a high- and a low-activity state, whose boundaries are the locus of a saddle-node bifurcation (for more details see [16]). In this context are not observable self-sustained oscillations, but only damped oscillations at the macroscopic level that reflect the oscillatory decay to the stable fixed point. This oscillatory decay will be considered here as representative of a seizure-like event, not being able to observe a stable limit cycle to describe the emergence of a fully developed seizure, as shown in other phenomenological mathematical models [186, 233], commonly used to describe a detailed taxonomy of seizures. In particular, seizure-like events will be used here as paradigm to investigate propagation of seizure-like activity in the network. A detailed comparison with the taxonomy of seizures described by other phenomenological models [186, 233, 234] and the possible extension of the single-population firing rate equations Eqs. (2.36) to show self-emergent periodic and bursting dynamics at the macroscopic level is reported in Section 1 of Appendix B.

4.3.1 Healthy Subjects

Phase and Bifurcation Diagrams

The analysis of the single-population firing rate equations Eqs. (2.36), performed in [16], has revealed that there are three distinct regions, when considering the phase diagram of the system as a function of the external drive $\bar{\eta}$ and synaptic weight J, in absence of time dependent forcing ($I(t) = 0$): (1) a single stable node equilibrium corresponding to a low-activity state, (2) a single stable focus (spiral) generally corresponding to a high-activity state, and (3) a region of bistability between low and high firing rate. In particular, in the region where the stable focus is observable, the system undergoes damped oscillatory motion towards this fixed point. The presence of damped oscillations at the macroscopic level reflects the transitory synchronous firing of a fraction of the neurons in the ensemble. While this behavior is common in network models of spiking neurons, it is not captured by traditional firing-rate models [46, 98, 235].

When considering the multi-population neural mass model (2.46) with homogeneously set $\bar{\eta}^{(k)} = \bar{\eta}$, the corresponding phase diagram Fig. 4.1(b) is qualitatively the same as the one shown in Fig 1 of [16], since the same attractors are observable. In the original model these attractors are single-population states, while they reflect multi-population states in the present case. Single-population low-activity (LA) and high-activity (HA) states translate into network LA and HA states. In the former all populations have low, in the latter high firing rates. We observe that the single-population bistability accurately reflects the hysteretic transition in the network when changing $\bar{\eta}$. In the following we will address how this relation between single-node and multi-population phase diagram occurs.

The network bifurcation diagrams shown in Fig. 4.1(a) for increasing σ values are obtained by performing an adiabatic analysis along two different protocols: up-sweep and down-sweep. Following the up-sweep protocol, the system's state variables r_k, v_k are initialized at $\bar{\eta} = -50$ with the values $r_k = 0$, $v_k = 0$; then the excitability is increased in steps $\Delta\bar{\eta} = 1.5$ until the maximal value $\bar{\eta} = 10$ is reached. At each step, the initial conditions for mean firing rates and mean membrane potentials correspond to the final state obtained for the previous $\bar{\eta}$ value. Note, that the average firing rate increases for increasing $\bar{\eta}$ values, both for the single node and for the network. Once the maximum $\bar{\eta}$ value is reached, the reverse procedure is performed, thus following the down-sweep protocol. This time the initial conditions correspond to the high-activity state at $\bar{\eta} = 10$, while the excitability is adiabatically decreased in steps $\Delta\bar{\eta} = 1.5$, until a low-activity state at $\bar{\eta} = -50$ is approached. For both protocols, the investigation of the nature of the dynamics emerging at each $\bar{\eta}$-step is done by using the same procedure: the system is simulated for a transient time $T = 2$ s, until it has reached an equilibrium state. At this time the firing rate averaged over all populations $\langle r^* \rangle$ is calculated and the next $\bar{\eta}$ iteration is started, using this final state as initial conditions.

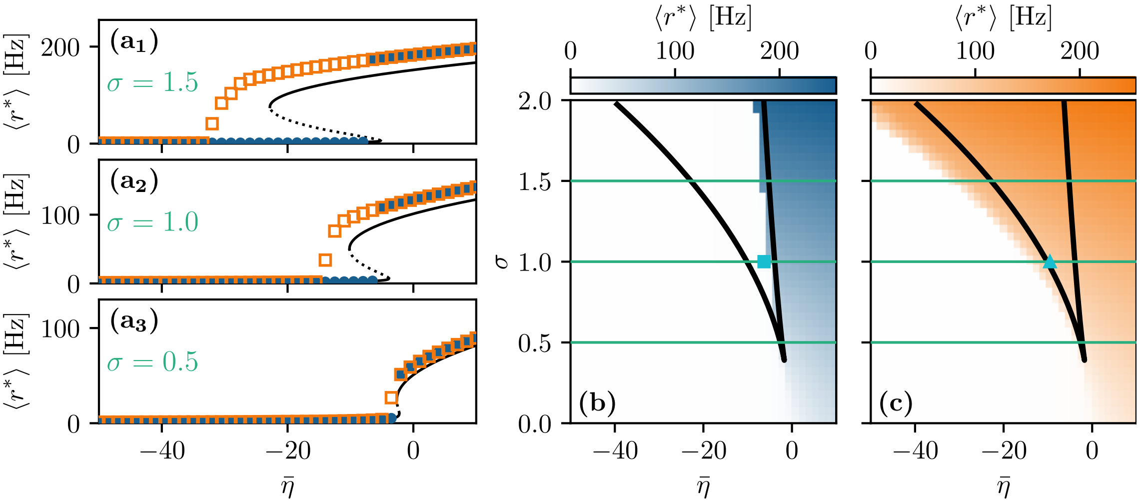

Figure 4.1: Phase and bifurcation diagrams for healthy subject H1. **(a)** Equilibrium firing rates $\langle r^* \rangle$ versus $\bar{\eta}$ for the up-sweep (blue dots) and down-sweep (orange squares). For each $\bar{\eta} \in [-50, 10]$ in steps of $\Delta\bar{\eta} = 1.5$ the system is initialized using the final state of the previous run and evolves for 2 s after which the average network firing rate in the equilibrium state is determined. Different panels correspond to different σ values: $\sigma = 1.5$ (a$_1$), $\sigma = 1$ (a$_2$), $\sigma = 0.5$ (a$_3$). The solid (dashed) black line corresponds to the stable (unstable) equilibria in the single-node case. **(b, c)** Maps of regimes as a function of σ and $\bar{\eta}$ showing the network average $\langle r^* \rangle$ color coded for **(b)** up-sweep and **(c)** down-sweep , obtained by following the same procedure as in (a) for $\sigma \in [0, 2]$ in steps of $\Delta\sigma = 0.05$. The black line indicates the single-node map of regimes like in [16]. In panels (b, c) the cyan square and triangle mark $\bar{\eta} = -6.3, -9.54$ respectively. Other parameter values are: $N_{\text{pop}} = 90$, $\tau_{\text{m}} = 20$ ms, $\Delta = 1$, $J_{kk} = 20$, $J_{kl} = 5\tilde{J}_{kl} \quad \forall k \neq l$.

The transition from LA to HA network dynamics is hysteretic: the system does not follow the same path during the up-sweep and the down-sweep protocol. When the system is initialized in the low activity regime, it remains there until a critical excitability value $\bar{\eta}_{\text{HA}}$ is reached. For further increase of the excitability, the average firing rate exhibits a rapid jump to higher values. However, when the system is initialized in the high-activity regime, this regime survives for a large $\bar{\eta}$ interval until it collapses toward a low-activity state at $\bar{\eta} < \bar{\eta}_{\text{LA}}$, where $\bar{\eta}_{\text{LA}} < \bar{\eta}_{\text{HA}}$. There is a considerable difference between the critical excitability values required to lead the system to a high-activity or a low-activity regime and the difference increases for increasing coupling strength σ. While the up-sweep protocol (blue dots) is well approximated by the bifurcation diagram of the single population, represented in Fig. 4.1(a) by the black (dashed and continuous) curve, this is no more true for the down-sweep protocol, where the coupling plays a role in determining the transition at the multi-population level (orange squares). This results in different phase diagrams for the two protocols: the maps of regimes is dominated by the low-activity (high-activity) state when following the up-sweep (down-sweep) protocol. Merging together these results we observe that the region of bistability between LA and HA network dynamics, is still identifiable by the original boundaries found for the single population in [16] (see black curve in Fig. 4.1(b, c), even though, for the multi-population system, the region is wider).

We can make further use of the single-population bifurcation diagram to understand the hysteretic transition of the multi-population model in more detail. First of all, the weight matrix $\{J_{kl}\}$ has its largest components on the diagonal ($J_{kk} = 20$), reflecting recurrent synapses. This means that synaptic inter-coupling plays a minor role, as long as the firing rates of the adjacent populations are small. During the up-sweep protocol, this condition is fulfilled, as all populations are initialized in a low activity regime. Under these conditions, the dynamics of all nodes is rendered identical and equal, approximately, to the single population dynamics. Consequently the single-population LA branch describes the multi-population LA behavior (in terms of $\langle r^* \rangle$) accurately as a function of $\bar{\eta}$. Secondly, as soon as the single-population LA state vanishes for large enough $\bar{\eta} > \bar{\eta}_{\mathrm{HA}}$, the individual nodes of the multi-population system all transit to the HA state.

In this HA regime, deviations of the network bifurcation diagram with respect to the single-population curve are observed. The populations in the system have large firing rates, such that the inter-coupling becomes a relevant contribution to the total current on each node. This explains why the LA branch of the network is located at higher firing rates with respect to the black single-population curve: The populations in the network behave, approximately, as decoupled, irrespectively of being subject, in the HA regime, to an additional current due to the inter-coupling. This effectively shifts the single-population bifurcation diagram towards smaller $\bar{\eta}$. Moreover this shift occurs for each population individually, depending on the matrix $\{J_{kl}\}$. During the down-sweep protocol, due to the population dependent shift, the HA population states vanish at different values of $\bar{\eta}$. Accordingly, whenever this occurs, the network average $\langle r^* \rangle$ decreases by a small amount, such that the network LA state is reached via various intermediate states. We can infer, using the same type of argument, that single-population LA states disappear for increasing $\bar{\eta}$ in a region around $\bar{\eta}_{\mathrm{HA}}$. They are not observed here, due to the nature of the up-sweep protocol and the initialization procedure of r_k, v_k.

From the reversed viewpoint we can hypothesize, that stable single-population HA states may take form near $\bar{\eta}_{\mathrm{LA}}$ for increasing $\bar{\eta}$, as well as stable LA states for decreasing $\bar{\eta}$ near $\bar{\eta}_{\mathrm{HA}}$. This implies that the network possesses complex multistability between many network states in the region $\bar{\eta}_{\mathrm{LA}} < \bar{\eta} < \bar{\eta}_{\mathrm{HA}}$. For these states the existence of LA and HA states of individual populations are interdependent: whether or not any given population can be in the LA or HA state is conditioned by the LA-HA configuration of all other populations. This not only demonstrates how multistability emerges in the multi-population system, but it also has influence on the response of the network towards transient input in such a setting. Most importantly, if such an input recruits one population into high activity, other populations might follow, leading to a cascade of recruitments.

Seizure-like Recruitment in Dependence of Perturbation Site and $\bar{\eta}$

To analyze the response of the multi-population system to transient current, we stimulate one population with a step function $I_{\mathrm{S}}(t)$ of amplitude $\Delta I = 10$ and duration $\Delta T = 0.4$ s. By setting $\bar{\eta} = -9.54$, the system is placed in the multistable regime [see cyan triangle in Fig. 4.1(c)], but, due to the low $\bar{\eta}$ value, it only allows for LA-HA configurations with most of the populations in LA. The stimulation with an external current $I_{\mathrm{S}}(t)$ allows the system to reach a configuration with more populations in the HA. This corresponds to equivalently choose, in the model, a higher excitability value for the single node such that it crosses the bistability region, thus reaching the HA regime. We start by initializing all nodes in the low-activity state and stimulating a single node [Fig. 4.2, column 1]. During the stimulation [Fig. 4.2(a_1)], the stable states of the network change, due to the strong additional current [Fig. 4.2(b_1)]. More specifically, the initial equilibrium vanishes and a new focus equilibrium of the system appears as the only stable network state. This focus is characterized by an LA-HA configuration for which only the stimulated node finds itself in HA while the rest remains in the LA regime; the focus is approached via damped oscillations in the time interval $0 < t < 0.4$ s [Fig. 4.2($\mathrm{c}_1, \mathrm{d}_1$)]. Due to the multistability in absence of stimulation, an identical LA-HA configuration exists. Thus, when the current is removed, the system is able to maintain the LA-HA configuration. However, the position of the focus equilibrium is shifted in absence of the transient input and is reached, again, via damped oscillations for $t > 0.4$ s.

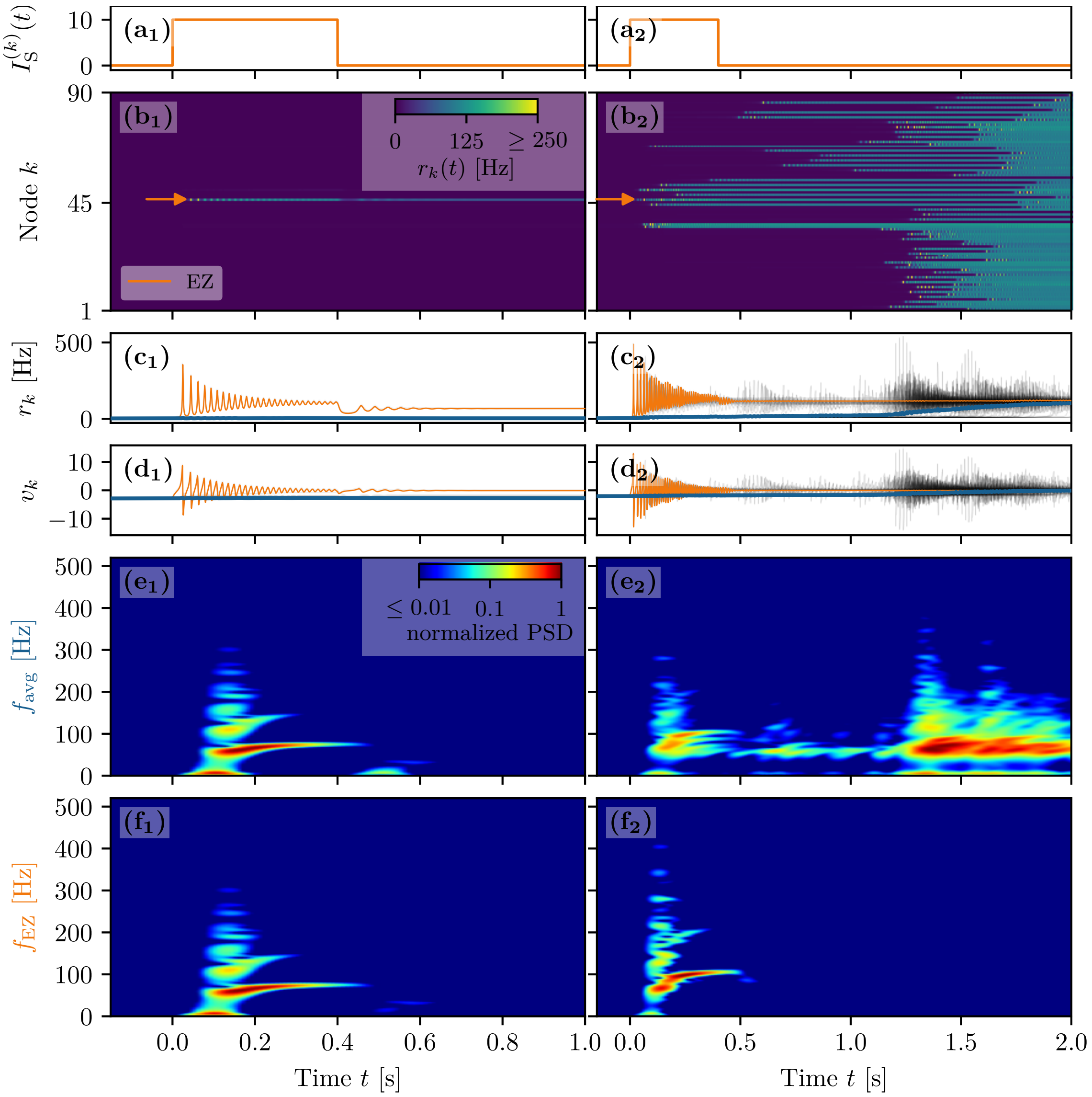

Figure 4.2: Spectrograms of mean membrane potentials for healthy subject H1. (a) Stimulation currents $I_S^{(k)}$. **(b)** Space-time plots of the population firing rates r_k, color-coding the value of the firing rate of each node, as a function of time. **(c)** Population firing rates r_k and **(d)** mean membrane potentials v_k for the EZ (orange) and other populations (black). The blue curves show the network average firing rate and membrane potential. Non-stimulated node dynamics is plotted as transparent gray curves: some of the nodes adapt their voltage to the stimulation of the EZ and change during stimulation. **(e)** Spectrogram of the network average membrane potential and **(f)** of the v_k of the EZ. Column **(1)** shows an asymptomatic seizure-like event for $\bar{\eta}^{(k)} = \bar{\eta} = -9.54$, column **(2)** a generalized seizure-like event for $\bar{\eta}^{(k)} = \bar{\eta} = -6.3$. In both cases the EZ node 46 is stimulated. For the estimation of the spectrograms see Section 1 of Appendix C. Other parameter values are: $N_{\mathrm{pop}} = 90$, $\tau_{\mathrm{m}} = 20$ ms, $\Delta = 1$, $J_{kk} = 20$, $\sigma = 1$, $J_{kl} = 5\tilde{J}_{kl} \quad \forall k \neq l$.

When the perturbation of a single node has no consequences on the dynamics of the other populations, as shown in Fig. 4.2(b₁ - d₁), we are in the presence of an *asymptomatic seizure-like event*, where the activity is limited to the epileptogenic zone (here represented by the stimulated node) and no propagation takes place. For higher excitability values ($\bar{\eta} = -6.3$, marked by a cyan rectangle in Fig. 4.1(b), the perturbation of a single node gives rise to a different response dynamics. In this case other brain areas are "recruited" and not only the perturbed node, but also other populations reach the high-activity regime by showing damped oscillations [Fig. 4.2(b_2 - d_2)]. In terms of pathological activity, the seizure-like event originates in the EZ (as a results of the stimulation) and propagates to the PZ, identified by the other regions which rapidly propagate the oscillatory activity. The recruitment of the regions in the propagation zone can happen either by independent activation of the single areas, or by activating multiple areas at the same time, in a *domino-like* effect [236], until the propagation involves almost all populations (*generalized seizure-like event*).

The transition of a single population to the HA regime, upon stimulus onset, is characterized by a transient activity in the $\alpha - \beta$ band (10-14 Hz) and a sustained activity in the γ band (40-80 Hz), present throughout the stimulation, as shown in Fig. 4.2(e_1, f_1). Here the spectrograms show time varying power spectral densities (PSD) of the mean membrane potentials averaged over the network [Fig. 4.2(e_1)] and for the single stimulated population [Fig. 4.2(f_1)]. When more populations are recruited at higher excitability values, in addition to the former activity, it is possible to observe γ activity at higher frequencies [Fig. 4.2(e_2, f_2)]. High-frequency oscillations, between 80 and 500 Hz, can be recorded with EEG and reflect the seizure-generating capability of the underlying tissue, thus being used as markers of the epileptogenic zone [237]. Moreover, even for the generalized seizure-like case, the low-frequency band activity is evoked whenever a brain area gets recruited, leading to a sustained signal in the time interval 1.1 s $< t <$ 1.8s, where a majority of the populations approach the HA state. Similar results have been obtained for all the other investigated subjects (results not shown).

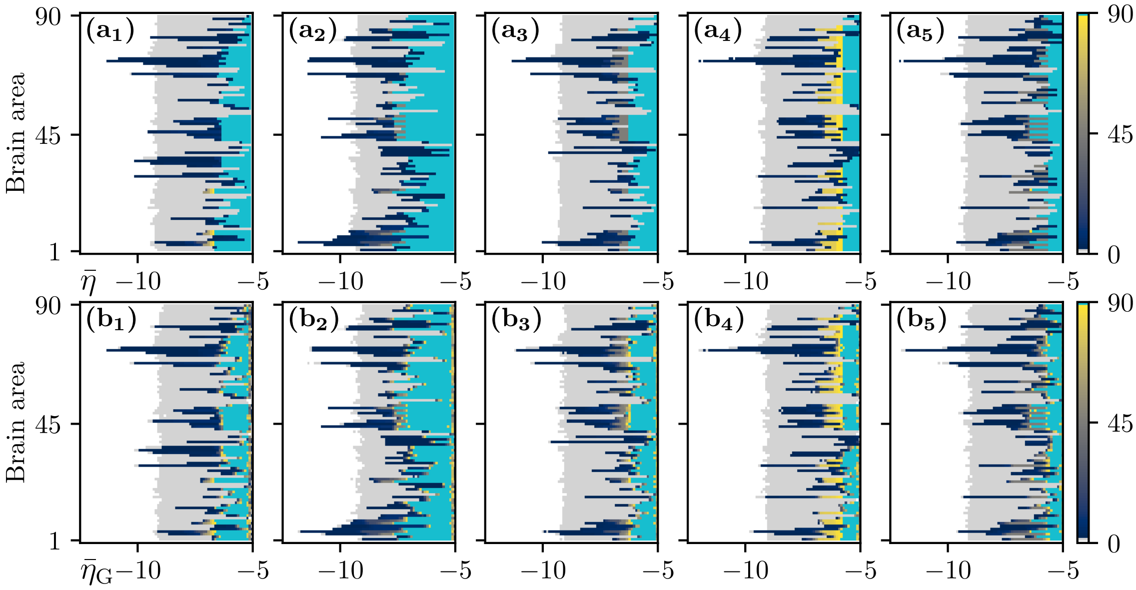

Figure 4.3: Number of recruited brain areas as a function of the excitability parameter $\bar{\eta}$. Columns **(1)** to **(5)** correspond to 5 exemplary healthy subject connectomes H1, H5, H12, H16, H19. The color code is as follow. White: no recruitment, gray: one area recruited (marks asymptomatic threshold), blue to yellow: intermediate number of recruitments, teal: 90 areas recruited (marks generalized threshold). For row **(1)** the $\bar{\eta}^{(k)}$ are uniformly distributed, given by $\bar{\eta}^{(k)} = \bar{\eta}$. For row **(2)** the $\bar{\eta}^{(k)}$ are Gaussian distributed, with mean $\bar{\eta}_G$ and standard deviation 0.1. In this case the results are averaged over 10 Gaussian realizations. Other parameters values are: $N_{\text{pop}} = 90$, $\Delta = 1$, $\sigma = 1$, $\Delta I = 10$, $\Delta T = 0.4$ s.

In the following we report a wide analysis of the impact of the perturbation site on the recruitment effect, for different excitability values. As before, we use a step current $I_S(t)$, with fixed amplitude $\Delta I = 10$ and duration $\Delta T = 0.4$ s, to excite a single population. In each run the stimulating current targets a different brain area and the number of recruitments, i.e. the number of populations, that pass from the LA state to the HA state, is counted. The $N_{\mathrm{pop}} = 90$ brain areas are targeted, one at a time, in 90 individual simulations. We repeat the procedure varying $\bar{\eta}$ in a range $[-15, -4]$, with steps of $\Delta\bar{\eta} = 0.1$. The results for five exemplary subjects are shown in Fig. 4.3(a).

If the perturbed area jumps back to the LA state when the stimulation is removed and no further recruitment takes place, then the total number of recruited areas is zero, here color coded in white. If the perturbed area remains in the HA state without recruiting other areas, we are in presence of an asymptomatic seizure-like event (blue regions). For every further recruited brain area, the color code changes from cyan to purple. If all brain areas are recruited, we observe a generalized seizure-like event (coded as red). For $\bar{\eta} < -9$, most of the targeted brain areas goes back to the LA state, when the perturbation ends, while for $\bar{\eta} \approx -9$, we generally observe asymptomatic seizure-like events for all the subjects and for most of the perturbation sites. For increasing $\bar{\eta}$ values, the probability for larger recruitment cascades increases, until the system exhibits generalized seizure-like events for $\bar{\eta} > -6$. However, some notable differences between brain areas and among the different subjects are observable. Brain area 72, for example, corresponding to the rh-CAU, exhibits asymptomatic seizure-like events at $\bar{\eta} > -11$ for most of the subjects, thus suggesting that the rh-CAU favors pathological behavior with respect to other brain areas. On the other hand, some brain areas are less likely to cause generalized seizure-like events, when stimulated, than others: Brain area 40, for example, the rh-PHIP[1], causes no generalized seizure-like events for any $\bar{\eta} > -5$. Note that, for very large $\bar{\eta}$ values, the system does not exhibit multistability anymore, but instead has only one stable state, namely the network HA state, corresponding to high firing rate of all populations. Approximately, this happens for $\bar{\eta} \in [-5.7, -4.9]$, with small variations among the subjects.

The scenario remains unchanged when we take into account heterogeneous excitabilities $\bar{\eta}^{(k)}$, as shown in Fig. 4.3(b). In this case $\bar{\eta}^{(k)}$ is drawn from a Gaussian distribution with mean $\bar{\eta}_{\mathrm{G}}$, thus mimicking the variability among different brain areas present in a real brain. The populations are stimulated, as before, one at a time in individual simulation runs. However, this time the procedure is repeated for varying $\bar{\eta}_{\mathrm{G}} \in [-15, -4]$, while keeping the standard deviation of the Gaussian distribution fixed at 0.1. Larger standard deviations (≥ 1) hinder the rich multistability of the network, by eliminating the bistability between LA and HA for individual populations, due to excessively small or large $\bar{\eta}^{(k)}$, thus impeding the analysis of the impact of the stimulation, as shown in Fig. A3 of Appendix B. In particular, for larger standard deviations, an increasing amount of nodes reaches the stable focus regime, thus being able to recruit other brain areas before the stimulation is applied, while nodes whose effective excitability turns out to be very small, are too far from the bistability region to be able to reach the HA regime. The results shown in Fig. 4.3 are obtained averaging over 10 Gaussian distribution realizations of the $\bar{\eta}$ parameter; slightly more variability becomes apparent especially when considering the threshold in $\bar{\eta}$ to observe generalized seizures. Indeed, the excitability threshold to observe generalized seizures is the most drastically affected as the standard deviation increases, see Fig. A3.

An overview over all the investigated subjects is possible when looking at Fig. 4.4(a), where the average over all subjects is reported. The averaging operation smears out the transition contours and, while the region of generalized seizure-like events shrinks, the region of accessibility of partial seizure-like events becomes wider, where a small percentage

---

[1] While the actual role of the specific regions might in reality be affected by other factors, not captured by the used structural connectivity estimate and the details of the current model, this highlights the effect of network structure on propensity to seizure-like events. The (para)hippocampal region is, in fact, one of the most commonly affected by epilepsy.

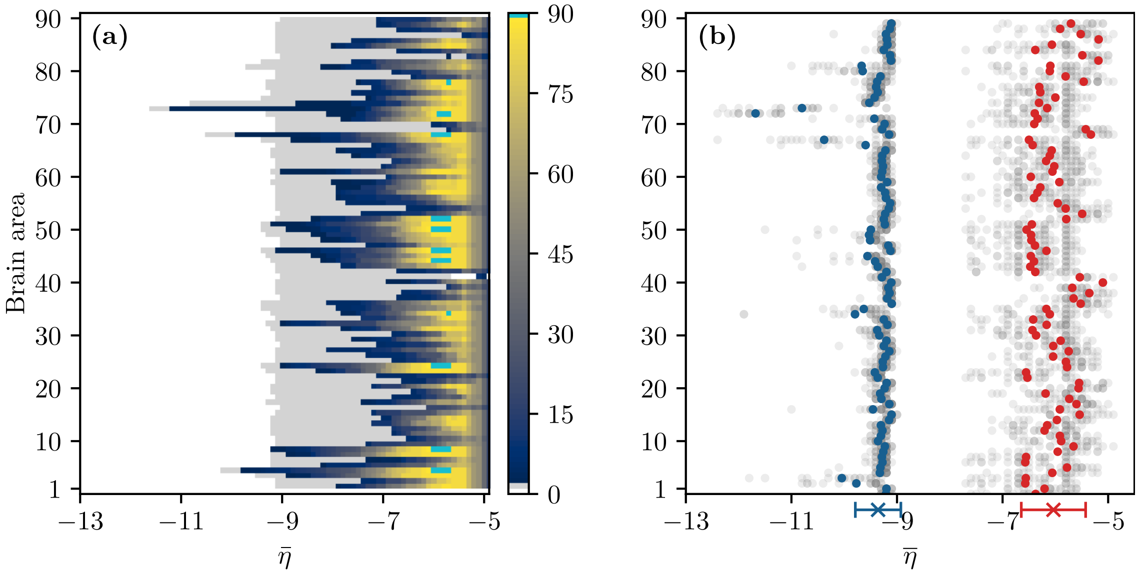

Figure 4.4: Thresholds of healthy subjects. **(a)** Number of recruited brain areas as a function of the excitability parameter $\bar{\eta}$, similar to what is shown in Fig. 4.3 row (1), but averaged across all 20 healthy subjects. The color code is as follow. White: no recruitment, gray: one area recruited (marks asymptomatic threshold), blue to yellow: intermediate number of recruitments, teal: 90 areas recruited (marks generalized threshold). **(b)** $\bar{\eta}$ threshold values for asymptomatic and generalized seizure-like events. Grey dots show the thresholds for each brain area and each subject. Blue and red dots show the average over $\bar{\eta}^{(k)}_{\text{asy}}$ and $\bar{\eta}^{(k)}_{\text{gen}}$ across all subjects. The blue and red cross at the bottom show the average value and its standard deviation for both thresholds across all subjects and across all areas. Parameters values are as in Fig. 4.3.

of nodes ($\sim 20\%$) are recruited. In Fig. 4.4(b) we report $\bar{\eta}^{(k)}_{\text{asy}}$ ($\bar{\eta}^{(k)}_{\text{gen}}$), i.e. the smallest $\bar{\eta}$ value for which an asymptomatic (generalized) seizure-like event occurs when stimulating population k. Grey dots indicate the individual thresholds $\bar{\eta}^{(k)}_{\text{asy}}$ and $\bar{\eta}^{(k)}_{\text{gen}}$ for each of the 20 subjects and 90 brain areas; the averages over all subjects are denoted by blue and red circles, respectively, for each $k \in [1, 90]$. Averaging these thresholds over all subjects and brain areas yields an asymptomatic threshold of $\bar{\eta}_{\text{asy}} = -9.36 \pm 0.43$ and a generalized threshold of $\bar{\eta}_{\text{gen}} = -6.04 \pm 0.38$. Brain areas 72, 73, 67, and 3 have lower thresholds for asymptomatic seizure-like events, areas 40, 86, and 82 have larger thresholds for generalized seizure-like events and do not fall within a standard deviation. The variability in the response among the different areas is more evident for $\bar{\eta}^{(k)}_{\text{gen}}$ values compared to the $\bar{\eta}^{(k)}_{\text{asy}}$ ones: the threshold values to obtain an asymptomatic seizure-like event are very similar among the areas and among the subjects, while the threshold values to obtain a generalized seizure-like event strongly depend on the stimulated area and on the subject.

The Role Played by Brain Area Network Measures on Enhancing Recruitment

As shown in Fig. 4.4(b), $\bar{\eta}^{(k)}_{\text{asy}}$ does not vary significantly among the subjects and among the brain areas; it mainly occurs in the range $\bar{\eta}^{(k)}_{\text{asy}} \in [-10, -9]$, with just few nodes ($k \in [72, 73, 67, 3]$) showing smaller values. Since each brain area is characterized by its own network measure, the first hypothesis that we aim to test, is the role played, on the identification of the threshold, by the different network measures. We will verify in the following that connection strength and shortest path length are determinant to identify the threshold $\bar{\eta}^{(k)}_{\text{gen}}$: generalized seizure-like events are enhanced by nodes forming a clique that rapidly communicate through a dense subgraph. In particular, we investigate the

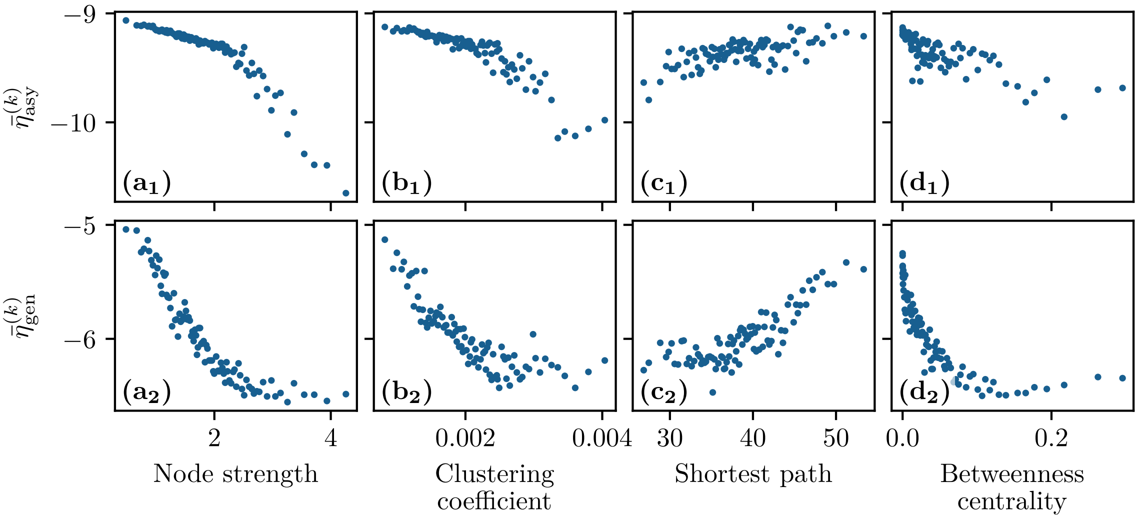

Figure 4.5: Thresholds versus network measures. Row **(1)** $\bar{\eta}_{\mathrm{asy}}^{(k)}$ for asymptomatic seizure-like events and row **(2)** $\bar{\eta}_{\mathrm{gen}}^{(k)}$ for generalized seizure-like events as a function of node measures: **(a)** node strength, **(b)** clustering coefficient, **(c)** average shortest path length, **(d)** betweenness centrality. For each panel, the thresholds $\bar{\eta}_{\mathrm{asy}}^{(k)}, \bar{\eta}_{\mathrm{gen}}^{(k)}$ are calculated for all $k \in [1, 90]$ brain areas and averaged over all 20 subjects. Parameters values are as in Fig. 4.3.

dependency of $\bar{\eta}_{\mathrm{asy}}^{(k)}$ on the node strength, clustering coefficient, shortest path length, and betweenness centrality of the corresponding brain area, as shown in Fig. 4.5(a). A very strong correlation between asymptomatic threshold and node strength becomes apparent: brain areas that are strongly connected, need a smaller excitability to pass from the LA to the HA regime [Fig. 4.5(a_1)]. The same holds true for the clustering coefficient, even though the relationship is less sharp [Fig. 4.5(b_1)]. Moreover it is possible to observe a direct correlation between $\bar{\eta}_{\mathrm{asy}}^{(k)}$ and shortest path length (i.e. shortest is the path smallest is the threshold value), while betweenness is smaller for higher threshold values [see Fig. 4.5(c_1) and Fig. 4.5(d_1), respectively].

When considering the threshold for generalized seizure-like events, we face a higher variability among different nodes (as shown in Fig. 4.4(b), $\bar{\eta}_{\mathrm{gen}}^{(k)}$ varies mainly between -6.5 and -5.5). The dependency of $\bar{\eta}_{\mathrm{gen}}^{(k)}$ on the node strength reveals a strong correlation: Areas with very small node strengths are characterized by large thresholds and are less likely to cause generalized seizure-like events. On the other hand, for large node strengths, $\bar{\eta}_{\mathrm{gen}}^{(k)}$ saturates at a value ≈ -6.5 [Fig. 4.5(a_2)]. The clustering coefficient, shown in Fig. 4.5(b_2), shows a similar relationship as the node strength, even though more scattered. This is not surprising since node strength and clustering coefficient are strongly correlated with each other (the Pearson Correlation coefficient in this case is $r = 0.75$, as shown in Fig. A4 of Appendix B), thus explaining the similarity between the analyses reported in Fig. 4.5 columns (1 - 2). Moreover, regarding the integration measure, it turns out that the average shortest path length correlates positively with $\bar{\eta}_{\mathrm{gen}}^{(k)}$ [Fig. 4.5(c_2)]. Brain areas that are characterized, on average, by a short path to all the other areas are more likely to cause generalized seizure-like events. Finally, the betweenness centrality correlates negatively with $\bar{\eta}_{\mathrm{gen}}^{(k)}$ [Fig. 4.5(d_2)]. This means that brain areas that are crossed by many shortest path lengths (large betweenness centrality) are more likely to cause generalized seizure-like events. For increasing node strength, clustering coefficient and betweenness centrality, we observe a saturation toward $\bar{\eta}_{\mathrm{gen}}^{(k)} \approx -6.5$, that corresponds to the critical excitability value, during the up-sweep simulation, at which the system jumps to the HA network state [Fig. 4.1(a_2)].

To explore the causal mechanisms of brain dynamics and understand the sequential mechanism of node recruitment in more detail, we investigate the timing at which different brain areas are recruited. For this, the excitability parameter $\bar{\eta}$, common to all populations, is set to the threshold value $\bar{\eta}_{\text{gen}}^{(k)}$ of the perturbed brain area k, ensuring complete recruitment of all populations, when perturbing populations $k \in [1, 90]$. The results shown

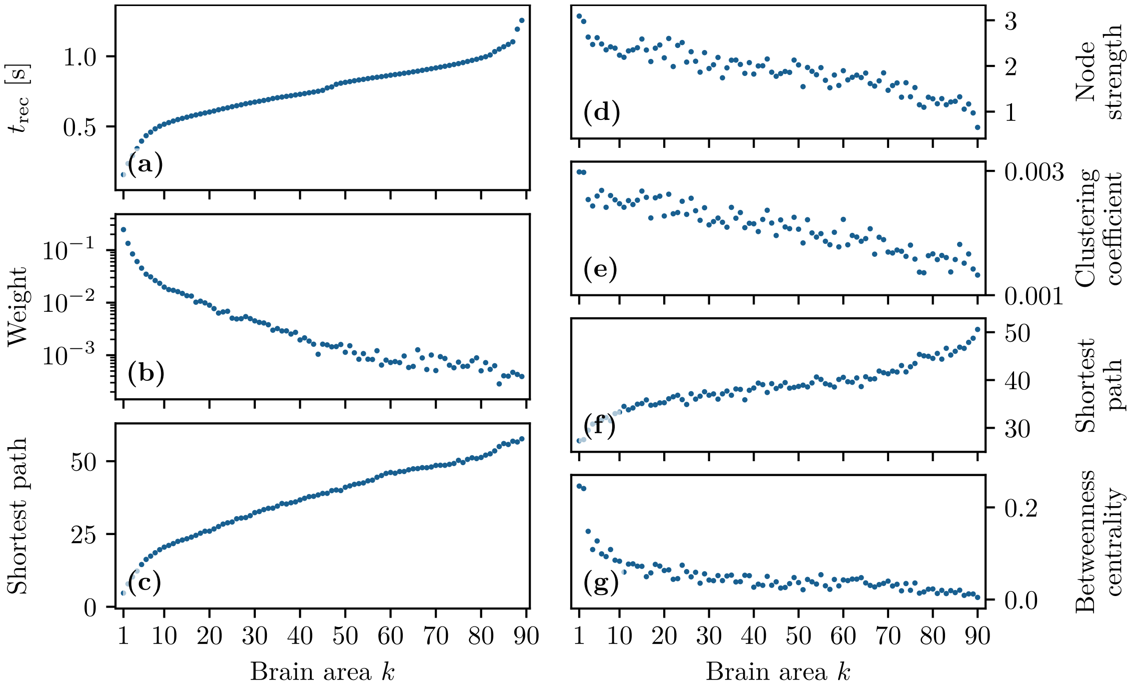

Figure 4.6: Recruitment order versus network measures. **(a)** Recruitment times reported in ascending order. **(b)** Connection weights between the recruited brain area and the EZ. **(c)** Shortest path between the recruited area and the EZ. **(d)** Connection weights between the recruited brain area and all the nodes except EZ. **(e)** Clustering coefficient between the recruited brain area and all the nodes except EZ. **(f)** Shortest path between the recruited area and all the other nodes except EZ. **(g)** Betweenness centrality between the recruited brain area and all the nodes except EZ. In all panels the brain areas are ordered according to their recruitment time, thus following the indexing of panel (a). The excitability $\bar{\eta}^{(k)}$ is set to the subject-specific threshold $\bar{\eta}_{\text{gen}}^{(k)}$, according to Fig. 4.3 for each subject separately. Data are averaged over all subjects and all the stimulated areas. Parameters: $N_{\text{pop}} = 90$, $\Delta = 1$, $\sigma = 1$, $\Delta I = 10$, $\Delta T = 0.4$ s as in Fig. 4.3.

in Fig. 4.6 are obtained by averaging over k and over the different subjects: in 90 individual simulations for each subject, a single brain area $k = 1, \ldots, 90$ is stimulated with an external step current $I_S(t)$, characterized by an amplitude $\Delta I = 10$ and a duration $\Delta T = 0.4$ s. For each k the recruitment time of all the other areas is registered. The stimulated brain area stands in for the EZ. The brain areas and corresponding node measures are sorted by the recruitment time in ascending order. The values for recruitment time [Fig. 4.6(a)], weight of a connection between a single area and the EZ [Fig. 4.6(b)] and shortest path [Fig. 4.6(c)] are finally obtained averaging over all the stimulated nodes and all the subjects (i.e. the average is performed over 1800 simulations across all 90 brain area perturbations times all 20 subjects). The same averaging procedure has been employed to obtain the data shown in Fig. 4.6(g - d). However, in this case, the node measures are evaluated over all the connections of the recruited node minus the connection to the EZ. While ignoring the link to the excited area (EZ), the overall network measure for connection weights [Fig. 4.6(d)], clustering coefficient [Fig. 4.6(e)], shortest path [Fig. 4.6(f)] and betweenness centrality [Fig. 4.6(g)] are reported.

On average, the first recruited brain area (labeled as 1) is connected to the EZ with a weight equal to 0.25 (1/4 of the maximum possible weight) and it is characterized by an average shortest path length to the EZ of less than 4.7. Moreover the area is recruited within an average time of less than 156 ms (calculated after the onset of the external perturbation current). However the first recruited area has, not only the strongest weight and the shortest path to the EZ but it also has, in general, the largest node strength, largest clustering coefficient, shortest average path length and largest betweenness centrality. Clearly, the seizure-like event spreads rapidly along the brain areas with strongest connection weights outgoing from the EZ; to the stronger weights are associated the shortest paths from the EZ. Overall, a region well connected is a region well recruited; this is related to the log-normal distribution of the weights (see Fig. A5 of Appendix B): few connections per node have a strong weight, thus allowing for fast recruitment. Note that the results for one exemplary subject and just one perturbed brain area per time (i.e. not averaged over all the brain areas and over all subjects) are comparable, even though the corresponding relationships are characterized by more variability (data not shown).

If we vary the amplitude ΔI of the perturbation current, the recruitment time will vary accordingly, decreasing for increasing ΔI. In Fig. 4.7 we show an exemplary case, obtained from the stimulation of one brain area (45), for a specific subject (results are similar for other trials). Irrespectively of the recruitment order, the time needed by the first ten recruited brain areas to pass from the LA to the HA state decreases slightly for increasing amplitude. However, this decrease reaches a saturation at a current value $\Delta I \approx 40$ already. The order of recruitment varies little: we observe some exchanges between the 4-*th* and 5-*th* and between the 9-*th* and 10-*th* recruited areas. For example,

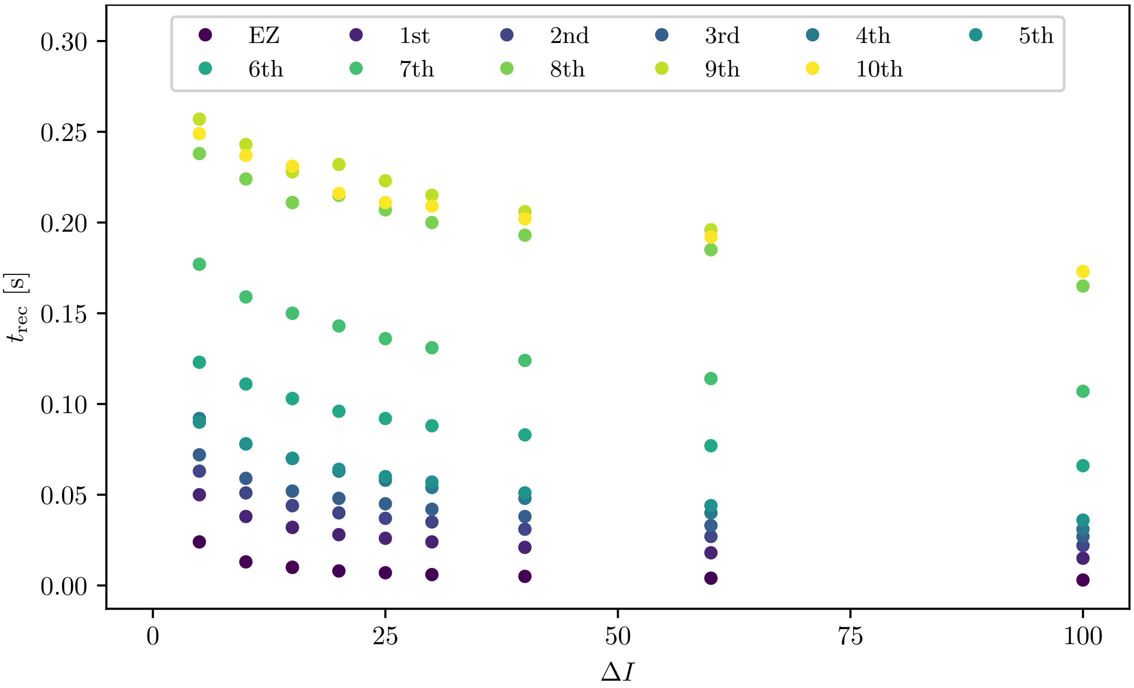

Figure 4.7: Dependence on input current (healthy subjects). Recruitment times of the first 10 recruited areas as a function of the input current ΔI. The order of the recruitment is color coded for each current strength and it changes slightly with different current strengths. Other parameters values are: $N_{\mathrm{pop}} = 90$, $\Delta = 1$, $\sigma = 1$, $\Delta T = 0.4$ s, $\bar{\eta}^{(k)} = \bar{\eta} = -6$, stimulation site: brain area $k = 45$ of subject H1.

for an amplitude $\Delta I = 15$, the 9-*th* recruited area (dark blue circles) gets recruited earlier than the 10-*th* area (pink dots) while, for very strong currents ($\Delta I = 100$), the 9-*th* area gets recruited latest. On the other hand we do not observe a significant change in the recruitment time and order if we increase the duration ΔT of the stimulation (see Fig. A6 of Appendix B).

4.3.2 Epileptic Patients

Phase and Bifurcation Diagrams

In this section the structural connectivity matrices of epileptic patients are employed and an analysis, analogous to the one in Section 4.3.1, is provided. We present the phase and bifurcation diagrams for the multi-population neural mass model, here employing the structural connectivity matrices of epileptic patients. As detailed before, the bifurcation diagrams for different σ values shown in Fig. 4.8(a) are obtained by performing an adiabatic scan along $\bar{\eta}^{(k)} = \bar{\eta}$, following the up- and down-sweep protocols.

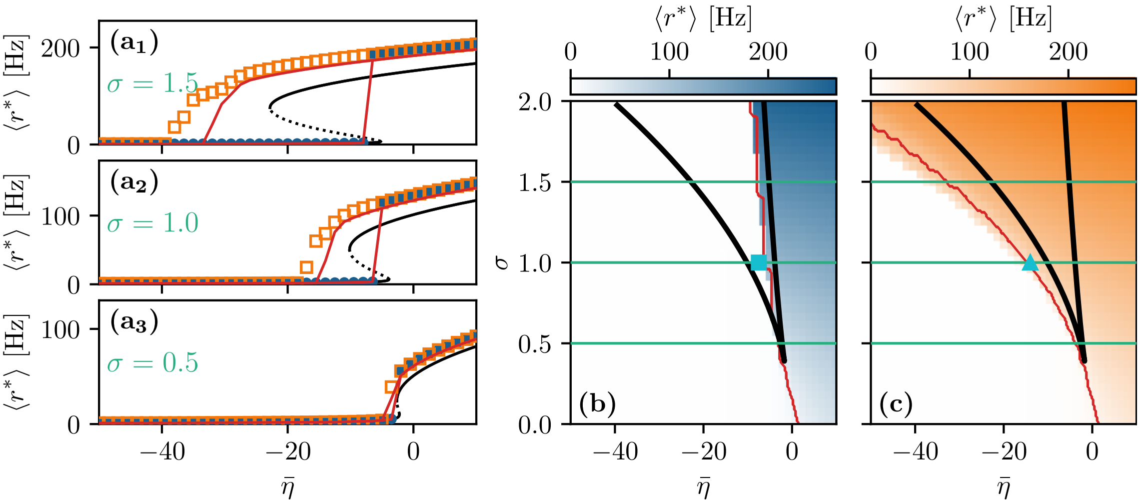

Figure 4.8: Phase and bifurcation diagrams for patient E6. (a) Equilibrium firing rates $\langle r^* \rangle$ versus $\bar{\eta}$ for the up-sweep (blue dots) and down-sweep (orange squares). For each $\bar{\eta} \in [-50, 10]$ in steps of $\Delta\bar{\eta} = 1.5$ the system is initialized using the final state of the previous run and evolves for 2 s after which the average network firing rate in the equilibrium state is determined. Different panels correspond to different σ values: $\sigma = 1.5$ (a$_1$), $\sigma = 1$ (a$_2$), $\sigma = 0.5$ (a$_3$). The solid (dashed) black line corresponds to the stable (unstable) equilibria in the single-node case. **(b, c)** Maps of regimes as a function of σ and $\bar{\eta}$ showing the network average $\langle r^* \rangle$ color coded for **(b)** up-sweep and **(c)** down-sweep , obtained by following the same procedure as in (a) for $\sigma \in [0, 2]$ in steps of $\Delta\sigma = 0.05$. The black line indicates the single-node map of regimes like in [16]. In (a) the dotted and in (b, c) the solid red line depicts the results for the healthy subject H1 reported in Fig. 4.1. In panels (b, c) the cyan square and triangle mark $\bar{\eta} = -7.5, -14$ respectively. Other parameter values are: $N_{\text{pop}} = 88$, $\tau_{\text{m}} = 20$ ms, $\Delta = 1$, $J_{kk} = 20$, $J_{kl} = 5\tilde{J}_{kl} \quad \forall k \neq l$.

As for the healthy subjects, the transition is hysteretic with $\bar{\eta}_{\text{LA}} < \bar{\eta}_{\text{HA}}$. However in this case, the width of the hysteretic transition is bigger, especially for larger σ values, as testified by the comparison with the dotted red curve, reported in Fig. 4.8(a), that represents the results shown in Fig. 4.1(a). This increased width can be translated in terms of the extension of the multistability region in the phase diagram [Fig. 4.8(b, c)], which turns out to be slightly larger than before. Also in this case the results for a healthy subject are reported for a better comparison [red curve in Fig. 4.8(b, c)]. The increase in size mainly occurs due to a shift of $\bar{\eta}_{\text{LA}}$, i.e. of the left boundary of the multistability regime. In this region, the transition from HA to LA, following the down-sweep, is more smooth and elongates towards smaller $\bar{\eta}$ values. This implies that, in this transition region, more single population HA states exist for epileptic patients than for healthy subjects. In other words, brain areas of epileptic subjects are more prone to recruitment[2].

While the phase diagram is obtained in the absence of time-varying input, we investigate the response of the multi-population system to transient stimulation in the following, based on the results reported in Fig. 4.9. As for the healthy subjects, a single population is excited by injecting a step current $I_S(t)$ of amplitude $\Delta I = 10$ and duration $\Delta T = 0.4$ s. Initially ($t < 0$), the system is in a multistable regime, starting in the low-activity network state. For small $\bar{\eta}$ values ($\bar{\eta} = -14$, identified by the triangle in Fig. 4.8(c), when a single node is stimulated, the system reacts analogously to the healthy subject case: during the stimulation only one stable network state exists, i.e. a focus equilibrium with a LA-HA configuration for which only the stimulated node is in HA [Fig. 4.9(b_1)]. This focus is approached via damped oscillations (0 s $< t <$ 0.4 s). When the stimulation is removed, the network maintains the LA-HA configuration, but approaches the new location of the focus again via damped oscillations [Fig. 4.9($\mathrm{c}_1, \mathrm{d}_1$)]. As a result, the stimulated node has large firing activity, while the remaining network is in a LA regime. For higher excitability values [$\bar{\eta} = -7.5$, square in Fig. 4.8(b)] the perturbation of a single node gives rise to a cascade of recruitments, where other brain areas, initially not perturbed, reach the HA regime by showing damped oscillations [Fig. 4.9(b_2 - d_3)]. With respect to the recruitment features shown in Fig. 4.2, we observe here a faster emergence of the generalized seizure-like event: once a brain area is stimulated, the others react, in substantial number, quite immediately.

Looking at the spectrograms, the transition of the stimulated population to the HA regime is characterized by a transient activity at low frequency ($<$ 20 Hz) and a sustained activity in the γ band (50-180 Hz), observable throughout the duration of the stimulus, as shown in Fig. 4.9(f_1), where the spectrogram for the single stimulated population is reported. Regarding the spectrogram of the mean membrane potentials averaged over the network population [Fig. 4.9(e_1)], it turns out that the low frequency activity in the δ, θ bands is present, while the activity at high frequency simply reflects the activity of the stimulated area. Activity in the δ band, together with multiple types of α-like rhythms have been recently found in a network of two Jansen-Rit neural mass models, representing two cortical regions, as a result of input changes in the other region [238], thus confirming that the range of possible activity varies with changes in the external inputs and interconnectivity gains.

In the case of large recruitment events, at larger excitability values, it is possible to observe γ activity at higher frequencies [Fig. 4.9($\mathrm{e}_2, \mathrm{f}_2$)], which is enhanced with respect to the situation where an asymptomatic seizure-like event is present. Moreover, comparing the spectrograms in Fig. 4.9 and those reported in Fig. 4.2, we see that the activity takes place at higher frequency ranges when considering structural connectivity matrices of epileptic patients and the activity is mainly concentrated in the EZ. A further comparison is possible, looking at Fig. 4.9(h), where the spectrograms for the healthy subject H2 are reported. With respect to the case shown in Fig. 4.2, here the excitability parameter has been increased in order to observe a faster *domino-like* effect, on the same temporal scale as for the epileptic patient. While high frequency oscillations ($>$ 200 Hz) are observable for the epileptic patient case, they are not detectable in Fig. 4.9(h_2) for the healthy subject case. The last statement may be qualified, however, by recent studies proposing high frequency oscillations (80-500 Hz) recorded not only at seizure onset but also between seizures (the interictal period), as a putative new marker of the epileptogenic focus [237].

---

[2] Please note that, irrespectively of the numerical results, any difference observed between the structural connectivity matrices obtained from the cohort of healthy subjects and epileptic patients may be (at least partially) ascribed to the different acquisition and processing procedures in the two research centers rather than due to disease-related causes.

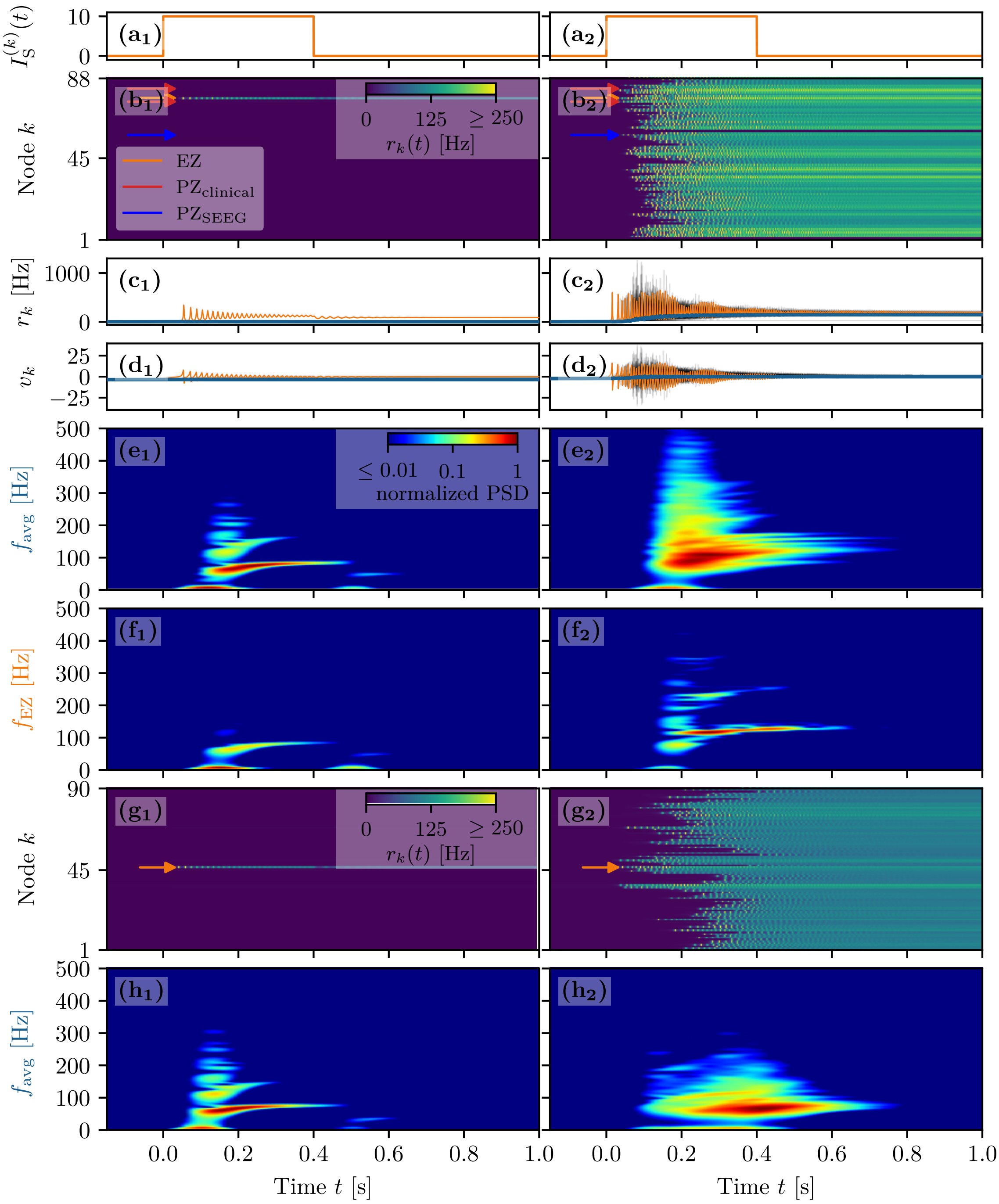

Figure 4.9: Spectrograms of mean membrane potentials for patient E6. **(a)** Stimulation currents $I_S^{(k)}$. **(b)** Space-time plots of the population firing rates r_k, color-coding the value of the firing rate of each node, as a function of time. **(c)** Population firing rates r_k and **(d)** mean membrane potentials v_k for the EZ (orange) and other populations (black). The blue curves show the network average firing rate and membrane potential. Non-stimulated node dynamics is plotted as transparent gray curves: some of the nodes adapt their voltage to the stimulation of the EZ and change during stimulation. **(e)** Spectrogram of the network average membrane potential and **(f)** of the v_k of the EZ. Column **(1)** shows an asymptomatic seizure-like event for $\bar{\eta} = -14$, column **(2)** a generalized seizure-like event for $\bar{\eta} = -7.5$. The EZ node 77 (rh-PrG) is stimulated. Other parameter values are: $N_{\text{pop}} = 88$, $\tau_{\text{m}} = 20$ ms, $\Delta = 1$, $\sigma = 1.25$, $J_{kk} = 20$, $J_{kl} = 5\tilde{J}_{kl} \quad \forall k \neq l$. For comparison the space-time plots of **(g)** the population firing rates r_k and **(h)** the spectrogram of the network average membrane potential for healthy subject H2 are shown. In accordance with the above panels, column (1) shows an asymptomatic seizure-like event (for $\bar{\eta} = -9.20$), column (2) a generalized seizure-like event (for $\bar{\eta} = -5.3$). The EZ node 46 is stimulated. For the estimation of the spectrograms see Section 1 of Appendix C. Other parameter values are: $N_{\text{pop}} = 90$, $\tau_{\text{m}} = 20$ ms, $\Delta = 1$, $J_{kk} = 20$, $\sigma = 1$, $J_{kl} = 5\tilde{J}_{kl} \quad \forall k \neq l$.

More specifically fast cortical ripples superimposed to interictal epileptiform discharges were correlated with the seizure onset zone and primary propagation area in neocortical epilepsy [239]. Neocortical ripples were also found to be more specifically confined to the seizure onset and propagation regions, and thus a better marker compared to interictal epileptiform discharges alone [240]. High frequency oscillations, as obtained via numerical experiments and shown in Fig. 4.9(e_2, f_2), are much more frequent in the seizure-like onset zone than outside, where they are often totally absent. The rather empty spectrograms of mean membrane potentials for patient E6 are a result of a rather rapid recruitment of a majority of nodes, thus giving rise to a strong signal change, immediately upon recruitment, which suppresses the rest of the signal in the spectrogram. At the same time the damped oscillations are all compressed within a narrow time window, and not very elongated in time, as it happens for healthy subjects [Fig. 4.2]. In other words, if the generalized seizure-like event is rapid, all the signals overlap, and this is especially clear looking at the strong low frequency bands. A fast generalized seizure-like event, in absence of high frequency oscillations outside the EZ, can be obtained for healthy subjects only increasing the excitability parameter: for higher $\bar{\eta}$ values, the recruitment is more sudden, as shown in Fig. 4.9(h_2). A difference between the signals obtained by numerically simulating the multi-population exact neural mass model and the high-frequency oscillations observed in human intracranial EEG studies can be found in the different oscillation amplitudes: High-frequency oscillations recorded during presurgical evaluation in patients, both at the seizure onset and during the interictal period, are characterized by a low amplitude [241–244], while this is not the case here. We can conjecture that higher amplitudes are related to the nature of the coupling, that we have chosen globally coupled and fully excitatory.

Temporal Recruitment of Clinically and SEEG Predicted Propagation Zones

In the following we test the clinical predictions for epileptic patients, by choosing the EZs, identified by clinical doctors via presurgical invasive evaluation, as perturbation sites. We investigate the recruitment times of different brain areas following such a perturbation and compare the order of recruitment with the experimental data given for each individual subject.

A general overview on the recruitment times of all brain areas, for all patients, is shown in Fig. 4.10. As perturbation sites, the clinical EZs, are used for all patients. For patients with several nodes detected in the EZ, all areas were stimulated simultaneously. The perturbation step current ($\Delta I = 10$, $\Delta T = 0.4$ s) is applied, to each perturbation site, in correspondence with the dashed vertical black line. The parameters are identical for almost all patients and are chosen such that at least 90% of the brain areas are recruited while still allowing multistability among various LA-HA configurations, including the network LA state. For each patient (identified via his/her number on the y-axis), the recruitment time of each brain area is reported: The gray dots represent the time values for each brain area. Superimposed on the grey dots are orange and blue dots that identify the brain areas belonging to the PZ, according to the non invasive ($\mathrm{PZ_{Clin}}$) or invasive ($\mathrm{PZ_{SEEG}}$) presurgical evaluation, respectively. The recruitment time averaged over all brain areas is identified, for each patient, by a green vertical line, while the boxes contain the second and third quartile of the distribution, and the whiskers have 1.5 the length of the InterQuartile Range (IQR) from the upper or lower quartiles. A one-sided Mann–Whitney U test has been performed to estimate the statistical significance of $\mathrm{PZ_{SEEG}}$ and $\mathrm{PZ_{clin}}$ recruitment times, as shown in Fig. A7 of Appendix B. Remarkably, the propagation zones $\mathrm{PZ_{Clin}}$ and $\mathrm{PZ_{SEEG}}$ turn out to be among the first recruited brain areas for all patients in the numerical experiments.

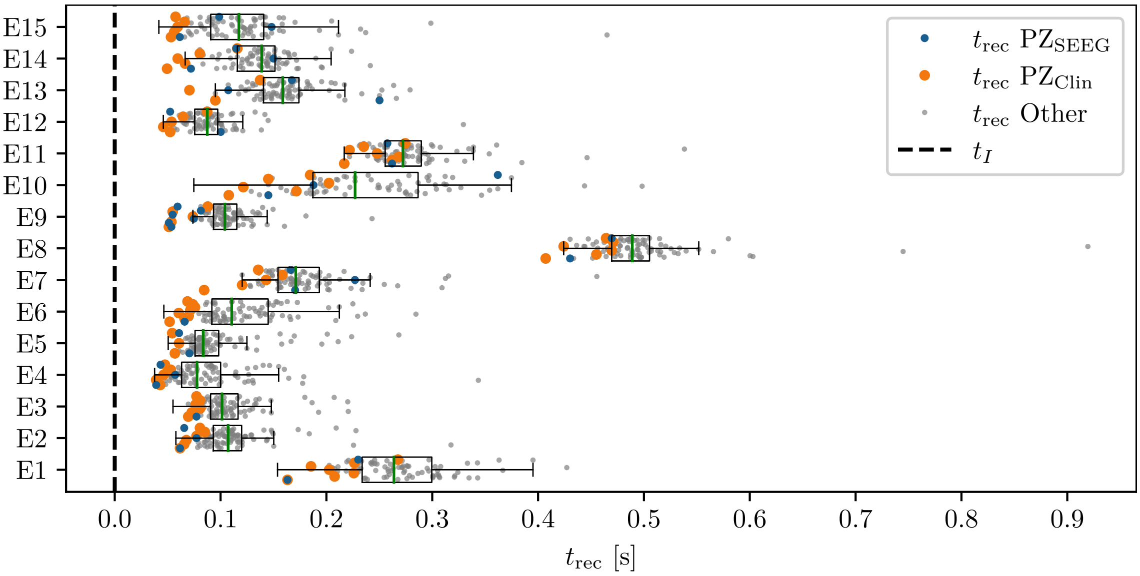

Figure 4.10: Recruitment times of all brain areas for the cohort of epileptic patients. The recruitment time, reported on the x-axis, identifies the time needed by a brain area to jump to the HA regime after the application of the perturbation current. The boxplots consist of the recruitment times of all brain areas for each patient. Patients are identified according to their numbers on the y-axis. The median is represented as a green vertical line while the boxes contain the second and third quartile of the distribution. The whiskers are chosen with maximum length 1.5×IQR and show the most extreme observed values that are within 1.5×IQR from the upper or lower quartiles. The gray dots represent the recruitment times for each brain area. The orange dots show the recruitment of a brain area clinically predicted to be part of the propagation zone PZ$_{\text{Clin}}$. The blue dots represents the recruitment of a brain area which is part of the propagation zone according to the SEEG measurements PZ$_{\text{SEEG}}$. Parameters: $N_{\text{pop}} = 88$, $\Delta = 1$, $\sigma = 1.25$, $\Delta I = 10$, $\Delta T = 0.4$ s, $\bar{\eta}^{(k)} = \bar{\eta} = -7.5$ (except for patients E1 ($\bar{\eta} = -6$) and E11 ($\bar{\eta} = -6.5$)).

However the temporal dynamics vary for all patients, with E8 and E1 having late recruitments. Looking at the set of the first ten recruited brain areas for each patient (reported in detail in Tables A5 to A7 of Appendix B), we notice that most of the areas, identified by clinicians as belonging to the PZ, are actually within this set: For patients E4, E5, E6, E9, E15 all the areas belonging to PZ$_{\text{Clin}}$ are among the first ten recruited areas, while the same holds true for patients E2, E3, E6 if we consider the areas identified by the stereotactic EEG analysis as belonging to the propagation zone (PZ$_{\text{SEEG}}$). In general a large number of the first ten recruited areas, as revealed by our simulations, coincides with the areas that are supposed to be crucial in the seizure spreading according to the medical doctors (e.g. for patients E2, E3, E10, E12, E13, E14). Moreover the predictability of the model is higher if we compare our results with the predictions PZ$_{\text{Clin}}$, while brain areas belonging to the predicted propagation zones, are in general recruited before the median recruitment time. However the model predictions are not good for the following cases: For patients E1, E8, E11, E14, the areas belonging to the PZ$_{\text{SEEG}}$ are only occasionally identified (half or less than half of the times), while for patients E1, E8, E11, other nodes are in generally recruited before those belonging to the PZ$_{\text{Clin}}$, that are identified with a percentage $< 50\%$. In all the former bad cases, the EZ has not been correctly identified, as results from the relative surgical outcomes (see Table 3). Therefore, the incorrect identification of the origin of seizure-like events may lead to a misleading identification of the PZ: In other words, a different potential EZ will lead to a different recruitment order, possibly closer to the experimental data.

To evaluate the dependence of the shown results on the chosen parameters, with the

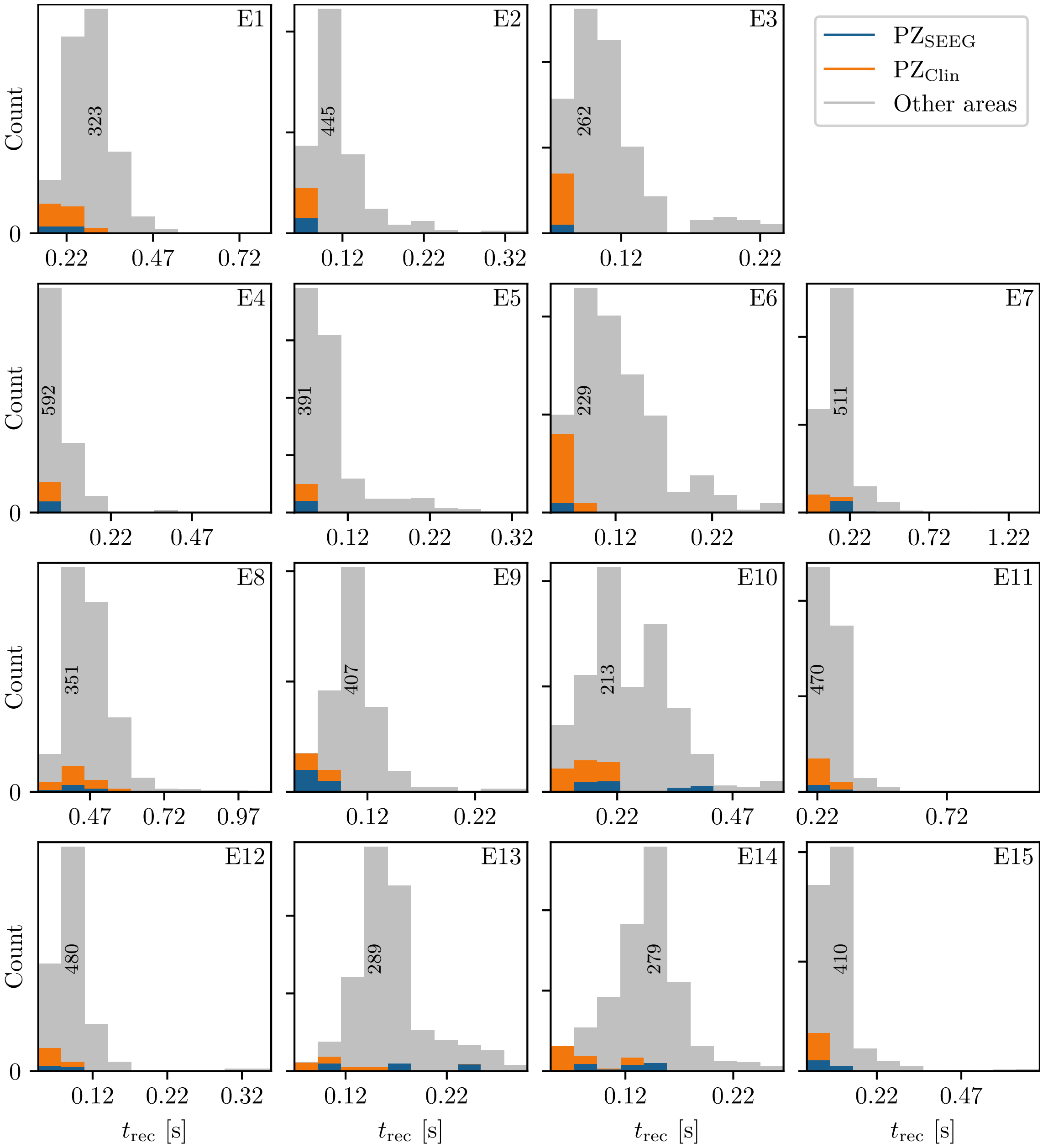

Figure 4.11: Histograms of recruitment times for all epileptic patients. For each patient (identified by his/her number), the recruitment times of all the brain areas are collected, once the EZ is stimulated. If several areas were identified in the EZ, they are all stimulated simultaneously. The EZ is chosen according to the presurgical evaluation (see Table A4 of Appendix B) and vary from one patient to the other. Parameters as in Fig. 4.10 except for $\bar{\eta}^{(k)} = -7.5 \pm 0.1$ (for E1 $\bar{\eta}^{(k)} = -6 \pm 0.1$, for E11 $\bar{\eta}^{(k)} = -6.5 \pm 0.1$). Results are averaged over 10 realizations of random Gaussian distributions.

idea in mind of going towards a more biologically realistic framework, we have repeated the previous numerical experiment by employing a random Gaussian distribution of the excitability parameter $\bar{\eta}^{(k)}$ (see Fig. 4.11). The distribution is centered at $\bar{\eta}_{\mathrm{G}} = -7.5$ with standard deviation 0.1 for all patients except E1 and E11. For the latter patients we shifted the center towards larger values, in order to get a sufficient number of recruitments when the EZ is stimulated. In all cases the results are averaged over 10 different random realizations of the distribution. More details on the impact of different realizations of $\bar{\eta}^{(k)}$ are given in Fig. A8 of Appendix B for one exemplary patient. For sufficiently larger standard deviations than the one employed (≥ 1), a too large fraction of the populations would not be able to exhibit bistability between LA and HA, highlighting the system sensitivity to finite parameter changes. However, for the chosen distribution, the results are comparable with the ones obtained with identical $\bar{\eta}^{(k)} = \bar{\eta}$, shown in Fig. 4.10. For patients E2, E3, E4, E5, E6, E9 the predicted propagation zones are always the first ones to be recruited. Moreover most of the areas are usually recruited in the first half of the recruitment process, rapidly increasing in number, once the areas in the propagation zones have been recruited (thus giving rise to a peak in the histogram). As a general remark, in view of the distributed nature of the excitabilities, recruitments at later times, with respect to the former case with homogeneous $\bar{\eta}^{(k)} = \bar{\eta}$, may now take place.

For patients with many nodes in the EZ, the recruitment process may result to be more complex, as it happens for patients E14 and E10, for which the histograms are less narrow, but instead widely distributed. However this cannot be taken as a general rule, since comparable histograms are obtained for patients E13 (one node in the EZ) and E8 (two nodes in the EZ), while for E15 and E12 (with both four nodes in the EZ) the histograms result to be very narrow, thus implying a fast recruitment process of most of the brain areas. The differences among the histograms can be partially justified by the facts that patients have specific connectomes with individual characteristics and by the analysis that we have proposed by choosing similar $\bar{\eta}$ values for all the patients. In this way we have preferred to have a general look on the multiple self-emergent dynamics in a group of patients, instead of fine-tuning the excitability parameter in order to obtain similar collective behaviors. What we observe here is strongly related to what we have presented in Fig. 4.9: the recruitment speed depends on the excitability parameter and on the individual network structure. Faster recruitment events may be obtained for different subjects by increasing the excitability value. In the following Section we try to understand, on the basis of network topological measures, the origin of the discrepancies among the clinical prediction of PZs and the first recruited areas predicted by the presented model.

Relationship Between DTI Network Structure and Temporal Seizure Recruitment

In order to understand the mechanism underlying the recruitment events, we evaluate the relationship between the network structure, in terms of topological measures, and the recruitment times of the first 10 recruited brain areas, as obtained through numerical experiments. For simplicity, we consider here patients with only one brain area in the EZ and we report, in Fig. 4.12, the potential EZ (orange circle) and the first 10 recruited areas in a graph representation. The results relative to all the other patients are reported in Figs. A9 to A11 of Appendix B. The first recruited areas are ordered according to their recruitment times in clockwise order. Moreover we indicate in blue the areas belonging to the PZ, as identified according to the presurgical invasive evaluation ($\mathrm{PZ}_{\mathrm{SEEG}}$). Black lines identify the weighted connections between all areas and their thickness is proportional to their weight. The sizes of the circles representing each brain area are proportional to their inverse recruitment time (A1-D1), to their weight connecting each area to the EZ (A2-D2), and to their inverse shortest path length between each node and the EZ (A3-D3), while the size of the orange EZ circle remains fixed.

Since in Fig. 4.12(a) the node size is proportional to the inverse recruitment time, large circles indicate early recruitment while small circles indicate late recruitments: Hence the circles become smaller clockwise. In Fig. 4.12(b) the node size is proportional to the weight connecting each area to the EZ and it turns out that, for all patients, the first recruited area has the strongest connecting weight. However, after a few recruitments this does not hold true anymore. There are many examples in which areas with a strong weight to the

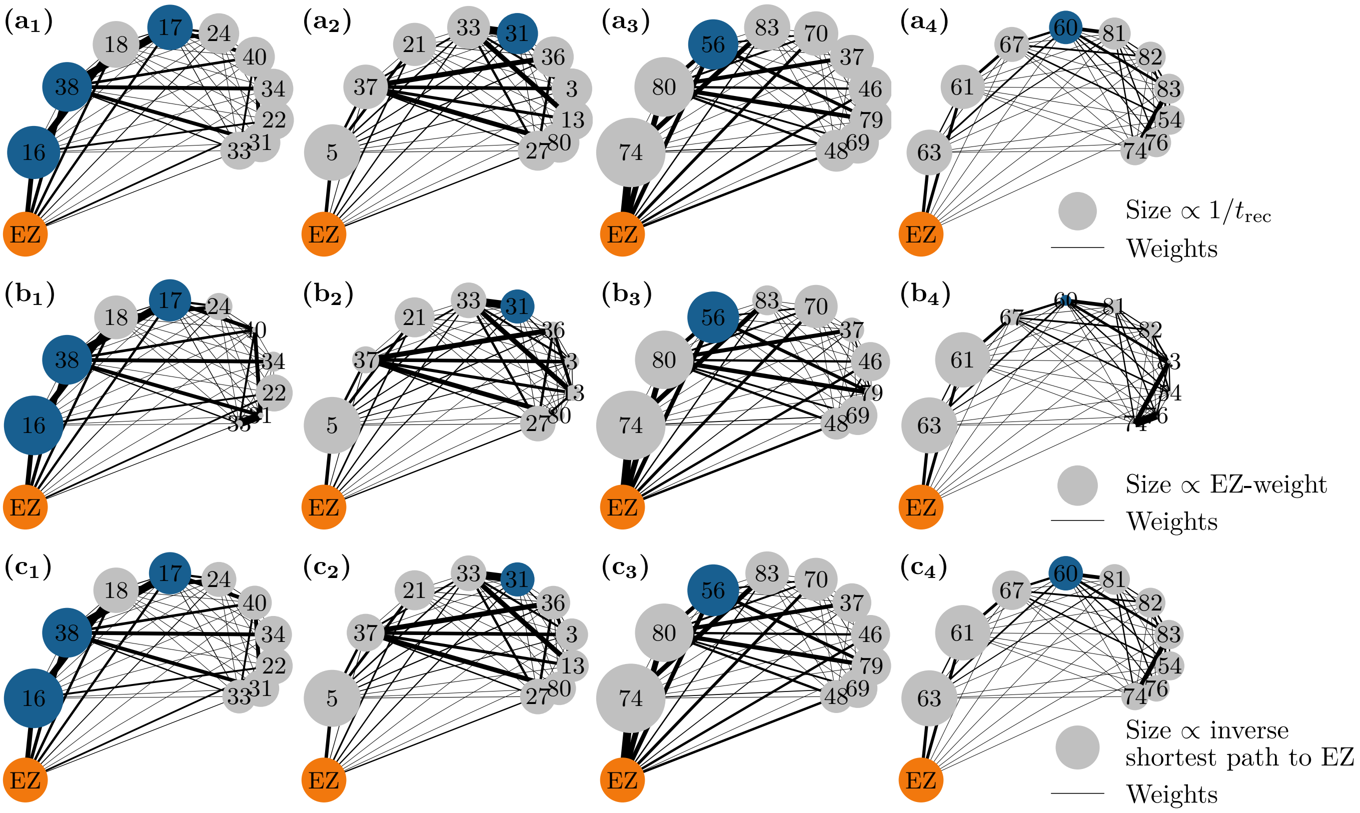

Figure 4.12: Recruitment order of epileptic patients, Graph plot of the first 10 recruited areas, ordered clockwise according to their recruitment times, as found via numerical experiments. **(a)** Node circle size corresponds to the inverse recruitment time, **(b)** to the connection strength to the EZ and **(c)** to the inverse shortest path length to the EZ. The size of the orange EZ remains fixed. Blue dots distinguish a recruited area to belong to the $\mathrm{PZ}_{\mathrm{SEEG}}$, i.e. the PZ identified according to the presurgical invasive evaluation. Columns **(1 - 4)** show the results for patients E2, E3, E6, E13. Parameters values are as in Fig. 4.10.

EZ (see e.g. area 46 or 48 for patient E6) are recruited much later than areas with very small weights (e.g. area 83 for FB). The seizure-like event propagates as a chain reaction and, therefore, the strongest connecting weight to the EZ is only decisive for the very first recruited area. Later, strong connections to other early recruited areas play a decisive role, as it is the case for area 83 in E6 which has a weak connection weight to the EZ. However, through its strong connection to area 74, its weighted shortest path length to the EZ is quite short, thus meaning that the weighted shortest path length to the EZ cannot be underestimated in order to find the recruitment ordering. Indeed, in Fig. 4.12(c) one can see the good predictability of the shortest path: the node size, proportional to the inverse shortest path length to EZ, decreases in general with later recruitment. This is expected, given the fact that the average shortest path to the EZ considers all connections in the network, not just the connections subgraph outgoing the EZ. An example of the high predictability of the shortest path is given by the node 38 in patient E2, which has a shorter path length to the EZ than node 18. Node 38 is recruited before node 18 irrespectively of its strong connection to node 16 and a connection strength to the EZ comparable with the one of node 38. However it is worth noticing that, in general, the nodes that are recruited before the areas belonging to the PZ, show either stronger connecting weights, or shortest path length to EZ.

For later recruitments, the prediction becomes even more difficult because one needs to account for the temporal order of the seizing brain areas. As shown before, the area which is first recruited, is the one with the strongest connection to the EZ. However, depending on the strength of the connection, the recruitment time changes and it increases for decreasing strength. In the case of patient E2 the recruitment of the second area is determined, more by the strength of the connections to the EZ (i.e. area 20) than by the connection to area 16, while, for the recruitments of the third and forth areas, the strong connections of node 18 to 16 and of node 17 to 38, i.e. the first and second recruited nodes, are fundamental. On the other hand, when the first recruited areas have strong connections to the EZ, as for example area 74 in patient E6, the successive recruitments are strongly influenced by the first recruited area, whose outgoing graph reveals areas that are recruited with high probability. Thus the connection to area 74 turns out to be, for the second, third, and fourth recruitment almost as important as the connection to the EZ (i.e. area 76). Finally, if we compare two late recruited areas that are characterized by the same shortest path length to the EZ, but with a path to the EZ that crosses very different nodes, we observe that the area with the path going through earlier recruited nodes is recruited earlier. The longer the seizure-like event propagates, the less important the shortest path length to the EZ becomes and the more important the path lengths to other recruited nodes become. This underlines the difficulty of predicting the seizure propagation in complex networks, however, it is possible to summarize some findings that hold true for almost all patients (including those shown in Figs. A9 to A11): The first recruited node is in general the one with the strongest connection to the EZ and the shortest path; strong connections to early recruited areas are fundamental to determine the recruitment order; nodes belonging to the $\mathrm{PZ}_{\mathrm{SEEG}}$, that are not identified by our simulations as first recruited nodes, show intermediate values of connection strength and shortest path, while the nodes that are recruited before are either more strongly connected to the EZ or to the previously recruited nodes.

To confirm the importance of the shortest path length and the strength of the connections outgoing the EZ in determining recruitment events, we report in Fig. 4.13 the recruitment time values as a function of the shortest path and the connection weights for the patients with a single node as potential EZ [Fig. 4.13(a, b)] and for all 15 epileptic patients [Fig. 4.13(c, d)]. In Fig. 4.13(b) the recruitment time is plotted over the logarithm of the weight, in Fig. 4.13(c) the values of the recruitment time are plotted as a function of the shortest path and in Fig. 4.13(d) as a function of the connection weight, ordered according to their recruitment order. In particular the order for recruitment, shortest path, and weight to EZ is ascending from small values to large values. This means that in Fig. 4.13(d) the areas with the strongest weights (87th, 86th, etc.) correspond to the areas that are recruited earliest (1st, 2nd, etc.). The ordering has been preferred to the specific values of the shortest path and connection weight when reporting data for all 15 patients, in order to obtain a better visualization. For patients E2, E3, E13, E6, the recruitment time grows almost linearly with the shortest path, while it decreases for increasing weights. This analysis is confirmed in Fig. A12 of Appendix B, where a regression fit is performed over the data shown in Fig. 4.13(a), thus underlying the approximately linear relationship between the shortest path length and the recruitment time for larger t_{rec}. The relationship is not anymore so evident when we consider different cases of potential EZs, that are composed of more that one area. However, in this case, it is still possible to affirm that the earliest recruitments are associated with the shortest path lengths and the strongest weights, while the nodes corresponding to $\mathrm{PZ}_{\mathrm{SEEG}}$ or $\mathrm{PZ}_{\mathrm{Clin}}$ that, according to our simulations, were recruited late, have very long shortest path lengths to the EZs or very small weights.

In general the recruitment mechanism is not completely defined by the shortest path length and the connection weight, therefore it is not possible to match the presurgical predictions in terms of $\mathrm{PZ}_{\mathrm{SEEG}}$ and $\mathrm{PZ}_{\mathrm{Clin}}$ if we try to identify the nodes belonging to

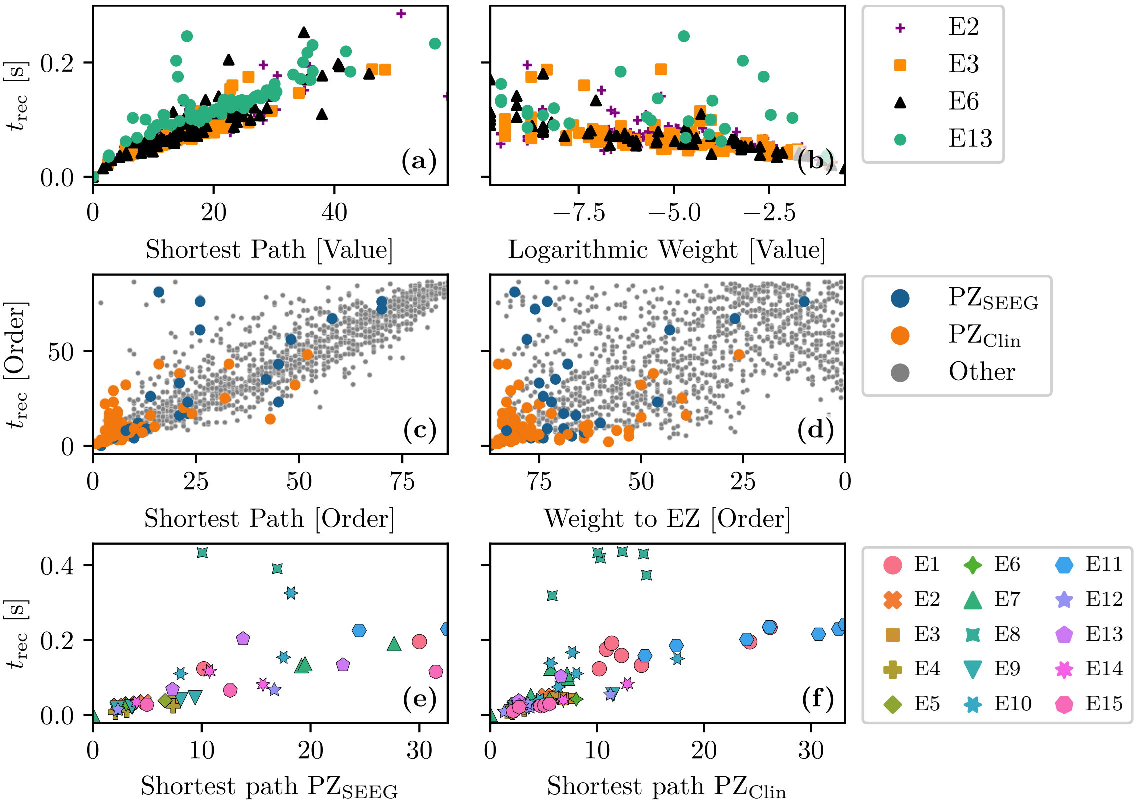

Figure 4.13: Relationship between network measure and recruitment time, as found via numerical experiments. (a) Shortest path to EZ; **(b)** Logarithmic value of the weight to the EZ for the four patients with a single-node EZ. In (a) all four EZs are shown at (0, 0) while in **(b)** the EZs are omitted. The recruitment time is calculated in seconds, after the perturbation current has started. In **(c, d)** the recruitment time values are plotted according to their order, as a function of shortest path to EZ (c) and weight to EZ (d) for all 15 patients. In (d) the x-axis was inverted for better comparison. **(e)** Recruitment times t_{rec} of the areas belonging to PZ_{SEEG} and **(f)** PZ_{Clin} as a function of the shortest path length to EZ, for all 15 patients. For patients with several nodes detected in the EZ, all areas were stimulated simultaneously. Parameter values are as in Fig. 4.10.

the PZ by calculating the first recruited nodes according to their shortest paths length or their connection weights. In particular, it turns out that the PZ_{SEEG} areas are well predicted by the investigated model if the shortest path length between the predicted PZ and the EZ is short, as shown in Fig. 4.13(e). However, for patients E8 and E10, the recruitments of the nodes belonging to PZ_{SEEG} happen much later when compared to brain areas of other patients with a similar shortest path length. Equivalently in Fig. 4.13(f) it is possible to observe that, for short values of the shortest path length (< 5), there is a linear correspondence between short recruitment times and PZ_{Clin} areas that are characterized by small values of the shortest path. However the areas belonging to PZ_{Clin} are still not identifiable, in terms of topological measures, for patient E8.

To conclude this Section on the influence of single connectome topology in determining activity spreading and area recruitment, we elaborate the data reported in Fig. 4.10 by sorting, from top to bottom, the patients according to their median shortest path length, calculated on all areas with respect to the EZ. In Fig. 4.14 the recruitment times of all brain areas for all patients are shown. Since patients are ordered according to their median shortest path length, the brain areas of E4 have, on average, the shortest paths to the EZ and the areas of E1 the longest. In general, it is possible to detect a slight trend, for the

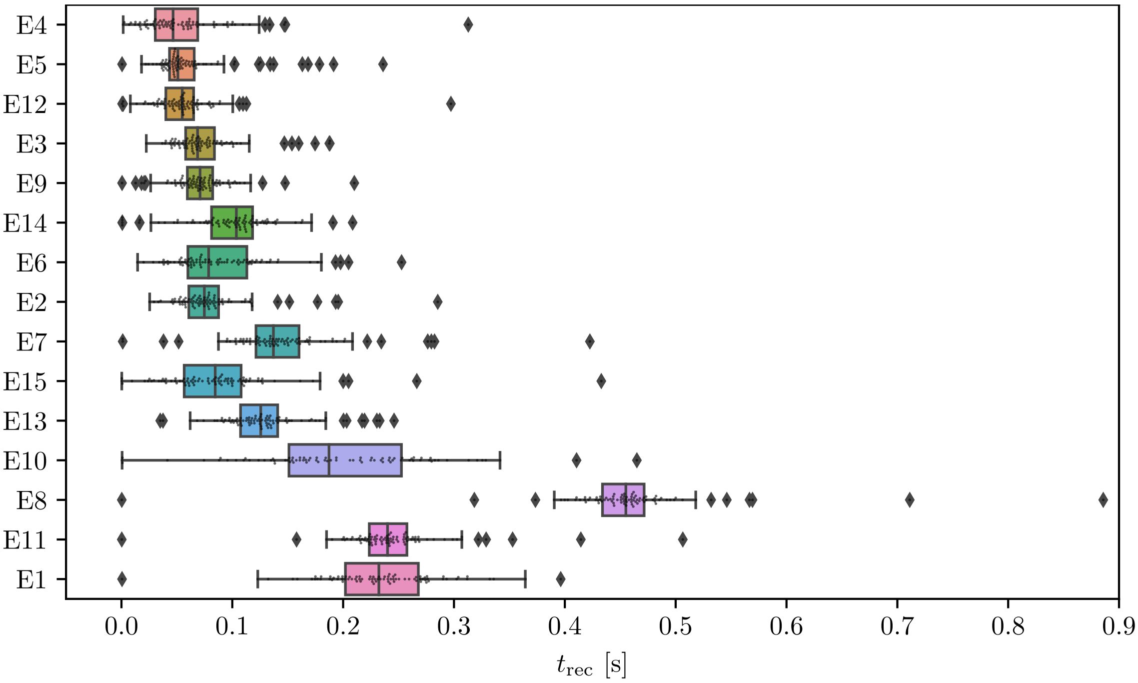

Figure 4.14: Recruitment times of all brain areas and all epileptic patients. The patients are sorted from top to bottom according to their median shortest path length, calculated by listing all the shortest path lengths of all areas to the EZ and then locating the number in the center of that distribution. Grey dots and diamonds show individual recruitments (we use two different symbols to highlight those values that are beyond the boxplot whiskers); boxes cover the 2nd and 3rd quartile and whiskers extend 1.5 times the interquantile range (whiskers are asymmetric, comprising the most extreme observed values that are within 1.5×IQR from the upper or lower quartiles). Parameters as in Fig. 4.10.

overall recruitment events, to delay with longer average shortest path lengths. More in detail, E10 and E8 show both very long and very short recruitment times, thus confirming the results obtained in Fig. 4.11 for Gaussian-distributed excitabilities. The scattering of the recruitment times for these patients reflects that, on average, their recruitment times are longer with respect to the other patients. However the mean recruitment times are comparable with those of E11, E1, that show comparatively late recruitments irrespectively of the fact that are characterized by a longer median shortest path. A common characteristic that brings together patients E10, E8, E11, E1 is the weak connection among the EZ and the first recruited area, that slows down the recruitment time (as already mentioned when discussing about Fig. 4.12), thus suggesting that is the interplay between connection strength and shortest path to determine the efficacy of seizure spreading and not the single topology measure alone.

The Impact of the Input Current Strength on the Recruitment Time

Following the same approach used to obtain the results shown in Fig. 4.7 for a healthy subject, we present here an analysis on the impact of the stimulation strength on the recruitment mechanism. Fig. 4.15 displays the recruitment times of the first ten recruited areas using different amplitudes ΔI of the step current $I_{\mathrm{S}}(t)$, while fixing the duration $\Delta T = 0.4$ s.

The analysis has been performed for patients E2 [Fig. 4.10(a)], E3 [Fig. 4.10(b)], E6 [Fig. 4.10(c)] and E13 [Fig. 4.10(d)], thus integrating the information on the dependency on topological measures presented in the previous section. As expected, the recruitment

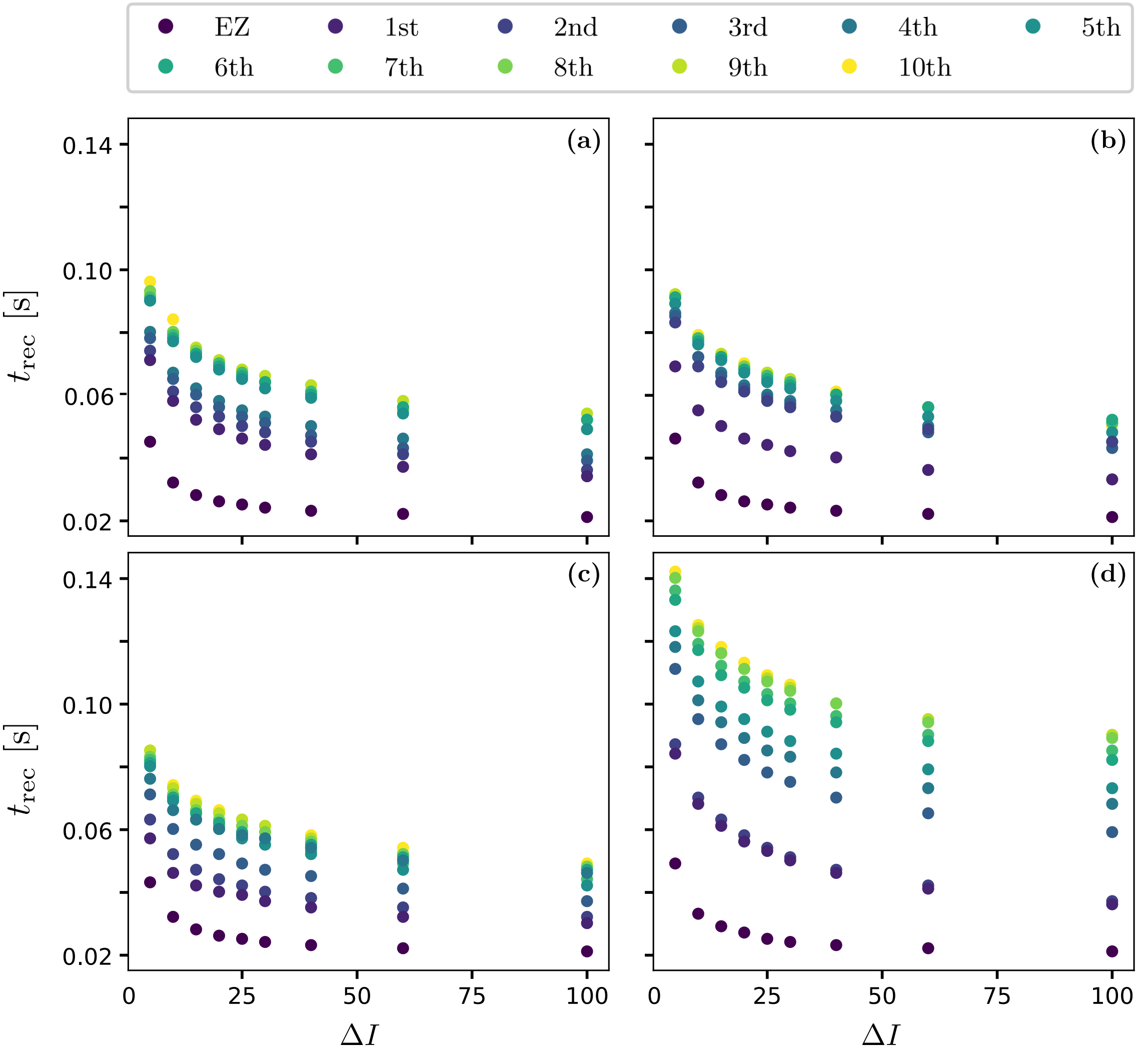

Figure 4.15: Dependence on input current (epileptic patients). **(a)** E2, **(b)** E3, **(c)** E6 and **(d)** E13. The strength of the input current is varied between 0 and 100 on the x-axis while its duration is kept unchanged at $\Delta T = 0.4$ s with respect to the previous numerical experiments. The order of the recruitment is color coded for each current strength from violet to yellow and it holds the same for all investigated patients. Parameters as in Fig. 4.10.

times decrease for larger amplitudes. However, the order of recruitment does not substantially change. This implies that, whenever we increase the amplitude, the recruitment mechanism remains unaffected: the same populations are involved in the seizure spreading and in the same order. What changes is the speed of the spreading and the time necessary to observe a generalized seizure-like event, which is smaller for stronger currents. As a general remark, the brain areas that are recruited after the first ones (i.e. the $5th$, $6th$,...,$10th$ recruited areas), tend to be recruited more simultaneously for increasing ΔI, thus leading to possible changes in the recruitment order. This can be appreciated especially for patient E2: For an amplitude $\Delta I = 10$, for example, the $10th$ brain area (pink) gets recruited later than the $9th$ area (dark blue), while for a very strong currents ($\Delta I = 100$) the darkblue area gets recruited latest whereas the pink area gets recruited earlier.

On the other hand if we vary the step current duration ΔT keeping the amplitude $\Delta I = 15$ fixed (see Fig. A13 of Appendix B), we do not observe any change in the recruitment times of the first 10 recruited areas, analogous to the healthy subject case presented in Fig. A6.

4.4 Discussion

Neural mass models have been actively used since the 1970s to model the coarse grained activity of large populations of neurons and synapses [7, 245]. They have proven especially useful in understanding brain rhythms [179, 246, 247], epileptic dynamics [186, 248], brain resonance phenomena [249], resting state [250, 251], task activity [252, 253], neurological and psychiatric disorders [254] and are very popular in the neuroimaging community [255, 256]. Moreover, the desire to understand large-scale brain dynamics as observed using EEG, MEG and functional MRI (fMRI) has prompted the increasing use of computational models [257]. Large-scale simulators such as The Virtual Brain (TVB) [258] and research infrastructures such as EBRAINS (http://ebrains.eu) make heavy use of networks of interconnected neural mass models and enable non-expert users to gain access to expert state-of-the-art brain network simulation tools.

Although motivated by neurobiological considerations, neural mass models are phenomenological in nature, and cannot hope to recreate some of the rich repertoire of responses seen in real neuronal tissue. In particular their state variables track coarse grained measures of the population firing rate or synaptic activity. At best they are expected to provide appropriate levels of description for many thousands of near identical interconnected neurons with a preference to operate in synchrony, but they cannot reproduce the variation of synchrony within a neuronal population which is believed to underlie the decrease or increase of power seen in given EEG frequency bands. Importantly, unlike its phenomenological counterpart, the next generation neural mass model we have implemented in this chapter, is an exact macroscopic description of an underlying microscopic spiking neurodynamics, and is a natural candidate for use in future large-scale human brain simulations. In addition to this, the inability of a single neural mass model to support event-related desynchronization/synchronisation [259] or to capture the onset of synchronous oscillations in networks of inhibitory neurons [46], reminds us that these phenomenological models could be improved upon. While building more detailed biophysically realistic models of neurons would increase the computational complexity and the difficulties to interpret the behavior of very high-dimensional models in a meaningful way, the next generation neural mass models here applied, are very much in the original spirit of neural mass modeling, yet importantly they can be interpreted directly in terms of an underlying spiking model. This exact derivation is possible for networks of quadratic integrate-and-fire neurons, representing the normal form of Hodgkin's class I excitable membranes [30], thanks to the analytic techniques developed for coupled phase oscillators [15]. This new generation of neural mass models has been recently used to describe the emergence of collective oscillations in fully coupled networks [27, 46, 133, 134] as well as in balanced sparse networks [36]. Furthermore, it has been successfully employed to reveal the mechanisms at the basis of theta-nested gamma oscillations [33, 87] and the coexistence of slow and fast gamma oscillations [135]. Finally it has been recently applied to modeling electrical synapses [35], working memory [98], the influence of transcranial magnetic stimulation on brain dynamics [260] and brain resting state activity [209].

In this chapter we have extended the single next generation neural mass model derived in [16] to a network of interacting neural mass models, where the topology is determined by structural connectivity matrices of healthy and epilepsy-affected subjects. In this way we are able to take into account both the macroscopic dynamics, self-emergent in the system due to the interactions among nodes, and the various differences related to the patient-specific analyses. However, the single population neural mass model does not take into account neither the synaptic kinetics nor the dynamics of the synaptic field characterizing the considered synapses, which is simply modeled as the linear superposition of δ-shaped post-synaptic potentials. Moreover, when extending the excitatory neural mass model derived in [16] to a multi-population network, we have considered only excitatory coupling in order to build a minimal model for the investigation of topologically-induced dynamical features. Therefore, the presented neural mass model is not able to reproduce depth-EEG epileptic signals, which represents one of the best successes of heuristic neural mass models [180].

In absence of external forcing, the phase diagram of the system as a function of the mean external drive $\bar{\eta}$ and synaptic weight J resembles that of the single neural mass model, since the same distinct regions can be observed: (1) a single stable node corresponding to a low-activity state, (2) a single stable focus (spiral) generally corresponding to a high-activity state, and (3) a region of bistability between low and high firing rate. However, when the system is subject to a transient external current, the scenario changes and is ruled by the interactions among different nodes. In this case, for low excitability values, a single stimulated node abandons the bistable region due to the applied current and it approaches, with damped oscillations, the high-activity state, which is a stable focus. On the other hand, for sufficiently high excitabilities, the single node stimulation leads to the recruitment of other brain areas that reach, as the perturbed node, the high-activity regime by showing damped oscillations. This activity mimics a seizure-like event and enables the modeling of propagation and recruitment: the seizure-like event originates in the EZ (as a results of the stimulation) and propagates to the PZ, identified by the other regions where the oscillatory activity propagates rapidly. It is distinct from an actual seizure, which would require the emergence of self-sustained activity in the high-activity state [186, 234, 261].

However transient activity, like the proposed seizure-like events, can play a potentially important role in localizing tissue involved in the generation of seizure activity, if read in the framework of stimulation of human epileptic tissue with consequent induction of rhythmic, self-terminating responses on the EEG or electrocorticogram (ECoG) [262–264]. From the dynamical systems perspective, one can hypothesize that complex stimulus responses are due to a space-dependent induction of self-terminating, spatio-temporal transients that are caused by brief perturbations in an excitable medium [185]. Accordingly, considering epileptic seizure dynamics as spatio-temporal patterns [183, 190] shifts attention on the self-organizing capabilities of spatio-temporal brain networks, thus proposing an alternative explanatory framework for epileptiform EEG to the time dependent modulation in system parameters [265–269].

Moreover, perturbation experiments, like the stimulation of human tissue, turns out to be fundamental in the context of functional brain mapping, as integral part of contemporary neurosurgery [270]. Surgical planning of the resection procedure depends substantially on the delineation of abnormal tissue, e.g., epileptic foci or tumor tissue, and on the creation of functional map of eloquent cortex in the area close to the abnormal tissue. Traditionally, different methodologies have been used to produce this functional map: electrical cortical stimulation [271–273], functional magnetic resonance imaging [274], positron emission tomography [275, 276], magnetoencephalography [277], evoked potentials [278] or passive recordings of electrocorticographic signals [279]. In particular, ECoG activity recorded from subdural electrodes, placed during surgical protocols, reflect task-related changes [280–287]: ECoG amplitudes in specific frequency bands carry substantial information about movement or language tasks and they usually increase with the task in the gamma (> 40 Hz) band. Extending the presented multi-population model, via the addition of synaptic dynamics and an inhibitory pool, to reproduce task-related change in ECoG activity, would be essential to extend its predictive power.

The spectrogram analysis has revealed that the recruitment process is characterized by high frequency γ oscillations, thus reproducing the high-frequency (γ-band) EEG activity typical of electrophysiological patterns in focal seizures of human epilepsy. Many hypotheses have been formulated on the origin of this fast activity: (i) the behavior of inhibitory interneurons in hippocampal or neocortical networks in the generation of gamma frequency oscillations [288, 289]; (ii) the nonuniform alteration of GABAergic inhibition in experimental epilepsy (reduced dendritic inhibition and increased somatic inhibition) [180, 290]; (iii) the possible depression of GABA$_{A,fast}$ circuit activity by GABA$_{A,slow}$ inhibitory postsynaptic currents [291, 292]; iv) the out of phase patterns of depolarizing GABAergic post-synaptic potentials onto pyramidal cells, generated by feed-forward activation of cortical interneurons [293]. In any case high-frequency EEG waves originating from one or several brain regions are the most characteristic electrophysiological pattern in focal seizures of human epilepsy and can be observed, in our numerical experiments, both for healthy subjects and epileptic patients, though with a distinction: for the same excitability value, the activity takes place at higher frequency ranges in epileptic patients and it is mainly concentrated in the EZ. Moreover high frequency γ oscillations (> 200 Hz) are observable in the epileptic patient's spectrogram only. Even though it is not possible to exclude discrepancies partially imputable to the different scanning and preparation procedure of the structural connectivity matrices for the cohort of healthy and epilepsy-affected subjects, it turns out that the recruitment process is faster in epileptic patients, for which it is possible to observe generalize seizure-like events for smaller values of the excitability parameter $\bar{\eta}$. In particular, when comparing the results obtained for healthy subjects and epileptic patients, it turns out that the time necessary to recruit areas in the PZ is usually smaller for epileptic patients. However, the first recruited area is, in general, the area with the stronger connection to the EZ, independently of the considered structural connectivity matrix. The recruitment time in both cases is influenced by the strength of the external perturbation ΔI, and decreases for increasing strength, while no dependence is shown on the duration of the external perturbation.

More specifically for healthy subjects we have investigated the dependence of the recruitment mechanism on the single subject, in terms of the position of the eventual EZ and in terms of the topological measures of the single connectome. Brain network models of healthy subjects comprise 90 nodes equipped with region specific next generation neural mass models and each subject is characterized by a specific structural large-scale connectivity amongst brain areas. The smallest excitability values for which an asymptomatic seizure-like event occurs ($\bar{\eta}^{(k)}_{\text{asy}}$) do not vary significantly from one subject to the other and do not show a relevant dependence on the stimulated area, while the smallest excitability values for which a generalized seizure-like event occurs ($\bar{\eta}^{(k)}_{\text{gen}}$), show fluctuations in the interval $(-7, -5)$ for all stimulated nodes and for all the subjects. Nonetheless we have found many similarities at the level of topological measures, since there is always a strong correlation between $\bar{\eta}^{(k)}_{\text{asy}}$ ($\bar{\eta}^{(k)}_{\text{gen}}$) and node strength, clustering coefficient and shortest path, thus meaning that a region well connected is a region well recruited.

For epileptic patients, we have systematically simulated the individual seizure-like propagation patterns and validated the numerical predictions of the PZ against clinical diagnosis and EEG signals. Patient-specific brain network models of epileptic patients comprise 88 nodes equipped with region specific next generation neural mass models and, for this set-up, we have studied the role of the large-scale connectome based on dMRI, in predicting the recruitment of distant areas through seizure-like events originating from a focal epileptogenic network. We have demonstrated that simulations and analytical solutions approximating the large-scale brain network model behavior significantly predict the propagation zone as determined by SEEG recordings and clinical expertise, with performances comparable to previous analyses on this set of data [201, 203], thus confirming the relevance of using a large-scale network modeling to predict seizure recruitment networks. However, some false positive are still observable, where populations not belonging to $\mathrm{PZ}_{\mathrm{SEEG}}$ or $\mathrm{PZ}_{\mathrm{Clin}}$ are first recruited. In these cases, the analysis on topological properties has revealed that nodes are easily recruited whenever they show strong connections to the EZ or to early recruited areas and that are closer to the EZ in terms of shortest path length. Therefore, nodes belonging to the $\mathrm{PZ}_{\mathrm{SEEG}}$ ($\mathrm{PZ}_{\mathrm{Clin}}$), that are not identified by our simulations as first recruited nodes, are characterized by intermediate values of connection strength and shortest path. Predictions are particularly not good for those patients whose EZ has not been correctly identified, as results from the relative surgical outcomes reported in Table A3. For these patients, the incorrect identification of the origin of seizure-like events may lead to a misleading identification of the PZ, since we are not able to identify, numerically, the recruitment of nodes not directly connected with the real EZ. Finally, comparing the results obtained for epileptic patients with those for healthy subjects, we infer a strong correlation between fast recruitment events and node strength, which is due to the fact that structural connectomes, both for healthy subjects and epileptic patients, are characterized by a log-normal distribution of the weights, where some connections, for each node, have a much stronger weight than the others. Moreover, the strong correlation between fast recruitment and clustering coefficient/shortest path suggests that we are in the presence of hierarchical connectivities, which have been shown to be important for the spreading of activity [129, 294] and the enhancement of the network susceptibility to seizure activity [295].

Most computational models of seizure propagation focus on small continuous spatial scales [267, 296, 297] or population of neurons [57, 298–303] while only small networks are commonly used to investigate the role of the topology and localization of the epileptogenic zone [187]. However functional, volumetric and electrographic data suggest a broad reorganization of the networks in epileptic patients [304–308], thus laying the foundations for a different approach based on large-scale connectomes to identify the recruitment networks. The large-scale character of partial seizure propagation in the human brain has been only recently investigated, using patient-specific dMRI data to systematically test the relevance of the large-scale network modeling in predicting seizure recruitment networks [201–203, 309]. In this framework of large-scale network modeling we can also place the results presented in this chapter, since we have confirmed the importance of patient-specific connectomes to identify the recruitment process. As shown above, the topological characteristics of connection strength and shortest path play a non-trivial role in determining the spreading of seizure-like events, together with the localization of the epileptogenic zone, while the next generation neural mass model, here employed for the first time to study seizure spreading, allows us to construct patient-specific brain models via a multiscale approach: the variability of brain regions, as extracted from the human brain atlas, can be introduced in the mean-field parameters, thanks to the exact correspondence between microscopic and macroscopic scales guaranteed by the model itself. The possibility to exactly move through the scales has not been fully exploited in this chapter, since we have focused our analysis on the extension of the single neural mass model to a multi-population model, without adding other relevant features to the original model. However it is possible to easily introduce, in the multi-population model, biologically relevant characteristics, keeping intact the exact correspondence between microscopic and macroscopic scales, such as short-term synaptic plasticity [98], synaptic delays [46], electrical coupling via gap junctions [35], chemical synapses [27], extrinsic and endogenous noise [37]. By adding short-term synaptic plasticity we expect to being able to reproduce the emergence of self-sustained activity in the high-activity state and therefore to describe a fully developed seizure. The introduction of synaptic delays and noise guarantees the possibility to observe chaotic dynamics, therefore allowing for the reproduction of more complex signals, like depth-EEG epileptic signals. Improving the predictive power of the model by the means of more biologically relevant characteristics and anatomical data (3D T1-weighted images, high angular and spatial dwRMI data, ion, energetic and neurotransmitter measurements available e.g. in the BigBrain and human brain atlas) will be the scope of further research.

Chapter 5

Emergence of bursting: a slow-fast approach

We report a detailed analysis on the emergence of bursting in the neural mass model with STP developed in Chapter 2 and studied in Chapter 3 in the context of working memory. Neural mass models are capable of mimicking the collective dynamics of large-scale neuronal populations in terms of a few macroscopic variables like mean membrane potential and firing rate. The one being used here is particularly important, as it represents an exact mean-field limit of synaptically coupled QIF neurons, which we recall are canonical models for type I excitability. In absence of synaptic dynamics, a periodic external current with a slow frequency ε can lead to burst-like dynamics. The firing patterns can be understood using techniques of singular perturbation theory, specifically slow-fast dissection. In the model with synaptic dynamics the separation of timescales leads to a variety of slow-fast phenomena and their role for bursting is rendered inordinately more intricate. Canards are one of the main slow-fast elements on the route to bursting. As explained in Chapter 2, they describe trajectories evolving nearby otherwise repelling locally invariant sets of the system and are found in the transition region from subthreshold dynamics to bursting. For values of the timescale separation nearby the singular limit $\varepsilon = 0$, we report peculiar jump-on canards, which block a continuous transition to bursting. In the biologically more plausible regime of ε this transition becomes continuous and bursts emerge via consecutive spike-adding transitions. The onset of bursting is of complex nature and involves mixed-type-like torus canards, which form the very first spikes of the burst and revolve nearby fast-subsystem repelling limit cycles. We provide numerical evidence for the same mechanisms to be responsible for the emergence of bursting in the quadratic integrate & fire network short-term synaptic plasticity. The main conclusions apply for the network, owing to the exactness of the mean-field limit.

Publication:
The results presented in this chapter are submitted to New Journal of Physics and available as pre-print [310]: H. Taher, D. Avitabile, and M. Desroches. "Bursting in a next Generation Neural Mass Model with Synaptic Dynamics: A Slow-Fast Approach". *arXiv:2109.06757v1 [nlin]* (Sept. 2021)

5.1 Introduction

As we have seen in the previous chapters, QIF networks and their neural mass counterparts can give rise to interesting dynamical regimes, typically evoked by bistability or multistability in the system. Indeed, in its simplest form, the original MPR model exhibits a parameter regime where a stable node and a focus coexist [16]. This is particularly relevant for the macroscopic response of neuronal ensembles when they are subject to an external current: bistability implies that a time dependent external drive can lead to interesting firing rhythms. A recent study takes into account synaptic dynamics in form of exponentially decaying action potentials and investigates the firing patterns emerging across spatial and specifically temporal scales [68].

In this chapter however, we want to explore a QIF network that accounts for synaptic dynamics in form of short-term synaptic plasticity, thus adding to the biological plausibility. To our knowledge, the role of STP in next generation neural mass models has received just little attention, despite being highly relevant in neuroscience. Previous macroscopic models of STP typically make use of the Wilson-Cowan (WC) model, hence are of heuristic nature [7, 39]. In Chapter 3 an extension of the MPR firing rate equations towards STP was employed, in order to model WM. The mean-field limit, in presence of STP, remains exact. Therefore one can exploit this limit, in order to get insight into the emergence of firing patterns in the network. An aspect that can lead to complex behavior is the timescale separation, which comes along with STP. Depression and facilitation might indeed act on different timescales. As an example, measurements in the prefrontal cortex suggest that the facilitation of synapses can be maintained for seconds, while depression decays within a few hundred milliseconds [90].

Synaptic dynamics and additional timescales enrich the dynamical landscape, by giving rise to bistability involving limit cycles. This is the foundation for bursting rhythms to emerge. Bursting refers to dynamics that alternates between a quiescent phase and rapid oscillations. When slowly forcing the population of QIF neurons, by virtues of a slowly drifting external current, the system can transit from a quasi-static motion to rapid oscillations associated with the presence of stable cycles in the system with constant external current.

Bursting has been found in various experimental studies in neuroscience [22, 23, 58–63] and theoretical approaches [64, 65, 311–314] not only aim at classifying the observed dynamics, but also mimicking and revealing the mechanisms responsible for the emergence of bursting. While bursting in spiking neural networks is subject of recent studies [315, 316], the mechanisms responsible for their emergence often remain unclear: exploring the state space of large-scale networks is tedious and the addition of slow-fast aspects complicates the problem. The exactness of the MPR model helps to overcome this limitation: analytic tools and bifurcation analysis applied to the neural mass model allow to draw conclusions for the microscopic network.

The main results of this chapter are related to the emergence of bursting in a QIF network with STP. In particular, we investigate the transition from subthreshold oscillations to bursting in presence of an external slow and periodic current. The forcing introduces a clear timescale separation into the problem, giving rise to intricate slow-fast phenomena and allowing for the application of slow-fast dissection methods, to be described later. As an outlook, the findings comprise a differentiation of the route to bursting, depending on the timescale separation. For strongly separated timescales, far away from biologically plausible scenarios, the route is complicated, possibly discontinuous in parameter space and it is related to a certain type of canards. Moderate timescale separations on the other hand reveal a number of intermingled slow-fast mechanisms that lead to a continuous transition from subthreshold oscillations to bursting and are related to different types of canards. Our results are supported by slow-fast arguments and numerical evidence.

A first illustration of the dynamical regime of interest in this chapter is displayed in Fig. 5.1. The response of a large-scale network, exhibiting STP and consisting of $N = 10^5$ QIF neurons, to a slow external sinusoidal current is depicted in Fig. 5.1(a). The second panel Fig. 5.1(b) shows the firing rate of the QIF network, as well as the firing rate of the mean-field limit. Both systems undergo a quiescence phase of low firing activity. When the external current exceeds a certain level, the systems start to burst, characterized by a rapid series of synchronized firing at high rates.

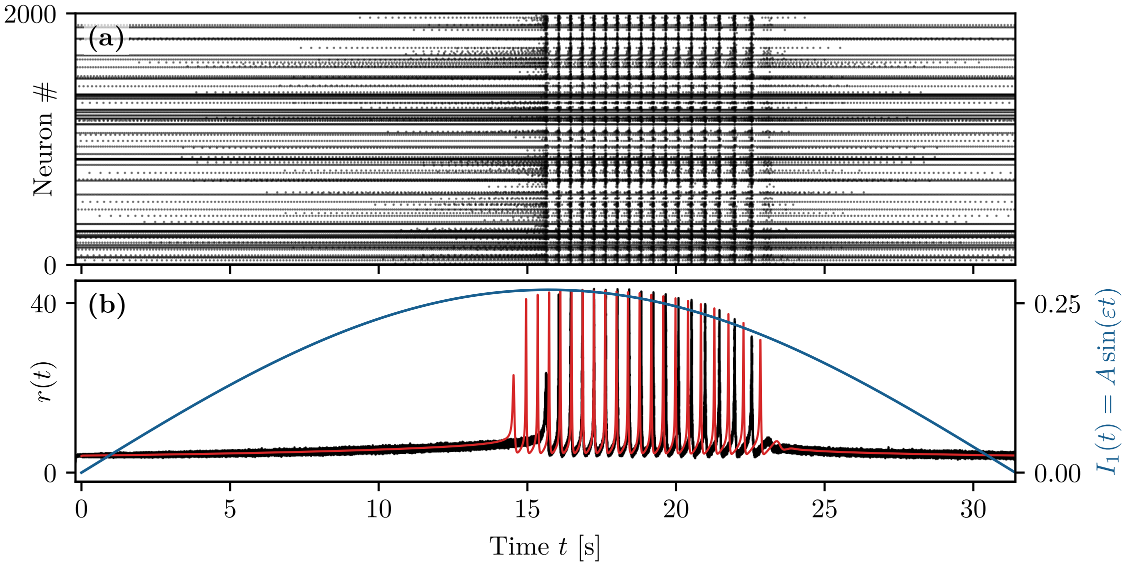

Figure 5.1: Spiking neuron network and mean-field limit. (a) Scatter plot of a subset of 2000 representative neurons out of 10^5. Each dot represent a spike. **(b)** Firing rate of the network (black) and of the corresponding mean-field limit (red). The blue curve shows a time dependent external current applied to the two systems and is of sinusoidal form.

In order to understand how these bursts emerge, we have to encapsulate two main aspects. First, in the upcoming Section 5.2, we will recall the QIF network model with STP as well as the corresponding mean-field limit, and we will analyze the state space structure and dynamics. Second, the presence of a slow external drive calls for the application of slow-fast dissection. We have introduced the slow-fast framework in Section 2.7 of Chapter 2. This generic methodology for timescale separated problems is applied to the present model in Section 5.3. Dissection is crucial for understanding the results in Section 5.4, where canards and in particular jump-on canards are studied using slow-fast arguments. This paves the way to investigate the mechanisms responsible for the emergence of bursting, as done in Section 5.5. Finally, in Section 5.6 the initially posed problem of bursting on macroscopic scale is approached by a comparison of mean-field dynamics versus QIF network dynamics in the bursting regime.

5.2 Periodically forced neural mass

Despite having a rather simple state-space structure, the original MPR model without STP can give rise to interesting periodic patterns when externally forced. In the absence of a time depending current, periodic solutions are absent. Instead one can find node, focus and saddle equilibria. However, there are regions of parameter space in which bistability between the node and focus appears. Hence slow periodic forcing, for example given by

$I_1 = A\sin(\varepsilon t), \quad 0 < \varepsilon \ll 1$, can lead to a hysteretic loop in these regions, as shown in [16]. In this case the trajectories consist of a low firing rate segment and a high firing rate segment with damped oscillations, related to the presence of foci in the system with constant I_1. Orbits of this type can already be seen as bursting patterns characterized by an alternation of slow drifts and fast oscillations. However, in the limit $\varepsilon = 0$ of infinitely slow forcing, the fast oscillations vanish. In that case, the resulting cycles can be classified as relaxation oscillations, which were introduced in Section 2.7.

The model of interest for our work is the canonical model for type I excitability: the QIF neuron. We recall from Chapter 2, that in a network of N synaptically coupled neurons in presence of m-STP the membrane potentials $V_i(t)$, depression $x(t)$ and facilitation $u(t)$ obey Eqs. (5.1).

$$\dot{V}_i = V_i^2 + \eta_i + Juxr + I_1(t) \tag{5.1a}$$

$$\dot{x} = \frac{1-x}{\tau_\mathrm{d}} - uxr \tag{5.1b}$$

$$\dot{u} = \frac{U_0 - u}{\tau_\mathrm{f}} + U_0(1-u)r \tag{5.1c}$$

The total current applied to the neuron is a sum of the constant component η_i, the synaptic current $Ju(t)x(t)r(t)$, with constant synaptic weight J and an external, possibly time-dependent, current $I_1(t)$[1]. Variable $r(t) = \frac{1}{N}\sum_{j=1}^{N} S_j(t)$ denotes the instantaneous firing rate and is composed of the single neuron spike trains $S_j(t) = \sum_{k:t_j(k)<t}\delta(t - t_j(k))$, where $t_j(k)$ denotes the k-th spike time of neuron j entering into the Dirac δ function.

The collective dynamics of the QIF network in presence of m-STP Eqs. (5.1) is captured by the neural mass model Eqs. (5.2) in an exact manner (see Section 2.3 in Chapter 2). Here we chose the form of the model, in which the membrane time constant has been eliminated via a rescaling of time and we will refer to it as neural mass model with short-term synaptic plasticity (NMSTP).

$$\dot{r} = \frac{\Delta}{\pi} + 2rv \tag{5.2a}$$

$$\dot{v} = v^2 - (\pi r)^2 + Juxr + \bar{\eta} + I_1(t) \tag{5.2b}$$

$$\dot{x} = \frac{1-x}{\tau_\mathrm{d}} - uxr \tag{5.2c}$$

$$\dot{u} = \frac{U_0 - u}{\tau_\mathrm{f}} + U_0(1-u)r \tag{5.2d}$$

We note that Eqs. (5.2) will evolve on the fastest timescale of our problem. This holds despite the fact that it already possesses multiple timescale via τ_d and τ_f. However, as we will discuss later, this inherent timescale separation of Eqs. (5.2) is subtle and not observable everywhere in state space. Nevertheless, it has significant impact on how the transition from subthreshold (non-bursting) behavior to bursting occurs (see also Sections 5.4.2 and 5.5.3).

5.2.1 Dynamics under constant forcing

Most of the parameters values used for Eqs. (5.2) will remain fixed in this chapter and if not stated differently given in Table 5.1. Note that time is measured in units of the membrane time constant τ_m. We will outline the different dynamical regimes in presence of a constant current $I_1(t) = $ const., using the above parameter values. The NMSTP

---

[1] In this chapter we use $I_\mathrm{S}(t) \equiv I_1(t)$ for clarity, see also Section 5.2.2.

Table 5.1: Parameters and their values, which are fixed throughout this work, if not stated differently.

Symbol	Description	Value
Δ	Width of Lorentzian	0.5
$\bar{\eta}$	Centre of Lorentzian	-1.7
J	Synaptic weight	30
U_0	Baseline utilization	0.1
τ_m	Membrane time constant	20 ms
τ_d	Depression timescale	200 ms/τ_m
τ_f	Facilitation timescale	1500 ms/τ_m

Eqs. (5.2) is able to generate periodic oscillations due to plastic synapses even in absence of time dependent forcing (I_1 = const.). Their existence depends on the exact choice of parameters values, one of the important ones being the total non-synaptic current given by $\bar{\eta}+I_1$. Limit cycles can arise via a plethora of bifurcation scenarios. Here we considered the case of a subcritical Hopf bifurcation followed by a fold of limit cycles, giving rise to stable oscillatory behaviour, when considering I_1 as a bifurcation parameter. In Fig. 5.2(a) the resulting bifurcation diagram is displayed.

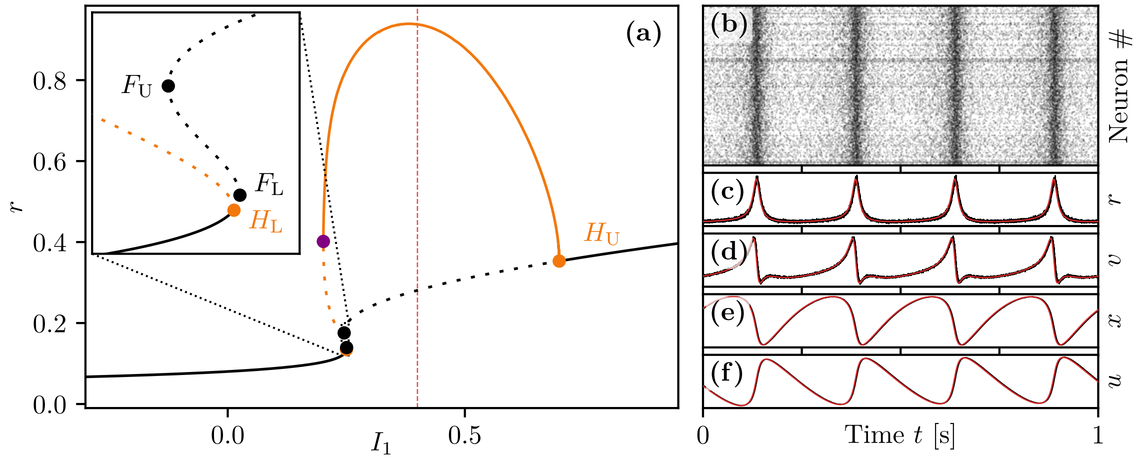

Figure 5.2: Solutions in presence of constant forcing and microscopic network. (a) Bifurcation diagram r versus I_1 of Eqs. (5.2). For $I_1 \lesssim 0.25$ there exists only one fixed point (FP, solid black line). At $I_1 \approx 0.25$ the FP destabilizes via a subcritical Hopf-Bifurcation (H_L, lower orange dot), creating a branch of unstable limit cycles (LC, orange dashed line). Two saddle-node bifurcations (black dots) of the unstable FP branch (dashed black line) occur in a narrow regime of I_1, folding the branch twice. Stability is regained for $I_1 \gtrsim 0.7$ at a supercritical Hopf-Bifurcation (H_U, upper orange dot). The branch of unstable LCs stabilizes (solid orange line) via a saddle-node bifurcation of cycles (purple dot) and vanishes at the second Hopf Bifurcation. The orange line marks the maximum firing rates of the LC branch. **(b)** Spike scatter plot for 20000 representative neurons of a network consisting of $N = 100000$ neurons for $I_1 = 0.4$ marked in panel a by a dashed red line. **(c - f)** Periodic solution $(r(t), v(t), x(t), u(t))$ vs. time t for $I_1 = 0.4$ marked in panel a by a dashed red line. The red curves show simulations results of the NMSTP, the black ones of the network Eqs. (5.1).

For currents $I_1 \lesssim 0.25$ we find a branch of stable node equilibria at low firing rates. The branch develops into a family of foci and destabilizes around $I_1 \approx 0.25$ via a subcritical Hopf bifurcation (H_L) followed by two saddle-node (fold) bifurcation at F_L and F_U (black dots), where $F_k = (r_k, v_k, x_k, u_k, I_k), \quad k \in \{\mathrm{L}, \mathrm{U}\}$, denotes the equilibrium and parameter values of the bifurcations. These folds can also be found in absence of STP, in which case the upper branch is stable. However, in Fig. 5.2(a) the instability persists throughout the S-shaped curve up until the upper supercritical Hopf bifurcation H_{U}. The lower Hopf bifurcation H_{L} generates a family of unstable limit cycles that undergoes a fold bifurcation of cycles, giving rise to stable periodic solutions.

One of these solutions $(r(t), v(t), x(t), u(t))$ is presented in Fig. 5.2(c - f) as a function of time. It is superimposed onto the corresponding variables calculated by simulating a QIF network governed by Eqs. (5.1) and consisting of $N = 100000$ neurons. A spike scatter plot can be found in Fig. 5.2(b) for this network. The average firing rate is estimated via binning of time, i.e, by counting the number of spikes per time bin of width $\Delta t = 10^{-2}$, while the average membrane potential reads $v(t) = \frac{1}{N}\sum_{j=1}^{N} V_j(t)$.

The primary mechanism driving the oscillations is an interplay of PBs[2] and the ensuing synaptic depression and facilitation. At the microscopic scale, population bursts are emitted via a cascade of spikes throughout the network, which as a consequence leads to the facilitation of synapses, leveraging the firing activity further; see Fig. 5.2(b, c, f). The consequent depression suppresses the activity, but recovers on the timescale τ_{d} allowing for the emittance of population bursts in a periodic manner.

Notably, in the I_1-interval depicted in the inset of Fig. 5.2(a) we find bistability between equilibria and limit cycles. We can therefore predict that a time dependent slow current $I_1(t)$ evolving across this region will lead to a dynamic transition from the equilibrium branch to the stable limit cycles, giving rise to bursting. This exact example can be found in Fig. 5.1.

Overall, in contrast to the QIF network without STP and original MPR model, where no limit cycles exist, STP gives rise to bistability among equilibria and cycles. In Ref. [16] a slow periodic currents leads to the emergence of macroscopic relaxation-type oscillations in the network. We want to investigate how the presence of STP impacts the response of the system towards such an input. Simulations of QIF networks are difficult computationally. However, the expected agreement of QIF network results and the NMSTP depicted in Fig. 5.2(b - f) justifies to perform the upcoming analysis using solely the NMSTP. We will return to the implications of the NMSTP dynamics for the network in Section 5.6.

5.2.2 Dynamics under slow periodic forcing

Owing to the previous observations in the system with constant forcing, we will introduce a slow periodic drive into the model via the external current I_1. We impose that it evolves periodically and on a timescale considerably larger than the slowest timescale of the neural mass, namely the facilitation decay time τ_{f}. In order to remain in a general framework, $I_1(t)$ will be sinusoidal, given by $I_1(t) = A\sin(\varepsilon t)$, with period $T = \frac{2\pi}{\varepsilon} \gg \tau_{\mathrm{f}}$ and amplitude A. Throughout this work we set $\tau_{\mathrm{f}} = 1500\,\mathrm{ms}/\tau_{\mathrm{m}} = 75$, therefore the separation between forcing and slowest intrinsic timescale of the fast subsystem is calculated as $\tau_{\mathrm{f}}/T = \varepsilon\frac{\tau_{\mathrm{f}}}{2\pi} \approx 10\varepsilon$.

Through the choice of I_1 to be explicitly time dependent, the system given in Eqs. (5.2) becomes non-autonomous. This in turn comes along with hurdles in the application of slow-fast dissection. Thus, in order to retrieve an autonomous system, a second forcing variable I_2 is introduced. The dynamics of (I_1, I_2) follows a Hopf normal form as given below.

$$\dot{I}_1 = \varepsilon g_1(I_1, I_2) = \varepsilon\left[I_1(a - I_1^2 - I_2^2) + I_2\right] \tag{5.3a}$$

$$\dot{I}_2 = \varepsilon g_2(I_1, I_2) = \varepsilon\left[I_2(a - I_1^2 - I_2^2) - I_1\right] \tag{5.3b}$$

---

[2] Population bursts are not related to *bursting* in the slow-fast dynamics sense.

The Hopf bifurcation at $a = 0$ gives rise to stable limit cycles of the form $(I_1, I_2) = A\cdot(\sin \varepsilon t, \cos \varepsilon t)$, with amplitude $A = \sqrt{a}$ and angular frequency ε, in the following referred to as *forcing cycle*. To assure equivalence of the explicitly defined $I_1(t) = A \sin(\varepsilon t)$ and the one generated by the Hopf form Eq. (5.3), the initial conditions $((I_1(t_0), I_2(t_0))$ will lie on $(I_1, I_2) = A \cdot (\sin \varepsilon t, \cos \varepsilon t)$. According to the definition in Section 2.7 of Chapter 2, the *full system* is given by the NMSTP in presence of slow external forcing, i.e, Eqs. (5.2) and Eq. (5.3).

To understand the impact of this slow forcing, it is advantageous to superimpose solutions of the full problem on the r vs. I_1 bifurcation diagram of the unforced system, this is at the core of the slow-fast dissection introduced by J. Rinzel [64, 65, 313]. In Fig. 5.3 we present solutions of Eqs. (5.2) and Eq. (5.3) for different values of the forcing amplitude A. An example of a purely slow trajectory is shown in Fig. 5.3(a$_1$ - c$_1$) and labeled $\gamma_0(t)$. The firing rate $r(t)$ [Fig. 5.3(b$_1$)], increases and decreases following the same pattern as the forcing $I_1(t)$ [Fig. 5.3(a$_1$)]. Moreover, in $r - I_1$ projection [Fig. 5.3(c$_1$)], it becomes clear that the dynamics takes place nearby the equilibrium branch of the unforced system. The forcing introduces a drift of the equilibrium, slow enough to be followed by the dynamics in an $\mathcal{O}(\varepsilon)$ neighbourhood of the branch.

While this example can be understood as a quasi-static motion, the more complex solutions $\gamma_1(t)$ to $\gamma_4(t)$ in columns (2) and (3) of Fig. 5.3, exhibit canard dynamics and bursting, respectively. A more rigorous analysis is required, including a slow-fast dissection of the model. For this we apply the framework introduced in Section 2.7 of Chapter 2 to the NMSTP.

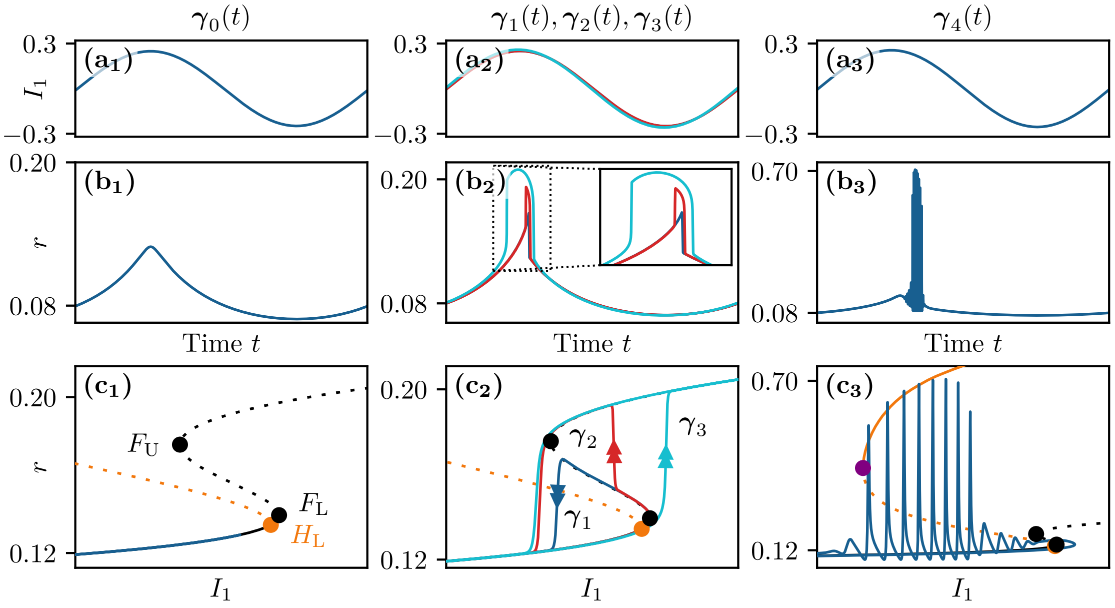

Figure 5.3: Typical solutions $\gamma_0(t)$ to $\gamma_4(t)$ of the full system. **(a)** Periodic forcing current $I_1(t)$ and **(b)** firing rate $r(t)$ vs. time t. **(c)** Same trajectories superimposed on the bifurcation diagram of the unforced system in r-I_1 projection. The parameter values are as follows: $\varepsilon = 10^{-5}$; γ_0: $A \approx 0.2487$; γ_1 to γ_3: in increasing order exponentially close to $A \approx 0.2507$; γ_4: $\varepsilon = 10^{-3}$, $A \approx 0.2553$.

5.3 Slow-fast analysis of the model

We will start a systematic investigation of the full system by dissecting it into slow and fast subsystem. The full problem represents a 4-fast 2-slow system with $\mathbf{X}_\text{f} = (r, v, x, u)$

and $\mathbf{X}_\mathrm{s} = (I_1, I_2)$. Their dynamics is governed by the right hand sides $\mathbf{F}(\mathbf{X}_\mathrm{f}, \mathbf{X}_\mathrm{s})$ and $\mathbf{G}(\mathbf{X}_\mathrm{s})$, recalled below in fast-time parametrization.

$$\dot{\mathbf{X}}_\mathrm{f} = \mathbf{F}(\mathbf{X}_\mathrm{f}, \mathbf{X}_\mathrm{s}) = \begin{pmatrix} \frac{\Delta}{\pi} + 2rv \\ v^2 + Juxr - (\pi r)^2 + I_1 \\ (1-x)/\tau_\mathrm{d} - uxr \\ (U_0 - u)/\tau_\mathrm{f} + U_0(1-u)r \end{pmatrix} \tag{5.4a}$$

$$\dot{\mathbf{X}}_\mathrm{s} = \varepsilon \mathbf{G}(\mathbf{X}_\mathrm{s}) = \varepsilon \begin{pmatrix} (I_1(a - I_1^2 - I_2^2) + I_2) \\ (I_2(a - I_1^2 - I_2^2) - I_1) \end{pmatrix} \tag{5.4b}$$

In the singular limit $\varepsilon \to 0$ associated with Eqs. (5.4) we obtain the fast subsystem given in Eqs. (5.5).

$$\dot{\mathbf{X}}_\mathrm{f} = \mathbf{F}(\mathbf{X}_\mathrm{f}, \mathbf{X}_\mathrm{s}) \tag{5.5a}$$

$$\dot{\mathbf{X}}_\mathrm{s} = \mathbf{0} \tag{5.5b}$$

Its equilibrium branches are shown in Fig. 5.2(a) and defined as $\{\mathbf{X}_\mathrm{f} | \dot{\mathbf{X}}_\mathrm{f} = 0\}$, with the slow variable coordinates acting as bifurcation parameters. This naturally coincides with the definition Eq. (5.6) of the critical manifold S_0.

$$\mathbf{F}(\mathbf{X}_\mathrm{f}, \mathbf{X}_\mathrm{s}) = \mathbf{0} \tag{5.6}$$

We can therefore already infer the shape of S_0. It corresponds to the cartersian product $S^* \times \{I_2 | I_2 \in \mathbb{R}\}$, where S^* denotes the S-shaped branch of equilibria of the fast subsystem and is given in Eq. (5.7).

$$S^* := \{(r, v, x, u, I_1) | \mathbf{F}(\mathbf{X}_\mathrm{f}, \mathbf{X}_\mathrm{s}) = \mathbf{0}\} \tag{5.7}$$

Hence the associated fold set $\mathcal{F}$ has two 1D connected components, namely the two lines $\mathcal{F}_\mathrm{U} := \{F_\mathrm{U}\} \times \{I_2 | I_2 \in \mathbb{R}\}$ and $\mathcal{F}_\mathrm{L} := \{F_\mathrm{L}\} \times \{I_2 | I_2 \in \mathbb{R}\}$. This means that the two fold lines are parametrized by I_2. These two fold lines of S_0, along $\mathcal{F}_\mathrm{L}$ and $\mathcal{F}_\mathrm{U}$, can be seen in Fig. 5.4, together with the critical manifold S_0 in I_1-I_2-r projection and the trajectories $\gamma_0(t)$ to $\gamma_4(t)$ of Fig. 5.3.

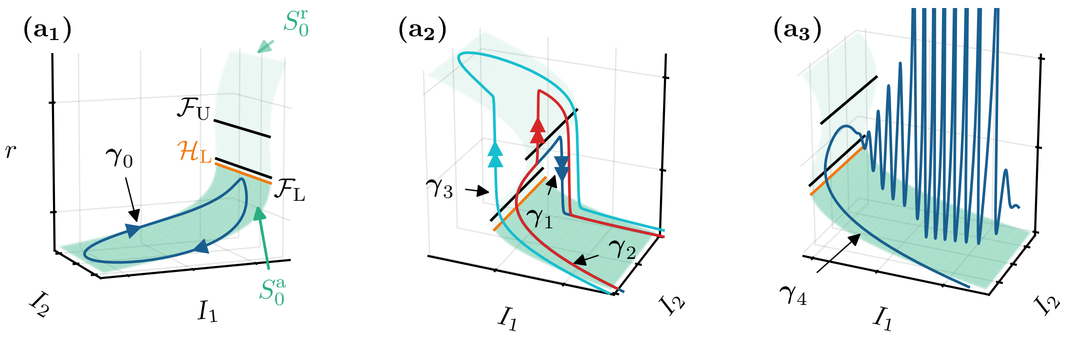

Figure 5.4: Slow-fast dissection and critical manifold. Solutions $\gamma_0(t)$ to $\gamma_4(t)$ of the full system superimposed on the critical manifold S_0 in (I_1, I_2, r)-space. The parameter values are identical to those in Fig. 5.3.

5.3.1 Singular dynamics: fast subsystem

Since points of S_0 are equilibria of the fast subsystem, we can associate local stability properties of the fast subsystem with the critical manifold. Stable (unstable) parts of the equilibrium branch in Fig. 5.2 will become attracting (repelling) sheets of the critical manifold. This property can be seen as an indicator for fast flow in the full system, distant from S_0. Here the fast dynamics dominates and (r, v, x, u) will be repelled and attracted accordingly. The stability changes along the set of Hopf bifurcation given by $\mathcal{H}_\mathrm{L} := \{H_\mathrm{L}\} \times \{I_2 | I_2 \in \mathbb{R}\}$ and $\mathcal{H}_\mathrm{U} := \{H_\mathrm{U}\} \times \{I_2 | I_2 \in \mathbb{R}\}$. Attracting (repelling) parts of S_0 are marked as green (light green) surfaces throughout this chapter, as can be seen in Fig. 5.4.

We can already exploit this in order to examine the full system dynamics further. To start with, $\boldsymbol{\gamma}_0(t)$ in Fig. 5.4(a$_1$) evolves entirely in the vicinity of the lower attracting sheet of the critical manifold S_0. This means that the dynamics is purely slow and in approximation bounded to S_0. For $\boldsymbol{\gamma}_1(t)$ we see the typical canard dynamics, since it follows the middle repelling part of S_0 for some time, before jumping to the bottom attracting sheet. Moreover, $\boldsymbol{\gamma}_2(t)$ in Fig. 5.4(a$_2$) resembles the behavior of a canard with a head, introduced in Section 2.7.2 of Chapter 2 in the context of the VdP oscillator. However, while in the VdP system the upper branch of the fast subsystem is attracting, we find the same behavior here, but with a repelling upper sheet of S_0. We will refer to this surprising solution of the full system as *jump-on* canard. Similarly, $\boldsymbol{\gamma}_3(t)$ exhibits a jump to the upper sheet, but in absence of a canard segment along the middle sheet. Finally, the bursting solution $\boldsymbol{\gamma}_4(t)$ in Fig. 5.4(a$_3$) has segments along the bottom sheet of S_0 and displays a short canard segment along the repelling middle sheet, before it pierces through the critical manifold S_0 and starts to burst. In order to understand the emergence of canards, jump-on canards and bursting, we will proceed with the analysis of the slow subsystem in the following.

5.3.2 Singular dynamics: slow subsystem

The slow-time parametrization[3] of Eqs. (5.4) is given in Eqs. (5.8).

$$\varepsilon \mathbf{X}_\mathrm{f}' = \mathbf{F}(\mathbf{X}_\mathrm{f}, \mathbf{X}_\mathrm{s}) \tag{5.8a}$$

$$\mathbf{X}_\mathrm{s}' = \mathbf{G}(\mathbf{X}_\mathrm{s}). \tag{5.8b}$$

Here the singular limit $\varepsilon \to 0$ yields the slow subsystem Eqs. (5.9), which has the critical manifold S_0 as the state space, as can be seen from $\mathbf{F}(\mathbf{X}_\mathrm{f}, \mathbf{X}_\mathrm{s}) = \mathbf{0}$.

$$\mathbf{0} = \mathbf{F}(\mathbf{X}_\mathrm{f}, \mathbf{X}_\mathrm{s}) \tag{5.9a}$$

$$\mathbf{X}_\mathrm{s}' = \mathbf{G}(\mathbf{X}_\mathrm{s}) \tag{5.9b}$$

Slow flow

As part of the slow-fast dissection of the model it is useful to calculate the slow flow Eq. (5.10) of the dissected system, which was derived in Section 2.7.1.

$$\frac{\mathrm{d}\mathbf{X}_\mathrm{f}}{\mathrm{d}\tau} \equiv \mathbf{X}_\mathrm{f}' = -\left(\frac{\partial \mathbf{F}}{\partial \mathbf{X}_\mathrm{f}}\right)^{-1} \left(\frac{\partial \mathbf{F}}{\partial \mathbf{X}_\mathrm{s}} \mathbf{X}_\mathrm{s}'\right) \tag{5.10}$$

To recall, values of $\mathbf{X}_\mathrm{f}$ on S_0 are determined via the algebraic conditions Eq. (5.9a), which entangle the fast variables to each other and to I_1. Given either r, v, x or u, the other

---

[3] The derivative with respect to slow time τ is denoted by $(\_)' := \mathrm{d}/\mathrm{d}\tau(\_) = \frac{1}{\varepsilon}(\dot{\_})$.

components can be calculated straightforwardly. In other words, it is sufficient to consider the slow flow of one the fast variables, here r, to understand the slow dynamics. Taken this into account we finally obtain the slow flow (r', I_1', I_2') given in Eqs. (5.11) and with g_1, g_2 from Eq. (5.3).

$$r' = g_1(I_1, I_2) A r (1 + r u \tau_\mathrm{d})(1 + r U_0 \tau_\mathrm{f})/D \tag{5.11a}$$

$$I_1' = g_1(I_1, I_2) \tag{5.11b}$$

$$I_2' = g_2(I_1, I_2) \tag{5.11c}$$

We can see the relevance of the denominator D, given in Eq. (5.12), by noting that $D = 0$ defines the fold set of S_0 at which the fast subsystem Jacobian $\frac{\partial \mathbf{F}}{\partial \mathbf{X}_\mathrm{f}}$ is singular.

$$D = 2\left[(\pi r)^2 + v^2\right](r\tau_\mathrm{d} u + 1)(r\tau_\mathrm{f} U_0 + 1) - Jxr(r\tau_\mathrm{f} U_0 + u) \tag{5.12}$$

Saddle-node bifurcations of the fast subsystem are characterized by the identical condition $\det\left(\frac{\partial \mathbf{F}}{\partial \mathbf{X}_\mathrm{f}}\right) = 0$ and are equivalent to the fold curves $\mathcal{F}_\mathrm{L}$ and $\mathcal{F}_\mathrm{U}$ shown in Fig. 5.4. Therefore, the slow flow is undefined along these lines and the slow subsystem fails to describe the slow dynamics. This is for example relevant for the canard trajectories $\gamma_1(t)$ and $\gamma_2(t)$ in Figs. 5.3 and 5.4, which projected onto the (r, I_2) plane cross $\mathcal{F}_\mathrm{L}$ transversely.

Desingularization

This limitation can be mitigated by introducing an auxiliary system and desingularizing Eqs. (5.11) through the application of a nonlinear time rescaling $\tau \mapsto D \cdot \tau$. One obtains the *desingularized reduced system* (DRS) given in Eqs. (5.13) with $\hat{\tau} := D\tau$.

$$\frac{\mathrm{d}r}{\mathrm{d}\hat{\tau}} = g_1(I_1, I_2) A r (1 + r u \tau_\mathrm{d})(1 + r U_0 \tau_\mathrm{f}) \tag{5.13a}$$

$$\frac{\mathrm{d}I_1}{\mathrm{d}\hat{\tau}} = g_1(I_1, I_2) \cdot D \tag{5.13b}$$

$$\frac{\mathrm{d}I_2}{\mathrm{d}\hat{\tau}} = g_2(I_1, I_2) \cdot D \tag{5.13c}$$

The DRS benefits from the fact that the singularities are resolved, allowing to investigate the slow dynamics near and on the fold lines $\mathcal{F}_\mathrm{L}$ and $\mathcal{F}_\mathrm{U}$. At the same time new equilibria are introduced satisfying $D = 0$. Additionally, as a consequence of the employed non-linear time rescaling, the flow direction is not preserved. At the fold curves, with $D = 0$, a change of sign of D takes place. Hence, between $\mathcal{F}_\mathrm{L}$ and $\mathcal{F}_\mathrm{U}$, i.e, on the middle sheet of S_0, the flow of the DRS is opposite to the slow flow.

Slow trajectories which entirely remain on the same sheet of S_0 can be easily understood using the slow flow Eqs. (5.11). Canard orbits evolve on attracting as well as repelling sheets of S_0 and therefore require a view on the dynamics near the folds. For this, we will determine the equilibria of the DRS Eqs. (5.13) in the following and analyze their invariant manifolds. Equilibria of the DRS which satisfy $D = 0$ necessarily coincide with a fold of S_0. As we will show in the following section, this gives rise to so-called *folded singularities*.

Folded saddle and folded homoclinics

Up to three focus equilibria of Eqs. (5.13) are located at $p_1 = (I_1, I_2, r) = (0, 0, r_k)$, where the r_k are points of S_0 given $(I_1, I_2) = (0, 0)$. In this chapter we will remain at $\bar{\eta}$ values for which only one equilibrium $p_0 = (0, 0, r_0)$ exists. This point is the only equilibrium of the slow flow Eqs. (5.11). In the DRS [Eqs. (5.13)] however, the condition $\{g_1(I_1, I_2) = 0, D = 0\}$ yields additional fixed points p_1 and p_2 located on the fold lines at $D = 0$.

The three equilibria of the DRS are displayed in Fig. 5.5(a) on S_0 in $r - I_2$ projection. In the full system, for sufficiently small A and ε, solutions lie close to the bottom, attracting, sheet of S_0. When the amplitude is increased, these cycles can pass very close to p_1 and start to follow the middle, repelling sheet. One way to understand this canard dynamics is to make use of the properties of the p_k in the DRS and their role for the slow subsystem.

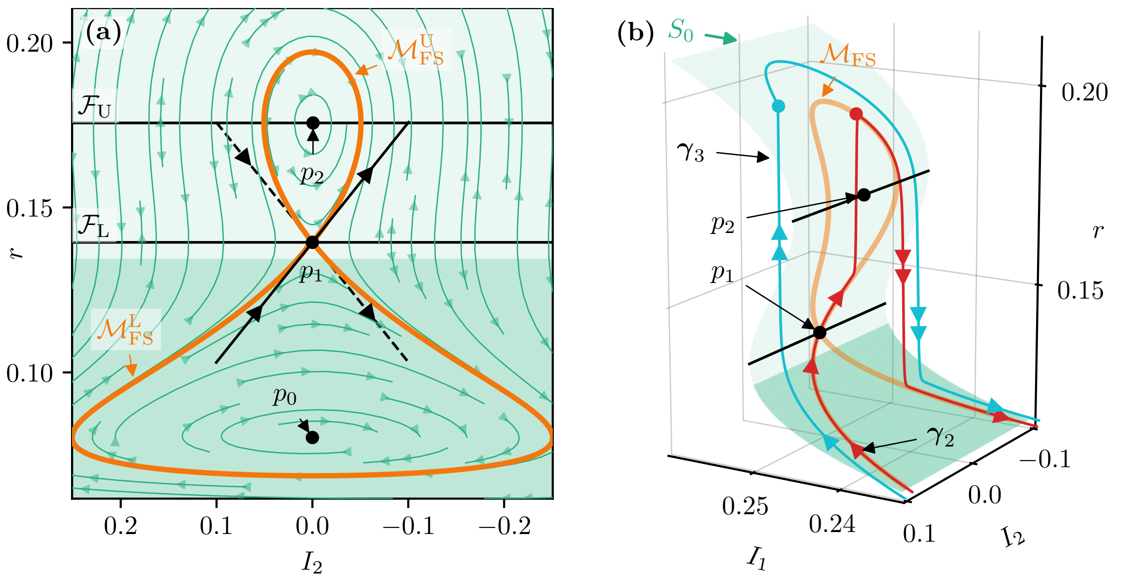

Figure 5.5: Folded-saddle singularity. (a) Critical manifold S_0 in $r - I_2$ projection superimposed with the slow flow [green arrows, see Eqs. (5.11)]. The black dots p_0 (unstable focus), p_1 (saddle), p_2 (center) denote equilibria of the DRS [Eqs. (5.13)]. The point p_1 denotes a folded-saddle equilibrium with the associated stable (unstable) eigendirection indicated by a solid (dashed) arrow along the slow flow. The orange curves $\mathcal{M}_\mathrm{FS}$ mark the stable and unstable manifolds of p_1, forming heteroclinic connections through p_1. **(b)** S_0 in (I_1, I_2, r)-space. The curves $\gamma_2(t)$ and $\gamma_3(t)$ are solutions of the full system. The objects p_1, p_2 and $\mathcal{M}_\mathrm{FS}$ depend on the choice of A, here they correspond to the value used to obtain $\gamma_3(t)$. Other parameters values are as in Figs. 5.3 and 5.4.

Located on the bottom sheet of S_0, p_0 results from the Hopf form given in Eq. (5.3) and is an unstable focus at $(I_1, I_2) = (0, 0)$. On the other hand, p_2 lies on the upper fold line $\mathcal{F}_\mathrm{U}$ and denotes a center, i.e., it has purely imaginary complex conjugate eigenvalues. The equilibrium p_1 can be found on the lower fold line $\mathcal{F}_\mathrm{L}$ and is of saddle type. At a specific value of A, namely, when the forcing cycle intersects with p_1, an 8-shaped double homoclinic connection $\mathcal{M}_\mathrm{FS} = \mathcal{M}_\mathrm{FS}^\mathrm{L} \cup \mathcal{M}_\mathrm{FS}^\mathrm{U}$ forms, consisting of two parts, which are connected via p_1; see the orange curve in Fig. 5.5(a, b). The connection $\mathcal{M}_\mathrm{FS}^\mathrm{L}$ is located on the lower sheet, while $\mathcal{M}_\mathrm{FS}^\mathrm{U}$ spans the middle and upper sheet of S_0. They revolve around the unstable focus p_0 and center p_2, respectively, and are the stable and unstable manifolds of p_1.

The points p_2, p_1, and in particular the invariant manifolds associated with p_1, play an important role for the slow subsystem. Due to the negative sign $D < 0$ on the middle sheet of S_0 the slow flow is reversed with respect to the DRS. As a consequence the DRS saddle p_1 and center p_2 become folded singularities of the slow subsystem. These *folded saddle* (p_1) and *folded center* (p_2) are not equilibria of the slow flow. However, for the slow dynamics they have similar impact on the dynamics as there unfolded counterparts, but with the crucial difference of reversed flow direction between $\mathcal{F}_\mathrm{L}$ and $\mathcal{F}_\mathrm{U}$. Accordingly, the folded saddle p_1 has significant influence on the dynamics of the slow subsystem along $\mathcal{M}_{\mathrm{FS}}$, as described in the following.

(i) First of all, trajectories in the DRS evolving on $\mathcal{M}_{\mathrm{FS}}$ necessarily approach p_1 asymptotically from the direction of the stable eigenvector, but can never pass through the saddle.

(ii) In the slow subsystem however, the folded saddle p_1 allows a pass-through along this direction. Below $\mathcal{F}_{\mathrm{L}}$ trajectories are attracted to and above repelled from p_1.

(iii) The double homoclinic connection $\mathcal{M}_{\mathrm{FS}}$ of the DRS is referred to as a *folded homoclinic* in the slow subsystem. For this solution the passage of trajectories through p_1 occurs in finite time [317].

(iv) Using the same type of argument, the invariant manifold $\mathcal{M}_{\mathrm{FS}}^{\mathrm{U}}$ around the folded center p_2 becomes disconnected at the two intersections with $\mathcal{F}_{\mathrm{U}}$, due to a reversal of the slow flow direction. Solutions of the slow subsystem on $\mathcal{M}_{\mathrm{FS}}^{\mathrm{U}}$ can not cross this line.

As a consequence of the previous properties (i)-(iv), a singular canard exists in the slow subsystem, given a specific value of A. It evolves along the folded homoclinic $\mathcal{M}_{\mathrm{FS}}$ below the bottom fold line $\mathcal{F}_{\mathrm{L}}$ and extends, while remaining on S_0, beyond the folded saddle p_1 until the upper fold $\mathcal{F}_{\mathrm{U}}$.

Singular canard orbits

For the construction of singular orbits, we note once more that the middle sheet of S_0 is repelling while the bottom sheet is attracting. Accordingly, a continuum of fast segments emerging from the middle sheet and connecting to the bottom sheet exist in the fast subsystem. This family of fast orbits collides with $\mathcal{M}_{\mathrm{FS}}$ and likewise with the singular canard described above. As a result, infinitely many singular orbits can be constructed, by merging the singular canard at arbitrary positions on the middle sheet of S_0, with fast segments.

These singular orbits evolve on the bottom sheet of S_0, continue through the folded saddle p_1, while following the folded homoclinic, and jump at different heights, in terms of the coordinate r, from the middle to the bottom sheet of S_0. The full system solution $\gamma_1(t)$ in Figs. 5.3 and 5.4 displays this type of dynamics. The singular canard, hence also the family of singular canard orbits, can at most reach the upper fold line F_{U}. Here the slow flow is undefined and the reduction of state space to S_0 fails to describe the dynamics. This is additionally reflected by the fact that $\mathcal{M}_{\mathrm{FS}}^{\mathrm{U}}$ is disconnected at the intersections with $\mathcal{F}_{\mathrm{U}}$, due to the folded property of p_2; see (iv) above. The singular canard orbit which reaches up until this point is the maximal canard.

5.4 Full system dynamics: beyond singular orbits and classical canards

The solutions $\gamma_0(t)$ to $\gamma_4(t)$ are results of numerical computations for $\varepsilon > 0$. As such, their slow segments evolve not on, but in an $\mathcal{O}(\varepsilon)$ neighborhood of S_0. This is to some extent an implication of Fenichel's theory [318]. For $0 < \varepsilon \ll 1$, it guarantees the existence of a *slow manifold* S_ε, that is in an $\mathcal{O}(\varepsilon)$ neighborhood of S_0, if S_0 is *normally hyperbolic* (see below). Additionally, S_ε is locally invariant under the flow of the full system. The theorem also states that stable and unstable manifolds associated to S_0 persist as $\mathcal{O}(\varepsilon)$

perturbations. In other words, the flow on S_ε can be seen as a perturbation of the flow on S_0; and the flow perpendicular to S_0 as a perturbation of the fast subsystem's flow. For normally hyperbolic critical manifolds, one can deduce that singular orbits persist for ε and perturb into an $\mathcal{O}(\varepsilon)$ neighborhood.

Normal hyperbolicity requires all eigenvalues of the Jacobian $\frac{\partial \mathbf{F}}{\partial \mathbf{X}_\mathrm{f}}|_{S_0}$ to have non-zero real part [319]. The theorem can therefore not be applied on $\mathcal{F}_\mathrm{L}$ and $\mathcal{F}_\mathrm{U}$, given that they describe lines of saddle-node bifurcations. However, one can consider the three sheets of S_0 separately, each one up to an $\mathcal{O}(\varepsilon)$ neighborhood of the folds. From this we can conclude the persistence of slow segments nearby S_0 for $\varepsilon > 0$, including the repelling segments within a canard solution, until close to the folds. Fenichel's theory does not encompass whether or not a connection of these segments exists. Yet, $\gamma_1(t)$ to $\gamma_3(t)$ exemplify such connection numerically: segments that evolve close to the bottom sheet of S_0 connect to segments close the middle sheet. A detailed treatment of these connections nearby the non-hyperbolic points, exceeds the scope of this work. For more rigorous approaches, we refer to non-standard analysis [66], matched asymptotics [320] and so-called blow-up techniques [321]. With these advanced methods, it is possible to show that orbits with canard segments of different length perturb at different parameter values within an exponentially narrow regime, thus leading to the canard explosion in the full system.

5.4.1 Jump-on canards

The construction of singular canard orbits linked with Fenichel's theorem explains the dynamics of $\gamma_1(t)$ in Figs. 5.3 and 5.4, where the forcing amplitude A is large enough to surpass the lower Hopf bifurcation H_L and the lower fold F_L. *Headless* canards, like this one, have a jump to the bottom branch in common. Slow-fast systems may also have canard solutions with a head. They usually appear in systems, which have two folds: the first one destabilizing, the second one stabilizing the branch. Headed canards jump onto this stable upper part. In 3D systems with an 1D or 2D S-shaped critical manifold, the upper sheet is typically unstable near the upper fold, thus preventing the existence of headed canards. Instead, past the maximal canard, fast oscillations related to the existence of limit cycles develop and lead to bursting solutions; see Section 5.5.

The trajectory $\gamma_2(t)$ in Figs. 5.3 and 5.4 has the characteristic dynamics of a headed canard. However, it is peculiar for various reasons. First of all, we can classify this type of dynamics as *jump-on canard*, since the trajectory lands (after the fast jump) on a seemingly repelling slow manifold. Moreover, the jump-on dynamics can occur after a regular canard segment, as for γ_2 or independent of that, like for γ_3. As a matter of fact, trajectories of the latter type resemble relaxation oscillations, like in VdP, despite the repelling upper sheet of S_0. This has an additional consequence: for small enough ε a continuous transition from subthreshold oscillations to bursting is blocked by jump-on canards. The fact that fast oscillations other than relaxation oscillations are absent beyond the maximal canard are novel and unexpected phenomena. In the following we will address how these solutions emerge. Their impact on the route towards bursting is discussed in details in Section 5.5.3.

The two solutions $\gamma_2(t)$ and $\gamma_3(t)$ are shown in Fig. 5.5(b) and Fig. 5.6 using two different projections. They exemplify two types of jump-on canards, that have an approach towards globally repelling equilibria of the fast subsystem in common. The cyan solution γ_3 represents an orbit which does not interact with the folded saddle p_1. It slowly evolves on the lower sheet of S_0, crosses the curve of Hopf bifurcations $\mathcal{H}_\mathrm{L}$ and reaches the lower fold curve $\mathcal{F}_\mathrm{L}$ at which the slow subsystem is singular. Fast dynamics come into play and expectedly the dynamics will approach attractors of the fast subsystem. Such attractors for the considered I_1 value at which the curve escapes S_0 are solely the stable limit cycles displayed in Fig. 5.2(a). Instead of entering a period of bursting, the cyan trajectories approaches the upper branch of unstable equilibria. As soon as it jumps onto on S_0, the slow subsystem becomes a valid limit anew and the curve remains on S_0 until it reaches $\mathcal{F}_\mathrm{U}$, where it jumps down to the stable sheet.

In the second case, $\boldsymbol{\gamma}_2$ in Fig. 5.5(b) and Fig. 5.6, the orbit possesses a canard segment and jumps from the repelling middle sheet to the repelling upper sheet of S_0. Similar to the previous case, it evolves on S_0 until $\mathcal{F}_\mathrm{U}$ and finally jumps down. The global motion is identical to that of a canard with a head in VdP.

Multiple elements of these singular cycles have to be understood. First of all, both cases have a similar slow segment in common, namely the part of the trajectory on the upper sheet of S_0. They can be approximated by solutions of the reduced problem Eqs. (2.51) and are enforced by the presence of p_2, around which the trajectory evolves. Since the center p_2 is folded, full rotations around it are not possible and the slow parts terminate at $\mathcal{F}_\mathrm{U}$, where the slow flow is undefined. Here the trajectory can be joined to a fast bit which connects from $\mathcal{F}_\mathrm{U}$ to the attracting sheet of S_0. After this part, the dynamics on S_0 is again governed by the slow subsystem and depending on the forcing amplitude A, the two orbits take different paths. The solution $\boldsymbol{\gamma}_3$ crosses $\mathcal{F}_\mathrm{L}$ far from p_1 and the slow segment on the attracting sheet stops; $\boldsymbol{\gamma}_2$ passes through a neighborhood of p_1 and exhibits canard dynamics before a jump occurs. These parts of the orbits are entirely described within the scope of the slow subsystem.

5.4.2 Nested timescale separation

Understanding the remaining segment that leads $\boldsymbol{\gamma}_2$ and $\boldsymbol{\gamma}_3$ towards the repelling sheet of S_0 requires a more detailed analysis. The mechanism is the same for both cases and will be discussed in the following. Since these pieces of the orbits evolve on the fast timescale we present a visualization of the curves in $I_1 - v - r$ space in Fig. 5.6. In this projection the critical manifold S_0 is shown as a green curve $r(I_1), v(I_1)$ with attracting (repelling) parts as a solid (dashed) line. In the singular limit, the jump-on points $\boldsymbol{\gamma}^*_{2,3} = (r^*_{2,3}, v^*_{2,3}, x^*_{2,3}, u^*_{2,3})$ of the jump-on canard solutions $\boldsymbol{\gamma}_2$ and $\boldsymbol{\gamma}_3$, marked by the red and cyan dots in Fig. 5.6, are of saddle-focus type. Linearization of the dynamics reveals a weakly and strongly attracting direction in a neighborhood of the jump-on points together with a repelling direction with complex conjugate eigenvalues. This suggests a 2D stable manifold leading to $\boldsymbol{\gamma}^*_{2,3}$. We will simplify the problem further by noting that the entire dynamics of jump-on canards takes place close to the surface $\mathcal{M}_{rv}$ defined in Eq. (5.14). On the one hand, for the slow pieces of the curve this observation is as expected, since by definition this conditions holds on S_0.

$$\dot{r} = 0 \Rightarrow r = -\frac{\Delta}{2\pi\tau_\mathrm{m} v} \quad \text{for } v \neq 0 \tag{5.14}$$

On the other hand, also the fast parts of the orbits remain on $\mathcal{M}_{rv}$. This implies a reduction of the fast dynamics to $\mathcal{M}_{rv}$ for the part of state space in which jump-on canards can be found. We will exploit this reduction and investigate a secondary differential-algebraic system resulting from the fast subsystem Eqs. (2.50) in which the flow $\dot{r}$ is equilibrated.

This latter step, without having a complete picture of the time scaling, is analogous to an additional dissection of the fast subsystem. In other words, the full system exhibits three timescales for what concerns jump-on canards: the dynamics of r takes place on a fast, that of (v, x, u) on an intermediate and that of (I_1, I_2) on a slow timescale. The

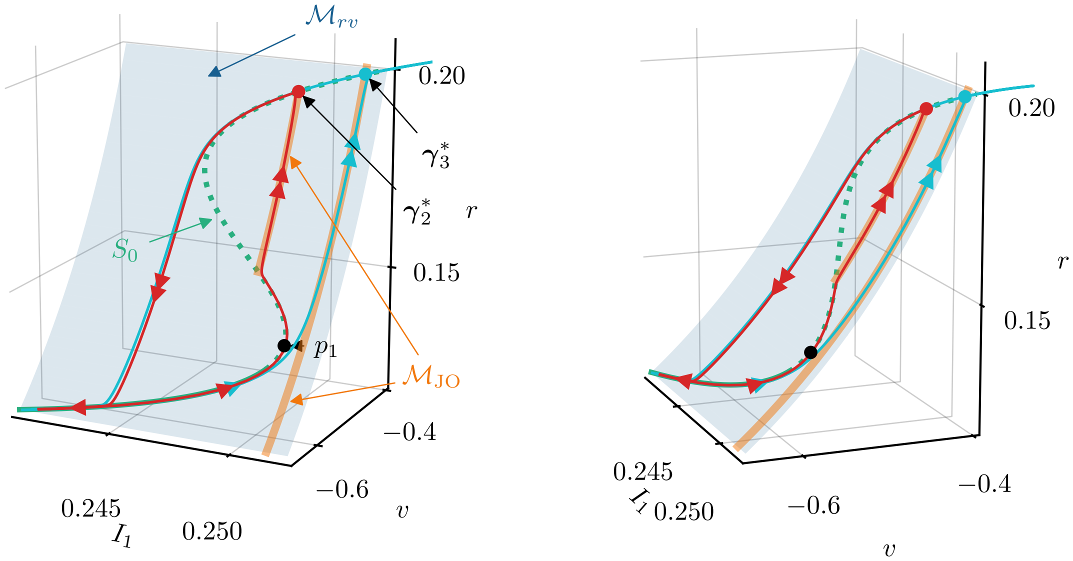

Figure 5.6: Jump-on canards. S_0 in I_1-v-r space (green curve). The blue surface $\mathcal{M}_{rv}$ is defined by $r = -\frac{\Delta}{\pi \tau_{\mathrm{m}} v}$. The curves $\gamma_{2,3}(t)$ are solutions of the full system and their jump-on points $\gamma_{2,3}^*$ on the upper repelling sheet of S_0 are marked by dots. Parameters values are as in Fig. 5.5.

equilibration $\dot{r} = 0$ eliminates the fastest of these scales and approximates the intermediate scale dynamics of jump-on canards, which takes place in the vicinity of $\mathcal{M}_{rv}$.

In this new framework $\mathcal{M}_{rv}$ describes a manifold on which the dynamics of (v, x, u) take place, while I_1, I_2 remain frozen. The jump-on points (v^*, x^*, u^*) [red and cyan dots in Fig. 5.6] are mutual points of $\mathcal{M}_{rv}$ and the upper sheet of S_0. In the reduced problem on $\mathcal{M}_{rv}$, (v^*, x^*, u^*) are of saddle type with eigenvalues $\lambda_1 \gg \lambda_2 \gg -\lambda_3 > 0$ and therefore have associated 1D stable manifolds $\mathcal{M}_{\mathrm{JO}} \subset \mathcal{M}_{rv}$ [orange curves in Fig. 5.6]. They exists for any value of I_1 after the upper fold. For values of I_1 beyond the lower fold, they extend down to $r = 0$. The family of 1D stable manifolds associated with the jump-on points can guide trajectories towards the upper repelling sheet of S_0 and this way leads to the existence of jump-on canards.

So far we have discussed singular orbits, for which the fast segments connect different sheets of the critical manifold S_0. In the case of regular canards, for $\varepsilon > 0$ small enough, these correspond to stable equilibria of the fast subsystem. For jump-on canards they might be unstable, but possess a stable direction, allowing to reach and stay on the repelling sheet of S_0. The main dynamics of these singular orbits takes place on S_0 and does not display phases of fast oscillations, as for bursting solutions, but only single fast jumps.

5.5 Slow-fast transition to bursting: a tale of two routes

Opposed to that, the solution $\gamma_4(t)$ [see Figs. 5.3 and 5.4] and the case initially illustrated in Fig. 5.1 exhibit bursts: a slow segment is followed by fast oscillations. Periodic solutions of the fast subsystem are the underpinning elements of bursting, such that a classification in terms of the fast subsystem's bifurcations appears appropriate. As shown in the bifurcation diagram Fig. 5.2(a), limit cycles originate and terminate at Hopf bifurcations, and change stability at a fold of cycles. Strictly following the classification of Izhikevich, bursting solutions in this system are of subcritical Hopf/fold cycle type. However, the subcritical Hopf bifurcation is closely followed by a fold of the underlying equilibrium branch. Due to a delay effect when surpassing the subcritical Hopf bifurcation [322–324], bursting can effectively be initiated at that fold; see e.g. Fig. 5.7(b_4). We will restrict our analysis to these cases. Here a more aptly description of the bursting type is fold/fold cycle, which corresponds to elliptic bursting in the classification of Rinzel [65].

In order to understand bursting solutions of the full system, we want to remain in the slow-fast dissection. However, the neural mass with STP in presence of periodic forcing turns out to be a peculiar system and numerically difficult to handle. We are constrained by two main factors. First of all, as soon as we leave the singular limit, i.e, for $\varepsilon > 0$, slow segments of trajectories diverge sensitively from the critical manifold. In other words, ε is required to be remarkably small to maintain a good agreement between between full system trajectories and singular orbits. Secondly, numerical simulation as well as numerical continuation of the full system for small enough ε are challenging, since the dynamics appears to be stiff and require high accuracy.

Therefore a clear view on the emergence of bursting can not be gained easily in this framework. For this reason we will provide, additionally to geometrical arguments, numerical evidence on how bursting forms in the present system, either via direct simulation or continuation using the full system. In general, bursts might emerge via a *spike-adding* mechanism, that is, the consecutive addition of spikes into the orbit, when varying a parameter (e.g., the forcing amplitude). For parabolic bursting this spike-adding is mediated by folded-saddle canards [317]; in square-wave bursters on the other hand, passages through a fast-subsystem saddle-homoclinic bifurcation and a folded node determine the number of large-amplitude oscillations in the burst and small-amplitude oscillations before the burst, respectively [325]. In the following, we report the spike-adding mechanism for the NMSTP. At its basis is an interaction of the canards dynamics invoked by the presence of the folded saddle p_1, as well as unexpected torus-canard dynamics. Moreover, we will point out the role of jump-on canards for this spike-adding transition.

5.5.1 Canard explosion and spike-adding

To start with, we consider the case $\varepsilon = 10^{-3}$ and investigate the full system dynamics by performing continuation with the forcing amplitude A as a parameter. We want to stress that this ε value, although very small, proves to be rather distant from the singular limit and slow-fast dissection arguments have to be taken with caution. The initial solution is for an A value corresponding to subthreshold oscillations, like $\boldsymbol{\gamma}_0(t)$ in Figs. 5.3 and 5.4, and is continued towards larger amplitudes.

As a solution measure the L_2-norm of this family is plotted vs. A in Fig. 5.7(a). The first part until $A = A^* \approx 0.25531851205$ is in the subthreshold regime. Around A^* a very sharp transition occurs, resembling a canard explosion. In this transition region the orbits already exhibit first spikes, here defined as the number n_s of local maxima of $r(t)$ for which $r(t) > 0.21$. This is followed up by a series of arches (on the solution branch) at $A > A^*$.

The arches are clearly related to the addition of new spikes to the orbit: with every termination of an arch, by means of a vertical dip of the curve, the number of spikes n_s increases. This behavior can be better observed for larger A, for which each arch is related to the adding of exactly one spike. Prior, the arches lay more dense along A and the spike adding appears to be of more complex nature. Despite the fact that the points of n_s vs. A depend on the choice of the r-threshold for which a spike is counted, it is evident that spikes are added consecutively. It is also clear that these bursting solutions emerge, in a continuous manner, from subthreshold oscillations.

A more detailed view on the full system dynamics near the explosive transition around $A = A^*$ is given in the columns (b - d) of Fig. 5.7. Column b shows the solution in

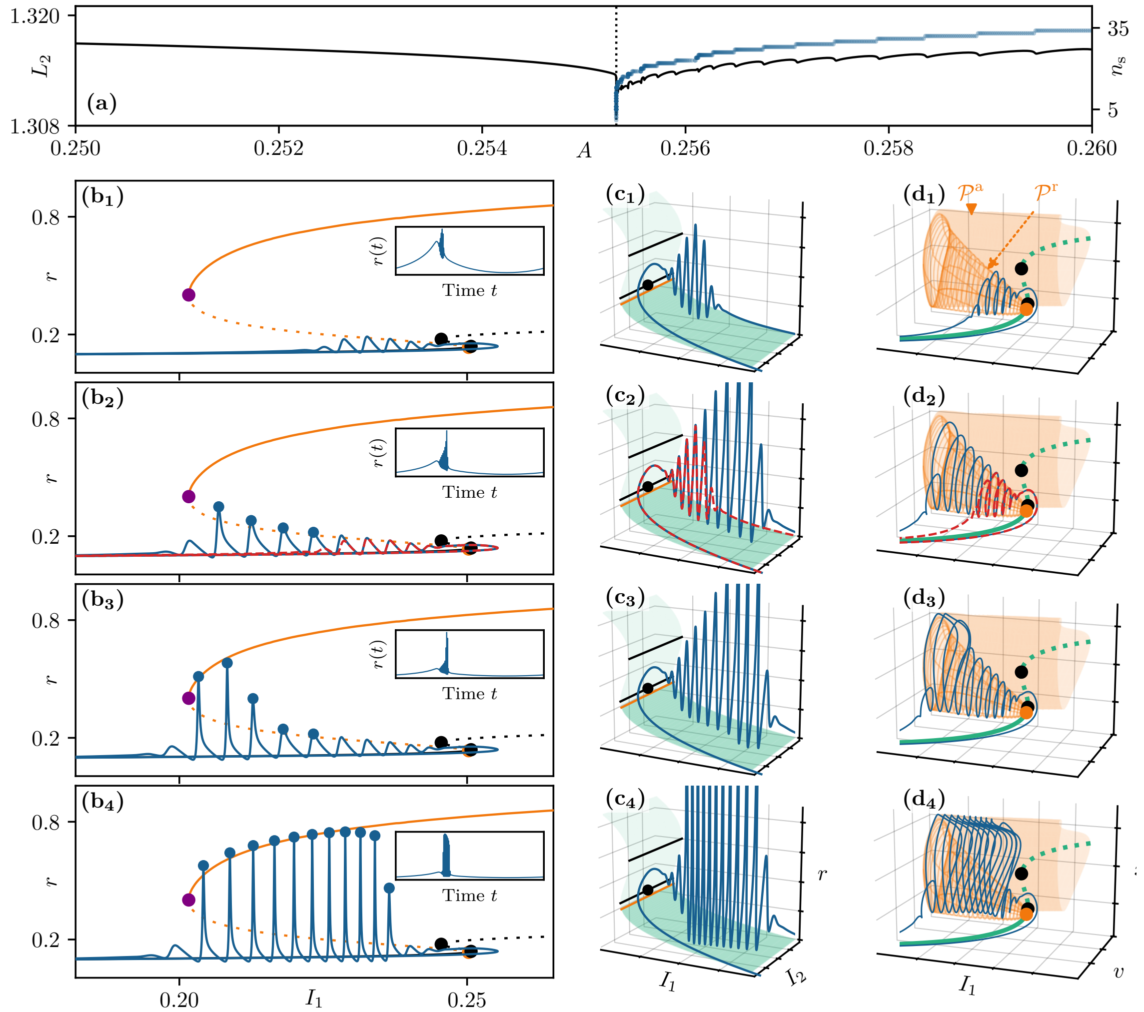

Figure 5.7: Emergence of bursting. **(a)** Bifurcation diagram of the full system. The black curve shows the L_2-norm of a family of periodic solutions vs. the forcing amplitude A. The blue dots show the number of spikes n_s, defined as the local maxima of for which $r(t) > 0.21\,\tau_\mathrm{m}^{-1}$. The dashed vertical line is located at $A = A^* = 0.25531851205$. **(b)** Solutions $(r(t), v(t), x(t), v(t), I_1(t), I_2(t))$ in $r - I$ projection superimposed on the bifurcation diagram of the fast subsystem. The insets show the solution in time. **(c - d)** Same solutions as in (b) and critical manifold S_0, for **(c)** in (I_1, I_2, r)-space and for **(d)** in (I_1, v, x)-space. In (d) attracting (repelling) sheets of S_0 are visualized as a green solid (dotted) line; the orange surface (wire frame) represents the family of stable (unstable) limit cycles of the fast subsystem [orange branch in column (b)]. Note that here the x-axis is inverted. In (b) the black dots denote $\mathcal{F}_\mathrm{L}$ and $\mathcal{F}_\mathrm{U}$, the orange dot $\mathcal{H}_\mathrm{L}$, while the black dots in (c) show the folded singularity p_1, assuming $A = A^*$. Spikes contributing to n_s are marked with blue dots. The dashed red curve shows the solution of the panels above. The A values in (b - d) are in increasing order from top to bottom and near A^*. Full system solutions obtained at $\varepsilon = 10^{-3}$.

$r - I_1$ projection superimposed on the fast subsystem's bifurcation diagram; column c in (I_1, I_2, r)-space together with S_0; column d in (I_1, v, x)-space.

In projection onto the (I_1, v, x)-space, the S_0 appears as a curve $(I_1, v(I_1), x(I_1))$. Additionally we show the family of fast subsystem limit cycles, which emerge at the lower subcritical Hopf bifurcation H_L. Unstable periodic solutions of this branch will be denoted by Γ^r, stable ones after the fold of cycles by Γ^a. Embedding these solutions $\Gamma^{\mathrm{a,r}}(I_1, t) = (r, v, x, u)(I_1, t)$ into the state space of the full system one obtains the surface $\mathcal{P} = \mathcal{P}^\mathrm{a} \cup \mathcal{P}^\mathrm{r}$, which consists of attracting and repelling parts $\mathcal{P}^{\mathrm{a,r}} = \{(\Gamma^{\mathrm{a,r}}(I_1, t), I_1) | t \in$

$[0, T(I_1)]\} \times \{I_2 | I_2 \in \mathbb{R}\}$, corresponding to stable and unstable branches of the solution family, respectively. The period $T(I_1)$ of these cycles depends on I_1.

Onset of fast oscillations ($\mathbf{b_1}$ - $\mathbf{d_1}$)

At the smallest of the chosen A values near A^* one can already observe fast oscillations, consisting of five not fully developed spikes. They occur after the trajectory has turned around the folded saddle p_1, marked by a black dot in (c_1). It is this motion around p_1, taking place in the vicinity of the critical manifold S_0, which has signs of a turning point, guiding the trajectory along the repelling sheet of S_0. Taking the rather large ε value into account, this turn hints at a canard segment arising due to the presence of the folded saddle p_1. After this segment, in (I_1, I_2, r)-space [Fig. 5.7(c_1)], the trajectory pierces through the repelling sheet of S_0 and fast oscillations set in. These results suggest that bursting is initiated at the termination of a canard segment, closely following the repelling middle sheet of S_0.

Taking the fast subsystem LC family $\Gamma^{\mathrm{a,r}}$ into account, a remarkable feature of the dynamics can be seen in (I_1, v, d) space [Fig. 5.7(d_1)]. The spikes of the burst appear to follow the family of unstable limit cycles, thus evolving near the repelling surface $\mathcal{P}^{\mathrm{r}}$. Unexpectedly, after piercing through the critical manifold, the bursting solution stays in the proximity of $\mathcal{P}^{\mathrm{r}}$, instead of being repelled from it. As I_1 slowly drifts towards smaller values, the trajectory remains close to $\mathcal{P}^{\mathrm{r}}$. These windings around $\mathcal{P}^{\mathrm{r}}$ correspond to the first not fully grown spikes of the full system solution. The spikes increase in amplitude, as I_1 decreases, but remain small; see Fig. 5.7(b_1) and inset. An enlargement of two full system trajectories in (I_1, v, x)-space is shown in Fig. 5.8, with two exponentially close A values near A^*.

Finally, the fast oscillations terminate via an escape from $\mathcal{P}^{\mathrm{r}}$. By approaching the bottom sheet of S_0, the dynamics change to that of a drifting equilibrium, passing from burst to quiescence.

Explosivity and spike-adding ($\mathbf{b_2}$ - $\mathbf{d_2}$)

At a slightly larger A value, close to A^*, a majority of the trajectory remains essentially unchanged, with respect to the previous A. The slowly drifting part along the bottom equilibrium branch of the fast subsystem and the canard segment, as well as the first oscillations, appear frozen. This is clear by comparing the blue trajectory with the red dashed curves in Fig. 5.7(b_2 - d_2), as well as in Fig. 5.8. The fact that part of the trajectory near the fold freezes, while the following part changes significantly, is a strong indication for explosivity of the solution, when varying the parameter. This strong sensitivity towards parameter changes is typical for canard dynamics. It is caused by the presence of repelling objects in the fast subsystem, typically, but not exclusively, equilibria, like the middle sheet of S_0.

Indeed, in Fig. 5.7(b_2 - d_2), the full system trajectory possesses a canard segment staying near the middle sheet of S_0, when it turns around the folded saddle p_1. Hence the sensitivity is to be expected. Moreover, during the fast oscillations, the bursting solution evolves close to $\mathcal{P}^{\mathrm{r}}$, thus adding an additional layer of sensitivity.

Compared to the previous case in Fig. 5.7(b_1 - d_1), the full system solution winds around $\mathcal{P}^{\mathrm{r}}$ more often until smaller values of I_1, before jumping back to S_0. The trajectory essentially remains close to $\mathcal{P}^{\mathrm{r}}$, but reaches up higher. This way, by passing through A^*, more and more spikes with increasing amplitude are added to the burst. These spikes are yet not fully grown to the amplitude of the stable limit cycles present in this I_1 region. Furthermore, we note that distance of the blue trajectory to $\mathcal{P}^{\mathrm{r}}$ increases, as it winds

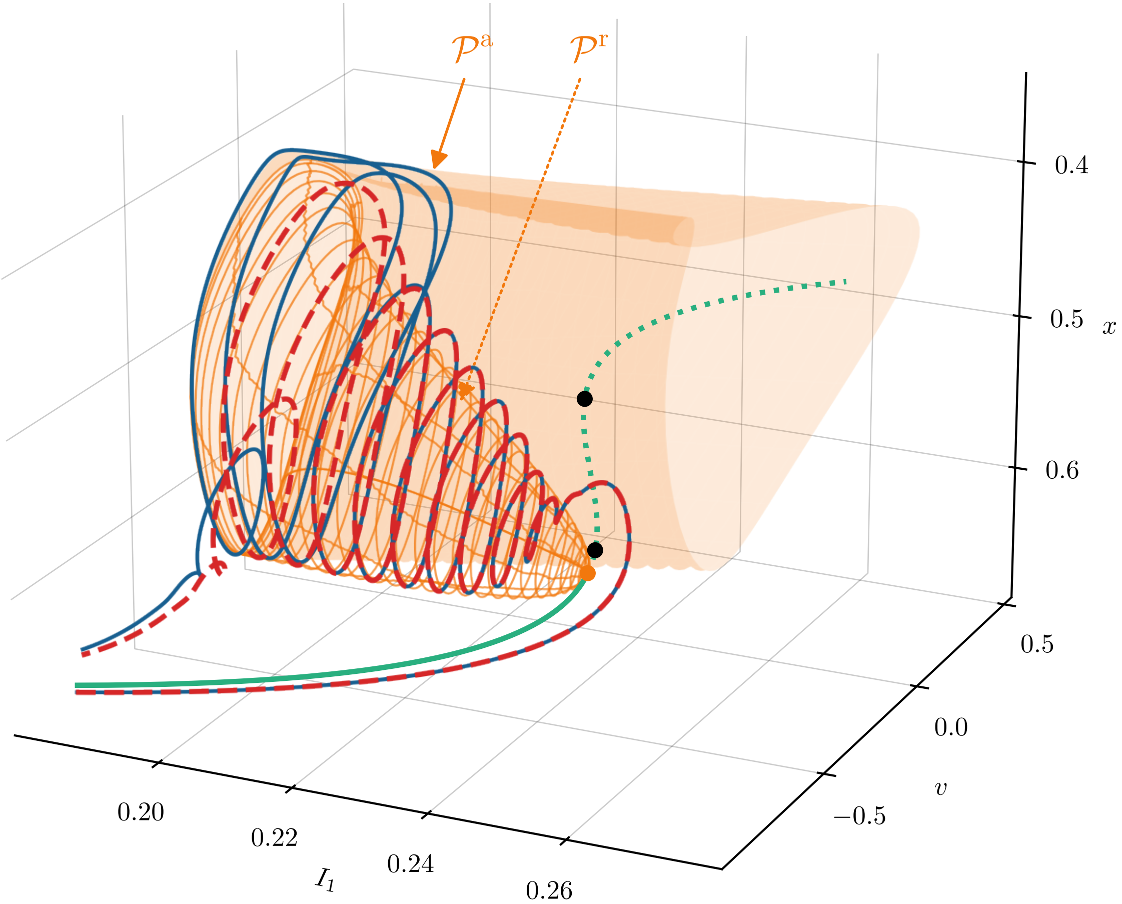

Figure 5.8: Mixed-type-like torus canards. enlargement of Fig. 5.7(d_2). Critical manifold in (I_1, v, x)-space with attracting (repelling) sheets of S_0 visualized as a green solid (dotted) line; the orange surface (wire frame) represents the family of stable (unstable) limit cycles of the fast subsystem [orange branch in column b], emerging from the lower Hopf bifurcation H_{L} (orange dot). The blue and red curves show solutions of the full system near the canard explosion. Forcing amplitude A for the blue trajectory is larger than for red and both exponentially close the canard explosion at A^*. Solutions obtained for $\varepsilon = 10^{-3}$.

around it, indicating some extent of repulsion near the surface; see also Fig. 5.7(b_2). This way, the full dynamics starts to escape from $\mathcal{P}^{\mathrm{r}}$ and gets attracted to $\mathcal{P}^{\mathrm{a}}$.

Emergence of bursting (b_3 - d_3)

As A increases further, the point at which the trajectory starts to escape from $\mathcal{P}^{\mathrm{r}}$ shifts towards the lower Hopf bifurcation H_{L}. In fact, the last two spikes are already repelled sufficiently to evolve close to the attracting surface $\mathcal{P}^{\mathrm{a}}$; see Fig. 5.7($\mathrm{b}_3, \mathrm{d}_3$). In other words, the number of revolutions near $\mathcal{P}^{\mathrm{r}}$ reduces, while the ones around $\mathcal{P}^{\mathrm{a}}$ increases. These oscillations near $\mathcal{P}^{\mathrm{a}}$ are of large amplitude and mark the start of a dense burst following for larger A.

Bursting (b_4 - d_4)

In this next step most of the windings around $\mathcal{P}^{\mathrm{r}}$ have vanished and the fast oscillations take place in the proximity of $\mathcal{P}^{\mathrm{a}}$. Additionally, the burst consists of more spikes in total, with respect to the first considered A value [Fig. 5.7(b_1 - d_1)].

Here, an additional spike-adding mechanism beyond the critical value A^* acts and is related to the period $T(I_1)$ of $\mathcal{P}^{\mathrm{a}}$ as a function of I_1. When A is beyond the canard explosion at A^* the full system dynamics approach $\mathcal{P}^{\mathrm{a}}$ right after surpassing the lower fold F_{L}, without the excursion on $\mathcal{P}^{\mathrm{r}}$. As the amplitude A is increased, this attraction to $\mathcal{P}^{\mathrm{a}}$ occurs at larger I_1 values. The period $T(I_1)$ of the fast subsystem limit cycles decreases with increasing I_1 and this finally leads to more windings around $\mathcal{P}^{\mathrm{a}}$. On top of this, the fraction of time for which the trajectory remains near $\mathcal{P}^{\mathrm{a}}$ increases. Both effects add more spikes to the burst and result in the spike-adding arches observed in Fig. 5.7(a).

The presented results already show the complexity of how bursts are generated, that is, via a transition through the canard explosion at $A = A^*$, which rather surprisingly leads the canard segment to evolve around the repelling object $\mathcal{P}^{\mathrm{r}}$. This is followed by spike growth via repulsion from $\mathcal{P}^{\mathrm{r}}$ and attraction to $\mathcal{P}^{\mathrm{a}}$, until all oscillations evolve near $\mathcal{P}^{\mathrm{a}}$.

5.5.2 Continuous route to bursting: spike-adding via mixed-type-like torus canards

Before the bursting transition, the full system dynamics can be described by a single slow frequency, determined by ε. After the transition, a full cycle consists of a slow phase followed by fast spiking. It is therefore characterized by the slow frequency and a fast one, given by properties of the fast subsystem. In the context of bursting and in slow-fast systems, whose fast subsystem has both stable and unstable cycles, this change of the dynamics, from one to two frequencies, hints at a torus (Neimark-Sacker) bifurcation in the full system.

This can indicate the existence of mixed type-torus canards (MTTCs). Indeed, the full system dynamics nearby the canard explosion not only exhibits a canard segment along the repelling sheet of S_0, but as well a canard segment on the repelling higher dimensional invariant set $\mathcal{P}^{\mathrm{r}}$. This clearly resembles mixed-type canards as described in [69]. Very similar MTTCs have been reported in [95], where they evidently arise in the singular limit $\varepsilon \to 0$. In particular Fig. 2 of [95] reports dynamics where a quasi-static motion of the full system along the attracting sheet of S_0 connects to a repelling set of limit cycles created by a subcritical Hopf bifurcation. In the NMSTP however, the understanding of mixed-type torus canards is more complex for various reasons and as we will show, only observed for small, but large enough ε.

First of all, in the ε regime for which we observe mixed-type torus canards, the timescale separation is small enough for the canard segment on the middle sheet of S_0 to persist as a strongly perturbed version of its singular counterpart. One can observe a turn around the lower fold $\mathcal{F}_{\mathrm{U}}$, mediated by the folded-saddle singularity p_1. It forces the trajectory to pierce through S_0, bringing it very close to $\mathcal{P}^{\mathrm{r}}$; see Fig. 5.8.

Secondly, the solutions $\Gamma^r \subset \mathcal{P}^{\mathrm{r}}$, despite being globally repelling, possess two stable Floquet multipliers. We argue that the associated stable directions, similar to the jump-on canard case (see Section 5.4.2), form due to the intrinsic timescales of the fast subsystem. Consequently, this means that stable manifolds can be associated with $\mathcal{P}^{\mathrm{r}}$: it can attract trajectories along certain directions.

Thirdly, for large enough ε, one can expect dynamics very distinct from singular orbits. In particular, solutions may not only evolve nearby, but also switch between different attracting branches of the fast subsystem. We observe this transition from the middle sheet of S_0 to $\mathcal{P}^{\mathrm{r}}$. Despite both being repulsive, the reasoning holds: the folded-saddle canard dynamics enforces the full system to stay close to the middle sheet of S_0; stable directions allow an attraction towards $\mathcal{P}^{\mathrm{r}}$; the large ε allows to bridge S_0 to $\mathcal{P}^{\mathrm{r}}$ and finally torus canard dynamics allow to follow $\mathcal{P}^{\mathrm{a}}$ closely, adding more and more spikes in the transition region around A^*.

5.5.3 Discontinuous route to bursting: block evoked by jump-on canards

The transition from subthreshold oscillations to bursting when increasing the forcing amplitude A explains the emergence of the very first spikes in the burst, which occur for forcing amplitudes exponentially close to A^*. They also show how the subsequent spike-adding process, reflected by the arches in Fig. 5.7(a), occurs. In the following we will extend the analysis of this transition, taking into account different values of the parameter ε. As an outlook, we will describe how, for ε values closer to the singular limit, jump-on canards interfere and block the transition.

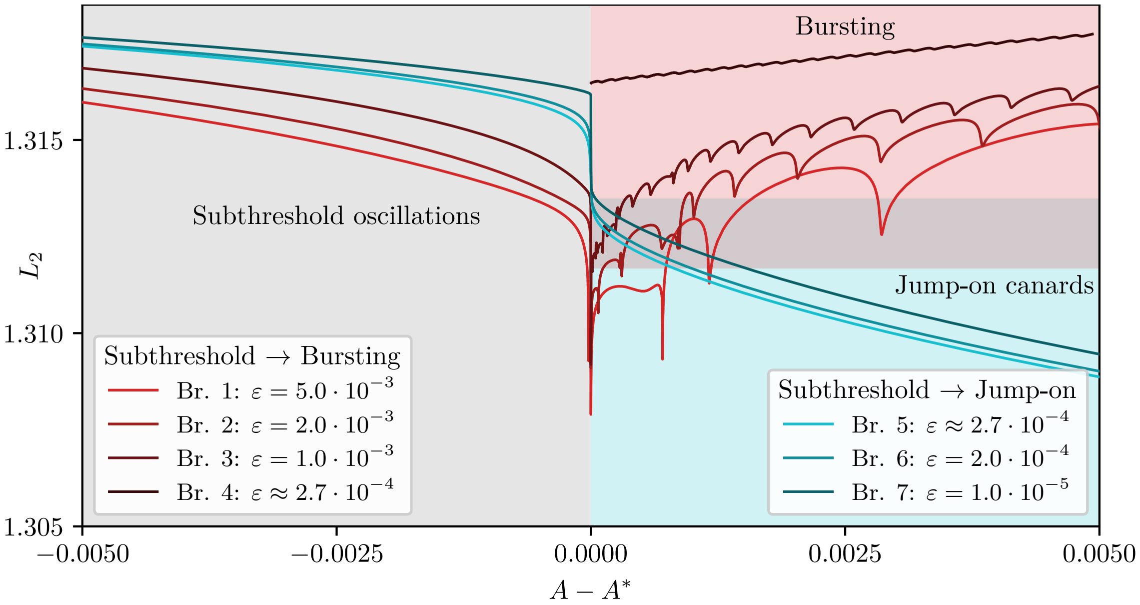

Figure 5.9: Families of bursting solutions and canards: The bifurcation diagram shows solution families of the full system in terms of the L_2-norm vs. the shifted forcing amplitude $A - A^*$. For all branches (br.) apart from br. 4, the A^* denotes the location of the canard explosion. For br. 4 on the other hand it marks the termination of continuation due to insufficient accuracy. There are two types of solution families: the ones which undergo a continuous transition from subthreshold oscillations to bursting (red curves) and those which transition from subthreshold to jump-on canard dynamics (cyan curves). Br. 4 and 5 have identical $\varepsilon \approx 2.667521298 \cdot 10^{-4}$.

In Fig. 5.9 solution families of periodic orbits are displayed, obtained via numerical continuation of the full system Eqs. (5.2) and Eq. (5.3). The figure comprises seven branches for ε values ranging from $\varepsilon = 5 \cdot 10^{-3}$ to $\varepsilon = 1 \cdot 10^{-5}$ and they are aligned to the canard explosion at $A = A^*$ (apart from branch 4). Branch 3 is identical to the one shown in Fig. 5.7 and undergoes a continuous transition from subthreshold oscillations to bursting.

As a general result, we find two types of solution families, which, beyond the canard explosion, i.e, for $A > A^*$, take different paths. For $\varepsilon \gtrapprox 2.7 \cdot 10^{-4}$ the branches display a continuous transition from subthreshold oscillations to bursting; see red curves in Fig. 5.9. For $\varepsilon \lessapprox 2.7 \cdot 10^{-4}$ on the other hand the branches evolve into families of jump-on canards (curves in Fig. 5.9). A value of $\varepsilon \approx 2.667521298 \cdot 10^{-4}$ separates the two ε regimes.

However, it is clear by considering branches 4 and 5 that bursting solutions do not cease to exist for smaller ε values. Instead they coexist with the jump-on type solutions.

It remains unclear how bursting forms for $\varepsilon \lessapprox 2.7 \cdot 10^{-4}$. Nevertheless the role of jump-on canards for the emergence of bursting becomes evident: for singular or small enough $\varepsilon \lessapprox 2.7 \cdot 10^{-4}$ regular canards are observed, evolving on the middle sheet of S_0. Beyond the maximal canard, the intrinsic timescales of the fast subsystem come into play and lead to the emergence of jump-on canards (see Section 5.4.2). They block a transition towards $\mathcal{P}$ and as a consequence, bursting remains absent for these solutions families.

For $\varepsilon \gtrapprox 2.7 \cdot 10^{-4}$ however, jump-on canards cease to exist. In the amplitude regime where they would be expected, the system approaches $\mathcal{P}^{\mathrm{a}}$ and bursts instead. The region around the canard explosion is populated by MTTCs and separates subthreshold oscillations from the bursting regime. It remains an open question for future work how the differentiation depending on ε occurs and in particular which possible bifurcations of the full dynamics result in the distinct regimes of continuous bursting transition and blocking jump-on canards.

5.6 Network behavior

The neural mass model with STP Eqs. (5.2) is an exact limit of the underlying QIF network Eqs. (5.1) as $N \to \infty$. We want to emphasize the benefits of neural mass models and their capability of describing neuronal dynamics at a macroscopic scale. In Fig. 5.2(b - f) results using the fast subsystem and the corresponding QIF network have been shown. For the original neural mass model [16] the exactness of the mean-field limit has been exploited in various studies in order to understand the collective dynamics of large neuronal populations [31–33, 46, 87, 98]. We want to note that STP, as opposed to exponential synapses used in Ref. [68], results in a substantially higher sensitivity towards finite size fluctuations and numerical errors, rendering the agreement of network and neural mass less clear, in particular in the canard regime.

Here we want to assess if the mechanisms leading to bursting in the neural mass model persists in a finite-sized network. To our knowledge such analysis, in particular in presence of short-term synaptic plasticity, has not been performed. For this we introduce the external periodic forcing $I_1 = A\sin(\varepsilon t)$ also into the network Eqs. (5.1) and investigate the QIF population dynamics nearby the canard explosion of the neural mass. In Fig. 5.10(a) the family of periodic solutions transitioning from subthreshold oscillation to bursting is shown for $\varepsilon = 2 \cdot 10^{-3}$. Two dashed black lines mark the values $A = 0.265$ and $A = 0.27$, respectively, for which neural mass (red) as well as QIF network trajectories (black) are depicted in Fig. 5.10(b, c). Row (b) shows the time series $x(t)$ vs. t, row (c) the trajectories in (I_1, v, x)-space.

The QIF network consists of $N = 100000$ neurons and $\varepsilon = 2 \cdot 10^{-3}$ is chosen to maintain reasonable computation times. In the network, the initial conditions are chosen according to fixed point values (r^*, v^*, x^*, u^*) obtained from the neural mass at $I_1 = 0$. However, initializing the network firing rate and average membrane potential at a given value is a non-trivial problem. To overcome this, the initial conditions of the QIF network are set to $V_i = v^* \quad$ for all $i = 1, \ldots, N$, $x = x^*$ and $u = u^*$. After a short transient, at time $t = 0$, the network has reached equilibrium and the forcing $I = A\sin(\varepsilon t)$ sets in.

We start the analysis by considering $A = 0.265$, marked by the left most dashed line in Fig. 5.10(a). It lays within the spike-adding arches of the neural mass, which displays bursting with a multitude of fully grown spikes; see red curves in Fig. 5.10($\mathrm{b}_1, \mathrm{c}_1$). They mainly evolve in the proximity of the invariant set $\mathcal{P}^{\mathrm{a}}$. This periodic solution of the full problem does not highlight a canard segment around the folded singularity p_1, which is to be expected, since A is not close enough to the canard explosion at A^*.

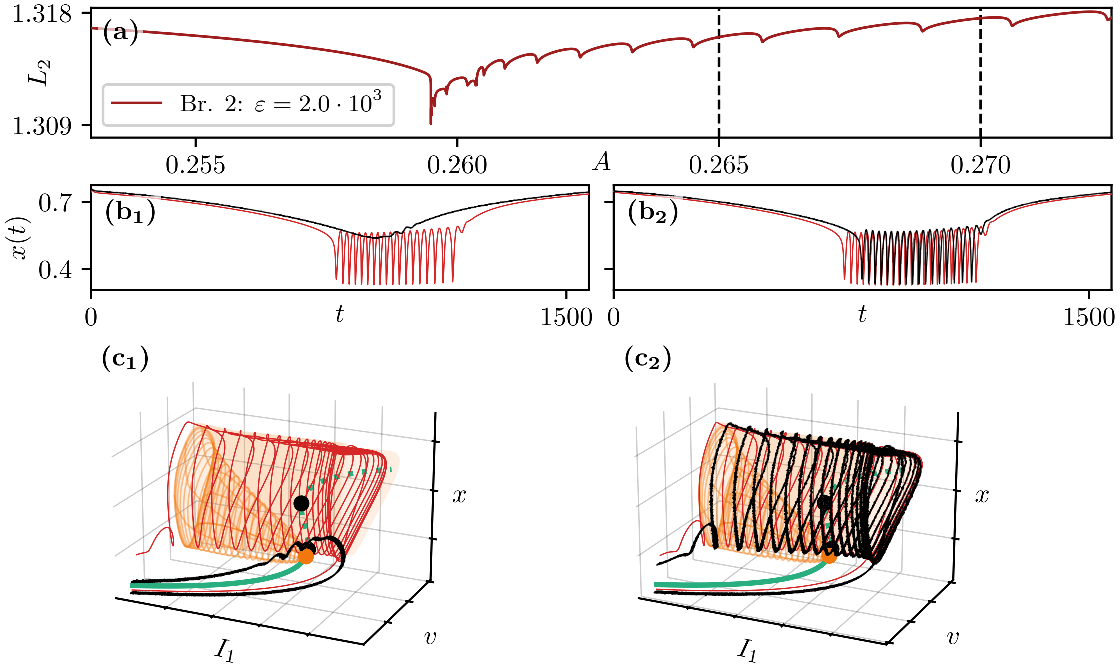

Figure 5.10: Bursting in the QIF network: **(a)** The bifurcation diagram shows a family of periodic orbits of the full neural mass system in terms of the L_2-norm vs. the forcing amplitude $A - A^*$. It corresponds to br. 2 in Fig. 5.9. The black dashed lines mark $A = 0.265$ and $A = 0.270$ respectively. **(b - c)** Trajectories of the full system (red) superimposed on results obtained by simulating the QIF network Eqs. (5.1) with $N = 100000$ neurons and in presence of sinusoidal forcing $I_1(t) = A \sin(\varepsilon t)$. In (b$_1$,c$_1$) the forcing amplitude is given by $A = 0.265$; in (b$_2$,c$_2$) by $A = 0.270$. Row b shows the time series of the solution in terms of $x(t)$ vs. time t. In row c they are shown in (I_1, v, x)-space together with the critical manifold S_0, with attracting (repelling) sheets as a solid (dashed) green line, and the invariant manifold $\mathcal{P}$ of the fast subsystem (orange wire frame and surface). The orange dot denotes $\mathcal{H}_{\mathrm{L}}$, the black dots $\mathcal{F}_{\mathrm{L}}$ and $\mathcal{F}_{\mathrm{U}}$. The x-axis is inverted in c.

On the other hand, the macroscopic state of the QIF network is found to be just at the start of the spike-adding process. The orbit possesses a canard segment: the turn around the lower fold F_{L} is evident. This is clear by looking at the black curve in Fig. 5.10(c$_1$). More strikingly, a few low-amplitude oscillations are picked up in the vicinity of the repelling invariant set $\mathcal{P}^{\mathrm{r}}$. This means that, despite the discrepancies, the mixed-type torus canards observed in the neural mass are also found in the QIF network. It is plausible to assume that spike-adding in the network follows the same mechanism as described in Section 5.5.

At the larger amplitude $A = 0.270$, shown in Fig. 5.10(b$_2$, c$_2$), the agreement between neural mass and network trajectory is more distinct. In both systems the canard segment is absent and they both exhibit bursting with a comparable number of large amplitude spikes. Taking also into account the previous case $A = 0.265$, it appears that the bifurcation structure of the network is shifted towards larger amplitudes with respect to the neural mass.

5.7 Discussion

The results of this work lay within the intersection of various fields including mean-field theory and slow-fast dynamics. First of all, we make use of recent developments of mean-field theory, namely the powerful OA ansatz, in order to understand the emergent dynamics of spiking neuronal networks on macroscopic scale.

Secondly, we aim at more biologically plausible models in this work, through the inclusion of synaptic dynamics, in form of STP, while preserving the exactness of the mean-field limit with respect to the QIF network. This adds more realism to the QIF network and neural mass, but at the same time adds to the complexity of the collective dynamics, even in absence of external forcing. In the part of parameter space chosen here, STP allows for the existence limit cycles, that are absent in the original model. As we have shown via extensive numerical evidence, STP leads to various peculiarities, when forcing the system slowly and periodically.

That leads to the third point, which we put our focus on: the treatment of the forced neural mass with STP using methods of singular perturbation theory, in particular slow-fast dissection. Without STP, slow external forcing already gives rise to bursts, as shown in [16]. The fast oscillations of these orbits vanish in the singular limit and relaxation oscillations remain. Accounting for STP, however, leads to more intricate dynamics.

One of the fundamental elements are canards. Expectedly, due to the slow harmonic passage through a fold of the S-shaped critical manifold, they appear as folded-saddle canards, which play a role for spike-adding in parabolic bursters. Here, despite the fact that the equilibrium destabilizing bifurcation is a subcritical Hopf bifurcation, the observed bursts are reminiscent of elliptic bursting (i.e., subcritical fold/fold of cycles bursting), due the slow passage through the Hopf bifurcation.

Concerning the full system dynamics, a folded saddle can be found, with associated explosive canard solutions. It separates quiescent orbits with purely slow dynamics from bursting ones. In this transition region we find an intriguing interplay of slow-fast effects: jump-on canards exist close enough to the singular limit and are associated with a subtle timescale separation of the neural mass, allegedly invoked by STP. They connect two repelling sheets of the critical manifold and more strikingly, block a continuous transition from quiescence to bursting.

Jump-on canards are one of the surprising elements of this work. However, they vanish when considering biologically more plausible frequencies of the periodic external current. Despite the rather insufficient timescale separation in this parameter regime, we find orbits which display a strongly perturbed canard segment. It is remarkable that these canards, as opposed to the jump-on case, do not block a continuous transition towards bursting, but much more promote it. Specifically they guide the trajectories into the proximity of unstable limit cycles of the fast subsystem. Here once again, an unexpected mechanisms sets in and allows attraction towards these globally repelling cycles. The final element to the spike-adding mechanisms in this region are rapidly oscillating segments that revolve around the branch of unstable limit cycles and consecutively add more spikes to the orbit.

Overall, the full dynamics nearby the canard explosion can be seen as mixed-type-like canards of peculiar nature: orbits evolve nearby the repelling middle sheet of the critical manifolds, as well nearby unstable limit cycles. Typically mixed-type canards are observed towards the singular limit, as they represent a slow-fast effect. The neural mass with STP exhibits mixed-type-like canards only for large enough forcing frequency; the phenomenon disappears for too slow forcing and is blocked by jump-on canards.

By virtue of the NMSTP model being the main subject of this work, we want to emphasize that it represents an exact limit of the QIF network with STP. Discrepancies between network and NMSTP arise due to numerical errors and finite-size fluctuations, especially under slow forcing. Nevertheless, our results clearly show a good agreement between the two models. In particular, the network simulations display the mixed-type-like torus canard dynamics, hence this can be regarded as a strong evidence for the same mechanisms to be responsible for burst spike-adding in the network.

In summary, the NMSTP turns out to be a useful approach in order to investigate the ensemble dynamics of neuronal populations in presence of STP. Slow-fast dissection reveals the mechanisms underlying burst generation on population level. As is it turns out, synaptic dynamics indeed enriches the complexity of the problem, by giving rise to peculiar jump-on and mixed-type-like torus canards, which both appear due to the timescales associated with STP.

Finally, while this work is in the scope of neural mass models and STP, the methodology of OA reduction and slow-fast dissection, coupled with numerical bifurcation analysis, can be applied to a much broader class of phase oscillator systems, like the Kuramoto model. This can lead to a better understanding of emerging collective slow-fast dynamics of large-scale networks.

Chapter 6

Conclusion and perspective

Next generation neural mass models have emerged from the seminal works of Ott and Antonsen and Montbrió, Pazó, and Roxin [15, 16]. Ever since they have inspired a large community of mathematicians, physicists and theoretical neuroscientists, to implement more plausible biophysical mechanisms and study large scale neuronal dynamics, with focus on different aspects. To recall and name a few examples, the exact MPR firing rate equations have been employed to study (1) the effect of time delay in populations of inhibitory neurons giving rise to collective chaos [31], (2) the crucial role of spike synchrony for fast oscillations [46], (3) the importance of oscillations in cognitive tasks [32], (4) nested cortical oscillations [33] and (5) the impact of electrical synapses on network synchronization [35]. This latter study is also an example for the versatility of the OA and MPR framework, which allow for the inclusion of relevant biophysical features, without losing the exactness of the mean-field limit. Some recent extensions of the exact neural mass model take into account fluctuation driven populations [37], spatially extended neural field models [260, 326] and spike-frequency adaptation [327].

Despite considering spiking networks of phenomenological QIF neurons and the corresponding mean-field limits, the above works demonstrate how simple mathematical descriptions can provide insight into biophysical problems. It is important to note that many of the cited works using the MPR framework draw fundamental conclusions regarding neuronal dynamics with respect to properties of the systems, which are ubiquitous in neuroscience, like time delay. These studies might allow for predictions of the expected dynamics in a much broader range of models, which possess (or do not possess) the same properties. An excellent example for this is spike synchrony, which is very relevant for cortical oscillations during working memory tasks.

This thesis gives a glimpse at what can be achieved with next generation neural mass models, but it also leaves open questions. Therefore, we will address several aspects which are relevant with regards to the studies in Chapters 3 to 5, but also to the model derivation in Chapter 2. In the following the key results of this thesis will be summarized and put in a broader context. We will also comment on the limitation of the neural mass model with short-term synaptic plasticity and give perspectives for future projects.

6.1 Working memory

The implementation of STP into the QIF network and exact mean-field framework in Chapter 2 is one possible extension of next generation neural mass models, aimed at the very specific application of the model towards working memory. In this thesis we have seen that first of all a QIF network with STP is able to reproduce basic working memory operations like information loading, maintenance and rehearsal, based on either populations bursts or persistent activity. Secondly and more importantly, the entire dynamics of the QIF network in presence of STP on mesoscopic scale is captured in an exact manner by the corresponding neural mass model.

Both models exhibit spike synchrony and thereby give rise to fast oscillations in the β-band, as observed in experimental studies with monkeys and humans. We can confirm one prediction of previous studies in the context of working memory, namely that these oscillations are absent in models that do not take into account spike synchrony, like the Wilson-Cowan model. Hence, using the next generation neural mass model with STP, we reported a better agreement with experimental results regarding powers of cortical oscillations in various frequency bands, compared to the WC model.

Moreover, thanks to the exactness and low dimension of the mean-field model, a systematic analysis revealed how the spectrograms are shaped by the interplay and resonances of fundamental frequencies in the system, which are linked to the number of items maintained in memory. One of the remarkable results of Chapter 3 is the analytical estimation of the maximum working capacity of around five items, which is in line with experimental studies.

6.1.1 Perspective

We want to address the validity and limitations of the mean-field approach that we have employed in order to study working memory. In particular, the comparison of microscopic system and neural mass in Chapter 3 was performed using descriptions of STP on different scales, in this thesis referred to as microscopic STP (μ-STP) with $3N$ equations in the network and mesoscopic STP (m-STP) with $N + 2$ equations. Naturally the former one represents a more accurate description of STP, by incorporating the dynamical evolution of the resources and utilization factors at the single neuron level. It is clear that the neural mass model with STP developed in this thesis does not represent an exact mean-field limit for the μ-STP case, as also pointed out in [328]. However the exactness is given for the m-STP network case, as we have shown in Chapters 2 and 3.

The justification for mainly using m-STP in this thesis was given by the Poissonian assumption, which allows to neglect correlations between the depression and facilitation variables [92], resulting in the m-STP equations. And indeed, when comparing the μ-STP network with the neural mass model that has m-STP at its basis (hence is not an exact description for μ-STP), we find remarkable agreement of the time traces, despite not taking into account correlations and fluctuations of the synaptic variables. The agreement is particularly good, when the network exhibits high firing rate dynamics, but discrepancies increase for low firing activity.

The influence of *firing rate heterogeneities* in the μ-STP network is also reported in [328]. The authors suggest that the agreement between the neural mass model developed in this thesis and the μ-STP network improve when heterogeneities are low. Independently, we have made similar considerations in Appendix A and find that *silent neurons* are at the core of the discrepancies between our neural mass model and the μ-STP network. First of all, we have only considered depressing synapses in absence of facilitation, but still found discrepancies, implying that the Poissonian assumption is not the root of the problem. Secondly, we find better agreement between the mean-field limit and μ-STP network for states in which silent neurons are sparse. This is in line with the approach in [328].

The neural mass model with STP proposed in this work suffices for the application to working memory, as we have demonstrated in Chapter 3. This is supported by the fact that working memory loading, maintenance and rehearsal are associated with enhanced firing rates, for example found in persistent state activity or population bursts. Overall, the model developed in this thesis represents an exact limit of the m-STP network and allows for a better understanding of phenomena relevant to questions of WM.

An exact macroscopic description of the dynamics in a QIF network with μ-STP is desirable and interesting to study from a mathematical point of view, but it remains an open question whether or not such a limit can be performed. The considerations in Appendix A and [92, 328] can be seen as a starting point to answer that.

6.2 All-brain modeling

In Chapter 4 experimentally obtained data were employed to model neuronal dynamics on the scale of the whole brain. In this thesis, structural connectomes obtained from diffusion-weighted MRI were used for the first time within a multi-population model, in which each network node, representing a brain area, obeys the dynamics of a MPR neural mass. With regards to the biophysical plausibility, it is important to note that we have deliberately refrained from implementing phenomena like STP or adaptation, in order to keep the model simple. This way we provide a proof-of-concept for idealized next generation neural mass models able to test clinical hypothesis of seizure propagation.

The healthy subject and epileptic patient connectomes are provided by different laboratories and do not use the same anatomical atlases for the segregation into brain areas. As such, direct comparisons of the data sets have to be taken with caution. Yet, in order to validate the applicability of the neural mass model, it was crucial to testify that with otherwise identical parameters, our approach yields distinct emerging dynamics, when comparing healthy subject to epileptic patient connectomes. Accordingly, we have reported numerical evidence, hinting at the epileptic patient connectomes to be more prone to seizure-like events, through a reduction of the external current required to trigger recruitments into the high activity states.

We also exploited the presurgical assessment, allowing to identify epileptogenic zones and in particular propagation zones for individual patients. Here we find good agreement between the recruitment order predicted by the multi-population model and the nodes which supposedly are propagation zones, according to the presurgical invasive and non-invasive evaluation. In summary, the results provided in Chapter 4 illustrate how next generation neural mass models can be used for clinically relevant studies on seizure propagation, despite being phenomenological and idealized.

6.2.1 Perspective

As mentioned above, the multi-population neural mass model employed to study seizure-like events is chosen to be minimalistic. Its major limitations are given by the absence of sustained collective oscillations and spontaneously emerging and terminating seizures. Hence, modeling fully developed seizures and their propagation is not possible.

In order to lift this limitation, the implementation of short-term synaptic plasticity into the multi-population model appears a natural choice. STP gives rise to stable limit cycles, as shown in this thesis, and contributes two additional timescales. Moreover, the multi-population model in presence of STP allows for heterogeneities in the depression and facilitation time constants of individual populations, which have also been reported experimentally [90]. Furthermore, the OA exact reduction methodology allows many other biophysical mechanisms to be implemented, rendering the model more sophisticated and realistic, but also more opaque.

In this context a compelling research line would be the assessment of the capabilities of the exact neural mass model in reproducing all-brain dynamics, when taking into account more detailed mechanisms. An effective method for this assessment has been performed in [329] and requires functional connectomes obtained from fMRI, in addition to the structural diffusion-weighted MRI connectomes. Functional MRI is based on the calculation of signal correlations among different brain regions. These correlations have to arise from structure. Therefore, one can feed the structural information into the dynamical model and measure the correlations arising in the numerical simulation, in order to estimate a fMRI connectome. This allows for an optimization loop, in which parameters are changed iteratively, in order to achieve a better match of the empirical functional connectomes and the simulated ones, thus benchmarking the model capabilities.

6.3 Slow-fast dynamics in large networks

The focus in Chapter 5 was on understanding the response of a spiking neural network to a periodic external drive. It is one of the first studies combining slow-fast dissection with the exact reduction methodology from statistical physics, to gain insight into the collective response of large coupled networks. A look into the original model by MPR already reveals an interesting bifurcation structure which displays bistability, an essential ingredient for complex dynamical behavior to arise, when periodically forcing the neural population. Motivated by this characteristic, we studied the extended model used for working memory, which in this thesis has proven to complexify the bifurcation structure by giving rise to stable limit cycles.

The slowly forced system exhibits disproportionately more convoluted slow-fast dynamics in presence of STP. Besides the classical canard, we reported jump-on canards, which at first appeared to be primarily a mathematical curiosity. A rigorous numerical investigation revealed their central role in blocking the continuous route from subthreshold oscillations to bursting, when considering extensive timescale separations.

For biologically more relevant separations, the route to bursting is continuous and shaped by mixed-type-like torus canard, which mediate a continuous spike-adding transition. Interestingly this behavior associated with the onset of bursting breaks down when approaching the singular limit. We provided evidence that shows the continuous transition to bursting via mixed-type-like torus canards also in the underlying microscopic network.

Studies which examine networks of phase oscillator are pervasive in physics and nonlinear dynamics. Models which describe phenomena that are very different from the above study on collective bursting in a spiking neural network might possess similar bifurcation scenarios, giving rise to the same slow-fast mechanisms reported here. The methodology employed in Chapter 5, i.e, mean-field theory coupled with slow-fast analysis, can be applied to other systems and shed light onto the emerging collective dynamics as a response to external drives.

6.3.1 Perspective

The slow-fast analysis of the neural mass model also brings up new intriguing questions. First of all, some details regarding the emergence of bursting in the non-continuous case remain unclear. In particular, the branch of bursting solutions for strong timescale separation, appears to be an *isola*, i.e, a disconnected branch. A problem we encounter here is the stiffness of the slow-fast dynamics, such that the numerical bifurcation analysis becomes challenging. One possible way of extending the analysis could be to construct a minimalistic model that exhibits the essential multi-timescale phenomena: jump-on and mixed-type-like torus canards. Two crucial elements for this could be the proximity of the saddle-node and subcritical Hopf bifurcations, as well as the subtle timescale separation in the fast subsystem.

Secondly, we have seen that a folded-saddle singularity can give rise to interesting canard dynamics and shapes the transition to bursting oscillations. Here the slow periodic Hopf forcing is partially responsible for the emergence of a folded saddle. However, the forcing dynamics does not need to be of Hopf form, in order to produce a periodic drive. Instead one could realize it through a feedback loop between the neural mass and forcing term. Depending on the exact choice, it is possible to obtain a *folded-node* singularity, replacing the folded saddle. In such a case we expect to observe *mixed-mode bursting oscillations* [325], which are solutions exhibiting both small-amplitude oscillations and bursts of large-amplitude oscillations. An interesting aspect to study in this case is the role of jump-on canards and if they impact the transition to bursting.

6.4 Beyond the MPR firing rate equations

To bring this dissertation to an end, let us address the plausibility of the employed neural mass models, which have quadratic integrate and fire neurons at their basis, hence are inherently phenomenological. The fact that QIF neurons are not biophysically grounded does not imply that they are not capable of describing neuronal dynamics accurately. As a matter of fact the phenomenological AdEx model has biophysically meaningful parameters, which can be fitted to empirical data. Moreover, one can link the AdEx to the QIF model as shown in Chapter 2. This opens up an interesting question, namely whether or not an exact mean-field limit in the OA framework can be performed, while maintaining the leak term and adaptation dynamics. The Izhikevich model stands out in terms of biological plausibility compared to most of the integrate and fire models. Hence, trying to obtain an exact macroscopic description for networks of Izhikevich neurons, including meaningful microscopic and macroscopic parameters which bridge the scales, appears to be a worthwhile future project.

Appendix A

The following appendix contains considerations, which are related to the implementation of short-term synaptic plasticity on microscopic level and the corresponding mean-field limit. Together with the pre-print [328] they provide first ideas on how a better mean-field limit can be performed, without relying on the mesoscopic description of STP described in [92]. They also give an intuition on why the neural mass model derived in this thesis is able to reproduce the dynamics of the QIF network in presence of microscopic STP to some extent, despite not being an exact limit.

1 Fully coupled QIF network with microscopic depression

We want to estimate the average resource $\langle X \rangle$ of a QIF network with microscopic depression. For simplicity we neglect facilitation. Following from Eqs. (2.37) in Chapter 2, the dynamics of a fully coupled QIF network with short-term depression and in absence of facilitation, i.e., $U(t) = \text{const.} = U_0$, reads

$$\dot{V}_i = V_i^2 + \eta_i + JU_0 \frac{1}{N} \sum_{j=1}^{N} X_j S_j \tag{6.1a}$$

$$\dot{X}_i = \frac{1 - X_i(t)}{\tau_\mathrm{d}} - U_0 X_i S_i \quad , \tag{6.1b}$$

with the spike train of the j-th neuron

$$S_j(t) = \sum_{t_j(k)<t} \delta(t - t_j(k)) \quad . \tag{6.2}$$

We define $I_i(t) = \eta_i + JU_0 \frac{1}{N} \sum_{j=1}^{N} X_j S_j$ as the total current that is applied to neuron i. When the network is in a quasi-equilibrium state, i.e, when $I_i(t) = \text{const}$ and if $I_i > 0$ is satisfied, the analytical solution of Eq. (6.1a) yields tonic firing at a frequency

$$f(I_i) = \frac{\sqrt{I_i}}{\pi} \quad . \tag{6.3}$$

Neurons with $I_i < 0$ decay to their resting potential $V = -\sqrt{|I_i|}$ and remain *silent* in approximation.

Silent neurons

For the set of silent neurons $\mathcal{N}_\mathrm{S}$, calculating the equilibrium X_S^* of the depression variable X_i is trivial. Since $S_i = 0$, X_i will converge to $X_\mathrm{S}^* = 1$.

Tonic neurons

For the set of tonic neurons $\mathcal{N}_\mathrm{T}$, one can coarse grain the spike train and set $S_i = f(I_i) = \frac{\sqrt{I_i}}{\pi}$ in approximation. The equilibrium depression variable for tonic neurons $X_{\mathrm{T,i}}^*$ depends on the index i and is given by

$$X^*_{\mathrm{T,i}} = \frac{1}{1 + \frac{\sqrt{I_i}}{\pi} U_0 \tau_\mathrm{d}} \quad . \tag{6.4}$$

In summary we have for the equilibrium X^*_i of neuron i:

$$X^*_i = \left\{ \begin{matrix} 1 & \text{if } I_i \leq 0 \\ \frac{1}{1+\frac{\sqrt{I_i}}{\pi} U_0 \tau_\mathrm{d}} & \text{if } I_i > 0 \end{matrix} \right\} \tag{6.5}$$

1.1 Ensemble average

In the limit $N \to \infty$ and given that the network is in quasi-equilibrium, we can calculate $\langle X^* \rangle$, as well as the mean firing rate $\bar{r}$ of the tonic neurons, using an integral. For this we have to take into account the PDF $g(\eta)$ and approximate further, by assuming that the contribution of the recurrent current is neglectable, in other words, $I_i = \eta_i$. This is justified by the fact that the present approach serves as an estimate for cases where many neurons are silent. We proceed by calculating the mean firing rate $\bar{r}$ of the tonic neurons[1]:

$$\bar{r} = \int_0^\infty \frac{\sqrt{\eta}}{\pi} g(\eta) \overset{(*)}{=} \frac{1}{\pi} \sqrt{\frac{\bar{\eta} + \sqrt{\bar{\eta}^2 + \Delta^2}}{2}} \tag{6.6}$$

$X^*_{\mathrm{T,i}}$ in the thermodynamic limit becomes $X^*_\mathrm{T}(\eta)$ and we can integrate:

$$\langle X^* \rangle = \int_{-\infty}^{\infty} X^*_\mathrm{T}(\eta) g(\eta) = \langle X^* \rangle_\mathrm{S} + \langle X^* \rangle_\mathrm{T} \tag{6.7}$$

$$= \int_{-\infty}^{0} 1 \cdot g(\eta) \mathrm{d}\eta + \int_0^\infty \frac{g(\eta)}{1 + U_0 \tau_\mathrm{d} \frac{\sqrt{\eta}}{\pi}} \mathrm{d}\eta \quad . \tag{6.8}$$

With the contribution $\langle X^* \rangle_\mathrm{S}$ of silent and $\langle X^* \rangle_\mathrm{T}$ of tonic neurons. To recall, $g(\eta)$ is a Lorentzian distribution given by $g(\eta) = \frac{1}{\pi} \frac{\Delta}{(\eta - \bar{\eta})^2 + \Delta^2}$. Using the cumulative distribution function of a Lorentzian, the first term can be calculated as:

$$\int_{-\infty}^{0} g(\eta) \mathrm{d}\eta = \frac{1}{2} - \frac{\arctan\left(\frac{\bar{\eta}}{\Delta}\right)}{\pi} \quad , \tag{6.9}$$

and is not only $\langle X^* \rangle_\mathrm{S}$, but at the same time the fraction of silent neurons. For the second term we obtain[1]:

$$\int_0^\infty \frac{g(\eta)}{1 + U_0 \tau_\mathrm{d} \frac{\sqrt{\eta}}{\pi}} \mathrm{d}\eta \overset{(*)}{=} \tag{6.10}$$

$$\frac{\pi \left(-2\pi^3 \bar{r} U_0 \tau_\mathrm{d} + 2\sqrt{R - (\pi r \bar{r})^2} U_0^3 \Delta \tau_\mathrm{d}^3 + 2\pi \bar{r} U_0^3 \bar{\eta} \tau_\mathrm{d}^3 + \pi^2 (\pi + 2\phi) - U_0^2 \tau_\mathrm{d}^2 \left(\pi \bar{\eta} + 2\bar{\eta}\phi + 2\Delta \log(R) + 4\Delta \log\left(\frac{U_0 \tau_\mathrm{d}}{\pi}\right)\right)\right)}{2(\pi^4 - 2\pi^2 U_0^2 \bar{\eta} \tau_\mathrm{d}^2 + R^2 U_0^4 \tau_\mathrm{d}^4)} ,$$

with $R = \sqrt{\bar{\eta}^2 + \Delta^2}$, $\phi = \arctan(\frac{\eta}{\Delta})$ and $\bar{r}$ from Eq. (6.6). Note that Eq. (6.10) is only valid for $\Delta, U_0, \tau_\mathrm{d} > 0$. A comparison of the analytical expression Eq. (6.10) and a numerically estimated integral is shown in Fig. A1.

---

[1] Result after $(*)$ obtained using Wolfram Mathematica [330].

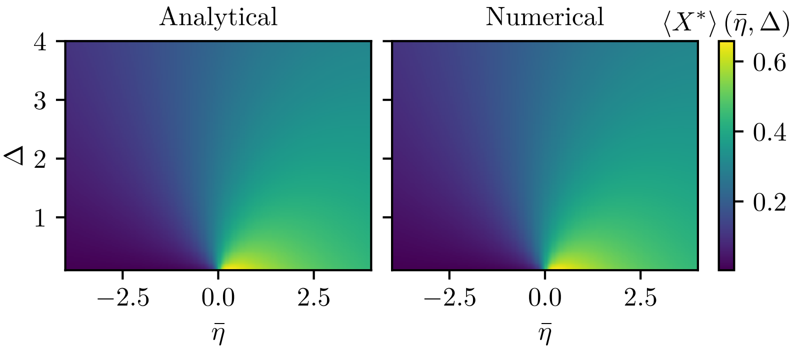

Figure A1: Comparison of Eq. (6.10) and a numerically estimated integral. Parameter values are: $U_0 = 0.2$, $\tau_\mathrm{d} = 200\,\mathrm{ms}$

1.2 Comparison to network simulation

Here we want to compare results obtained by simulating Eq. (6.1) with the above estimations, taking into account different parameter sets, in order to reflect cases in which the network consists of a variable number of silent neurons. Additionally we perform a comparison with the neural mass model, derived in Chapter 2, but here in absence of facilitation. The neural mass model obeys:

$$\dot{r} = \frac{\Delta}{\pi} + 2rv \tag{6.11a}$$

$$\dot{v} = v^2 - (\pi r)^2 + JU_0 xr + \bar{\eta} + I_\mathrm{S}(t) \tag{6.11b}$$

$$\dot{x} = \frac{1-x}{\tau_\mathrm{d}} - U_0 xr \quad . \tag{6.11c}$$

We hypothesize that the meanfield limit above does not take into account silent neurons. Instead the dynamics of $x(t)$ follows from the assumption, that all $X_i(t)$ are driven by the firing rate r, as stated below.

$$\dot{X}_i = \frac{1 - X_i}{\tau_\mathrm{d}} - U_0 X_i r \tag{6.12}$$

Taking the network simulation, we mimic this behavior, by calculating a different mean of X, given by

$$\langle X^* \rangle_\mathrm{MF} = \frac{1}{N_\mathrm{T}} \sum_{i \in \mathcal{N}_\mathrm{T}} X_i + X_\mathrm{S} X_\mathrm{T,i}(\bar{r}) \quad . \tag{6.13}$$

We denote the set and number of tonic neurons by N_T and $\mathcal{N}_\mathrm{T}$ respectively. Moreover, X_S reflects the fraction of silent neurons and $\bar{r}$ is the estimated firing rate of tonic neurons from Eq. (6.6). Essentially, in Eq. (6.13) we assume that tonic neurons contribute to the total average $\langle X^* \rangle_\mathrm{MF}$ through their actual values X_i, while silent neurons contribute as if X_i would be driven by the mean firing rate $\bar{r}$ of the tonic neurons. A comparison of the estimation is given in Fig. A2. From column (1) to (4) the parameters are such, that the number of silent neurons (obtained from the network simulation) decreases. In column (1) we find good agreement between Eqs. (6.6) and (6.10) (orange) and network (black). At the same time time we have agreement between Eq. (6.13) (red) and Eq. (6.11) (blue). The same holds for column (b). As we approach smaller numbers of silent neurons the discrepancy of the estimates and the network results increases. However, for vanishingly small number of silent neurons, network Eq. (6.1) and meanfield Eq. (6.11) start to coincide.

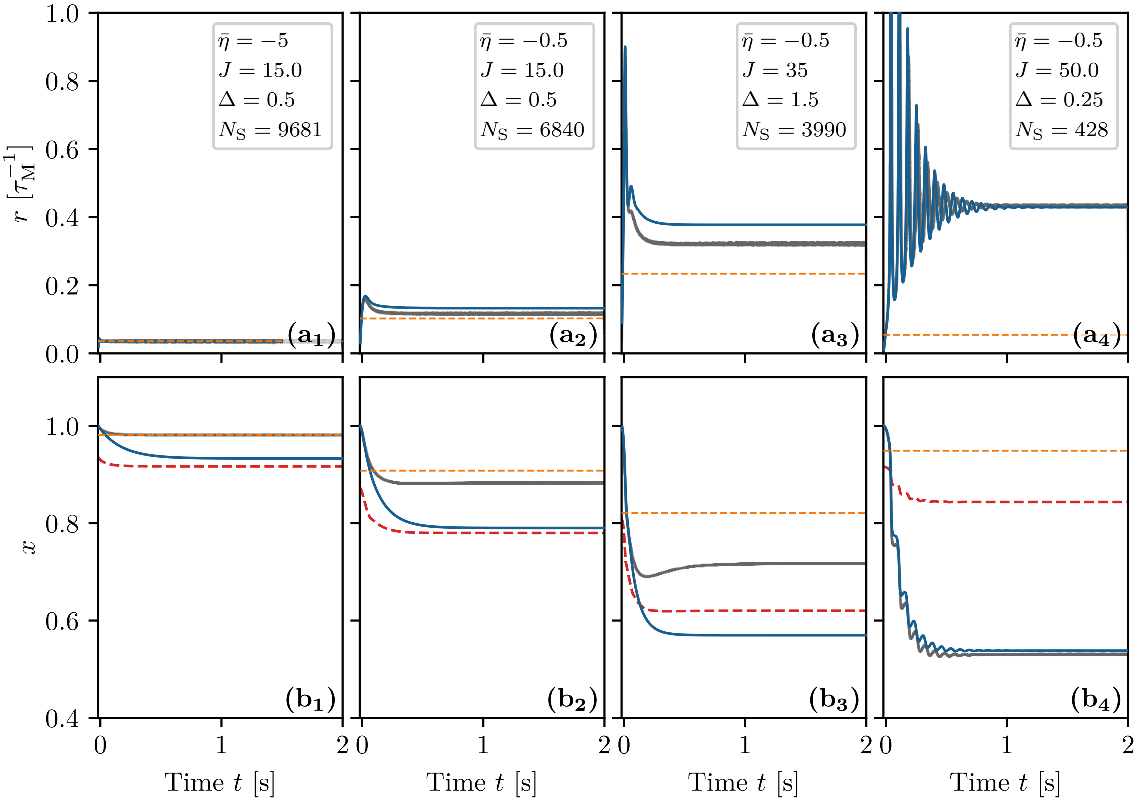

Figure A2: Comparison of numerical simulations and analytical estimates. (a) Mean firing rate $r(t)$ and **(b)** mean depression $x(t)$ versus time t, obtained from simulation of Eq. (6.1) (black line) and Eq. (6.11) (blue line). In (a) the dashed orange line marks $\bar{r}$ from Eq. (6.6); in (b) $\langle X^* \rangle$ from Eq. (6.10). The dashed red line in (b) marks Eq. (6.13). The number of silent neurons N_S is given by the number of neurons in the network, which do not emit any spike in $1\,\text{s} \leq t \leq 2\,\text{s}$. Other parameter values are: number of QIF neurons $N = 10000$,$U_0 = 0.2$, $\tau_d = 200\,\text{ms}$, $\tau_m = 20\,\text{ms}$.

In summary, these results suggest that the mean-field model Eq. (6.11) describes the collective dynamics of Eq. (6.1) accurately, whenever silent neurons are sparse (gray versus blue curve in Fig. A2). This is in line with the results in [328], in which *firing rate heterogeneities* has been suggested as the cause for discrepancies. Additionally, the above results suggest that the dynamics of the mean-field model Eq. (6.11) describes a network, in which depression variables X_i of neurons, which are actually silent in Eq. (6.1), are instead driven by the network's mean firing rate (blue versus red curve in Fig. A2).

Appendix B

1 Minimal biophysical models of seizure dynamics

The detection of epileptic seizures via electrophysiological recordings allowed for the establishment of a detailed taxonomy of seizures. The majority of seizures recorded in humans and experimental animal models can be described by a generic phenomenological mathematical model, the Epileptor [186]. In this model, seizure events are driven by a slow permittivity variable and occur via saddle node and homoclinic bifurcations at seizure onset and offset, respectively. The saddle-node bifurcation at the onset of ictal discharges was chosen based on experimentally observed features, such as fixed frequency and fixed amplitude of abruptly starting oscillations, and a shift of baseline field potential. The homoclinic bifurcation at the offset of ictal discharges, on the other hand, reproduces the logarithmic scaling of interspike intervals when approaching seizure offset. As part of the dynamic repertoire of the Epileptor, the epileptic attractor is described in terms of a self-sustained limit cycle that comes from the destabilization of the physiological activity while multiple types of transitions allow for the accessibility of seizure activity, status epilepticus and depolarization block, that coexist, as verified experimentally in [232].

The Epileptor model has been reduced to a minimal canonical mathematical representation of high codimension (up to 4) that, appropriately tuned, can display several types of fast-slow behaviors [234]. The model contains two subsystems acting at different time scales, in which the fast subsystem is unfolded in a plane showing several bifurcation paths of a high codimension singularity. The slow subsystem steers the fast one back and forth along these paths leading to fast-slow (aka bursting) behavior, mimicking epileptiform activity. The model is able to produce almost all the classes of bursting predicted for systems with a planar fast subsystem, including the Epileptor class, and has been demonstrated to be the dominant class, so-called dynamotype, in empirical epilepsy data [261]. Other dynamotypes have been also found empirically.

When performing the analysis of the single-population firing rate equations Eqs. (2.36), it turns out that, in the absence of forcing, the only attractors are fixed points. As it becomes clear in Section 4.3.1, a stable node and a stable focus are observable, separated by a bistability region between a high- and a low-activity state, whose boundaries are the locus of a saddle-node bifurcation (for more details see [16]). In this context are not observable self-sustained oscillations, but only damped oscillations at the macroscopic level that reflect the oscillatory decay to the stable fixed point. This oscillatory decay will here be considered as representative of a seizure-like event, not being able to observe a stable limit cycle to describe the emergence of a fully developed seizure as in the Epileptor. However, seizure-like events can be used as paradigm to investigate propagation of seizure-like activity in the network. Furthermore, a recently developed model of interictal and ictal discharges, called Epileptor-2 [233], makes links to underlying physiology and suggests how to eventually obtain all observed dynamotypes for the exact neural mass model Eqs. (2.36) and enable transitions towards fully developed seizure activity.

Epileptor-2 is a simple population-type model that includes four principal variables, i.e. the extracellular potassium concentration, the intracellular sodium concentration, the membrane potential and the synaptic resource diminishing due to short-term synaptic depression. A QIF neuron model, whose dynamics is ruled by an equation similar to Eq. (1), is used as an observer of the population activity. While the potassium accumulation governs the transition from the silent state to the state of ictal discharge, the sodium accumulated during the discharge, activates the sodium-potassium pump, which terminates the ictal discharge by restoring the potassium gradient, thus polarizing the neuronal membranes. This means that, in high potassium conditions, Epileptor-2 produces bursts of bursts, described as ictal-like discharges.

Therefore, the association of a slow subsystem describing ion concentration variations together with a fast subsystem, identified by Eqs. (4), should give rise to self-emergent periodic and bursting dynamics at the macroscopic level, thus allowing us to identify different combinations of onset/offset bifurcations. Whenever not sufficient, it will be possible to investigate the dynamics emergent in the exact neural mass model, provided with short-term synaptic plasticity, when subject to a global feedback acting on a slow timescale, describing ion concentration variations. The exact neural mass model, when equipped with short-term synaptic plasticity, shows a more complex dynamics that eventually results in a bifurcation diagram that provides stable limit cycles [98]. However the introduction of short-term plasticity, itself, adds complexity to the dynamics, allowing for the emergence of bursting activity [39].

2 Supplementary Figures and Tables

Label	Region	Abbreviation	Label	Region	Abbreviation
1	Precentral Gyrus	PRE	46	Cuneus	Q
2	Precentral Gyrus	PRE	47	Lingual Gyrus	LING
3	Superior Frontal Gyrus	F1	48	Lingual Gyrus	LING
4	Superior Frontal Gyrus	F1	49	Superior Occipital Gyrus	O1
5	Superior Frontal Gyrus Orbital Part	F1O	50	Superior Occipital Gyrus	O1
6	Superior Frontal Gyrus Orbital Part	F1O	51	Middle Occipital Gyrus	O2
7	Middle Frontal Gyrus	F2	52	Middle Occipital Gyrus	O2
8	Middle Frontal Gyrus	F2	53	Inferior Occipital Gyrus	O3
9	Middle Frontal Gyrus Orbital Part	F2O	54	Inferior Occipital Gyrus	O3
10	Middle Frontal Gyrus Orbital Part	F2O	55	Fusiform Gyrus	FUSI
11	Inferior Frontal Gyrus Opercular Part	F3OP	56	Fusiform Gyrus	FUSI
12	Inferior Frontal Gyrus Opercular Part	F3OP	57	Postcentral Gyrus	POST
13	Inferior Frontal Gyrus Triangular Part	F3T	58	Postcentral Gyrus	POST
14	Inferior Frontal Gyrus Triangular Part	F3T	59	Superior Parietal Gyrus	P1
15	Inferior Frontal Gyrus Orbital Part	F3O	60	Superior Parietal Gyrus	P1
16	Inferior Frontal Gyrus Orbital Part	F3O	61	Inferior Parietal Gyrus	P2
17	Rolandic Operculum	RO	62	Inferior Parietal Gyrus	P2
18	Rolandic Operculum	RO	63	Supramarginal Gyrus	SMG
19	Supplementary Motor Area	SMA	64	Supramarginal Gyrus	SMG
20	Supplementary Motor Area	SMA	65	Angular Gyrus	AG
21	Olfactory Cortex	OC	66	Angular Gyrus	AG
22	Olfactory Cortex	OC	67	Precuneus	PQ
23	Superior Frontal Gyrus Medial	F1M	68	Precuneus	PQ
24	Superior Frontal Gyrus Medial	F1M	69	Paracentral Lobule	PCL
25	Superior Frontal Gyrus Medial Orbital	F1MO	70	Paracentral Lobule	PCL
26	Superior Frontal Gyrus Medial Orbital	F1MO	71	Caudate Nucleus	CAU
27	Gyrus Rectus	GR	72	Caudate Nucleus	CAU
28	Gyrus Rectus	GR e	73	Putamen	PUT
29	Insula	IN	74	Putamen	PUT
30	Insula	IN	75	Pallidum	PAL
31	Anterior Cingulate and paracingulate gyri	ACIN	76	Pallidum	PAL
32	Anterior Cingulate and paracingulate gyri	ACIN	77	Thalamus	THA
33	Median Cingulate and paracingulate gyri	MCIN	78	Thalamus	THA
34	Median Cingulate and paracingulate gyri	MCIN	79	Heschl Gyrus	HES
35	Posterior Cingulate Gyrus	PCIN	80	Heschl Gyrus	HES
36	Posterior Cingulate Gyrus	PCIN	81	Superior Temporal Gyrus	T1
37	Hippocampus	HIP	82	Superior Temporal Gyrus	T1
38	Hippocampus	HIP	83	Heschl Gyrus	HES
39	ParaHippocampal Gyrus	PHIP	84	Temporal Pole: superior temporal gyrus	T1P
40	ParaHippocampal Gyrus	PHIP	85	Temporal Pole: superior temporal gyrus	T1P
41	Amygdala	AMYG	86	Temporal Mid	T2
42	Amygdala	AMYG	87	Temporal Mid	T2
43	Calcarine fissure and surrounding cortex	V1	88	Temporal Pole: middle temporal gyrus	T2P
44	Calcarine fissure and surrounding cortex	V1	89	Middle Temporal Gyrus	T2
45	Cuneus	Q	90	Inferior Temporal Gyrus	T3

Table A1: Cortical and subcortical regions, according to the Automated Anatomical Labeling atlas 1(AAL1) [212]. Odd/even numbers correspond to the left/right hemisphere.

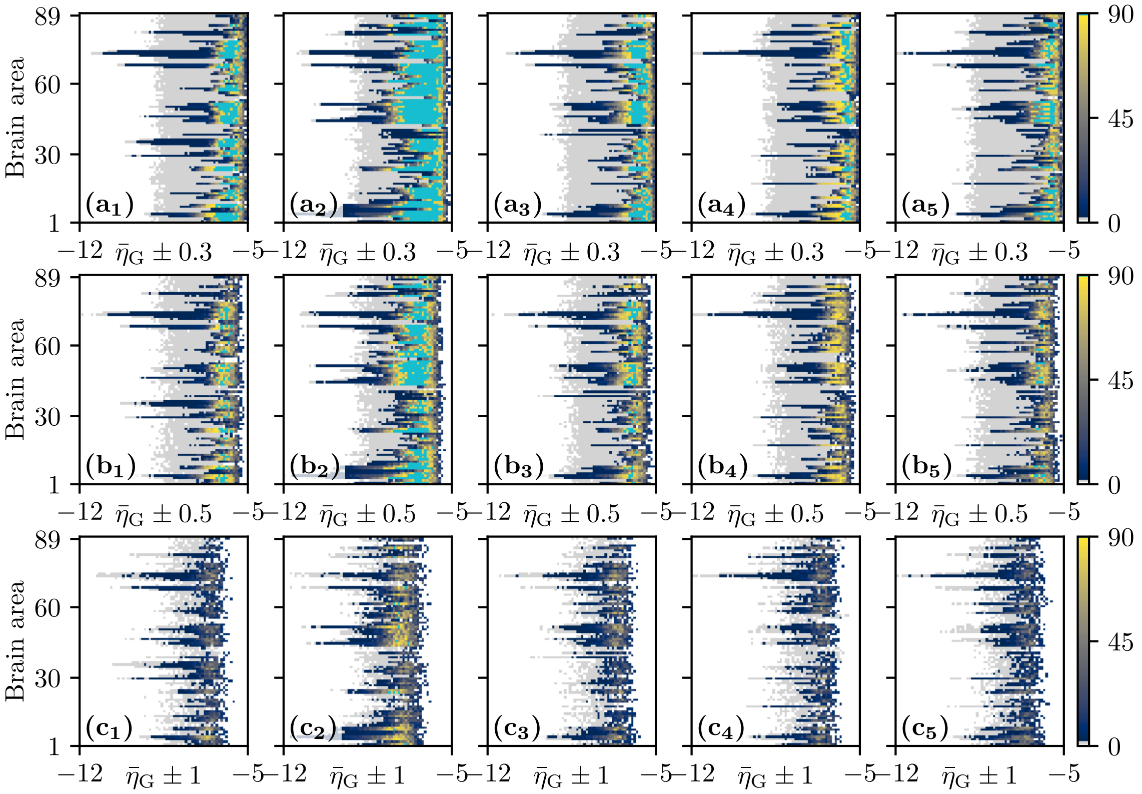

Figure A3: Number of recruited brain areas as a function of the excitability parameter $\bar{\eta}_G$. Columns **(1)** to **(2)** correspond to 5 exemplary healthy subject connectomes H1, H5, H12, H16, H19 as in in Fig. 4.3. Here $\bar{\eta}_G$ represents the mean value of a Gaussian distribution with increasing standard deviations σ_G. **(a)** $\sigma_G = 0.3$; **(b)** $\sigma_G = 0.5$; **(c)** $\sigma_G = 1$. The color code is as follow. White: no recruitment, gray: one area recruited (marks asymptotic threshold), blue to yellow: intermediate number of recruitments, teal: 90 areas recruited (marks generalized threshold). For very large values of $\bar{\eta}_G$ (usually $\bar{\eta}_G > -5$), the system enters the stable focus regime before the stimulation is applied. In that case $\bar{\eta}^{(k)}_{\text{gen}}$ is not defined because no brain areas are recruited as a result of the applied stimulation current: for this reason white color, corresponding to no recruited areas, is visible also in the right part of the different panels. For increasing standard deviation values, the effective excitability of the more and more nodes turn out to be close to the one that allows the system to be in the stable focus regime, therefore the probability of finding nodes in the stable focus regime increases. As a result, more and more nodes enter the HA state and recruite the other areas before the stimulation current is applied. This means that, for increasing standard deviation, $\bar{\eta}^{(k)}_{\text{gen}}$ become less defined while $\bar{\eta}^{(k)}_{\text{asy}}$ move to larger values of $\bar{\eta}_G$, still remaining better identifiable for increasing heterogeneity. Other parameters values are: $N_{\text{pop}} = 90$, $\Delta = 1$, $\sigma = 1$, $I_S = 10$, $\Delta T = 0.4$ s.

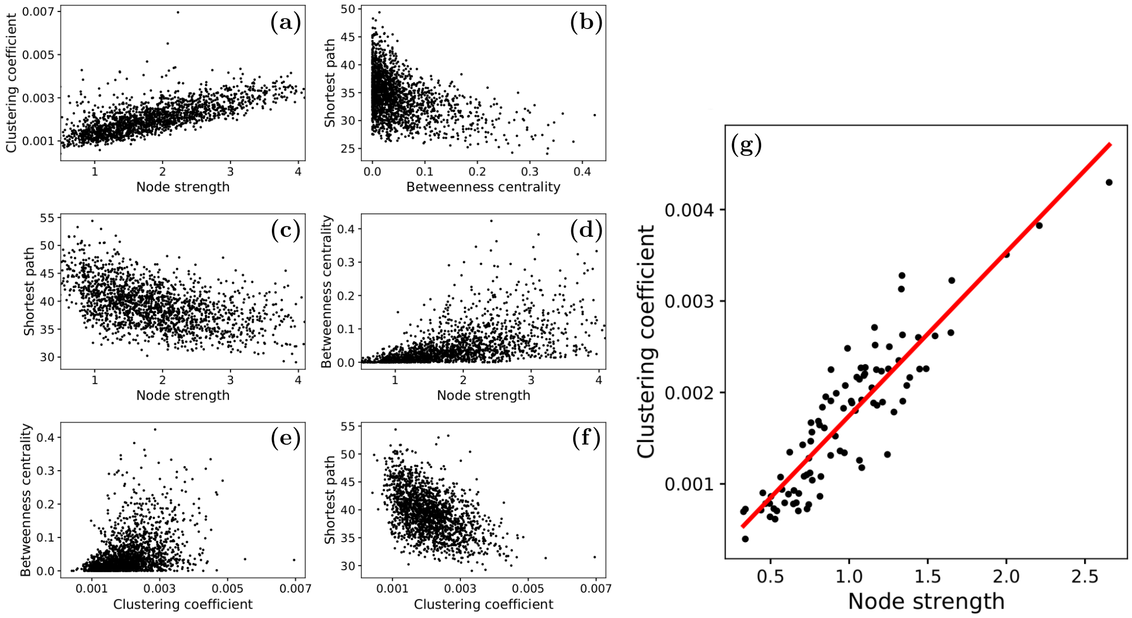

Figure A4: Network measure correlations of healthy subjects. Panels **(a - f)** are obtained plotting independently all node values for all the subjects ($90 \times 20 = 1800$ data points). **(g)** Data is averaged over all 20 subjects. The single node values are averaged over the different subjects and afterwards, the correlation between node strength and clustering coefficient is estimated. Infinite values were excluded. The Pearson correlation of clustering coefficient and node strength of the averaged healthy DTI topology is $r = 0.9$ and much stronger compared to the average of all individual topologies $r = 0.75$ from panel (a).

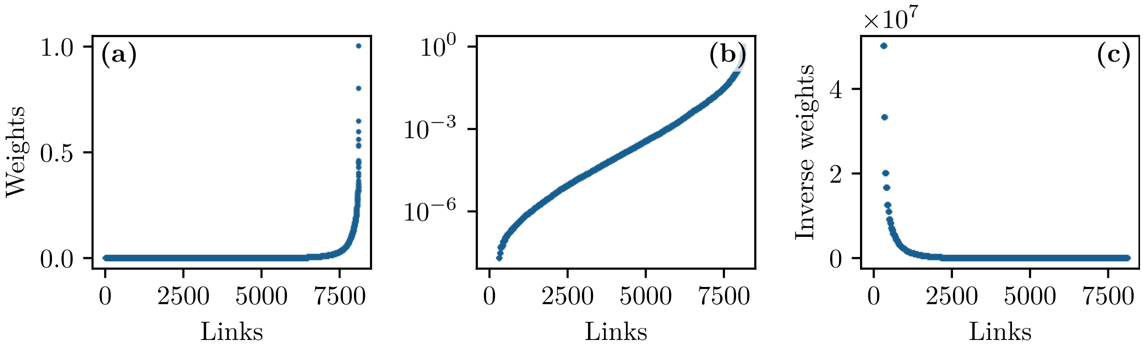

Figure A5: Weight Distribution of the DTI graphs. The weight distribution with weights on the x-axis in ascending order. **(a)** Weight distribution, **(b)** logarithmic weight distribution and **(c)** inverse weight distribution of the healthy averaged DTI graph. Note that **(b)** matches the curve of recruitment times in Fig. 4.6(a).

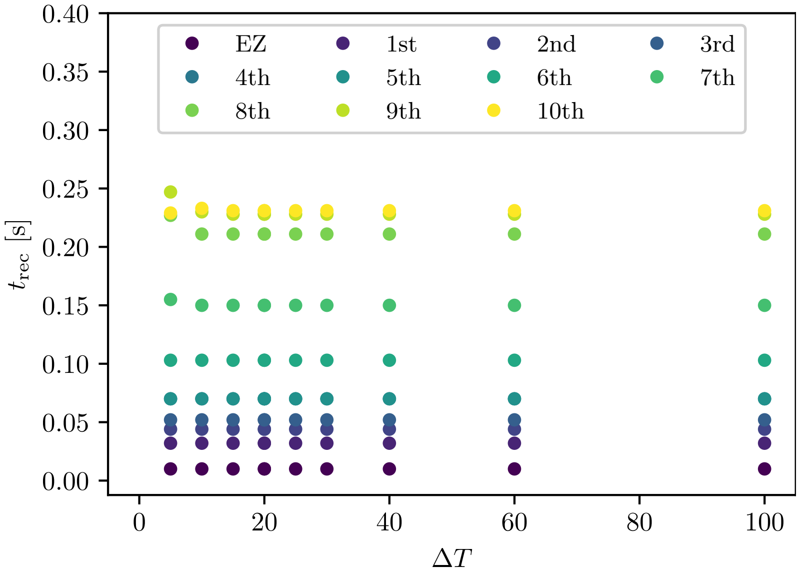

Figure A6: Input current duration variation. Dependence of the recruitment time on the current duration ΔT while the current strength is kept constant at $\Delta I = 15$. The y-axis shows the recruitment times of the first 10 recruited areas for each current strength. Blue is the EZ, green is the first recruited area, red the second, etc. The recruitment times are independent of the pulse duration. Parameters: $N_{\text{pop}} = 90$, $\sigma = 1$, $\Delta = 1$, $\bar{\eta} = -6$, $\Delta I = 15$, stimulation site: brain area $k = 45$ for the healthy H1.

Label	Region	Abbreviation	Label	Region	Abbreviation
1	Unknown				
2	Brain-Stem				
3	Left-Cerebellum Cortex		46	Right-Cerebellum-Cortex	
4	Left-Thalamus Proper	lh-Th	47	Right-Thalamus Proper	rh-Th
5	Left-Caudate	lh-Cd	48	Right-Caudate	rh-Cd
6	Left-Putamen	lh-Pu	49	Right-Putamen	rh-Pu
7	Left-Pallidum	lh-Pal	50	Right-Pallidum	rh-Pal
8	Left-Hippocampus	lh-Hi	51	Right-Hippocampus	rh-Hi
9	Left-Amygdala	lh-Amg	52	Right-Amygdala	rh-Amg
10	Left-Accumbens-Area		53	Right-Accumbens Area	
11	Left-unknown		54	Right-unknown	
12	Left-bankssts		55	Right-bankssts	
13	Left-Caudal Anterior Cingulate	lh-CACC	56	Right-Caudal Anterior Cingulate	rh-CACC
14	Left-Caudal Middle Frontal	lh-CMFG	57	Right-Caudal Middle Frontal	rh-CMFG
15	Left-Cuneus	lh-Cun	58	Right-Cuneus	rh-Cun
16	Left-Entorhinal Cortex	lh-EntC	59	Right-Entorhinal cortex	rh-EntC
17	Left-Fusiform Gyrus	lh-FuG	60	Right-Fusiform Gyrus	rh-FuG
18	Left-Inferior Parietal Cortex	lh-IPC	61	Right-Inferior Parietal Cortex	rh-IPC
19	Left-Inferior Temporal Gyrus	lf-ITG	62	Right-Inferior Temporal Gyrus	rh-ITG
20	Left-Isthmus Cingulate Cortex	lh-ICC	63	Right-Isthmus Cingulate Cortex	rh-ICC
21	Left-Lateral Occipital Cortex	lh-LOCC	64	Right-Lateral Occipital Cortex	rh-LOCC
22	Left-Lateral Orbito Frontal Cortex	lh-LOFC	65	Right-Lateral Orbito Frontal Cortex	rh-LOFC
23	Left-Lingual Gyrus	lf-LgG	66	Right-Lingual Gyrus	rh-LgG
24	Left-Medial Orbito Frontal Cortex	lh-MOFC	67	Right-Medial Orbito Frontal Cortex	rh-MOFC
25	Left-Middle Temporal Gyrus	lh-MTG	68	Right-Middle Temporal Gyrus	rh-MTG
26	Left-Parahippocampal Gyrus	lh-PHiG	69	Right-Parahippocampal Gyrus	rh-PHiG
27	Left-Paracentral Cortex	lh-PaC	70	Right-Paracentral Cortex	rh-PaC
28	Left-Pars Opercularis	lh-Pop	71	Right-Pars Opercularis	rh-Pop
29	Left-Pars Orbitalis	lh-POr	72	Right-Pars Orbitalis	rh-POr
30	Left-Pars Triangularis	lh-PT	73	Right-Pars Triangularis	rh-PT
31	Left-Pericalcarine	lh-PC	74	Right-Pericalcarine	rh-PC
32	Left-Postcentral Gyrus	lh-PoG	75	Right-Postcentral Gyrus	rh-PoG
33	Left-Posterior Cingulate Gyrus	lh-PCG	76	Right-Posterior Cingulate Gyrus	rh-PCG
34	Left-Precentral Gyrus	lh-PrG	77	Right-Precentral Gyrus	rh-PrG
35	Left-Precuneus Cortex	lh-PCunC	78	Right-Precuneus Cortex	rh-PCunC
36	Left-Rostral Anterior Cingulate Cortex	lh-RACC	79	Right-Rostral Anterior Cingulate Cortex	rh-RACC
37	Left-Rostral Middle Frontal Gyrus	lh-RMFG	80	Right-Rostral Middle Frontal Gyrus	rh-RMFG
38	Left-Superior Frontal Gyrus	lh-SFG	81	Right-Superior Frontal Gyrus	rh-SFG
39	Left-Superior Parietal Cortex	lh-SPC	82	Right-Superior Parietal Cortex	rh-SPC
40	Left-Superior Temporal Gyrus	lh-STG	83	Right-Superior Temporal Gyrus	rh-STG
41	Left-Supramarginal Gyrus	lh-SMG	84	Right-Supramarginal Gyrus	rh-SMG
42	Left-Frontal Pole	lh-FP	85	Right-Frontal Pole	rh-FP
43	Left-Temporal Pole	lh-TmP	86	Right-Temporal Pole	rh-TmP
44	Left-Transverse Temporal Pole	lh-TTmP	87	Right-Transverse Temporal Pole	rh-TTmP
45	Left-Insula	lh-Ins	88	Right-Insula	rh-Ins

Table A2: Cortical and subcortical regions, according to the Desikan-Killiany atlas [213].

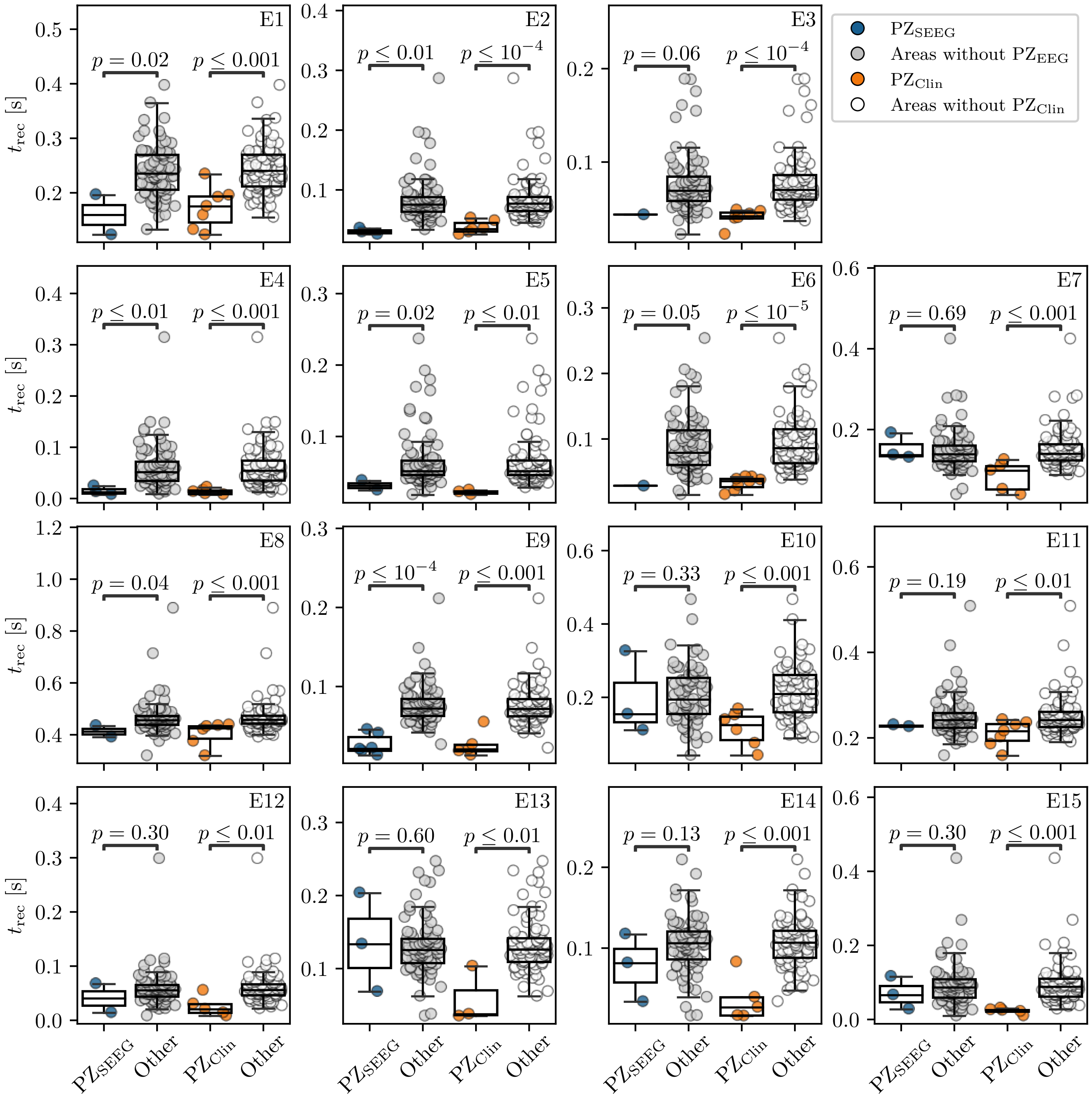

Figure A7: Statistical significance of $\mathrm{PZ_{SEEG}}$ and $\mathrm{PZ_{clin}}$ recruitment times. The figure shows the recruitment times of all brain areas on the y-axis. Blue (orange) dots correspond to $\mathrm{PZ_{SEEG}}$ ($\mathrm{PZ_{clin}}$). The grey dots correspond to all brain areas except for the EZ and the areas identified as $\mathrm{PZ_{SEEG}}$; the white dots to all brain areas except for the EZ and the areas identified as $\mathrm{PZ_{Clin}}$. Note that some brain areas of the PZ are either identified as $\mathrm{PZ_{SEEG}}$ or $\mathrm{PZ_{Clin}}$ while others are identified as both $\mathrm{PZ_{SEEG}}$ and $\mathrm{PZ_{Clin}}$. Therefore the set of grey and white dots is very similar but not identical. A one-sided Mann-Whitney U test detected significantly earlier recruitment of the $\mathrm{PZ_{SEEG}}$ ($p < 0.05$) for patients E1, E2, E4, E5, E8, and E9. For the $\mathrm{PZ_{Clin}}$, the recruitment was significantly earlier for all patients.

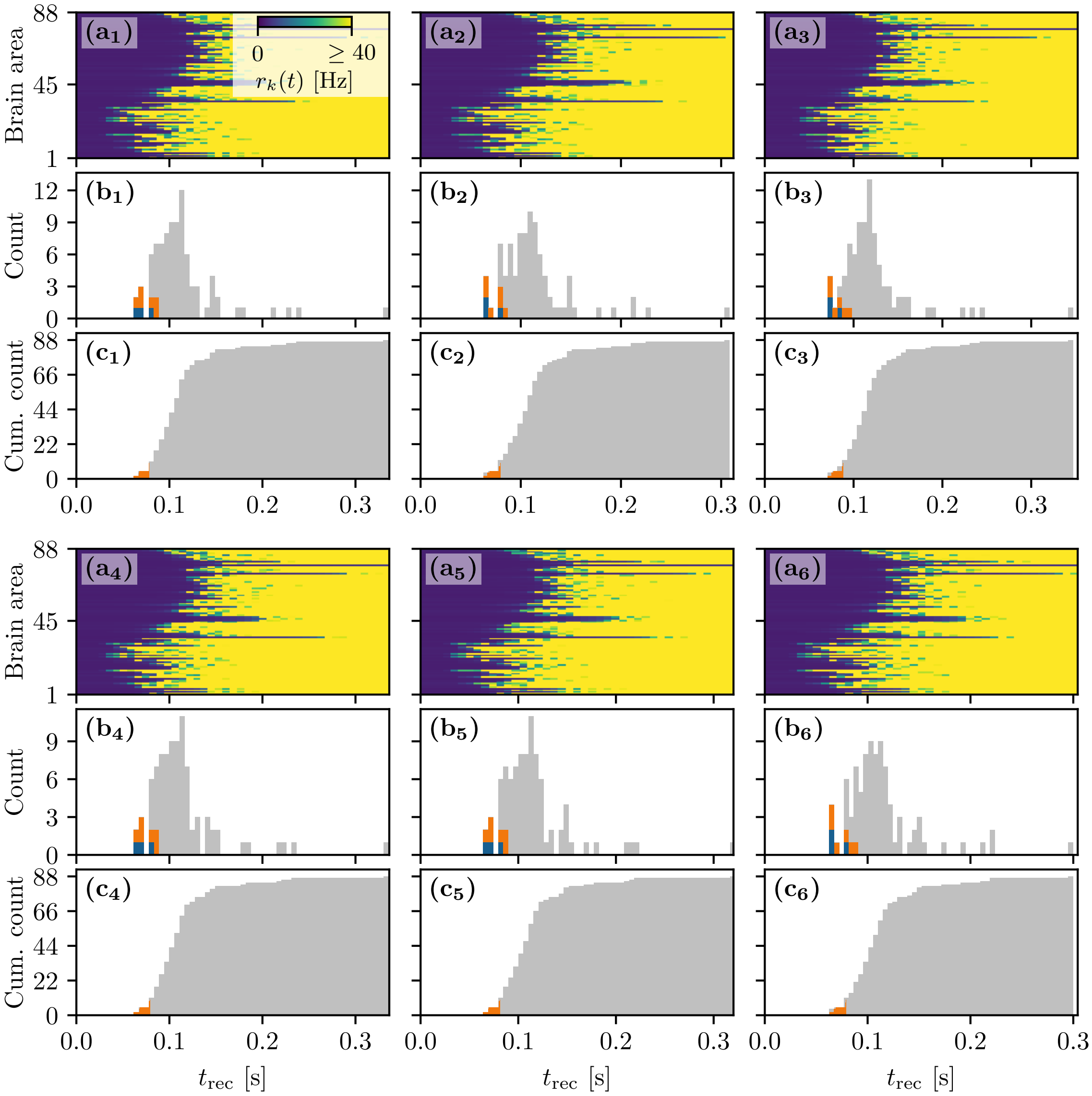

Figure A8: Recruitment times for patient E2 obtained for 6 different realizations of Gaussian distributions for $\bar{\eta}_k$. **(a)** Spacetime plots of the average firing rates of all brain areas. **(b)** Histograms of the recruitment times. Orange (blue) bins identify those recruited area that belong to PZ_{Clin} (PZ_{SEEG}). **(c)** Cumulative histograms of the recruitment times. Orange bins: first 10 recruited areas. Parameters as in Fig. 4.10. For one exemplary patient, E2, we show here in detail the impact of different realizations of $\bar{\eta}^{(k)}$, drawn from a Gaussian distribution (centred at $\bar{\eta}_G = -7.5$ with standard deviation 0.1), on the recruitment times of the brain areas. In particular we have considered it to be sufficient to present results for six out of ten realizations, due to the large similarities between the outcomes. Space-time plots of the average firing rates give an immediate visualization of the recruitment events for each brain area. We find that the pattern of recruitment does not change substantially for different realizations of the $\bar{\eta}^{(k)}$. The EZ is localized in the area lh-LOCC, that corresponds to node $k = 21$: The firing rate of this population increases immediately upon stimulation, thus giving rise to the recruitment mechanism. The brain areas in the PZ are rapidly recruited: In general the first ten areas are always recruited in less then 0.1s, followed by a continuous increase of the number of recruited nodes. Finally, it is worth noticing that the first recruited areas correspond to those predicted clinically.

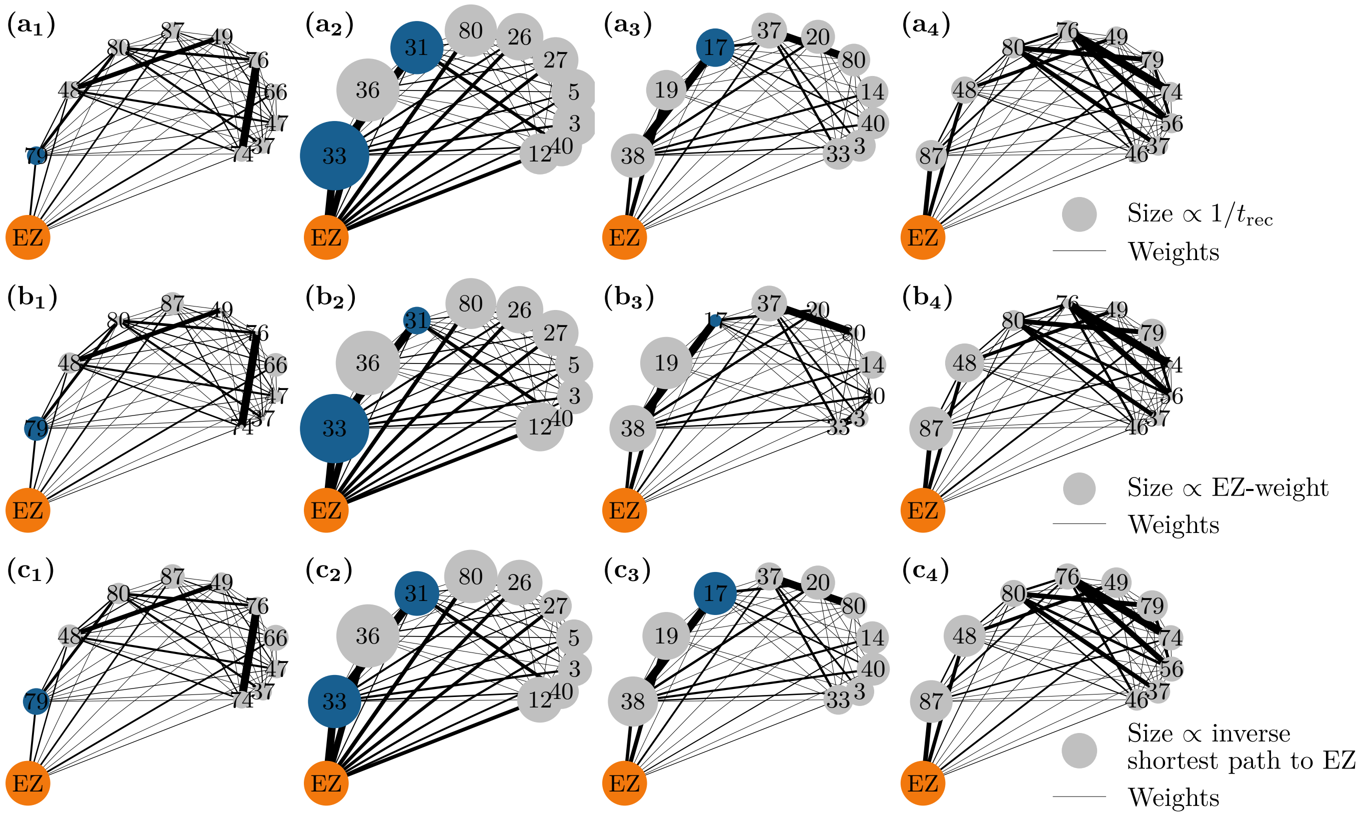

Figure A9: Graph plots for the epileptic patients with more than one area in the EZ. Same as Fig. 4.12 but for the patients with more than one area in the EZ (orange node). All areas belonging to the EZ are merged into one for visualization clarity, keeping intact the recruitment order, the recruitment times and the connection weights to the areas in the EZ. **(a)** Node size corresponds to the inverse recruitment time, **(b)** to the connection strength to the EZ (A2-D2) and **(c)** to the inverse shortest path length to the EZ. The size of the orange EZ circle remains fixed. Blue dots distinguish recruited areas to belong to the $\mathrm{PZ}_{\mathrm{SEEG}}$, i.e. the PZ identified according to the presurgical invasive evaluation. Results are obtained for patients E1 (column 1), E4 (column 2), E5 (column 3), E7 (column 4). Note that patient E1 has very weak connections outgoing the EZ which results in very late recruitment times indicated by small circle sizes in A1. For patient E4, the first ten recruited nodes are strongly connected with the EZ. The recruitment of node 31 before node 80 (stronger connected to the EZ with respect to the previous one), is justified by the strong connection to node 36 and the comparable shortest path length. For patient E5 the shortest path length is more determinant than the connection strength to the EZ to determine the recruitment order. In particular are strongly connected the nodes sequentially recruited, thus explaining the recruitment of node 17, weakly connected to the EZ, but strongly connected to the previously recruited node. Patient E4, on the other hand, has very strong connections outgoing the EZ and very short recruitment times indicated by large circle sizes in B1. As shown in Fig. 4.12, the first recruited node is usually the one with the strongest connection strength to the EZ and with the shortest path to the EZ (apart for the case B3). Parameters are as in Fig. 4.10)

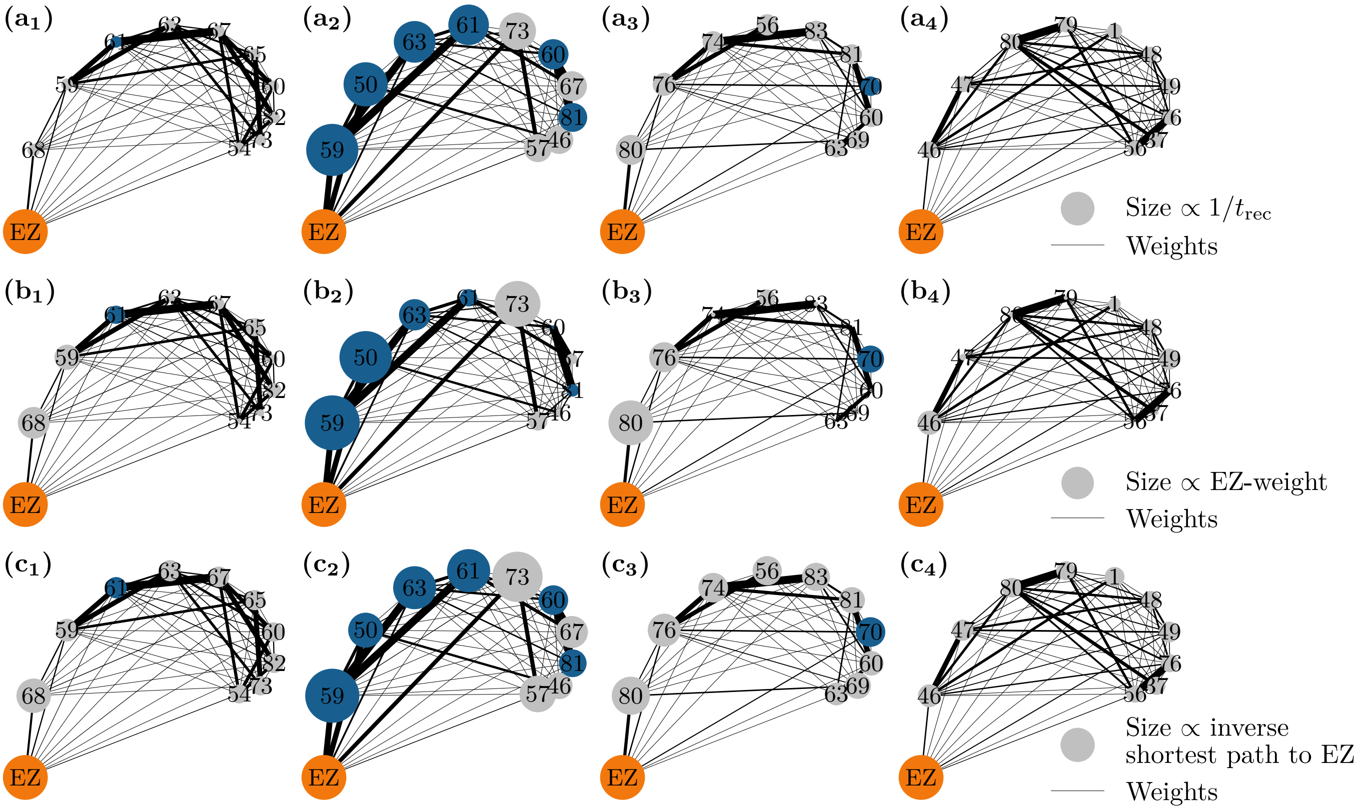

Figure A10: Graph plots for the epileptic patients with more than one area in the EZ. Same as Fig. A9 but for patients E8 (column 1), E9 (column 2), E10 (column 3), E11 (column 4). For patient E8, the first two recruited areas show strong connection strengths to the EZ, while the areas recruited later are all characterized by shortest path to the EZ and by strong connections between sequentially recruited nodes. Looking at the graph plots for patient E9, the first four recruited nodes are both strongly connected with the EZ and among them. Node 73, which do not result to belong to the $\mathrm{PZ}_{\mathrm{SEEG}}$, is recruited, according to our simulations, due to its topological characteristics: proximity to the EZ, in terms of shortest path length, and high coupling strength. For patient E10, the node 70 (belonging to the $\mathrm{PZ}_{\mathrm{SEEG}}$), do not result to be first recruited due to its middle values of connection strength and shortest path, while the nodes that are recruited before are either more strongly connected to the EZ or to the previously recruited node. For patient E11 the recruitment order is mostly determined, as before, by the shortest path length and by the connection strength between sequentially recruited node. As shown in Fig. 4.12, the first recruited node, for all patients, is the one with the strongest connection strength to the EZ and with the shortest path to the EZ. Parameters are as in Fig. 4.10.

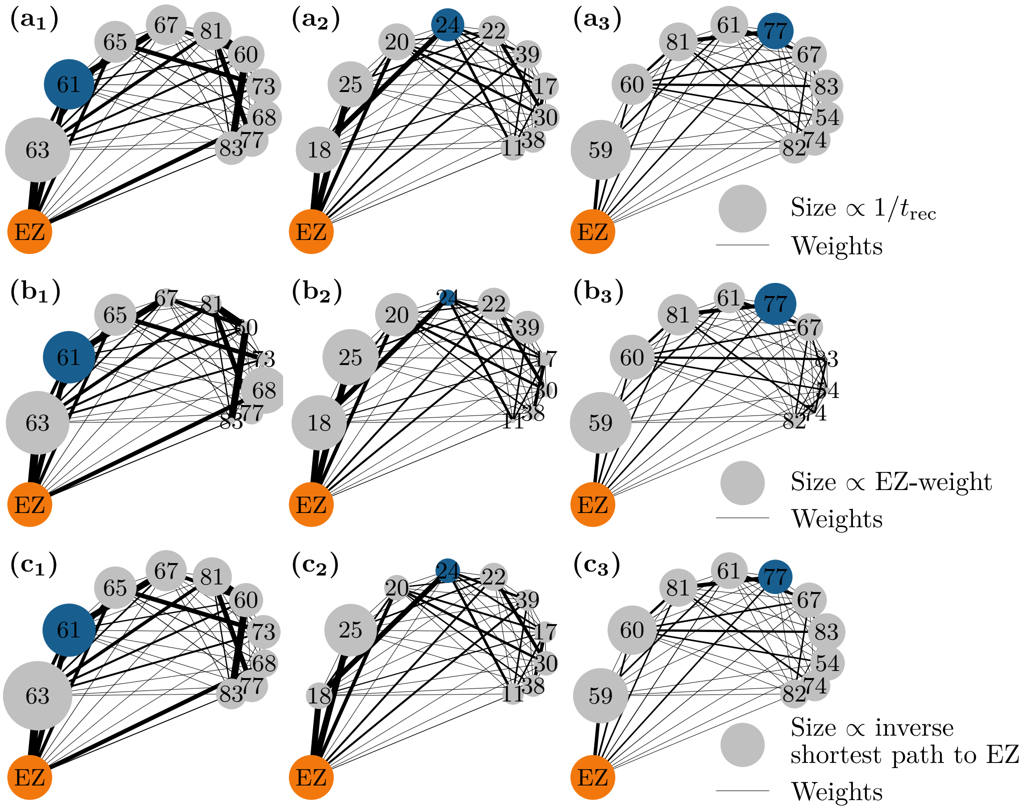

Figure A11: Graph plots for the epileptic patients with more than one area in the EZ. Same as Fig. A9 but for patients E12 (column 1), E14 (column 2), E15 (column 3). For patients E12 and E15 the recruitment order is mostly determined by the shortest path length to the EZ, supported by the connection strength, which results to be determinant for the first 4-5 recruited nodes. Node 77, belonging to the PZ_{SEEG} for patient E15, do not result to be first recruited due to its middle values of connection strength and shortest path, while the nodes that are recruited before are either more strongly connected to the EZ or to the previously recruited node. On the other hand, for patient E14, the connection strength turns out to be more important than the shortest path to determine the recruitment order. It is worth noticing that node 24, closer to the EZ and strongly connected to node 18, is recruited before nodes 22 and 39 that are more strongly connected to the EZ, but less close in terms of shortest path. As shown in Fig. 4.12, the first recruited node is usually the one with the strongest connection strength to the EZ and with the shortest path to the EZ (apart for the case B3). Parameters as in Fig. 4.10.

Patient	Gender	Epilepsy duration (years)	Age at seizure onset (years)	Epilepsy type	Surgical procedure	Surgical outcome	MRI	Histopathology	Side
E1	F	14	8	Temporo -frontal	Sr	III	Anterior temporal necrosis	Gliosis	R
E2	F	14	9	Occipital	Sr	III	N	FCD type 1	L
E3	M	35	7	Insular	GK	I	N	NA	L
E4	F	18	5	SMA	Sr	I	N	FDC type 2	L
E5	F	23	7	Parietal	Sr	I	FCD SPC	FCD type 2	L
E6	F	16	7	Premotor	Th	II	N	NA	R
E7	M	45	11	Temporo -frontal	Sr	I	FCD F	FCD type 2	R
E8	M	5	28	Temporal	Sr	III	Temporopolar hypersignal	FCD type 1	R
E9	F	18	20	Occipital	N	NO	N	NA	R
E10	M	11	18	Frontal	Sr	I	Frontal necrosis (post-trauma)	Gliosis	R
E11	F	10	17	Temporal	Gk	II	Hyppocampal sclerosis	NA	R
E12	M	15	14	Temporal	N	NO	N	NA	R
E13	M	29	7	Temporal	Sr	I	Cavernoma	Cavernoma	R
E14	M	28	35	Temporal	Sr	III	N	Gliosis	L
E15	F	24	4	Occipital	N	NO	PVH	NA	R

Table A3: Clinical characteristics of the patients. N, normal; L, left; R, right; Th, thermocoagulation; Gk, Gamma knife; Sr, surgical resection; NO, not operated; PVH, periventricular nodular heterotopia; FCD, focal cortical dysplasia; SPC, superior parietal cortex; F, Frontal; NA, not available.

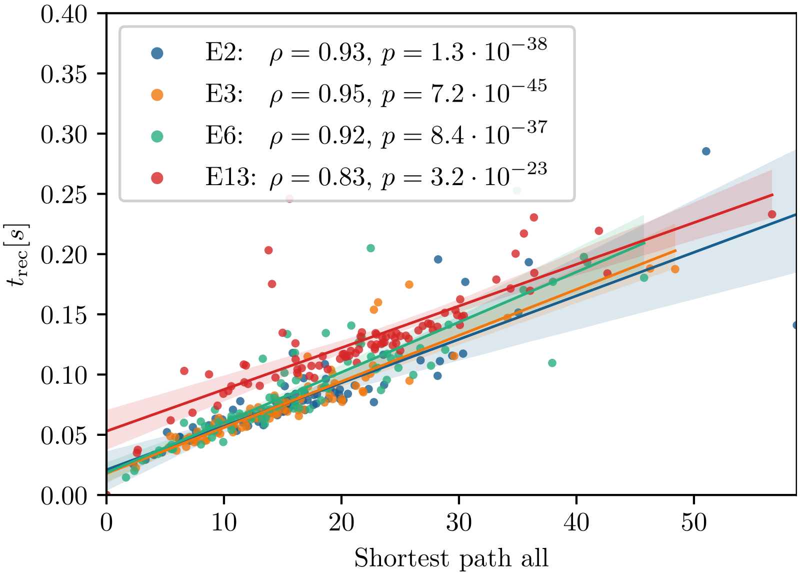

Figure A12: Recruitment time and Shortest Path. The recruitment times t_{rec} as a function of the shortest path to the EZ are shown for four patients and all brain areas. Same as Fig. 4.13(a), with a regression fit that underlines the approximately linear relationship between the shortest path length and the recruitment time. Spearman correlation coefficients ρ and corresponding p-values are significant. Parameters are as in Fig. 4.10.

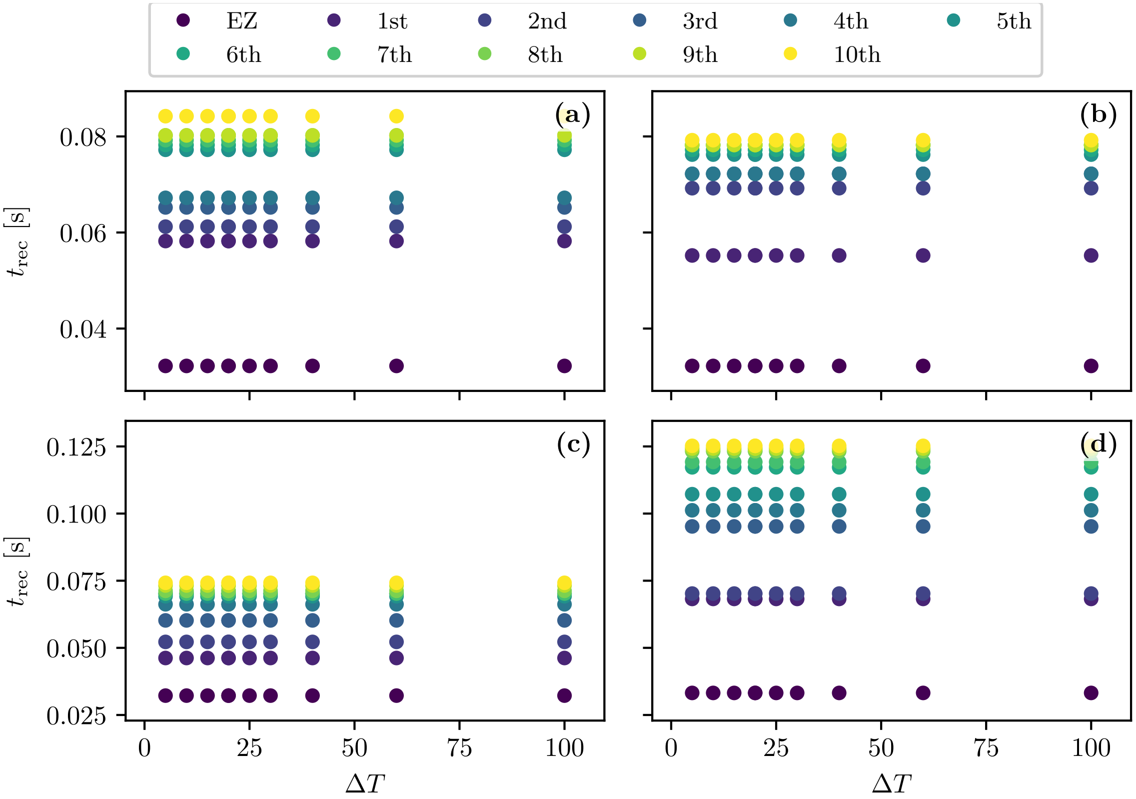

Figure A13: Input Current Duration Variation. Dependence of the recruitment time on the current duration ΔT, while the current strength is kept constant at $\Delta I = 15$, for epileptic patients **(a)** E2; **(b)** E3; **(c)** E6; **(d)** E13. The y-axis shows the recruitment times of the first 10 recruited areas for each current strength. Blue is the EZ, green is the first recruited area, red the second, etc. The recruitment times are independent of the pulse duration. Parameters: $\sigma = 4$, $\Delta = 1$, $\bar{\eta} = -12.5$, $\Delta I = 15$.

Patient	EZ location	PZ location SEEG	PZ clinical prediction
E1	rLOFC, rTmP	rRMFG, lRMFG	rRMFG, rMOFC, rPOr, rIns rPu, rPT, rAccumbes
E2	lLOCC	lFuG, lPC, lSPC	lFuG, lSPC, lITG, lIPC, lPC, lLgG
E3	lIns	lPoG	lPu, lLOFC, lSMG, lPrG, lPop, lPoG
E4	lPCG, lCMFG, lSFG	lPrG, lSPC, lPoG	lRMFG, lPrG, rSFG, lCACC, lPaC
E5	lPCG, lPCunC	lPoG, lIPC	lICC, lIPC, lSPC
E6	rPrG	rCMFG	rPoG, rCMFG, rPop, rSFG rTh, rPu, rPaC, rSMG
E7	rAmg, rTmP, rLOFC	rFuG, lPHiG, rITG	rTmP, rIns, rPu, rMOFC, rPOr, rRMFG
E8	rAmg, rHi	rITG, rTmP	rPHiG, rEntC, rTmP, rFuG, rPal, rTh
E9	rLgG, rPHiG	rHi, rFuG, rIPC, rLOCC, rSPC, rITG	rFuG, rHi, rPC, rLOCC, rICC
E10	rMOFC, rFP, rRMFG, rPOr	rPop, rMTG, rLOFC	rSFG, rPT, rPrG, rCd, rPop, rPu
E11	rHi, rAmg	rLOFC, rMTG	rTh, rLOFC, rRACC, rIns rCd, rPu, rMOFC
E12	rHi, rFuG, rEntC, rTmP	lFuG, rITG	rITG, rLOCC, rLgG, rPHiG, rAmg
E13	rFuG	rEntC, rIPC, rHi	rITG, rLOCC, rTmP
E14	lAmg, lHi, lEntC, lFuG lTmP, rEntC	lMTG, rMTG, lIns	lITG, lLOCC, lPHiG, lLgG lCerebellum
E15	rLgG, rLOCC, rCun, rPC	lPCunC, lCun, rPHiG	rFuG, rIPC, rITG, rMTG, rSPC

Table A4: Results of Propagation zone prediction for each patient. Abbreviations are given in Table A2.

Patient	Recruitment order	Recruitment time (s)	Type	Region
E1	0	0.0	EZ	rh-LOFC
E1	1	0.0005	EZ	rh-TmP
E1	2	0.123	$\mathrm{PZ}_{\mathrm{SEEG}}$, $\mathrm{PZ}_{\mathrm{Clin}}$	rh-RMFG
E1	3	0.1324	$\mathrm{PZ}_{\mathrm{Clin}}$	rh-Pu
E1	4	0.1546	other	rh-SFG
E1	5	0.1587	$\mathrm{PZ}_{\mathrm{Clin}}$	rh-Ins
E1	6	0.1718	other	rh-Pal
E1	7	0.1747	other	rh-PrG
E1	8	0.175	other	rh-MOFC
E1	9	0.1769	other	rh-Cd
E1	10	0.1797	other	lh-SFG
E1	11	0.1801	other	rh-PoG
E2	0	0.0	EZ	lh-LOCC
E2	1	0.0255	$\mathrm{PZ}_{\mathrm{SEEG}}$, $\mathrm{PZ}_{\mathrm{Clin}}$	lh-FuG
E2	2	0.0294	$\mathrm{PZ}_{\mathrm{SEEG}}$, $\mathrm{PZ}_{\mathrm{Clin}}$	lh-SPC
E2	3	0.0333	$\mathrm{PZ}_{\mathrm{Clin}}$	lh-ITG
E2	4	0.0354	$\mathrm{PZ}_{\mathrm{SEEG}}$, $\mathrm{PZ}_{\mathrm{Clin}}$	lh-IPC
E2	5	0.045	other	lh-MTG
E2	6	0.046	other	lh-SMG
E2	7	0.0466	other	lh-PCunC
E2	8	0.0479	$\mathrm{PZ}_{\mathrm{Clin}}$	lh-LgG
E2	9	0.0482	other	lh-PoG
E2	10	0.0521	other	lh-PrG
E3	0	0.0	EZ	lh-Ins
E3	1	0.0224	$\mathrm{PZ}_{\mathrm{Clin}}$	lh-Pu
E3	2	0.0369	other	lh-SFG
E3	3	0.0394	$\mathrm{PZ}_{\mathrm{Clin}}$	lh-LOFC
E3	4	0.04	$\mathrm{PZ}_{\mathrm{Clin}}$	lh-PrG
E3	5	0.0438	$\mathrm{PZ}_{\mathrm{SEEG}}$, $\mathrm{PZ}_{\mathrm{Clin}}$	lh-PoG
E3	6	0.0446	other	lh-RMFG
E3	7	0.0451	other	lh-Th
E3	8	0.0453	other	lh-CMFG
E3	9	0.0459	other	rh-SFG
E3	10	0.0465	$\mathrm{PZ}_{\mathrm{Clin}}$	lh-Pop
E4	0	0.0	EZ	lh-SFG
E4	1	0.0016	EZ	lh-CMFG
E4	2	0.0026	EZ	lh-PCG
E4	3	0.007	$\mathrm{PZ}_{\mathrm{SEEG}}$, $\mathrm{PZ}_{\mathrm{Clin}}$	lh-PrG
E4	4	0.0085	$\mathrm{PZ}_{\mathrm{Clin}}$	lh-RMFG
E4	5	0.0122	$\mathrm{PZ}_{\mathrm{SEEG}}$	lh-PoG
E4	6	0.0126	$\mathrm{PZ}_{\mathrm{Clin}}$	rh-SFG
E4	7	0.0155	$\mathrm{PZ}_{\mathrm{Clin}}$	lh-PaC
E4	8	0.0168	other	lh-Pop
E4	9	0.0168	other	lh-Pu
E4	10	0.0175	other	lh-Th
E4	11	0.0211	other	lh-SMG
E4	12	0.0212	$\mathrm{PZ}_{\mathrm{Clin}}$	lh-CACC
E5	0	0.0	EZ	lh-PCunC
E5	1	0.0006	EZ	lh-PCG
E5	2	0.0181	$\mathrm{PZ}_{\mathrm{Clin}}$	lh-SPC
E5	3	0.0219	$\mathrm{PZ}_{\mathrm{Clin}}$	lh-ICC
E5	4	0.0244	$\mathrm{PZ}_{\mathrm{SEEG}}$, PZ_{clin}	lh-IPC
E5	5	0.0284	other	lh-SFG
E5	6	0.0318	other	lh-LOCC
E5	7	0.0345	other	rh-SFG
E5	8	0.0363	other	lh-Cun
E5	9	0.0364	other	lh-SMG
E5	10	0.0366	other	lh-Th
E5	11	0.0374	other	lh-PrG

Table A5: List of the first 10 recruited brain areas for each patient. The column “Type” indicates whether the recruited area belongs or not to the PZ estimated via presurgical invasive ($\mathrm{PZ}_{\mathrm{SEEG}}$) or non-invasive ($\mathrm{PZ}_{\mathrm{Clin}}$) evaluation.

Patient	Recruitment order	Recruitment time (s)	Type	Region
E6	0	0.0	EZ	rh-PrG
E6	1	0.0146	PZ_{Clin}	rh-PoG
E6	2	0.02	PZ_{Clin}	rh-SFG
E6	3	0.0287	PZ_{SEEG}, PZ_{Clin}	rh-CMFG
E6	4	0.0342	PZ_{Clin}	rh-SMG
E6	5	0.0369	PZ_{Clin}	rh-Pop
E6	6	0.038	other	lh-SFG
E6	7	0.0382	PZ_{Clin}	rh-Th
E6	8	0.0396	other	rh-RMFG
E6	9	0.0417	PZ_{Clin}	rh-PaC
E6	10	0.042	PZ_{Clin}	rh-Pu
E7	0	0.0	EZ	rh-LOFC
E7	1	0.0012	EZ	rh-TmP
E7	2	0.0012	EZ	rh-Amg
E7	3	0.0379	PZ_{Clin}	rh-Ins
E7	4	0.0516	PZ_{Clin}	rh-Pu
E7	5	0.0875	other	rh-SFG
E7	6	0.0949	other	rh-PrG
E7	7	0.0954	other	rh-Pal
E7	8	0.098	PZ_{Clin}	rh-RMFG
E7	9	0.1027	other	rh-PoG
E7	10	0.1031	other	rh-CMFG
E7	11	0.1034	other	lh-SFG
E7	12	0.1067	other	rh-Th
E8	0	0.0	EZ	rh-Hi
E8	1	0.0003	EZ	rh-Amg
E8	2	0.3184	PZ_{Clin}	rh-PHiG
E8	3	0.3735	PZ_{Clin}	rh-FuG
E8	4	0.3905	PZ_{SEEG}	rh-ITG
E8	5	0.3965	other	rh-LOCC
E8	6	0.3999	other	rh-MTG
E8	7	0.4027	other	rh-LgG
E8	8	0.4097	other	rh-IPC
E8	9	0.4106	other	rh-STG
E8	10	0.4137	other	rh-PC
E8	11	0.4179	other	rh-bnks
E9	0	0.0	EZ	rh-LgG
E9	1	0.0006	EZ	rh-PHiG
E9	2	0.0128	PZ_{SEEG}, PZ_{Clin}	rh-FuG
E9	3	0.0181	PZ_{SEEG}, PZ_{Clin}	rh-Hi
E9	4	0.0205	PZ_{SEEG}, PZ_{Clin}	rh-LOCC
E9	5	0.0217	PZ_{SEEG}	rh-ITG
E9	6	0.0264	PZ_{Clin}	rh-PC
E9	7	0.0408	PZ_{SEEG}	rh-IPC
E9	8	0.0417	other	rh-MTG
E9	9	0.0453	PZ_{SEEG}	rh-SPC
E9	10	0.0483	other	rh-Th
E9	11	0.0483	other	rh-Cun
E10	0	0.0	EZ	rh-RMFG
E10	1	0.0006	EZ	rh-MOFC
E10	2	0.0008	EZ	rh-FP
E10	3	0.0008	EZ	rh-POr
E10	4	0.0414	PZ_{Clin}	rh-SFG
E10	5	0.0745	PZ_{Clin}	rh-PrG
E10	6	0.0882	other	rh-PoG
E10	7	0.0894	other	rh-CMFG
E10	8	0.0957	other	rh-SMG
E10	9	0.1035	other	rh-SPC
E10	10	0.1103	PZ_{SEEG}, PZ_{Clin}	rh-Pop
E10	11	0.1119	other	rh-IPC
E10	12	0.1155	other	rh-PaC

Table A6: Continued from Table A5.

Patient	Recruitment order	Recruitment time (s)	Type	Region
E11	0	0.0	EZ	rh-Hi
E11	1	0.0003	EZ	rh-Amg
E11	2	0.158	$\mathrm{PZ}_{\mathrm{Clin}}$	rh-Th
E11	3	0.185	$\mathrm{PZ}_{\mathrm{Clin}}$	rh-Cd
E11	4	0.19	other	rh-SFG
E11	5	0.1993	other	rh-RMFG
E11	6	0.2006	other	BS
E11	7	0.2015	$\mathrm{PZ}_{\mathrm{Clin}}$	rh-Pu
E11	8	0.2035	other	rh-Pal
E11	9	0.2072	other	rh-PrG
E11	10	0.2084	other	lh-SFG
E11	11	0.2123	other	rh-CMFG
E12	0	0.0	EZ	rh-FuG
E12	1	0.0006	EZ	rh-Hi
E12	2	0.0014	EZ	rh-EntC
E12	3	0.0016	EZ	rh-TmP
E12	4	0.008	$\mathrm{PZ}_{\mathrm{Clin}}$	rh-LOCC
E12	5	0.0137	$\mathrm{PZ}_{\mathrm{SEEG}}$, $\mathrm{PZ}_{\mathrm{Clin}}$	rh-ITG
E12	6	0.0202	$\mathrm{PZ}_{\mathrm{Clin}}$	rh-LgG
E12	7	0.0215	other	rh-MTG
E12	8	0.0243	other	rh-SPC
E12	9	0.0267	other	rh-IPC
E12	10	0.0288	other	rh-PC
E12	11	0.0298	$\mathrm{PZ}_{\mathrm{Clin}}$	rh-PHiG
E12	12	0.0324	other	rh-PCunC
E12	13	0.0325	other	rh-SMG
E13	0	0.0	EZ	rh-FuG
E13	1	0.035	$\mathrm{PZ}_{\mathrm{Clin}}$	rh-LOCC
E13	2	0.0375	$\mathrm{PZ}_{\mathrm{Clin}}$	rh-ITG
E13	3	0.062	other	rh-MTG
E13	4	0.0683	$\mathrm{PZ}_{\mathrm{SEEG}}$	rh-IPC
E13	5	0.0742	other	rh-SPC
E13	6	0.084	other	rh-STG
E13	7	0.0864	other	rh-SMG
E13	8	0.0903	other	rh-bnks
E13	9	0.0907	other	rh-PrG
E13	10	0.0922	other	rh-PoG
E14	0	0.0	EZ	lh-Hi
E14	1	0.0	EZ	lh-FuG
E14	2	0.0008	EZ	lh-EntC
E14	3	0.0008	EZ	lh-TmP
E14	4	0.0008	EZ	rh-EntC
E14	5	0.0008	EZ	lh-Amg
E14	6	0.016	$\mathrm{PZ}_{\mathrm{Clin}}$	lh-ITG
E14	7	0.0166	$\mathrm{PZ}_{\mathrm{Clin}}$	lh-PHiG
E14	8	0.0266	$\mathrm{PZ}_{\mathrm{Clin}}$	lh-LOCC
E14	9	0.0336	$\mathrm{PZ}_{\mathrm{SEEG}}$	lh-MTG
E14	10	0.0391	$\mathrm{PZ}_{\mathrm{Clin}}$	lh-LgG
E14	11	0.0474	other	lh-STG
E14	12	0.0504	other	lh-IPC
E15	0	0.0	EZ	rh-LOCC
E15	1	0.0003	EZ	rh-PC
E15	2	0.0003	EZ	rh-LgG
E15	3	0.0008	EZ	rh-Cun
E15	4	0.0095	$\mathrm{PZ}_{\mathrm{Clin}}$	rh-FuG
E15	5	0.021	$\mathrm{PZ}_{\mathrm{Clin}}$	rh-IPC
E15	6	0.024	$\mathrm{PZ}_{\mathrm{Clin}}$	rh-SPC
E15	7	0.0253	$\mathrm{PZ}_{\mathrm{Clin}}$	rh-ITG
E15	8	0.0272	$\mathrm{PZ}_{\mathrm{SEEG}}$	rh-PCunC
E15	9	0.0293	$\mathrm{PZ}_{\mathrm{Clin}}$	rh-MTG
E15	10	0.0338	other	rh-SMG
E15	11	0.0361	other	rh-bnks
E15	12	0.0374	other	rh-PoG

Table A7: Continued from Tables A5 and A6.

Appendix C

1 Spectrogram Estimation

In order to generate the spectrograms shown in Chapters 3 and 4 the *signal* package, which is part of the SciPy library [151], is used. The subroutine *stft* (short time Fourier transform, STFT) generates Fourier transforms $\mathcal{F}[s(t)](t,f)$ of a signal $s(t)$ within a running time window of length ΔT_{win} at time t. The STFT is performed using overlapping windows (95% overlap) throughout this work. For Figs. 3.3 to 3.5, 4.2 and 4.9 the window length is set to $\Delta T_{\text{win}} = 0.2$ s, leading to a sufficiently fine resolution in time and frequency. For Figs. 3.8 to 3.10, it is set to $\Delta T_{\text{win}} = 1$ s, resulting in a better frequency resolution and decrease of time-resolution. The colors in the spectrograms code the normalized power spectral density $|\mathcal{F}[v_k(t)](t,f)|^2/(\max|\mathcal{F}[v_k(t)](t,f)|^2)$ obtained from voltage signals v_k of different populations. For better visibility a log10 scale is used and values $< 10^{-2}$ set to 10^{-2}. To obtain the data f_{avg} shown in Figs. 4.2 and 4.9 the Fourier transforms of the individual voltage signals v_k of different populations are first calculated giving rise to individual power spectral densities, which are subsequently averaged over the populations. Finally the spectrograms in Figs. 3.3 to 3.5, 4.2 and 4.9 are shifted to the right by 0.1 s and in Figs. 3.8 to 3.10 by 0.35 s to preserve causality in correspondence of the stimulus onset.

Since the average membrane potential is not accessible for the firing rate model Eqs. (3.5) and (3.7), in this case we made use of simulated local field potentials LFP_k in order to estimate the spectrograms. By following [331], we have estimated the local field potentials for the three populations appearing in the multi-item architecture displayed in Fig. 3.2 as the sum of the absolute values of the synaptic inputs stimulating each populations:

$$\text{LFP}_0 = -[|J_{\text{ie}}|(r_1 + r_2) + |J_{\text{ii}}|r_0] \tag{6.14a}$$

$$\text{LFP}_1 = -[|J_{\text{ee}}^{(\text{s})}|x_1u_1r_1 + |J_{\text{ee}}^{(\text{c})}|x_2u_2r_2 + |J_{\text{ei}}|r_0] \tag{6.14b}$$

$$\text{LFP}_2 = -[|J_{\text{ee}}^{(\text{s})}|x_2u_2r_2 + |J_{\text{ee}}^{(\text{c})}|x_1u_1r_1 + |J_{\text{ei}}|r_0] \tag{6.14c}$$

where we neglect the constant current components for the calculation of the LFPs, as they do not contribute to the frequency spectra. Furthermore, to make a comparison possible with experimental measurements where high (low) activity states correspond to a minimum (maximum) value of the LFPs, we reversed the sign of the synaptic inputs in (6.14).

2 Numerical methods

Numerical bifurcation analysis

The results in Fig. 2.2(b), Fig. 2.5, Fig. 3.14, Fig. 5.2(a), Fig. 5.3, Fig. 5.4, Fig. 5.5(b), Fig. 5.6, Fig. 5.7, Fig. 5.8 and Fig. 5.9 Fig. 5.10(a) have been obtained using the continuation software AUTO-07p [153].

Neural mass simulations

The numerical integration of neural mass models of the form Eq. (2.46) was performed in Python, using the adaptive Dormand-Prince method [332].

QIF network simulation

Direct simulations of the QIF network with STP given in Eqs. (2.44) were performed in Python. The numerical integration requires simplifications of the problem, in order to maintain reasonable computation times. For this we followed the method suggested in [16]. First of all, the network is integrated using the Euler scheme, with a timestep $dt = 10^{-4}$. Second, the limit $V_{\text{thresh}} \to \infty$ is not realizable numerically. However, one can approximate the time T_∞ required for the membrane potential of a QIF neuron to evolve from a value $V_{\max}$ to infinity as $T_\infty \approx \frac{1}{V_{\max}}$, given that the total input I to that neuron fulfills $\sqrt{I} \ll V_{\max}$. The time from negative infinity to $V_i = -V_{\max}$ is given by the same expression. As soon as a neuron crosses the threshold $V_i > V_{\max}$ it is reset to $V_i = -V_{\max}$ and enters into a refractory period of $2T_\infty = 2/V_{\max}$, for which its dynamics is deactivated. This is to account for the integration from $V_i = V_{\max}$ to infinity and from negative infinity to $V_i = -V_{\max}$. A spike is registered at half of this refractory period, via an instantaneous change of all membrane potentials and the synaptic variables, as stated below.

$$V_i(t^+) = \frac{J}{N} u(t^-) x(t^-) \tag{6.15}$$

$$x(t^+) = x(t^-) - \frac{1}{N} u(t^-) x(t^-) \tag{6.16}$$

$$u(t^+) = u(t^-) + \frac{1}{N} U_0 (1 - u(t^-)) \tag{6.17}$$

For clarity the time before the increment is denoted by t^-, the time after by t^+.

Deterministic Lorentzian distribution

The QIF network simulations use values of the Lorentzian distributed constant currents η_i, that are deterministically set as given below.

$$\eta_i = \bar{\eta} + \Delta \tan\left(\frac{\pi(2i - N - 1)}{2(N+1)}\right) \tag{6.18}$$

Code availability

The simulation results presented in this thesis were obtained using Python. The code is available under: https://github.com/halgurdtaher/MeanfieldQIF. The example "MesoscopicSTP" reproduces the results reported in Fig. 3.1(b) of Chapter 3.

Bibliography

[1] L. Squire et al. *Fundamental Neuroscience*. Academic press, 2012.

[2] V. N. Friedhoff et al. "Models of Stochastic Ca2+ Spiking". *The European Physical Journal Special Topics* (June 2021).

[3] A. Newton et al. "Using NEURON for Reaction-Diffusion Modeling of Extracellular Dynamics". *Front Neuroinform* 12 (2018).

[4] P. Sanz Leon et al. "The Virtual Brain: A Simulator of Primate Brain Network Dynamics". *Frontiers in Neuroinformatics* 7 (2013), p. 10.

[5] K. S. Türker and R. K. Powers. "Black Box Revisited: A Technique for Estimating Postsynaptic Potentials in Neurons". *Trends in Neurosciences* 28.7 (July 2005), pp. 379–386.

[6] B. Pesaran et al. "Investigating Large-Scale Brain Dynamics Using Field Potential Recordings: Analysis and Interpretation". *Nature Neuroscience* 21.7 (July 2018), pp. 903–919.

[7] H. R. Wilson and J. D. Cowan. "Excitatory and Inhibitory Interactions in Localized Populations of Model Neurons". *Biophysical Journal* 12.1 (Jan. 1972), pp. 1–24.

[8] J. J. Hopfield. "Neurons with Graded Response Have Collective Computational Properties like Those of Two-State Neurons". *Proceedings of the National Academy of Sciences* 81.10 (May 1984), pp. 3088–3092.

[9] G. Mongillo, O. Barak, and M. Tsodyks. "Synaptic Theory of Working Memory". *Science* 319.5869 (Mar. 2008), pp. 1543–1546.

[10] Y. Mi, M. Katkov, and M. Tsodyks. "Synaptic Correlates of Working Memory Capacity". *Neuron* 93.2 (Jan. 2017), pp. 323–330.

[11] R. Moreno-Bote, J. Rinzel, and N. Rubin. "Noise-Induced Alternations in an Attractor Network Model of Perceptual Bistability". *Journal of Neurophysiology* 98.3 (Sept. 2007), pp. 1125–1139.

[12] W. Erlhagen and G. Schöner. "Dynamic Field Theory of Movement Preparation". *Psychological Review* 109.3 (2002), pp. 545–572.

[13] E. Thelen et al. "The Dynamics of Embodiment: A Field Theory of Infant Perseverative Reaching". *Behavioral and Brain Sciences* 24.1 (Feb. 2001), pp. 1–34.

[14] K.-F. Wong and X.-J. Wang. "A Recurrent Network Mechanism of Time Integration in Perceptual Decisions". *Journal of Neuroscience* 26.4 (Jan. 2006), pp. 1314–1328.

[15] E. Ott and T. M. Antonsen. "Low Dimensional Behavior of Large Systems of Globally Coupled Oscillators". *Chaos: An Interdisciplinary Journal of Nonlinear Science* 18.3 (Sept. 2008), p. 037113.

[16] E. Montbrió, D. Pazó, and A. Roxin. "Macroscopic Description for Networks of Spiking Neurons". *Physical Review X* 5.2 (June 2015), p. 021028.

[17] C. van Vreeswijk and H. Sompolinsky. "Chaos in Neuronal Networks with Balanced Excitatory and Inhibitory Activity". *Science* 274.5293 (Dec. 1996), pp. 1724–1726.

[18] N. Brunel. "Dynamics of Sparsely Connected Networks of Excitatory and Inhibitory Spiking Neurons". *Journal of Computational Neuroscience* 8.3 (May 2000), pp. 183–208.

[19] S. Majhi et al. "Chimera States in Neuronal Networks: A Review". *Physics of Life Reviews* 28 (Mar. 2019), pp. 100–121.

[20] M. Canepari et al. "Experimental Analysis of Neuronal Dynamics in Cultured Cortical Networks and Transitions between Different Patterns of Activity". *Biological Cybernetics* 77.2 (Aug. 1997), pp. 153–162.

[21] S. F. Farmer. "Rhythmicity, Synchronization and Binding in Human and Primate Motor Systems". *The Journal of Physiology* 509.1 (1998), pp. 3–14.

[22] W. B. Adams and J. A. Benson. "The Generation and Modulation of Endogenous Rhythmicity in the Aplysia Bursting Pacemaker Neurone R15". *Progress in Biophysics and Molecular Biology* 46.1 (Jan. 1985), pp. 1–49.

[23] M. Womack and K. Khodakhah. "Active Contribution of Dendrites to the Tonic and Trimodal Patterns of Activity in Cerebellar Purkinje Neurons". *Journal of Neuroscience* 22.24 (Dec. 2002), pp. 10603–10612.

[24] V. N. Murthy and E. E. Fetz. "Synchronization of Neurons during Local Field Potential Oscillations in Sensorimotor Cortex of Awake Monkeys". *Journal of Neurophysiology* 76.6 (Dec. 1996), pp. 3968–3982.

[25] T. Paus, P. K. Sipila, and A. P. Strafella. "Synchronization of Neuronal Activity in the Human Primary Motor Cortex by Transcranial Magnetic Stimulation: An EEG Study". *Journal of Neurophysiology* 86.4 (Oct. 2001), pp. 1983–1990.

[26] G. Buzsáki, C. A. Anastassiou, and C. Koch. "The Origin of Extracellular Fields and Currents — EEG, ECoG, LFP and Spikes". *Nature Reviews Neuroscience* 13.6 (June 2012), pp. 407–420.

[27] S. Coombes and Á. Byrne. "Next Generation Neural Mass Models". *Nonlinear Dynamics in Computational Neuroscience*. Ed. by F. Corinto and A. Torcini. PoliTO Springer Series. Cham: Springer International Publishing, 2019, pp. 1–16.

[28] E. Ott and T. M. Antonsen. "Long Time Evolution of Phase Oscillator Systems". *Chaos: An Interdisciplinary Journal of Nonlinear Science* 19.2 (May 2009), p. 023117.

[29] Y. Kuramoto. "International Symposium on Mathematical Problems in Theoretical Physics". *Lecture notes in Physics* 30 (1975), p. 420.

[30] G. B. Ermentrout and N. Kopell. "Parabolic Bursting in an Excitable System Coupled with a Slow Oscillation". *SIAM Journal on Applied Mathematics* 46.2 (Apr. 1986), pp. 233–253.

[31] D. Pazó and E. Montbrió. "From Quasiperiodic Partial Synchronization to Collective Chaos in Populations of Inhibitory Neurons with Delay". *Physical Review Letters* 116.23 (June 2016), p. 238101.

[32] H. Schmidt et al. "Network Mechanisms Underlying the Role of Oscillations in Cognitive Tasks". *PLOS Computational Biology* 14.9 (Sept. 2018), e1006430.

[33] M. Segneri et al. "Theta-Nested Gamma Oscillations in Next Generation Neural Mass Models". *Frontiers in Computational Neuroscience* 14 (2020), p. 47.

[34] B. Pietras et al. "Exact Firing Rate Model Reveals the Differential Effects of Chemical versus Electrical Synapses in Spiking Networks". *Physical Review E* 100.4 (Oct. 2019), p. 042412.

[35] E. Montbrió and D. Pazó. "Exact Mean-Field Theory Explains the Dual Role of Electrical Synapses in Collective Synchronization". *Physical Review Letters* 125.24 (Dec. 2020), p. 248101.

[36] M. di Volo and A. Torcini. "Transition from Asynchronous to Oscillatory Dynamics in Balanced Spiking Networks with Instantaneous Synapses". *Physical Review Letters* 121.12 (Sept. 2018), p. 128301.

[37] D. S. Goldobin, M. di Volo, and A. Torcini. "Reduction Methodology for Fluctuation Driven Population Dynamics". *Physical Review Letters* 127.3 (July 2021), p. 038301.

[38] M. V. Tsodyks and H. Markram. "The Neural Code between Neocortical Pyramidal Neurons Depends on Neurotransmitter Release Probability". *Proceedings of the National Academy of Sciences* 94.2 (Jan. 1997), pp. 719–723.

[39] M. Tsodyks, K. Pawelzik, and H. Markram. "Neural Networks with Dynamic Synapses". *Neural computation* 10.4 (1998), pp. 821–835.

[40] S. Funahashi, C. J. Bruce, and P. S. Goldman-Rakic. "Mnemonic Coding of Visual Space in the Monkey's Dorsolateral Prefrontal Cortex". *Journal of neurophysiology* 61.2 (1989), pp. 331–349.

[41] E. K. Miller, C. A. Erickson, and R. Desimone. "Neural Mechanisms of Visual Working Memory in Prefrontal Cortex of the Macaque". *Journal of Neuroscience* 16.16 (1996), pp. 5154–5167.

[42] R. Romo et al. "Neuronal Correlates of Parametric Working Memory in the Prefrontal Cortex". *Nature* 399.6735 (1999), pp. 470–473.

[43] D. Trübutschek et al. "A Theory of Working Memory without Consciousness or Sustained Activity". *eLife* 6 (July 2017). Ed. by T. Pasternak, e23871.

[44] L. Postman and L. W. Phillips. "Short-Term Temporal Changes in Free Recall". *Quarterly journal of experimental psychology* 17.2 (1965), pp. 132–138.

[45] A. B. Morrison, A. R. Conway, and J. M. Chein. "Primacy and Recency Effects as Indices of the Focus of Attention". *Frontiers in human neuroscience* 8 (2014), p. 6.

[46] F. Devalle, A. Roxin, and E. Montbrió. "Firing Rate Equations Require a Spike Synchrony Mechanism to Correctly Describe Fast Oscillations in Inhibitory Networks". *PLOS Computational Biology* 13.12 (Dec. 2017). Ed. by S. Gruen, e1005881.

[47] B. Spitzer, E. Wacker, and F. Blankenburg. "Oscillatory Correlates of Vibrotactile Frequency Processing in Human Working Memory". *Journal of Neuroscience* 30.12 (2010), pp. 4496–4502.

[48] M. Siegel, M. R. Warden, and E. K. Miller. "Phase-Dependent Neuronal Coding of Objects in Short-Term Memory". *Proceedings of the National Academy of Sciences* 106.50 (2009), pp. 21341–21346.

[49] M. Lundqvist et al. "Gamma and Beta Bursts Underlie Working Memory". *Neuron* 90.1 (2016), pp. 152–164.

[50] F. Rosenow and H. Lüders. "Presurgical Evaluation of Epilepsy". *Brain : a journal of neurology* 124.9 (2001), pp. 1683–1700.

[51] J. Talairach and J. Bancaud. "Lesion," Irritative" Zone and Epileptogenic Focus". *Stereotactic and Functional Neurosurgery* 27.1-3 (1966), pp. 91–94.

[52] F. Bartolomei et al. "Neural Networks Involving the Medial Temporal Structures in Temporal Lobe Epilepsy". *Clinical neurophysiology* 112.9 (2001), pp. 1746–1760.

[53] S. S. Spencer. "Neural Networks in Human Epilepsy: Evidence of and Implications for Treatment". *Epilepsia* 43.3 (2002), pp. 219–227.

[54] M. P. Richardson. "Large Scale Brain Models of Epilepsy: Dynamics Meets Connectomics". *Journal of Neurology, Neurosurgery & Psychiatry* 83.12 (2012), pp. 1238–1248.

[55] M. Goodfellow et al. "Computer Models to Inform Epilepsy Surgery Strategies: Prediction of Postoperative Outcome". *Brain : a journal of neurology* 140.5 (2017), e30–e30.

[56] M. A. Lopes et al. "An Optimal Strategy for Epilepsy Surgery: Disruption of the Rich-Club?" *PLoS computational biology* 13.8 (2017), e1005637.

[57] M. A. Lopes, M. Goodfellow, and J. R. Terry. "A Model-Based Assessment of the Seizure Onset Zone Predictive Power to Inform the Epileptogenic Zone". *Frontiers in computational neuroscience* 13 (2019), p. 25.

[58] B. W. Connors and M. J. Gutnick. "Intrinsic Firing Patterns of Diverse Neocortical Neurons". *Trends in Neurosciences* 13.3 (Mar. 1990), pp. 99–104.

[59] C. M. Gray and D. A. McCormick. "Chattering Cells: Superficial Pyramidal Neurons Contributing to the Generation of Synchronous Oscillations in the Visual Cortex". *Science* 274.5284 (Oct. 1996), pp. 109–113.

[60] P. Schwindt, J. A. O'Brien, and W. Crill. "Quantitative Analysis of Firing Properties of Pyramidal Neurons From Layer 5 of Rat Sensorimotor Cortex". *Journal of Neurophysiology* 77.5 (May 1997), pp. 2484–2498.

[61] H. Su et al. "Extracellular Calcium Modulates Persistent Sodium Current-Dependent Burst-Firing in Hippocampal Pyramidal Neurons". *Journal of Neuroscience* 21.12 (June 2001), pp. 4173–4182.

[62] R. Amir et al. "Oscillatory Mechanism in Primary Sensory Neurones". *Brain* 125.2 (Feb. 2002), pp. 421–435.

[63] J. Wellmer et al. "Long-Lasting Modification of Intrinsic Discharge Properties in Subicular Neurons Following Status Epilepticus". *European Journal of Neuroscience* 16.2 (2002), pp. 259–266.

[64] J. Rinzel. "Bursting Oscillations in an Excitable Membrane Model". *Ordinary and Partial Differential Equations (Proceedings of the Eighth Conference Held at Dundee, Scotland, June 25-29, 1984)*. Ed. by B. D Sleeman and R. J. Jarvis. Vol. **1511**. Lecture Notes in Mathematics. Springer, 1985, pp. 304–316.

[65] J. Rinzel. "A Formal Classification of Bursting Mechanisms in Excitable Systems". *Mathematical Topics in Population Biology, Morphogenesis and Neurosciences (Proceedings of an International Symposium Held in Kyoto, November 10-15, 1985)*. Ed. by E. Termato and M. Yumaguti. Vol. **71**. Lecture Notes in Biomathematics. Springer, 1987, pp. 267–281.

[66] E. Benoît et al. "Chasse Au Canard". *Collectanea Mathematica* **32**.1-2 (1981), pp. 37–119.

[67] M. Ciszak et al. "Emergent Excitability in Populations of Nonexcitable Units". *Physical Review E* 102.5 (2020), p. 050201.

[68] D. Avitabile, M. Desroches, and G. B. Ermentrout. "Cross-Scale Excitability in Networks of Quadratic Integrate-and-Fire Neurons" (Aug. 2021).

[69] M. Desroches et al. "Canards of Mixed Type in a Neural Burster". *Physical Review E* 85.2 (2012), p. 021920.

[70] G. Stuart, N. Spruston, and M. Häusser. *Dendrites*. Oxford University Press, 2016.

[71] A. L. Hodgkin. "The Local Electric Changes Associated with Repetitive Action in a Non-Medullated Axon". *The Journal of physiology* 107.2 (1948), pp. 165–181.

[72] L. Lapique. "Recherches Quantitatives Sur l'excitation Electrique Des Nerfs Traitee Comme Une Polarization." *Journal of Physiology and Pathololgy* 9 (1907), pp. 620–635.

[73] N. Brunel and M. C. W. van Rossum. "Lapicque's 1907 Paper: From Frogs to Integrate-and-Fire". *Biological Cybernetics* 97.5 (Dec. 2007), pp. 337–339.

[74] R. Moreno et al. "Response of Spiking Neurons to Correlated Inputs". *Physical Review Letters* 89.28 (Dec. 2002), p. 288101.

[75] G. C. Cardarilli et al. "Spiking Neural Networks Based on LIF with Latency: Simulation and Synchronization Effects". *2013 Asilomar Conference on Signals, Systems and Computers*. Nov. 2013, pp. 1838–1842.

[76] E. Izhikevich. "Which Model to Use for Cortical Spiking Neurons?" *IEEE Transactions on Neural Networks* 15.5 (Sept. 2004), pp. 1063–1070.

[77] E. Izhikevich. "Simple Model of Spiking Neurons". *IEEE Transactions on Neural Networks* 14.6 (Nov. 2003), pp. 1569–1572.

[78] Ş. Mihalaş and E. Niebur. "A Generalized Linear Integrate-and-Fire Neural Model Produces Diverse Spiking Behaviors". *Neural Computation* 21.3 (Mar. 2009), pp. 704–718.

[79] A. Geminiani et al. "Complex Dynamics in Simplified Neuronal Models: Reproducing Golgi Cell Electroresponsiveness". *Frontiers in Neuroinformatics* 12 (2018), p. 88.

[80] R. Brette and W. Gerstner. "Adaptive Exponential Integrate-and-Fire Model as an Effective Description of Neuronal Activity". *Journal of Neurophysiology* 94.5 (Nov. 2005), pp. 3637–3642.

[81] C. Cakan and K. Obermayer. "Biophysically Grounded Mean-Field Models of Neural Populations under Electrical Stimulation". *PLOS Computational Biology* 16.4 (Apr. 2020), e1007822.

[82] T. Górski, D. Depannemaecker, and A. Destexhe. "Conductance-Based Adaptive Exponential Integrate-and-Fire Model". *Neural Computation* 33.1 (Jan. 2021), pp. 41–66.

[83] B. Ermentrout. "Type I Membranes, Phase Resetting Curves, and Synchrony". *Neural Computation* 8.5 (July 1996), pp. 979–1001.

[84] R. FitzHugh. "Impulses and Physiological States in Theoretical Models of Nerve Membrane". *Biophysical journal* 1.6 (1961), pp. 445–466.

[85] J. Nagumo, S. Arimoto, and S. Yoshizawa. "An Active Pulse Transmission Line Simulating Nerve Axon". *Proceedings of the IRE* 50.10 (1962), pp. 2061–2070.

[86] C. Morris and H. Lecar. "Voltage Oscillations in the Barnacle Giant Muscle Fiber". *Biophysical Journal* 35.1 (July 1981), pp. 193–213.

[87] A. Ceni et al. "Cross Frequency Coupling in next Generation Inhibitory Neural Mass Models". *Chaos: An Interdisciplinary Journal of Nonlinear Science* 30.5 (2020), p. 053121.

[88] D. Pazó and E. Montbrió. "Low-Dimensional Dynamics of Populations of Pulse-Coupled Oscillators". *Physical Review X* 4.1 (Jan. 2014), p. 011009.

[89] H. Markram, Y. Wang, and M. Tsodyks. “Differential Signaling via the Same Axon of Neocortical Pyramidal Neurons”. *Proceedings of the National Academy of Sciences* 95.9 (1998), pp. 5323–5328.

[90] Y. Wang et al. “Heterogeneity in the Pyramidal Network of the Medial Prefrontal Cortex”. *Nature Neuroscience* 9.4 (Apr. 2006), pp. 534–542.

[91] M. di Volo et al. “Synchronous Dynamics in the Presence of Short-Term Plasticity”. *Physical Review E* 87.3 (2013), p. 032801.

[92] V. Schmutz, W. Gerstner, and T. Schwalger. “Mesoscopic Population Equations for Spiking Neural Networks with Synaptic Short-Term Plasticity”. *The Journal of Mathematical Neuroscience* 10.1 (2020), pp. 1–32.

[93] B. Van der Pol. “LXXXVIII. On “Relaxation-Oscillations””. *The London, Edinburgh, and Dublin Philosophical Magazine and Journal of Science* 2.11 (1926), pp. 978–992.

[94] M. Brøns. “Bifurcations and Instabilities in the Greitzer Model for Compressor System Surge”. *Math. Eng. Ind* 2.1 (1988), pp. 51–63.

[95] E. Baspinar, D. Avitabile, and M. Desroches. “Canonical Models for Torus Canards in Elliptic Bursters”. *Chaos: An Interdisciplinary Journal of Nonlinear Science* 31.6 (June 2021), p. 063129.

[96] G. N. Benes et al. “An Elementary Model of Torus Canards”. *Chaos: An Interdisciplinary Journal of Nonlinear Science* 21.2 (2011), p. 023131.

[97] J. Burke et al. “A Showcase of Torus Canards in Neuronal Bursters”. *The Journal of Mathematical Neuroscience* 2.1 (2012), pp. 1–30.

[98] H. Taher, A. Torcini, and S. Olmi. “Exact Neural Mass Model for Synaptic-Based Working Memory”. *PLOS Computational Biology* 16.12 (Dec. 2020), e1008533.

[99] M. A. Just and P. A. Carpenter. “A Capacity Theory of Comprehension: Individual Differences in Working Memory.” *Psychological review* 99.1 (1992), p. 122.

[100] P. Goldman-Rakic. “Cellular Basis of Working Memory”. *Neuron* 14.3 (1995), pp. 477–485.

[101] R. W. Engle et al. “Working Memory, Short-Term Memory, and General Fluid Intelligence: A Latent-Variable Approach.” *Journal of experimental psychology: General* 128.3 (1999), p. 309.

[102] J. M. Fuster. *Memory in the Cerebral Cortex: An Empirical Approach to Neural Networks in the Human and Nonhuman Primate.* MIT press, 1999.

[103] E. K. Vogel and M. G. Machizawa. “Neural Activity Predicts Individual Differences in Visual Working Memory Capacity”. *Nature* 428.6984 (2004), pp. 748–751.

[104] C. H. Chatham and D. Badre. “Multiple Gates on Working Memory”. *Current opinion in behavioral sciences* 1 (2015), pp. 23–31.

[105] J. M. Fuster and G. E. Alexander. “Neuron Activity Related to Short-Term Memory”. *Science (New York, N.Y.)* 173.3997 (1971), pp. 652–654.

[106] E. K. Miller and J. D. Cohen. “An Integrative Theory of Prefrontal Cortex Function”. *Annual review of neuroscience* 24.1 (2001), pp. 167–202.

[107] A. H. Lara and J. D. Wallis. “The Role of Prefrontal Cortex in Working Memory: A Mini Review”. *Frontiers in systems neuroscience* 9 (2015), p. 173.

[108] M. Dipoppa, M. Szwed, and B. S. Gutkin. “Controlling Working Memory Operations by Selective Gating: The Roles of Oscillations and Synchrony”. *Advances in cognitive psychology* 12.4 (2016), p. 209.

[109] C. Constantinidis et al. "Persistent Spiking Activity Underlies Working Memory". *Journal of Neuroscience* 38.32 (2018), pp. 7020–7028.

[110] A. Compte et al. "Synaptic Mechanisms and Network Dynamics Underlying Spatial Working Memory in a Cortical Network Model". *Cerebral cortex* 10.9 (2000), pp. 910–923.

[111] C. K. Machens, R. Romo, and C. D. Brody. "Flexible Control of Mutual Inhibition: A Neural Model of Two-Interval Discrimination". *Science (New York, N.Y.)* 307.5712 (2005), pp. 1121–1124.

[112] A. Gevins et al. "High-Resolution EEG Mapping of Cortical Activation Related to Working Memory: Effects of Task Difficulty, Type of Processing, and Practice." *Cerebral cortex (New York, NY: 1991)* 7.4 (1997), pp. 374–385.

[113] O. Jensen and C. D. Tesche. "Frontal Theta Activity in Humans Increases with Memory Load in a Working Memory Task". *European journal of Neuroscience* 15.8 (2002), pp. 1395–1399.

[114] C. Tallon-Baudry et al. "Induced γ-Band Activity during the Delay of a Visual Short-Term Memory Task in Humans". *Journal of Neuroscience* 18.11 (1998), pp. 4244–4254.

[115] M. W. Howard et al. "Gamma Oscillations Correlate with Working Memory Load in Humans". *Cerebral cortex* 13.12 (2003), pp. 1369–1374.

[116] B. Pesaran et al. "Temporal Structure in Neuronal Activity during Working Memory in Macaque Parietal Cortex". *Nature neuroscience* 5.8 (2002), pp. 805–811.

[117] K. Wimmer et al. "Transitions between Multiband Oscillatory Patterns Characterize Memory-Guided Perceptual Decisions in Prefrontal Circuits". *Journal of Neuroscience* 36.2 (2016), pp. 489–505.

[118] P. Sauseng et al. "Brain Oscillatory Substrates of Visual Short-Term Memory Capacity". *Current biology* 19.21 (2009), pp. 1846–1852.

[119] J. E. Lisman and M. A. Idiart. "Storage of 7+/-2 Short-Term Memories in Oscillatory Subcycles". *Science (New York, N.Y.)* 267.5203 (1995), pp. 1512–1515.

[120] O. Jensen and J. E. Lisman. "Novel Lists of 7+/-2 Known Items Can Be Reliably Stored in an Oscillatory Short-Term Memory Network: Interaction with Long-Term Memory." *Learning & Memory* 3.2-3 (1996), pp. 257–263.

[121] N. Kopell, M. A. Whittington, and M. A. Kramer. "Neuronal Assembly Dynamics in the Beta1 Frequency Range Permits Short-Term Memory". *Proceedings of the National Academy of Sciences* 108.9 (2011), pp. 3779–3784.

[122] M Shafi et al. "Variability in Neuronal Activity in Primate Cortex during Working Memory Tasks". *Neuroscience* 146.3 (2007), pp. 1082–1108.

[123] C. R. Hussar and T. Pasternak. "Memory-Guided Sensory Comparisons in the Prefrontal Cortex: Contribution of Putative Pyramidal Cells and Interneurons". *Journal of Neuroscience* 32.8 (2012), pp. 2747–2761.

[124] S. Fujisawa et al. "Behavior-Dependent Short-Term Assembly Dynamics in the Medial Prefrontal Cortex". *Nature neuroscience* 11.7 (2008), p. 823.

[125] M. Lundqvist, P. Herman, and A. Lansner. "Theta and Gamma Power Increases and Alpha/Beta Power Decreases with Memory Load in an Attractor Network Model". *Journal of cognitive neuroscience* 23.10 (2011), pp. 3008–3020.

[126] N. S. Rose et al. "Reactivation of Latent Working Memories with Transcranial Magnetic Stimulation". *Science (New York, N.Y.)* 354.6316 (2016), pp. 1136–1139.

[127] E. K. Miller, M. Lundqvist, and A. M. Bastos. “Working Memory 2.0”. *Neuron* 100.2 (2018), pp. 463–475.

[128] M. Tsodyks, A. Uziel, and H. Markram. “Synchrony Generation in Recurrent Networks with Frequency-Dependent Synapses”. *The Journal of neuroscience : the official journal of the Society for Neuroscience* 20.1 (2000), pp. 825–835.

[129] S. Luccioli et al. “Clique of Functional Hubs Orchestrates Population Bursts in Developmentally Regulated Neural Networks”. *PLoS Computational Biology* 10.9 (2014).

[130] J. D. Murray et al. “Stable Population Coding for Working Memory Coexists with Heterogeneous Neural Dynamics in Prefrontal Cortex”. *Proceedings of the National Academy of Sciences* 114.2 (2017), pp. 394–399.

[131] T. B. Luke, E. Barreto, and P. So. “Complete Classification of the Macroscopic Behavior of a Heterogeneous Network of Theta Neurons”. *Neural computation* 25.12 (2013), pp. 3207–3234.

[132] C. R. Laing. “Derivation of a Neural Field Model from a Network of Theta Neurons”. *Physical Review E* 90.1 (2014), p. 010901.

[133] C. R. Laing. “Phase Oscillator Network Models of Brain Dynamics”. *Computational models of brain and behavior* (2017), pp. 505–517.

[134] G. Dumont and B. Gutkin. “Macroscopic Phase Resetting-Curves Determine Oscillatory Coherence and Signal Transfer in Inter-Coupled Neural Circuits”. *PLoS computational biology* 15.5 (2019), e1007019.

[135] H. Bi et al. “Coexistence of Fast and Slow Gamma Oscillations in One Population of Inhibitory Spiking Neurons”. *Physical Review Research* 2.1 (2020), p. 013042.

[136] M. Okun, A. Naim, and I. Lampl. “The Subthreshold Relation between Cortical Local Field Potential and Neuronal Firing Unveiled by Intracellular Recordings in Awake Rats”. *Journal of neuroscience* 30.12 (2010), pp. 4440–4448.

[137] E. K. Vogel, A. W. McCollough, and M. G. Machizawa. “Neural Measures Reveal Individual Differences in Controlling Access to Working Memory”. *Nature* 438.7067 (2005), pp. 500–503.

[138] D. J. Amit and N. Brunel. “Model of Global Spontaneous Activity and Local Structured Activity during Delay Periods in the Cerebral Cortex.” *Cerebral cortex (New York, NY: 1991)* 7.3 (1997), pp. 237–252.

[139] E. Fino and R. Yuste. “Dense Inhibitory Connectivity in Neocortex”. *Neuron* 69.6 (2011), pp. 1188–1203.

[140] P. Tiesinga and T. J. Sejnowski. “Cortical Enlightenment: Are Attentional Gamma Oscillations Driven by ING or PING?” *Neuron* 63.6 (2009), pp. 727–732.

[141] M. Dipoppa and B. S. Gutkin. “Flexible Frequency Control of Cortical Oscillations Enables Computations Required for Working Memory”. *Proceedings of the National Academy of Sciences* 110.31 (2013), pp. 12828–12833.

[142] M. K. van Vugt et al. “Hippocampal Gamma Oscillations Increase with Memory Load”. *Journal of Neuroscience* 30.7 (2010), pp. 2694–2699.

[143] F. Roux et al. “Gamma-Band Activity in Human Prefrontal Cortex Codes for the Number of Relevant Items Maintained in Working Memory”. *Journal of Neuroscience* 32.36 (2012), pp. 12411–12420.

[144] J. A. Lewis-Peacock and K. A. Norman. “Competition between Items in Working Memory Leads to Forgetting”. *Nature Communications* 5.1 (2014), pp. 1–10.

[145] Y.-C. Lai and T. Tél. *Transient Chaos: Complex Dynamics on Finite Time Scales.* Vol. 173. Springer Science & Business Media, 2011.

[146] J. M. Cortes et al. “Short-Term Synaptic Plasticity in the Deterministic Tsodyks–Markram Model Leads to Unpredictable Network Dynamics”. *Proceedings of the National Academy of Sciences* 110.41 (2013), pp. 16610–16615.

[147] S. Olmi, A. Politi, and A. Torcini. “Stability of the Splay State in Networks of Pulse-Coupled Neurons”. *The Journal of Mathematical Neuroscience* 2.1 (2012), p. 12.

[148] S. Kornblith, T. J. Buschman, and E. K. Miller. “Stimulus Load and Oscillatory Activity in Higher Cortex”. *Cerebral Cortex* 26.9 (2016), pp. 3772–3784.

[149] N. Cowan. “The Magical Number 4 in Short-Term Memory: A Reconsideration of Mental Storage Capacity”. *Behavioral and brain sciences* 24.1 (2001), pp. 87–114.

[150] N. Cowan. “The Magical Mystery Four: How Is Working Memory Capacity Limited, and Why?” *Current directions in psychological science* 19.1 (2010), pp. 51–57.

[151] P. Virtanen et al. “SciPy 1.0: Fundamental Algorithms for Scientific Computing in Python”. *Nature Methods* 17 (2020), pp. 261–272.

[152] F. Devalle, E. Montbrió, and D. Pazó. “Dynamics of a Large System of Spiking Neurons with Synaptic Delay”. *Physical Review E* 98.4 (2018), p. 042214.

[153] E. J. Doedel et al. “AUTO-07P: Continuation and Bifurcation Software for Ordinary Differential Equations” (2007).

[154] P. Dayan and L. F. Abbott. *Theoretical Neuroscience: Computational and Mathematical Modeling of Neural Systems.* Computational Neuroscience Series, 2001.

[155] M. Gerster et al. “Patient-Specific Network Connectivity Combined With a Next Generation Neural Mass Model to Test Clinical Hypothesis of Seizure Propagation”. *Frontiers in Systems Neuroscience* 15 (2021), p. 79.

[156] W. H. Organization et al. *Atlas: Epilepsy Care in the World.* World Health Organization, 2005.

[157] P. Kwan and M. J. Brodie. “Early Identification of Refractory Epilepsy”. *New England Journal of Medicine* 342.5 (2000), pp. 314–319.

[158] O. David et al. “Imaging the Seizure Onset Zone with Stereo-Electroencephalography”. *Brain : a journal of neurology* 134.10 (2011), pp. 2898–2911.

[159] J. S. Duncan et al. “Brain Imaging in the Assessment for Epilepsy Surgery”. *The Lancet Neurology* 15.4 (2016), pp. 420–433.

[160] F Bartolomei et al. “The Presurgical Evaluation of Epilepsies”. *Revue neurologique* 158.5 Pt 2 (2002), 4S55–64.

[161] P. J. Basser et al. “In Vivo Fiber Tractography Using DT-MRI Data”. *Magnetic resonance in medicine* 44.4 (2000), pp. 625–632.

[162] K. M. Leyden et al. “What Does Diffusion Tensor Imaging (DTI) Tell Us about Cognitive Networks in Temporal Lobe Epilepsy?” *Quantitative imaging in medicine and surgery* 5.2 (2015), p. 247.

[163] M. E. Ahmadi et al. “Side Matters: Diffusion Tensor Imaging Tractography in Left and Right Temporal Lobe Epilepsy”. *American journal of neuroradiology* 30.9 (2009), pp. 1740–1747.

[164] B. Bernhardt et al. “Imaging Structural and Functional Brain Networks in Temporal Lobe Epilepsy”. *Frontiers in human neuroscience* 7 (2013), p. 624.

[165] L. Bonilha et al. "Medial Temporal Lobe Epilepsy Is Associated with Neuronal Fibre Loss and Paradoxical Increase in Structural Connectivity of Limbic Structures". *Journal of Neurology, Neurosurgery & Psychiatry* 83.9 (2012), pp. 903–909.

[166] M. N. DeSalvo et al. "Altered Structural Connectome in Temporal Lobe Epilepsy". *Radiology* 270.3 (2014), pp. 842–848.

[167] P. Besson et al. "Structural Connectivity Differences in Left and Right Temporal Lobe Epilepsy". *Neuroimage* 100 (2014), pp. 135–144.

[168] J. De Tisi et al. "The Long-Term Outcome of Adult Epilepsy Surgery, Patterns of Seizure Remission, and Relapse: A Cohort Study". *The Lancet* 378.9800 (2011), pp. 1388–1395.

[169] I. Najm et al. "Temporal Patterns and Mechanisms of Epilepsy Surgery Failure". *Epilepsia* 54.5 (2013), pp. 772–782.

[170] D. Freestone et al. "Patient-Specific Neural Mass Modeling-Stochastic and Deterministic Methods". *Recent Advances in Predicting and Preventing Epileptic Seizures*. World Scientific, 2013, pp. 63–82.

[171] F. Hutchings et al. "Predicting Surgery Targets in Temporal Lobe Epilepsy through Structural Connectome Based Simulations". *PLoS computational biology* 11.12 (2015), e1004642.

[172] M Goodfellow et al. "Estimation of Brain Network Ictogenicity Predicts Outcome from Epilepsy Surgery". *Scientific reports* 6.1 (2016), pp. 1–13.

[173] A. N. Khambhati et al. "Virtual Cortical Resection Reveals Push-Pull Network Control Preceding Seizure Evolution". *Neuron* 91.5 (2016), pp. 1170–1182.

[174] N. Sinha et al. "Predicting Neurosurgical Outcomes in Focal Epilepsy Patients Using Computational Modelling". *Brain : a journal of neurology* 140.2 (2017), pp. 319–332.

[175] P. J. Karoly et al. "Seizure Pathways: A Model-Based Investigation". *PLoS computational biology* 14.10 (2018), e1006403.

[176] F. Bartolomei et al. "Defining Epileptogenic Networks: Contribution of SEEG and Signal Analysis". *Epilepsia* 58.7 (2017), pp. 1131–1147.

[177] P. Besson et al. "Anatomic Consistencies across Epilepsies: A Stereotactic-EEG Informed High-Resolution Structural Connectivity Study". *Brain : a journal of neurology* 140.10 (2017), pp. 2639–2652.

[178] M. A. Lopes et al. "The Role of Excitability and Network Structure in the Emergence of Focal and Generalized Seizures". *Frontiers in neurology* 11 (2020), p. 74.

[179] F. L. Da Silva et al. "Model of Brain Rhythmic Activity". *Kybernetik* 15.1 (1974), pp. 27–37.

[180] F Wendling et al. "Epileptic Fast Activity Can Be Explained by a Model of Impaired GABAergic Dendritic Inhibition". *European Journal of Neuroscience* 15.9 (2002), pp. 1499–1508.

[181] S. N. Kalitzin, D. N. Velis, and F. H. L. da Silva. "Stimulation-Based Anticipation and Control of State Transitions in the Epileptic Brain". *Epilepsy & Behavior* 17.3 (2010), pp. 310–323.

[182] J. Touboul et al. "Neural Mass Activity, Bifurcations, and Epilepsy". *Neural computation* 23.12 (2011), pp. 3232–3286.

[183] G. Baier et al. "The Importance of Modeling Epileptic Seizure Dynamics as Spatio-Temporal Patterns". *Frontiers in physiology* 3 (2012), p. 281.

[184] M. A. Kramer et al. “Human Seizures Self-Terminate across Spatial Scales via a Critical Transition”. *Proceedings of the National Academy of Sciences* 109.51 (2012), pp. 21116–21121.

[185] M. Goodfellow, K. Schindler, and G. Baier. “Self-Organised Transients in a Neural Mass Model of Epileptogenic Tissue Dynamics”. *NeuroImage* 59.3 (2012), pp. 2644–2660.

[186] V. K. Jirsa et al. “On the Nature of Seizure Dynamics”. *Brain : a journal of neurology* 137.8 (2014), pp. 2210–2230.

[187] J. R. Terry, O. Benjamin, and M. P. Richardson. “Seizure Generation: The Role of Nodes and Networks”. *Epilepsia* 53.9 (2012), e166–e169.

[188] P. N. Taylor et al. “Towards a Large-Scale Model of Patient-Specific Epileptic Spike-Wave Discharges”. *Biological cybernetics* 107.1 (2013), pp. 83–94.

[189] M. A. Kramer et al. “Mechanisms of Seizure Propagation in a Cortical Model”. *Journal of computational neuroscience* 22.1 (2007), pp. 63–80.

[190] M. Goodfellow, K. Schindler, and G. Baier. “Intermittent Spike–Wave Dynamics in a Heterogeneous, Spatially Extended Neural Mass Model”. *Neuroimage* 55.3 (2011), pp. 920–932.

[191] F. Bartolomei, M. Guye, and F. Wendling. “Abnormal Binding and Disruption in Large Scale Networks Involved in Human Partial Seizures”. *EPJ Nonlinear Biomedical Physics* 1.1 (2013), p. 4.

[192] I. Toyoda et al. “Early Activation of Ventral Hippocampus and Subiculum during Spontaneous Seizures in a Rat Model of Temporal Lobe Epilepsy”. *Journal of Neuroscience* 33.27 (2013), pp. 11100–11115.

[193] A. Destexhe and T. J. Sejnowski. “G Protein Activation Kinetics and Spillover of Gamma-Aminobutyric Acid May Account for Differences between Inhibitory Responses in the Hippocampus and Thalamus”. *Proceedings of the National Academy of Sciences* 92.21 (1995), pp. 9515–9519.

[194] W. Van Drongelen et al. “Emergent Epileptiform Activity in Neural Networks with Weak Excitatory Synapses”. *IEEE Transactions on Neural Systems and Rehabilitation Engineering* 13.2 (2005), pp. 236–241.

[195] G. G. Turrigiano. “The Self-Tuning Neuron: Synaptic Scaling of Excitatory Synapses”. *Cell* 135.3 (2008), pp. 422–435.

[196] J. R. Cressman et al. “The Influence of Sodium and Potassium Dynamics on Excitability, Seizures, and the Stability of Persistent States: I. Single Neuron Dynamics”. *Journal of computational neuroscience* 26.2 (2009), pp. 159–170.

[197] G. Ullah et al. “The Influence of Sodium and Potassium Dynamics on Excitability, Seizures, and the Stability of Persistent States: II. Network and Glial Dynamics”. *Journal of computational neuroscience* 26.2 (2009), pp. 171–183.

[198] E. Brocke et al. “Efficient Integration of Coupled Electrical-Chemical Systems in Multiscale Neuronal Simulations”. *Frontiers in computational neuroscience* 10 (2016), p. 97.

[199] M. Schirner et al. “Inferring Multi-Scale Neural Mechanisms with Brain Network Modelling”. *Elife* 7 (2018), e28927.

[200] R. Lindroos et al. “Basal Ganglia Neuromodulation over Multiple Temporal and Structural Scales Simulations of Direct Pathway MSNs Investigate the Fast Onset of Dopaminergic Effects and Predict the Role of Kv4. 2”. *Frontiers in Neural Circuits* 12 (2018), p. 3.

[201] T. Proix et al. "Individual Structural Connectivity Defines Propagation Networks in Partial Epilepsy". *Brain : a journal of neurology* 140 (2017), pp. 641–654.

[202] T. Proix et al. "Predicting the Spatiotemporal Diversity of Seizure Propagation and Termination in Human Focal Epilepsy". *Nature communications* 9.1 (2018), pp. 1–15.

[203] S. Olmi et al. "Controlling Seizure Propagation in Large-Scale Brain Networks". *PLoS computational biology* 15.2 (2019), e1006805.

[204] A. Fuchs, V. K. Jirsa, and J. S. Kelso. "Theory of the Relation between Human Brain Activity (MEG) and Hand Movements". *Neuroimage* 11.5 (2000), pp. 359–369.

[205] V. K. Jirsa et al. "Spatiotemporal Forward Solution of the EEG and MEG Using Network Modeling". *IEEE transactions on medical imaging* 21.5 (2002), pp. 493–504.

[206] V. Jirsa et al. "Towards the Virtual Brain: Network Modeling of the Intact and the Damaged Brain". *Archives italiennes de biologie* 148.3 (2010), pp. 189–205.

[207] J. Goldman et al. "Brain-Scale Emergence of Slow-Wave Synchrony and Highly Responsive Asynchronous States Based on Biologically Realistic Population Models Simulated in The Virtual Brain". *bioRxiv : the preprint server for biology* (2020).

[208] M. L. Kringelbach et al. "Dynamic Coupling of Whole-Brain Neuronal and Neurotransmitter Systems". *Proceedings of the National Academy of Sciences* 117.17 (2020), pp. 9566–9576.

[209] G. Rabuffo et al. "Neuronal Cascades Shape Whole-Brain Functional Dynamics at Rest". *bioRxiv : the preprint server for biology* (2020).

[210] V. K. Jirsa. "Dispersion and Time Delay Effects in Synchronized Spike–Burst Networks". *Cognitive neurodynamics* 2.1 (2008), pp. 29–38.

[211] S. Petkoski and V. Jirsa. "Renormalization of the Brain Connectome: Duality of Particle and Wave". *bioRxiv : the preprint server for biology* (2020).

[212] N. Tzourio-Mazoyer et al. "Automated Anatomical Labeling of Activations in SPM Using a Macroscopic Anatomical Parcellation of the MNI MRI Single-Subject Brain". *Neuroimage* 15.1 (2002), pp. 273–289.

[213] R. S. Desikan et al. "An Automated Labeling System for Subdividing the Human Cerebral Cortex on MRI Scans into Gyral Based Regions of Interest". *Neuroimage* 31.3 (2006), pp. 968–980.

[214] T. Melicher et al. "White Matter Changes in First Episode Psychosis and Their Relation to the Size of Sample Studied: A DTI Study". *Schizophrenia Research* 162.1 (2015), pp. 22–28.

[215] Y. Lecrubier et al. "The Mini International Neuropsychiatric Interview (MINI). A Short Diagnostic Structured Interview: Reliability and Validity According to the CIDI". *Eur. Psychiatry* 12.5 (1997), pp. 224–231.

[216] S. Smith et al. "Tract-Based Spatial Statistics: Voxelwise Analysis of Multi-Subject Diffusion Data". *Neuroimage* 31.4 (2006), pp. 1487–1505.

[217] S. Smith et al. "Advances in Functional and Structural MR Image Analysis and Implementation as FSL". *Neuroimage* 23 (2004), S208–S219.

[218] S. Smith. "Fast Robust Automated Brain Extraction". *Human Brain Mapping* 17.3 (2002), pp. 143–155.

[219] D. Rueckert et al. "Nonrigid Registration Using Free-Form Deformations: Application to Breast MR Images". *IEEE Transactions on Medical Imaging* 18.8 (1999), pp. 712–721.

[220] J. Cabral et al. "Structural Connectivity in Schizophrenia and Its Impact on the Dynamics of Spontaneous Functional Networks". *Chaos (Woodbury, N.Y.)* 23.4 (2013), p. 046111.

[221] M. Schirner et al. "An Automated Pipeline for Constructing Personalized Virtual Brains from Multimodal Neuroimaging Data". *NeuroImage* 117 (2015), pp. 343–357.

[222] T. Proix et al. "How Do Parcellation Size and Short-Range Connectivity Affect Dynamics in Large-Scale Brain Network Models?" *NeuroImage* 142 (2016), pp. 135–149.

[223] B. Fischl. "FreeSurfer". *Neuroimage* 62.2 (2012), pp. 774–781.

[224] M. Jenkinson et al. "Fsl". *Neuroimage* 62.2 (2012), pp. 782–790.

[225] J. Tournier. "MRtrix Package". *Brain Research Institute, Melbourne, Australia, https://github. com/jdtournier/mrtrix3. Available at: https://github. com/jdtournier/mrtrix3* (2010).

[226] S. Fuhrmann et al. "Direct Resampling for Isotropic Surface Remeshing." *VMV* (2010), pp. 9–16.

[227] J. Tournier, F. Calamante, and A. Connelly. "Robust Determination of the Fibre Orientation Distribution in Diffusion MRI: Non-Negativity Constrained Super-Resolved Spherical Deconvolution". *Neuroimage* 35.4 (2007), pp. 1459–1472.

[228] R. E. Smith et al. "Anatomically-Constrained Tractography: Improved Diffusion MRI Streamlines Tractography through Effective Use of Anatomical Information". *Neuroimage* 62.3 (2012), pp. 1924–1938.

[229] R. E. Smith et al. "SIFT: Spherical-Deconvolution Informed Filtering of Tractograms". *Neuroimage* 67 (2013), pp. 298–312.

[230] A. Barrat et al. "The Architecture of Complex Weighted Networks". *Proceedings of the National Academy of Sciences of the United States of America* 101.11 (2004), pp. 3747–3752.

[231] S. Boccaletti et al. "Complex Networks: Structure and Dynamics". *Physics reports* 424.4-5 (2006), pp. 175–308.

[232] K. El Houssaini, C. Bernard, and V. K. Jirsa. "The Epileptor Model: A Systematic Mathematical Analysis Linked to the Dynamics of Seizures, Refractory Status Epilepticus and Depolarization Block". *Eneuro* (2020).

[233] A. V. Chizhov et al. "Minimal Model of Interictal and Ictal Discharges "Epileptor-2"". *PLoS computational biology* 14.5 (2018), e1006186.

[234] M. L. Saggio et al. "Fast–Slow Bursters in the Unfolding of a High Codimension Singularity and the Ultra-Slow Transitions of Classes". *The Journal of Mathematical Neuroscience* 7.1 (2017), pp. 1–47.

[235] E. S. Schaffer, S. Ostojic, and L. F. Abbott. "A Complex-Valued Firing-Rate Model That Approximates the Dynamics of Spiking Networks". *PLoS computational biology* 9.10 (2013), e1003301.

[236] J. Creaser et al. "Domino-like Transient Dynamics at Seizure Onset in Epilepsy". *PLoS computational biology* 16.9 (2020), e1008206.

[237] J Jacobs et al. "High-Frequency Oscillations (HFOs) in Clinical Epilepsy". *Progress in neurobiology* 98.3 (2012), pp. 302–315.

[238] S. Ahmadizadeh et al. "Bifurcation Analysis of Two Coupled Jansen-Rit Neural Mass Models". *PloS one* 13.3 (2018), e0192842.

[239] F. Khadjevand, J. Cimbalnik, and G. A. Worrell. "Progress and Remaining Challenges in the Application of High Frequency Oscillations as Biomarkers of Epileptic Brain". *Current opinion in biomedical engineering* 4 (2017), pp. 87–96.

[240] S. Wang et al. "Ripple Classification Helps to Localize the Seizure-Onset Zone in Neocortical Epilepsy". *Epilepsia* 54.2 (2013), pp. 370–376.

[241] P. Allen, D. Fish, and S. Smith. "Very High-Frequency Rhythmic Activity during SEEG Suppression in Frontal Lobe Epilepsy". *Electroencephalography and clinical neurophysiology* 82.2 (1992), pp. 155–159.

[242] R. D. Traub et al. "A Possible Role for Gap Junctions in Generation of Very Fast EEG Oscillations Preceding the Onset of, and Perhaps Initiating, Seizures". *Epilepsia* 42 (2001), pp. 153–170.

[243] G. A. Worrell et al. "High-Frequency Oscillations and Seizure Generation in Neocortical Epilepsy". *Brain : a journal of neurology* 127.7 (2004), pp. 1496–1506.

[244] M. Zijlmans et al. "High-Frequency Oscillations as a New Biomarker in Epilepsy". *Annals of neurology* 71.2 (2012), pp. 169–178.

[245] L. Zetterberg, L Kristiansson, and K Mossberg. "Performance of a Model for a Local Neuron Population". *Biological cybernetics* 31.1 (1978), pp. 15–26.

[246] F. L. Da Silva et al. "Models of Neuronal Populations: The Basic Mechanisms of Rhythmicity". *Progress in Brain Research*. Vol. 45. Elsevier, 1976, pp. 281–308.

[247] R. C. Sotero et al. "Realistically Coupled Neural Mass Models Can Generate EEG Rhythms". *Neural computation* 19.2 (2007), pp. 478–512.

[248] F. Wendling et al. "Computational Models of Epileptiform Activity". *Journal of neuroscience methods* 260 (2016), pp. 233–251.

[249] A. Spiegler et al. "Modeling Brain Resonance Phenomena Using a Neural Mass Model". *PLoS computational biology* 7.12 (2011), e1002298.

[250] A. Ghosh et al. "Noise during Rest Enables the Exploration of the Brain's Dynamic Repertoire". *PLoS computational biology* 4.10 (2008), e1000196.

[251] G. Deco, V. K. Jirsa, and A. R. McIntosh. "Emerging Concepts for the Dynamical Organization of Resting-State Activity in the Brain". *Nature Reviews Neuroscience* 12.1 (2011), pp. 43–56.

[252] R. Huys, D. Perdikis, and V. K. Jirsa. "Functional Architectures and Structured Flows on Manifolds: A Dynamical Framework for Motor Behavior." *Psychological review* 121.3 (2014), p. 302.

[253] T. Kunze et al. "Transcranial Direct Current Stimulation Changes Resting State Functional Connectivity: A Large-Scale Brain Network Modeling Study". *Neuroimage* 140 (2016), pp. 174–187.

[254] B. S. Bhattacharya and F. N. Chowdhury. *Validating Neuro-Computational Models of Neurological and Psychiatric Disorders*. Vol. 14. Springer, 2015.

[255] P. A. Valdes-Sosa et al. "Model Driven EEG/fMRI Fusion of Brain Oscillations". *Human brain mapping* 30.9 (2009), pp. 2701–2721.

[256] R. J. Moran, D. A. Pinotsis, and K. J. Friston. "Neural Masses and Fields in Dynamic Causal Modeling". *Frontiers in computational neuroscience* 7 (2013), p. 57.

[257] I. Bojak and M. Breakspear. "Neuroimaging, Neural Population Models For" (2014).

[258] P. Sanz-Leon et al. "Mathematical Framework for Large-Scale Brain Network Modeling in The Virtual Brain". *Neuroimage* 111 (2015), pp. 385–430.

[259] G. Pfurtscheller and F. L. Da Silva. "Event-Related EEG/MEG Synchronization and Desynchronization: Basic Principles". *Clinical neurophysiology* 110.11 (1999), pp. 1842–1857.

[260] Á. Byrne et al. "Next-Generation Neural Mass and Field Modeling". *Journal of neurophysiology* 123.2 (2020), pp. 726–742.

[261] M. L. Saggio et al. "A Taxonomy of Seizure Dynamotypes". *Elife* 9 (2020), e55632.

[262] D. Flanagan et al. "Single-Pulse Electrical Stimulation Helps to Identify Epileptogenic Cortex in Children". *Epilepsia* 50.7 (2009), pp. 1793–1803.

[263] J. Jacobs et al. "Value of Electrical Stimulation and High Frequency Oscillations (80–500 Hz) in Identifying Epileptogenic Areas during Intracranial EEG Recordings". *Epilepsia* 51.4 (2010), pp. 573–582.

[264] A. Valentin et al. "Responses to Single Pulse Electrical Stimulation Identify Epileptogenesis in the Human Brain in Vivo". *Brain : a journal of neurology* 125.8 (2002), pp. 1709–1718.

[265] M. Breakspear and V. K. Jirsa. "Neuronal Dynamics and Brain Connectivity". *Handbook of Brain Connectivity*. Springer, 2007, pp. 3–64.

[266] M. A. Kramer, H. E. Kirsch, and A. J. Szeri. "Pathological Pattern Formation and Cortical Propagation of Epileptic Seizures". *Journal of the Royal Society Interface* 2.2 (2005), pp. 113–127.

[267] J. Kim, J. Roberts, and P. Robinson. "Dynamics of Epileptic Seizures: Evolution, Spreading, and Suppression". *Journal of theoretical biology* 257.4 (2009), pp. 527–532.

[268] F. Marten et al. "Onset of Polyspike Complexes in a Mean-Field Model of Human Electroencephalography and Its Application to Absence Epilepsy". *Philosophical Transactions of the Royal Society A: Mathematical, Physical and Engineering Sciences* 367.1891 (2009), pp. 1145–1161.

[269] B. A. Lopour and A. J. Szeri. "A Model of Feedback Control for the Charge-Balanced Suppression of Epileptic Seizures". *Journal of computational neuroscience* 28.3 (2010), pp. 375–387.

[270] S. Sagar et al. "Functional Brain Mapping: Overview of Techniques and Their Application to Neurosurgery". *Neurosurgical review* 42.3 (2019), pp. 639–647.

[271] K Hara et al. "Representation of Primary Motor Cortex in Humans: Studied with Chronic Subdural Grid". *Epilepsia* 32.SUPPL. (1991), pp. 23–24.

[272] G. A. Ojemann. "Cortical Organization of Language". *Journal of Neuroscience* 11.8 (1991), pp. 2281–2287.

[273] S. Uematsu et al. "Motor and Sensory Cortex in Humans: Topography Studied with Chronic Subdural Stimulation". *Neurosurgery* 31.1 (1992), pp. 59–72.

[274] A. Chakraborty and A. W. McEvoy. "Presurgical Functional Mapping with Functional MRI". *Current opinion in neurology* 21.4 (2008), pp. 446–451.

[275] R. G. Bittar et al. "Localization of Somatosensory Function by Using Positron Emission Tomography Scanning: A Comparison with Intraoperative Cortical Stimulation". *Journal of neurosurgery* 90.3 (1999), pp. 478–483.

[276] P. Meyer et al. "Preoperative Motor System Brain Mapping Using Positron Emission Tomography and Statistical Parametric Mapping: Hints on Cortical Reorganisation". *Journal of Neurology, Neurosurgery & Psychiatry* 74.4 (2003), pp. 471–478.

[277] O. Ganslandt et al. "Functional Neuronavigation with Magnetoencephalography: Outcome in 50 Patients with Lesions around the Motor Cortex". *Journal of neurosurgery* 91.1 (1999), pp. 73–79.

[278] D. Dinner et al. "Invasive Methods of Somatosensory Evoked Potential Monitoring". *Journal of Clinical Neurophysiology* 3.2 (1986), pp. 113–130.

[279] P. Brunner et al. "A Practical Procedure for Real-Time Functional Mapping of Eloquent Cortex Using Electrocorticographic Signals in Humans". *Epilepsy & Behavior* 15.3 (2009), pp. 278–286.

[280] N. E. Crone et al. "Functional Mapping of Human Sensorimotor Cortex with Electrocorticographic Spectral Analysis. I. Alpha and Beta Event-Related Desynchronization." *Brain: a journal of neurology* 121.12 (1998), pp. 2271–2299.

[281] N. E. Crone et al. "Functional Mapping of Human Sensorimotor Cortex with Electrocorticographic Spectral Analysis. II. Event-Related Synchronization in the Gamma Band." *Brain: a journal of neurology* 121.12 (1998), pp. 2301–2315.

[282] F Aoki et al. "Increased Gamma-Range Activity in Human Sensorimotor Cortex during Performance of Visuomotor Tasks". *Clinical Neurophysiology* 110.3 (1999), pp. 524–537.

[283] F Aoki et al. "Changes in Power and Coherence of Brain Activity in Human Sensorimotor Cortex during Performance of Visuomotor Tasks". *Bio Systems* 63.1-3 (2001), pp. 89–99.

[284] N. E. Crone et al. "Induced Electrocorticographic Gamma Activity during Auditory Perception". *Clinical neurophysiology* 112.4 (2001), pp. 565–582.

[285] A. Sinai et al. "Electrocorticographic High Gamma Activity versus Electrical Cortical Stimulation Mapping of Naming". *Brain : a journal of neurology* 128.7 (2005), pp. 1556–1570.

[286] K. J. Miller et al. "Spectral Changes in Cortical Surface Potentials during Motor Movement". *Journal of Neuroscience* 27.9 (2007), pp. 2424–2432.

[287] E. C. Leuthardt et al. "Electrocorticographic Frequency Alteration Mapping: A Clinical Technique for Mapping the Motor Cortex". *Operative Neurosurgery* 60.suppl_4 (2007), ONS–260.

[288] J. G. Jefferys, R. D. Traub, and M. A. Whittington. "Neuronal Networks for Induced '40 Hz' Rhythms". *Trends in neurosciences* 19.5 (1996), pp. 202–208.

[289] M. A. Whittington et al. "Inhibition-Based Rhythms: Experimental and Mathematical Observations on Network Dynamics". *International journal of psychophysiology* 38.3 (2000), pp. 315–336.

[290] R. Cossart et al. "Dendritic but Not Somatic GABAergic Inhibition Is Decreased in Experimental Epilepsy". *Nature neuroscience* 4.1 (2001), pp. 52–62.

[291] J. A. White et al. "Networks of Interneurons with Fast and Slow γ-Aminobutyric Acid Type A (GABAA) Kinetics Provide Substrate for Mixed Gamma-Theta Rhythm". *Proceedings of the National Academy of Sciences* 97.14 (2000), pp. 8128–8133.

[292] M. I. Banks, J. A. White, and R. A. Pearce. "Interactions between Distinct GABAA Circuits in Hippocampus". *Neuron* 25.2 (2000), pp. 449–457.

[293] M. Shamas et al. "On the Origin of Epileptic High Frequency Oscillations Observed on Clinical Electrodes". *Clinical Neurophysiology* 129.4 (2018), pp. 829–841.

[294] M. Kaiser, M. Goerner, and C. C. Hilgetag. "Criticality of Spreading Dynamics in Hierarchical Cluster Networks without Inhibition". *New Journal of Physics* 9.5 (2007), p. 110.

[295] R. J. Morgan and I. Soltesz. "Nonrandom Connectivity of the Epileptic Dentate Gyrus Predicts a Major Role for Neuronal Hubs in Seizures". *Proceedings of the National Academy of Sciences* 105.16 (2008), pp. 6179–6184.

[296] D. Hall and L. Kuhlmann. "Mechanisms of Seizure Propagation in 2-Dimensional Centre-Surround Recurrent Networks". *PLoS One* 8.8 (2013), e71369.

[297] M. Ursino and G.-E. La Cara. "Travelling Waves and EEG Patterns during Epileptic Seizure: Analysis with an Integrate-and-Fire Neural Network". *Journal of theoretical biology* 242.1 (2006), pp. 171–187.

[298] R. Miles, R. D. Traub, and R. Wong. "Spread of Synchronous Firing in Longitudinal Slices from the CA3 Region of the Hippocampus". *Journal of Neurophysiology* 60.4 (1988), pp. 1481–1496.

[299] D. Golomb and Y. Amitai. "Propagating Neuronal Discharges in Neocortical Slices: Computational and Experimental Study". *Journal of neurophysiology* 78.3 (1997), pp. 1199–1211.

[300] A. Compte et al. "Cellular and Network Mechanisms of Slow Oscillatory Activity (¡ 1 Hz) and Wave Propagations in a Cortical Network Model". *Journal of neurophysiology* 89.5 (2003), pp. 2707–2725.

[301] M. Bazhenov et al. "Cellular and Network Mechanisms of Electrographic Seizures". *Drug Discovery Today: Disease Models* 5.1 (2008), pp. 45–57.

[302] T. Chouzouris et al. "Chimera States in Brain Networks: Empirical Neural vs. Modular Fractal Connectivity". *Chaos: An Interdisciplinary Journal of Nonlinear Science* 28.4 (2018), p. 045112.

[303] M. Gerster et al. "FitzHugh–Nagumo Oscillators on Complex Networks Mimic Epileptic-Seizure-Related Synchronization Phenomena". *Chaos: An Interdisciplinary Journal of Nonlinear Science* 30.12 (2020), p. 123130.

[304] J. P. Lieb et al. "Inter-Hemispheric Propagation of Human Mesial Temporal Lobe Seizures: A Coherence/Phase Analysis". *Electroencephalography and clinical neurophysiology* 67.2 (1987), pp. 101–119.

[305] J. P. Lieb et al. "Role of the Frontal Lobes in the Propagation of Mesial Temporal Lobe Seizures". *Epilepsia* 32.6 (1991), pp. 822–837.

[306] R. M. Cassidy and K. Gale. "Mediodorsal Thalamus Plays a Critical Role in the Development of Limbic Motor Seizures". *Journal of Neuroscience* 18.21 (1998), pp. 9002–9009.

[307] D. S. Rosenberg et al. "Involvement of Medial Pulvinar Thalamic Nucleus in Human Temporal Lobe Seizures". *Epilepsia* 47.1 (2006), pp. 98–107.

[308] G. Bettus et al. "Decreased Basal fMRI Functional Connectivity in Epileptogenic Networks and Contralateral Compensatory Mechanisms". *Human brain mapping* 30.5 (2009), pp. 1580–1591.

[309] T. Proix et al. "Permittivity Coupling across Brain Regions Determines Seizure Recruitment in Partial Epilepsy". *Journal of Neuroscience* 34.45 (2014), pp. 15009–15021.

[310] H. Taher, D. Avitabile, and M. Desroches. "Bursting in a next Generation Neural Mass Model with Synaptic Dynamics: A Slow-Fast Approach". *arXiv:2109.06757v1 [nlin]* (Sept. 2021).

[311] R. E. Plant and M. Kim. "On the Mechanism Underlying Bursting in the Aplysia Abdominal Ganglion R15 Cell". *Mathematical Biosciences* 26.3 (Jan. 1975), pp. 357–375.

[312] J. L. Hindmarsh and R. M. Rose. "A Model of Neuronal Bursting Using Three Coupled First Order Differential Equations". *Proceedings of the Royal society of London. Series B. Biological sciences* 221.1222 (1984), pp. 87–102.

[313] J. Rinzel. "A Formal Classification of Bursting Mechanisms in Excitable Systems". *International Congress of Mathematicians, Berkeley, California, USA, August 3-11, 1986*. Vol. **II**. American Mathematical Society, 1987, pp. 1578–1593.

[314] E. M. Izhikevich. "Neural Excitability, Spiking and Bursting". *International Journal of Bifurcation and Chaos* 10.06 (June 2000), pp. 1171–1266.

[315] B. J. Bacak et al. "Mixed-Mode Oscillations and Population Bursting in the Pre-Bötzinger Complex". *elife* 5 (2016), e13403.

[316] E. K. Ersöz et al. "Canard-Induced Complex Oscillations in an Excitatory Network". *Journal of mathematical biology* 80.7 (2020), pp. 2075–2107.

[317] M. Desroches, M. Krupa, and S. Rodrigues. "Spike-Adding in Parabolic Bursters: The Role of Folded-Saddle Canards". *Physica D: Nonlinear Phenomena* 331 (2016), pp. 58–70.

[318] N. Fenichel. "Geometric Singular Perturbation Theory for Ordinary Differential Equations". *Journal of differential equations* 31.1 (1979), pp. 53–98.

[319] G. Hek. "Geometric Singular Perturbation Theory in Biological Practice". *Journal of mathematical biology* 60.3 (2010), pp. 347–386.

[320] W. Eckhaus. "Relaxation Oscillations Including a Standard Chase on French Ducks". *Asymptotic Analysis II—*. Springer, 1983, pp. 449–497.

[321] M. Krupa and P. Szmolyan. "Extending Geometric Singular Perturbation Theory to Nonhyperbolic Points—Fold and Canard Points in Two Dimensions". *SIAM Journal on Mathematical Analysis* 33.2 (Jan. 2001), pp. 286–314.

[322] A. I. Neishtadt. "Prolongation of the Loss of Stability in the Case of Dynamic Bifurcations. I". *Differentsial'nye Uravneniya* 23.12 (1987), pp. 2060–2067, 2204.

[323] A. I. Neishtadt. "Prolongation of the Loss of Stability in the Case of Dynamic Bifurcations. II". *Differentsial'nye Uravneniya* 24.2 (1988), pp. 226–233, 364.

[324] S. M. Baer, T. Erneux, and J. Rinzel. "The Slow Passage through a Hopf Bifurcation: Delay, Memory Effects, and Resonance". *SIAM Journal on Applied mathematics* 49.1 (1989), pp. 55–71.

[325] M. Desroches, T. J. Kaper, and M. Krupa. "Mixed-Mode Bursting Oscillations: Dynamics Created by a Slow Passage through Spike-Adding Canard Explosion in a Square-Wave Burster". *Chaos: An Interdisciplinary Journal of Nonlinear Science* 23.4 (2013), p. 046106.

[326] Á. Byrne et al. "Mean-Field Models for EEG/MEG: From Oscillations to Waves". *Brain Topography* (May 2021).

[327] R. Gast, H. Schmidt, and T. R. Knösche. "A Mean-Field Description of Bursting Dynamics in Spiking Neural Networks with Short-Term Adaptation". *Neural Computation* 32.9 (Sept. 2020), pp. 1615–1634.

[328] R. Gast, T. R. Knösche, and H. Schmidt. "Mean-Field Approximations of Networks of Spiking Neurons with Short-Term Synaptic Plasticity". *arXiv preprint arXiv:2101.06057* (2021).

[329] F. Palesi et al. "The Importance of Cerebellar Connectivity on Simulated Brain Dynamics". *Frontiers in Cellular Neuroscience* 14 (2020), p. 240.

[330] W. R. Inc. *Mathematica, Version 12.3.1*. Champaign, IL, 2021.

[331] A. Mazzoni et al. "Encoding of Naturalistic Stimuli by Local Field Potential Spectra in Networks of Excitatory and Inhibitory Neurons". *PLOS Computational Biology* 4.12 (Dec. 2008), pp. 1–20.

[332] J. R. Dormand and P. J. Prince. "A Family of Embedded Runge-Kutta Formulae". *Journal of computational and applied mathematics* 6.1 (1980), pp. 19–26.

Glossary

μ-STP	Microscopic STP. 17, 18, 29–31, 50, 53, 119
AdEx	Adaptive Exponential Integrate-and-Fire. 7–9, 122
CO	Collective oscillation. 27, 32, 35, 37, 39–41, 43
dMRI	Diffusion MRI. v, 4, 59, 61, 63, 90, 91
DRS	Desingularized reduced system. 102–104
DTI	Diffusion tensor weighted imaging. 61
EEG	Electroencephalography. v, 1–4, 27, 35, 50, 59–61, 64, 70, 79, 80, 88–90, 92
EZ	Epileptogenic zone. 4, 59, 64, 69, 70, 74, 75, 77–86, 89–91, 132–140
fMRI	Functional MRI. 88, 120, 121
HA	High activity. 4, 66–68, 70, 71, 73–77, 80
HWHM	Half width at half maximum. 13, 15
iEEG	Intracranial EEG. 4, 59
LA	Low activity. 4, 66–68, 71, 73, 75, 77, 79, 82
LC	Limit cycle. 97, 110
LFP	Local field potential. 1, 2, 4, 27, 36, 42, 51
m-STP	Mesoscopic STP. 17, 18, 29–31, 35, 42, 50, 56, 96, 119
MEG	Magnetoencephalography. 1, 59, 88
MPR	Montbrió, Pazó, Roxin. iii, v, viii, 2, 3, 15, 94, 95, 98, 118, 120–122
MRI	Magnetic resonance imaging. 1, 4, 58, 59, 61, 63, 64, 88, 120
NMSTP	Neural mass with short-term synaptic plasticity. 96, 98, 99, 112, 116, 117
OA	Ott-Antonsen. 3, 12, 13, 115, 117, 118, 120, 122

PB	Population burst. 3, 27, 29, 30, 32, 34, 35, 37–39, 42, 44–46, 49, 51–53, 55, 56, 98
PDF	Probability density function. 12, 13, 124
PET	Positron emission tomography. 59
PFC	Prefrontal cortex. 15, 26, 27, 34, 37, 42, 47, 50, 52
PZ	Propagation zone. 4, 59, 64, 70, 79, 80, 82, 83, 85, 89, 90, 132–134, 138
QIF	Quadratic integrate & fire. iii, v, vi, viii, 2, 5, 7–10, 12–19, 27–29, 31, 35, 37, 50, 56, 57, 93–96, 98, 114–116, 118, 119, 122, 123, 125, 126
SEEG	Stereotactic EEG. 4, 59, 61, 64, 80, 91, 138
SNIC	Saddle-node on invariant circle. 7, 9, 10
STP	Short-term synaptic plasticity. iii–vi, 3, 5, 15–18, 20, 24, 27–31, 35, 36, 50, 53, 54, 93–95, 98, 108, 116, 118–120, 123
VdP	Van der Pol. 20–24, 101
WC	Wilson-Cowan. 2, 3
WM	Working memory. 3, 15, 25–28, 31–38, 42, 45, 47, 48, 50–53, 55, 56, 94, 119